The Circumstellar Environments of Dusty Main Sequence Stars

Antonio S. Hales Gebrim

Thesis submitted for the Degree of Doctor of Philosophy
of the University of London

Department of Physics & Astronomy
UNIVERSITY COLLEGE LONDON

January 2007

ProQuest LLC
789 East Eisenhower Parkway
P.O. Box 1346
Ann Arbor, MI 48106-1346

"Si la historia interminable,
se escrbiese a si misma,
seria solo un sofisma
este mundo admirable"
Michael Ende

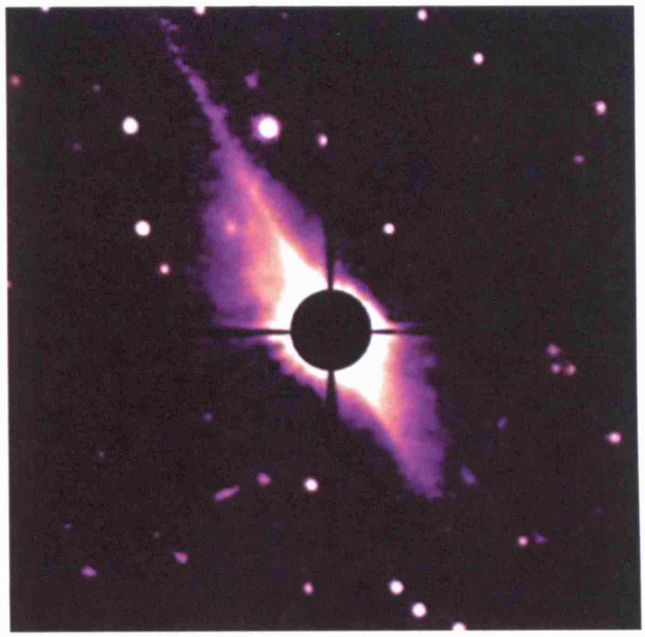

The dust disk around Beta Pictoris. The edge-on disk was discovered by Smith & Terrile (1984) at Las Campanas observatory, and represents the very first evidence of particulate material orbiting another main sequence star than our sun. At the time this picture was taken (22 years before the writing of this thesis), no planets beyond the solar system had been discovered yet. This image represented the beginning of a new research field devoted to understanding how planetary systems like our own form from dusty disks like the one discovered around Beta Pictoris (Picture adapted from Kalas & Jewitt (1995)).

ABSTRACT

Our current understanding of the formation of planetary systems is strongly linked to astronomical observations of gas and dust around young stars. This thesis is dedicated to studying the physical conditions acting in the circumstellar environments of pre-main sequence and early main sequence dusty stars. These early stellar ages correspond to the timescales over which planets are thought to be formed.

The first part of this work is dedicated to a search for dusty early A-type stars in the northern galactic plane. Data from the IPHAS Hα survey is first used to select a sample of galactic A-type stars. This sample is then correlated with data from the Spitzer Space Telescope in order to search for 8 microns and 24 microns excesses associated with warm dust orbiting the stars. The improved photometric sensitivities of these new galactic surveys allow the list of known galactic 'Vega-like' sources to be extended to unexplored optical magnitude ranges ($13.5 < r < 18.5$ mags). Only 1.1% of a sample of 3062 A-type stars with available optical to mid-infrared spectral energy distributions showed detectable excesses at 8 microns. Searching over 1860 stars observed at 24 microns yielded similar statistical results (1.2%). Only 10 stars have both 8 and 24 micron excesses. These results support the idea that warm dust located relatively close to the stars is rare in main sequence systems. Follow-up observations of this new sample of dust-excess stars will provide better insights into the properties of the systems.

Resolved images are crucial for understanding the dynamics and evolution of protoplanetary disks. Observing the detailed disk structure requires high-contrast, high-spatial resolution imaging very close to the bright central star. As a consequence, only a hand-

ful of these systems have yet been resolved. The second part of this work shows how near-infrared Polarimetric Imaging on the 3.8 meter United Kingdom Infrared Telescope can be used to obtain reflected-light images of dust-disks around dust excess stars. This technique allows one to automatically suppress the unpolarised light from the central star, increasing the dynamic range for detecting polarised light scattered by the dust present in circumstellar discs. The detections of extended disks around the classical T Tauri star TW Hya and the Herbig Ae star HD 169142 are reported, as well as the strong but spatially unresolved polarization signals measured toward two other Herbig Ae stars. Monte Carlo scattering simulations are used to fit the J-, H- and K-band polarization images of the disk around TW Hya, providing new constraints on the geometry of TW Hya's disk.

The third part of this thesis is dedicated to studying the gas content and dynamics around dust-excess stars. The evolution of circumstellar gas is thought to be strongly linked to the formation of gaseous giant planets similar to Jupiter, Saturn and most currently known extra-solar planets. However, the timescales over which circumstellar gas discs dissipate remains poorly constrained, mainly due to the observational difficulties associated with detecting small amounts of circumstellar gas. An analysis of high-resolution (R$\sim$50 000) optical spectroscopic data of a sample of 'Vega-like' candidates from the catalogue of Mannings & Barlow (1998) is presented. Analysis of the stellar spectra allows one to search for narrow absorption features due to circumstellar gas and possible Falling Evaporating Bodies, similar to the ones seen in the β Pictoris system. None of the stars from this sample show emission line activity in either Hα, Ca II or Na I, indicating that accretion of material onto the stars has ceased and suggesting they are true main sequence Vega-like stars. Four stars were found to exhibit narrow absorption features near the cores of the photospheric Ca II and Na I D lines, with HD 110058 being the strongest candidate to host a β Pictoris-like gas disk. If confirmed, HD 110058 would represent the Vega-like star with the lowest $L_{IR}/L_{\star}$ value (3.7×10^{-4}) around which a CS gas disk has been detected.

ACKNOWLEDGEMENTS

I would like to thank Mike Barlow for his close guidance and strong example, and continuous support as my advisor; Simon Casassus for his direction, advice and friendship throughout these early years in Astronomical Research.

I would also like to thank the members of Fundación Andes and of the Particle Physics and Astronomy Research Council, who through the GEMINI studentship put their trust in me and gave me the unique opportunity to carry out this research. Special acknowledgements are also due to Janet Drew, Tim Gledhill, Jeremy Yates, Ian Howarth and Ian Crawford for their invaluable input and useful discussions.

Thanks to Jo Fabbri, Fab Sidoli, Tom Bell and all members of Group A, for their friendship and companionship during my years at UCL; thanks for always being there to help me overcome all kinds of astronomy-related and sometimes not so astronomy related problems. Special thanks to my friend Nick Wright, who I had the pleasure to meet in those long observing nights in La Palma. The world is enriched by people like you! And my kind thanks to my colleague and friend at UCL, Mark Sterling, who I had the pleasure to discover in the realms of the Physics Labs. Thank you for all those unique roof discussions, and for showing me so many good and different ways of approaching this life.

I would like to dedicate this work firstly to my parents Leila and Patricio, to my very beloved sister Teresa, to my grandmothers Adela and Salem, and to the loving memory of my grandfathers Raffic and Alejandro. And to Matilde, who with her love urges me to become a better man.

Infinite thanks to my very closest friends Guy, Gabriel, Felipe, Ney, Sebastian and Vicente; I will always be in debt to each of you for your close and loyal friendship through all these years. And for the fact that each one of you made the long journey across the pond to bring me love and laughter around a pint of good English Ale.

And finally, I would like to acknowledge every single soul I have crossed in this path. Your love, support and understanding have enabled me to become who I am, to achieve what I now have, and to project myself into the future with the same restless and curious spirit that once led my granparents from distant Syria, Jordan and Palestine to the remote corners of Brazil and Chile.

Contents

List of Figures

List of Tables

CHAPTER 1

Introduction

Humans have always speculated on how the earth, the Sun and the remaining planets within our Solar System formed. Every society along history has adopted its own preferred cosmogonical scenario. But it was not until Immanuel Kant, who in 1755 with the publishing of his *Theory of Heavens* (Kant, Hastie & Ley 1968) set the first steps for a scientific understanding on how the planets came to be. He proposed that the sun and the planets formed from the collapse of a *rotating cloud of dispersed particles.* This hypothetical *Solar Nebula* had a disc-like, flattened, shape due to the combined effects of accretion and a rotation, and could at least qualitatively account for forming planets that would have roughly co-planar orbits and similar direction of rotation, as seen in our solar system. During the past two centuries Kant's initial idea was reshaped in order to tie it to the increasing understanding of the physics of star formation. Viscous accretion disks were predicted to exist around young stellar systems (Shakura & Sunyaev 1973; Lynden-Bell & Pringle 1974), but still by the early 1980s there was no direct observational evidence of the presence of any disks orbiting other stars. That evidence would become real with the advent of space-based telescopes and with the invention of electronic detectors, which together would allow to detect and record thermal emission from astronomical objects at temperatures similar to those of the planets, asteroids and comets in our solar system.

The discovery of dust orbiting main sequence (MS) stars in 1984 is considered one of the most important achievements of the Infrared Astronomy Satellite (IRAS) space telescope. IRAS, a joint-venture between the United Kingdom, the United States and the

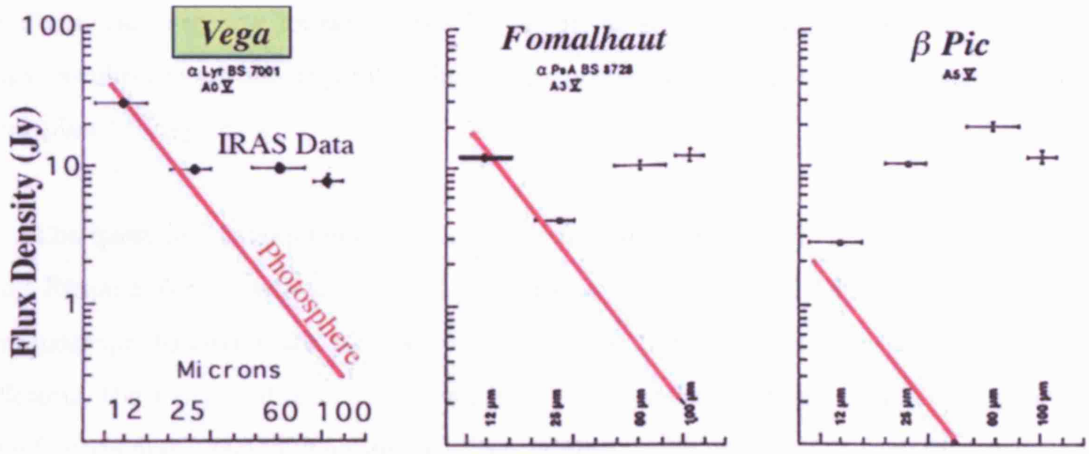

Figure 1.1: Vega and Vega-like SEDs, adapted from Backman & Paresce (1993). The solid line represents the Rayleigh-Jeans extrapolated flux of the stellar spectrum. All stars show notable excess fluxes than expected from the stellar photospheres. Note that only the star β Pictoris shows an excess at 12 μm.

Netherlands, aimed to provide new views of the Universe at wavelengths that are unreachable beneath the Earth's atmosphere. It flew in 1983, and during one of the calibration runs, it detected that several main sequence stars, including the photometric standard Vega, exhibited large mid- and far-infrared excesses when compared to the extrapolated stellar spectra. The emission could not be ascribed purely to the stellar photospheres. It was concluded that it would arise from a circumstellar (CS) disc or ring of solid particles orbiting the stars (Aumann 1984). This represented the first time that particulate material was discovered around a MS star (the first extra solar planet was to be discovered only eleven years later (Mayor & Queloz 1995)). Great interest was taken in these objects because of their similarity with the Solar System's asteroid belt and Kuiper Belt Objects (KBOs) and because of their possible relevance to the formation of planetary systems.

Figure 1.1 shows three IRAS spectral energy distributions (SEDs) presented by Fred Gillet at the January 1984 Protostars and Planets II conference (PPII). All the stars show enormous infrared excesses when compared to the stellar SEDs. Astronomers are nowadays used to these kind of photospheric-deviating SEDs, but when Fred Gillett showed them for the first time they caused a complete revolution in the Astronomical community. It was called the *Vega phenomenon*, and member stars were dubbed *Vega-like*. The four stars around which this phenomena was discovered, Vega, Fomalhaut, ϵ Eridani and β

Pictoris stars are now known as the Fab Four, as since the day of their discovery they have revolutionised our understanding of the process that leads to the formation of stars and planetary systems.

The quest for planets began. Someone in the audience at PPII phoned Bradley Smith and Richard Terrile, who were at Las Campanas Observatory in Chile testing an optical coronograph to search for moons around Uranus. They pointed the coronograph to β Pictoris, the most southern of the Fab Four stars, and almost instantaneously produced the famous first image of a debris disk (reproduced in Figure 1.2). The emission was found to be extended up to 25 arcseconds in the North East direction, corresponding to approximately 500 astronomical units (AU) at β Pictoris' distance of 19.3 parsecs (Crifo et al. 1997). The interpretation was that the light of the disk seen in this optical image comes mainly from scattering of the stellar photons by sub-micron-sized particles located in a disk, which appears to be seen close to edge-on. In addition, the disk appeared asymmetric, with the North-Eastern side being notably larger than the South-Western component. The 1984 image of the β Pictoris disk was the first of many lights to be unshaded in our understanding of the process of planet formation.

One of the key conclusions drawn out from this discovery was that not only disks exist around stars, but that they may persist until the stars are established in the MS. Simple calculations led astronomers to conclude that the timescales for dust-removal by Poynting-Robertson drag and radiation pressure are shorter than the age of the disk, suggesting that the dust present in Vega-like stars is constantly being replenished (Backman & Paresce 1993), probably from collisions between larger bodies.

1.1 Current paradigm of star and planet formation

When the first dust disks orbiting MS stars where discovered, astronomers wondered whether a substantial link connected these disks with the formation and/or the presence of planets (KBOs indeed are trapped in a gravitational 3:2 resonance with Neptune). In addition to the discovery of dusty discs around main sequence systems, IRAS observations showed that 30% of young (age $<$ 1 Myr), low-mass ($0.5 - 2$ $M_{\odot}$), solar-type stars had

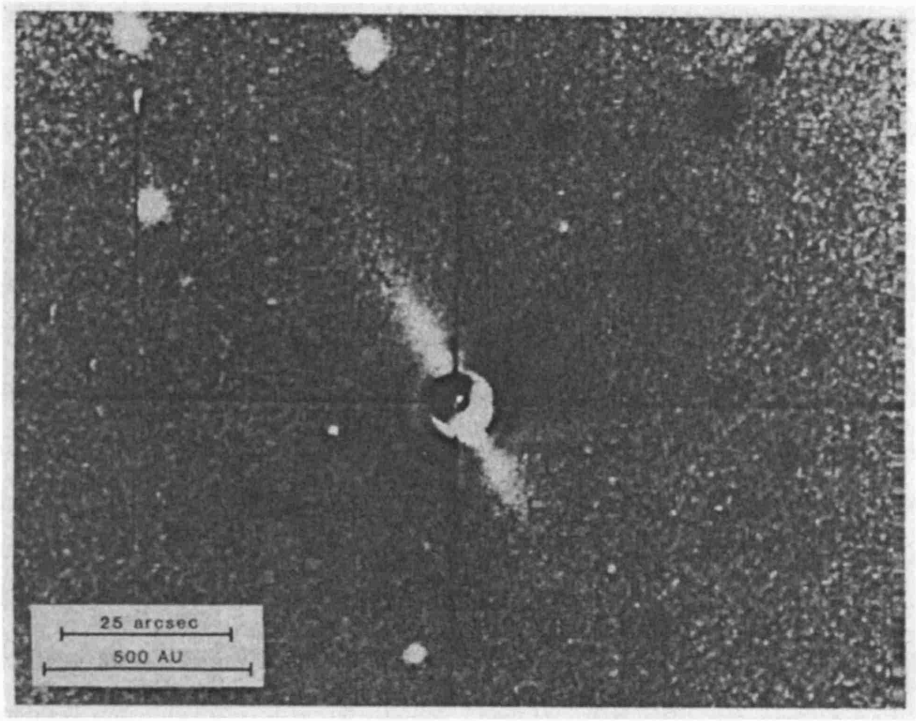

Figure 1.2: β Pictoris discovery image, adapted from Smith & Terrile (1984). The optical image (centred at 0.89 μm) was obtained at the 2.5 m du Pont telescope at Las Campanas observatory in Chile. The image represented the very first resolved image of a circumstellar disk. The emission corresponds to the reflection of stellar light by an edge-on disk of solid particles.

strong infrared fluxes (Rucinski 1985). These stars, named T Tauri after their proto-type, were originally singled out because of their strong photometric variability and spectral emission features which suggested that, despite having already ignited hydrogen-burning in their cores, they were still accreting material. Indeed, the near- and mid-infrared excess of T Tauri stars had already been identified with ground-based observation and associated with hot circumstellar material (e.g., Mendoza V. 1968; Cohen & Kuhi 1979). Nine years after the discovery of the *Vega phenomenon*, at PPIII it had become well-established that circumstellar accretion disks are common around young stars (Strom et al. 1993). The amounts of dust detected in T Tauri systems were found to be proportionally much larger than the ones observed in more evolved dusty main sequence systems. This matched well the ideas of star and planet forming from a primordial cloud that is dissipated as the age of the system increases. Another key discovery of IRAS was the identification of proto-stellar objects that were still deeply embedded in their parent clouds (Beichman et al. 1986), which were associated to the first stages of star formation.

Significant improvements in the area have been achieved in the past 2 decades, both thanks to the improvement of observational techniques and to theoretical developments (as reviewed in Backman & Paresce (1993), Lagrange et al. (2000), Zuckerman (2001) and Meyer et al. (2007)). IRAS proved that circumstellar disks are common around young stars, and discovered the existence of the more evolved debris-disks probably similar to our Kuiper belt. These early results allowed theoreticians to sketch our current theory of star and planet formation: stars form from a cloud of dust and gas; as they evolve they accrete or dissipate most of their parent material, with the remaining particles grouping into a flattened, disk-like structure. It is within this disk and from the material available on it that planets are thought to form. In a process that is not well understood yet, most of the gas and dust will clear-out or be accreted onto the star or planets, after which a mature planetary system like our own will be unveiled (our solar system is almost completely depleted of gas, and with most of the dust trapped into planets and planetesimals in well defined orbits).

Today we marvel at the wealth of the diverse observational results. SED modelling has become instrumental in constraining current evolutionary models (Sylvester et al. 1996; Whitney et al. 2003*ba*). Ground and space-based resolved imaging at different wavelengths show striking features in CS disks, most of them likely to be caused by the presence of shepherding planets (Zuckerman 2001). Gas and dust chemical evolution produces high processing during the evolution of the systems, which may lead to the formation of complex molecules and crystalline dust-grains [1]. In addition, over 178 planets have been discovered[2] around other stars than our sun (named *extra-solar planets* or *exo-planets*). This proved that planetary systems are not rare objects among nearby sun-like stars, but posed the difficult problem of explaining their unexpected characteristics (most exoplanets known to date have Jupiter-masses and they orbit very close to the host star).

There exists today, however, a more or less robust evolutionary sequence for the formation of stars and their by-products, disks and planets. Below, I will overview the current accepted paradigm of star and planet formation, following the Class 0 to Class III evo-

[1] Complex organic molecules, such as amino-acids, are thought to be precursors of simple life organisms on earth. Their detection in space would be a big impact to our understanding on how life emerged on earth. Please refer to Gilmour & Sephton (2004) for a complete introduction to the new science of Astrobiology

[2] as listed on July 2006 at the Carnegie Planet Quest website at `http://exoplanets.org/`

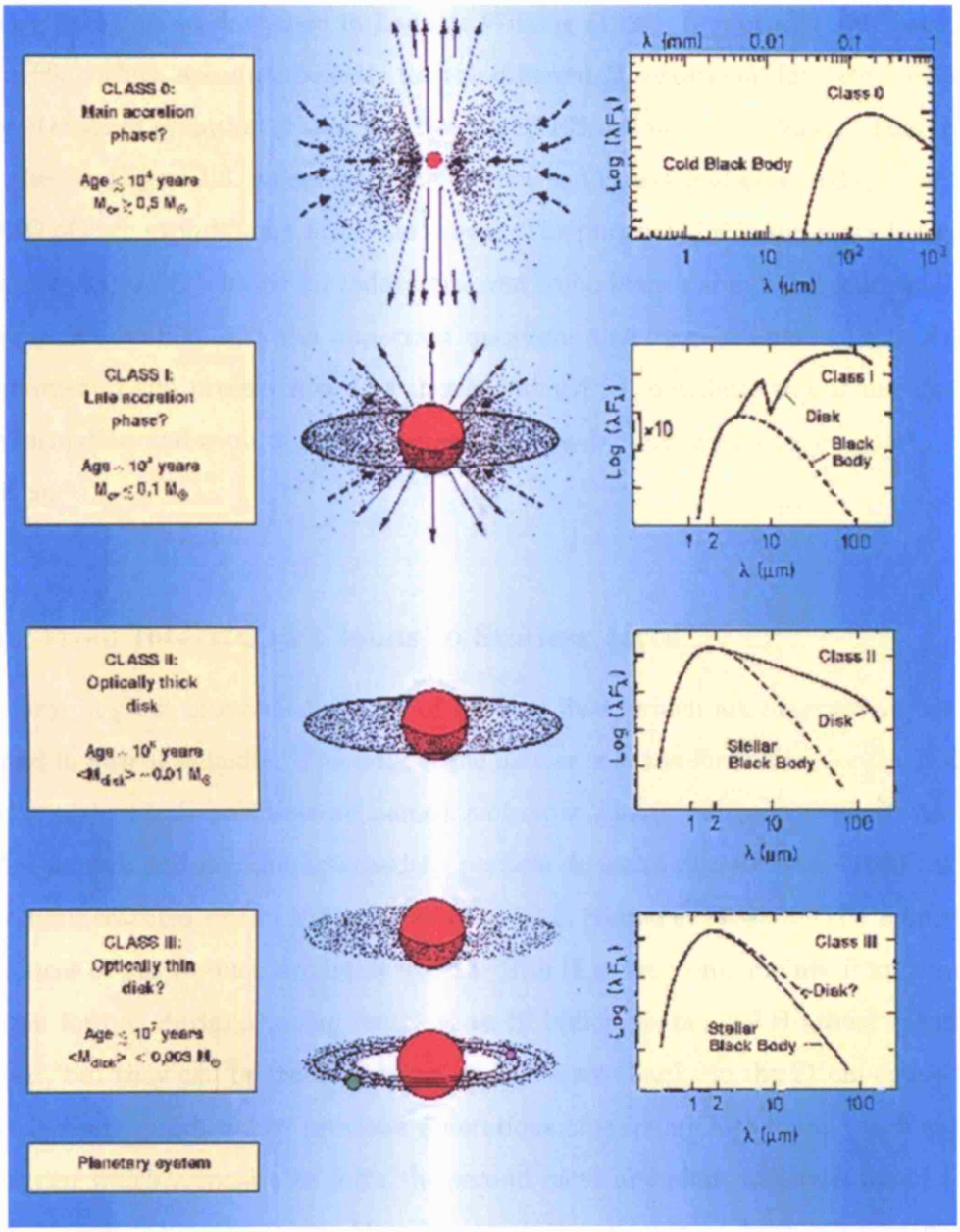

Figure 1.3: The evolutionary sequence of Star Formation. System parameters (age, mass), geometrical structure and modelled SED are shown. An embedded Class 0 source has initially the SED of a cold black body (T< 30 K). As a disk forms and the original clouds begins to dissipate, the star becomes detectable as a warm black body but is still obscured at visual wavelengths (Class I). During the Class II or T Tauri phase all the gas and dust concentrates in a flared disk (*flared* or *flaring* means that the scale-height of the disk increases with radius), and the star has a relatively flat optical to mm SED. It is at this stage, between 1 to 10 Myr, that planets are thought to form. The debris disk or Class III phase is when most planetesimals are destroyed or trapped into resonant orbits. After the debris produced by these collisions is washed-out, the system will become a mature planetary system like our own. Figure from André et al. (1993), courtesy Spitzer Science Center `http://ssc.spitzer.caltech.edu`.

lutionary prescription described in Lada & Wilking (1984), Shu et al. (1987) and André et al. (1993) which accounts broadly for the different observational features seen at each proposed stage of evolution (Kenyon & Hartmann 1995; Cotera et al. 2001). This sequence is sketched in Figure 1.3, where both the geometrical aspect and observed optical to sub-mm SED of each evolutionary stage are shown. The purpose of this summary is to present a brief description of what is nowadays believed to be known about the process of planet formation and to highlight the important questions that remain unanswered. Following this summary I will present how this thesis is aimed to contribute to our understanding of the formation and evolution of planetary systems by tackling some of these important questions.

1.1.1 From Interstellar Clouds to Starless cores

Stars form in giant interstellar clouds of gas and dust, which are observed in our Milky Way and in nearby galaxies. The bulk of the matter is in the form of molecular hydrogen, H_2, located in what are therefore named *molecular clouds*. Molecular clouds have sizes of a *few parsecs* and are characterised by particle densities of over $100 - 1000$ cm^{-3} and kinetic temperatures within the range $\sim 10 - 30$ K (Dame et al. 2001).The relative mass abundances of gas to dust is roughly 100 : 1. The H atoms come mainly from primordial hydrogen formed during the Big Bang, 11 to 16 billion years ago. H atoms are not easy to detect, but they can be traced in their neutral state thanks to the 21 cm emission line. Other elements, produced by previous generations of stars are also found (such as carbon and oxygen which associate to form the second most abundant molecule found in these clouds, carbon monoxide (CO). Metallic elements condense at high temperatures, and combine with oxygen and other elements to form microscopic dust grains of sizes smaller than 0.1 microns across. H_2 molecules are thought to form on the surface of these dust grains. H_2 is very difficult to observe because the temperatures in molecular clouds are too cold to excite its transitional levels. Therefore, most information on molecular clouds and the early stages of star formation come from observations of CO and to continuum emission from dust. These are observable mainly in the radio, mm and sub-mm domains, with the lowest frequency (J=0-1) rotational transition of CO occurring at 115 GHz.

Resolved observations of molecular clouds in the Milky Way and in nearby galaxies

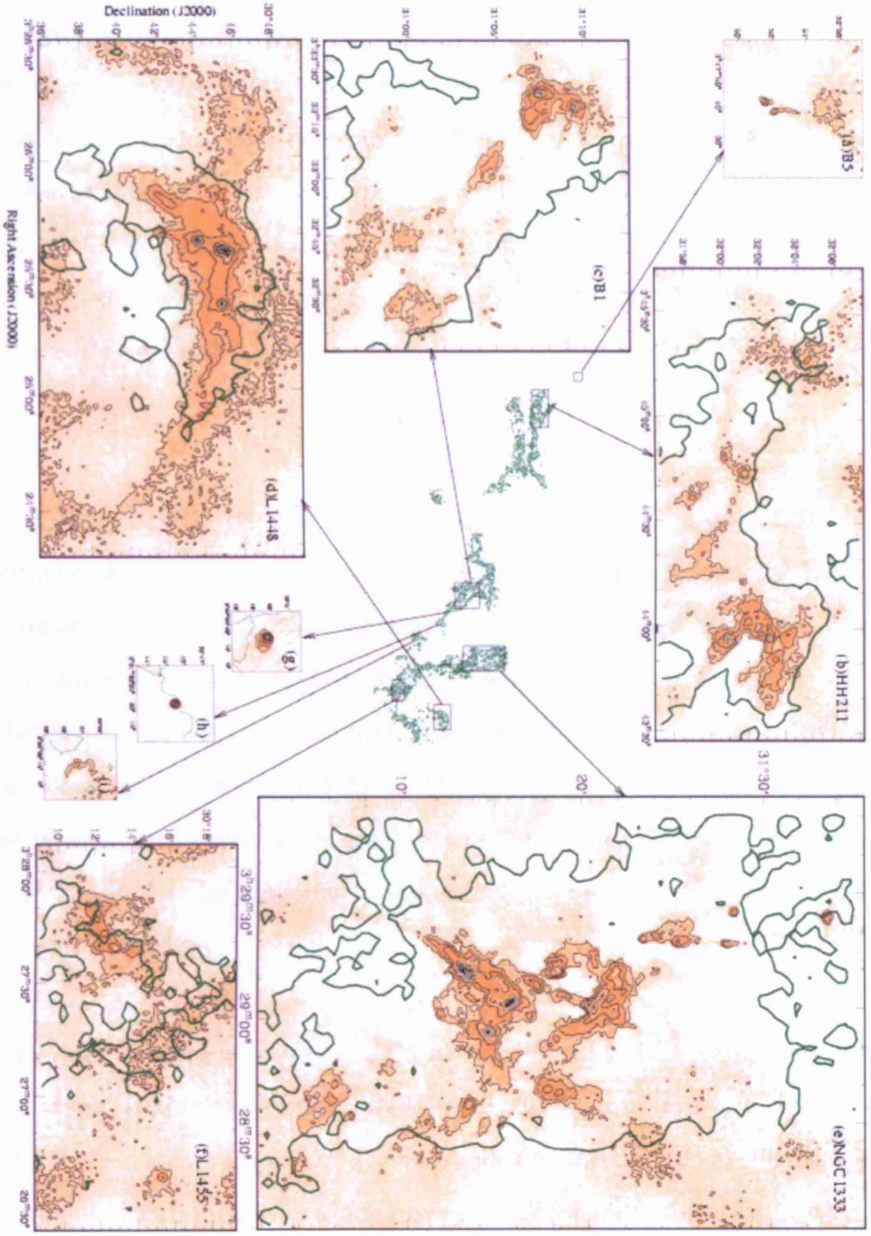

Figure 1.4: SCUBA dust continuum maps of the Perseus clouds, revealing dense filamentary structure in the cores of large CO molecular clouds. Black contours are for 850 μm while white contours are for 450 μm. Dark green contours (thick grey contours) are where the $C^{18}O$ integrated intensity = 1 K km s^{-1}. The filament mass per unit length is 5-11 $M_{\odot}$ per 0.1 pc, providing sufficient material for localised star formation along the filament. The intensity-scale (greyscale) is 850 μm continuum from 0 (white) to 2281 mJy/beam (black). From Hatchell et al. (2005).

have been possible thanks to the current generation of large radio telescopes and interferometers. Filaments, clumpiness and other inhomogeneities are observed at all scales. Figure 1.4 shows these types of structures, as seen in a large Star Forming region in Perseus (Hatchell et al. 2005). Clumps of dust continuum emission are seen at the centres of denser regions of molecular gas. It is when one of these dense cores becomes gravitationally unstable that a star begins to form. If one considers that only thermal motions prevent the constituents of the cloud from collapse, gravitational instability will occur when the mass of the cloud surpasses a critical value first derived by Jeans in 1902. For a molecular cloud of temperature T and local density ρ

$$M_{\rm J} = \left(\frac{5K_BT}{G\mu m_{\rm H}}\right)^{3/2}\left(\frac{3}{4\pi\rho}\right)^{1/2}, \tag{1.1}$$

where $k_{\rm B} = 1.381 \times 10^{-23}4$ JK^{-1} is the Boltzmann constant, $G = 6.673 \times 10^{-11}$m^{3}kg^{-1}s^{-2} is the gravitational constant and $m_{\rm H} = 1.674 \times 10^{27}$ kg is the mass of the Hydrogen atom. These gravitationally unstable fragments are called 'pre-stellar' or 'starless' cores. Their formation is thought to be triggered by shock-waves from supernovae or by interstellar radiation fields (which would not explain the formation of first-generation stars). Once a molecular cloud core has reached $M = M_{\rm J}$, it will enter the collapse phase. Interestingly, observations have revealed molecular clouds in which $M > M_{\rm J}$ without collapsing, suggesting that other forces (probably magnetic) may be preventing the clouds from self-collapse (Shu et al. 1987).

The dark, cold centres of pre-stellar cores were first studied intensively with the construction of visual extinction maps (Alves et al. 2001), but are now better understood with gas and dust continuum observations at mm wavelengths. Molecular line observations with mm and sub-mm telescopes have revealed a rich chemistry, characterised by strong depletions of certain molecular species (Tafalla et al. 2004). Figure 1.5 shows the intensity maps from Tafalla et al. (2004) for 1.2 mm dust continuum and emission lines observed toward the pre-stellar core L1498. The dust continuum emission peaks at the center of the cloud and its extension corresponds to $\sim$ 15000 AU. The gas composition shows clear differentiation: while CO and CS are almost absent in the centre of the core, NH_3 and N_2H^+ are stronger in the central parts. They are understood as a consequence of selective freeze-out of molecular gas onto dust grains (particularly CO, Bergin 2003). The temperature structures are studied using these different tracers for the different parts

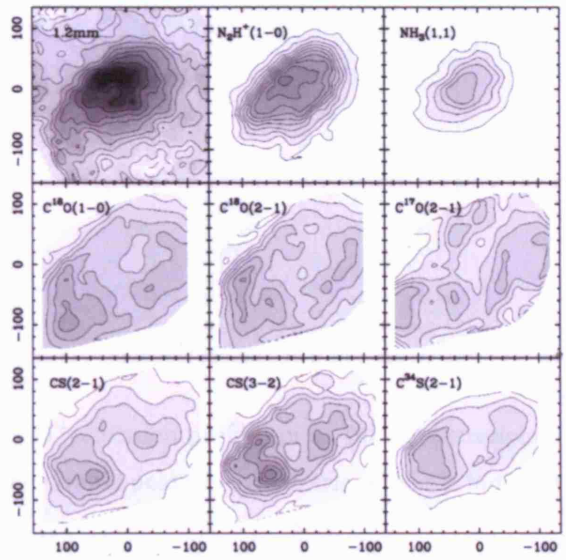

Figure 1.5: Intensity maps for continuum and different lines observed toward the pre-stellar core L1498. The images show the systematic dichotomy between centrally-peaked and centrally-depressed morphologies. Size-scales are in arcseconds from the estimated centre of the core. The top row shows that the 1.2 mm continuum, N2H+, and NH3 correspond to centrally-peaked tracers, while the two lower rows present the maps of centrally-depressed species, such as the lisotopomers of CO (middle row) and the isotopomers of CS (bottom row). From Tafalla et al. (2004).

of the objects. Core temperatures have found to be of a few $10 - 20$ K (hence the denomination 'cold-cores') and are almost independent from the radial distance from the centre.

Line emission profiles of gas in pre-stellar cores show the effects of a general inward motion on large scales ($0.1 - 0.3$pc). Spatially resolved imaging of these lines allows for the construction of velocity-gradient maps, which show unexpected variations that have been attributed to variations in the contraction time in different parts of the core (Tafalla et al. 2004). Line profiles are indicative of accretion, with characteristic double-peaked profiles due to the infalling material (as seen in the HCO^+ lines of the NGC 1333 SF region by Walsh et al. (2006), Figure 1.6). The infall asymmetry extends over $\sim$3.9 pc and is the largest reported in any SF region and is not limited to any single protostar or dense core.

At these early stages of star formation the dust grains present in the cloud are very small, typically smaller than 0.1μm. Although they do not play an important role in the dynamics of the system, current developments are showing that dust grains are key for the chemical evolution of the material via surface reactions (Herbst 2005). It is still not

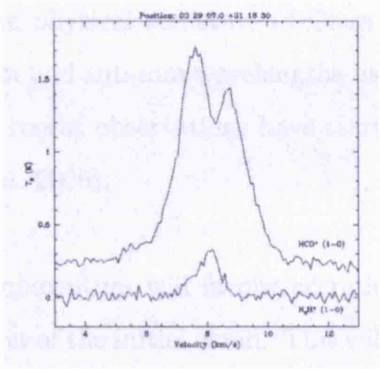

Figure 1.6: HCO^+ and N_2H^+ emission profiles in an infalling envelope (Class 0), as published by Walsh et al. (2006). The double-peaked asymmetric profile is indicative of accreting material.

clear whether smaller particles, such as Polycyclic aromatic hydrocarbons (PAH), may be present. It is believed that if present, such a population of small particles would increase the coupling of dust and gas in pre-stellar cores (Bergin 2003). A radio/mid-IR correlation of emission in the dark cloud LDN 1622 led Casassus et al. (2006) to conclude that the cloud had a population rich in very small grains (VSG) whose rotational velocities emit dielectric dipole emission in the radio domain.

1.1.2 The Class 0/collapse phase

After reaching M_J, the dense core will start to build-up mass faster and faster, as its gravitational field becomes increasingly stronger. This phase is also called the free-fall phase, as there are almost no forces resisting gravity and it occurs on size- scales of a *ten thousands* of AUs. Free-fall will only end when the gravitational energy released by contraction of parental cloud heats the medium (when in Equation 1.1 T^3 begins to increase quicker than ρ). The free-fall time for a cloud is independent of its initial radius and depends only on its initial density. Taking the value of $\rho = 3.3 \times 10^{-19}$g cm^{-3}, usually observed in molecular clouds, gives $t_{ff} \sim 10^4 - 10^5$ years. These timescales for the collapse phase are very small compared to the life of low-mass solar-type stars (of the order of $\sim 10^9$ years), and are even shorter in the case of higher mass stars.

This early stage of stellar evolution, named Class 0, was singled-out by André et al. (1993) and will determine the subsequent evolution of the star. In the case of low-mass stars similar to our Sun, it is defined that for a Class 0 source the mass of the CS material

satisfies $M_{env} > 0.5\,M_{\odot}$. The physical structure of Class 0 objects and their chemical composition are studied at mm and sub-mm wavelengths using tracers similar to the ones found in pre-stellar cores and recent observations have started to reveal unambiguous evidence of infall (Chandler et al. 2005).

Conservation of angular momentum will favour accretion in the direction parallel to the average direction of rotation of the initial cloud. This will rapidly lead to the formation of a circumstellar (CS) disk from which planets are thought to form. The free-fall phase will define the mass of the future star, the mass of the CS disk and hence, the amount of material available to produce planets. It will also determine the chemical composition of the disk.

An important difference between a Class 0 source and a pre-stellar core is that Class 0 sources have a central source that starts to heat the envelope from the inside rather than only from a weak external radiation field (Lee et al. 2003). Fits to observed sub-mm data show that temperature decreases with increasing distance from the core's centre, as modelled by Jørgensen et al. (2005) and shown in Figure 1.7. The temperature at the centre of Class 0 objects can reach a few $\sim$ 1000 K, decaying to $\sim$ 20 K at a radius of 1000 AU. The rise in temperatures triggers the evaporation of certain species. CO is the first molecule to evaporate, at 20 K (van Dishoeck et al. 2005). However, proto-stellar chemical observations are more sensitive to intermediate and high-mass stars (mainly because there is more material to be detected) and in consequence the early stages of low-mass stars remain poorly understood.

Models of the evolution of dust in collapsing cores predict only minor changes in dust properties at this early stage (Natta et al. 2007). Major changes only will occur once most dust particles are collected into a circumstellar disc.

1.1.3 The class I/protostellar phase

The star-to-be enters a slow phase in which it slowly contracts as it re-radiates the heat away. The accretion and ejection have decreased by almost an order of magnitude and the protostellar mass is close to the final mass. This phase, known as the *protostellar* phase or

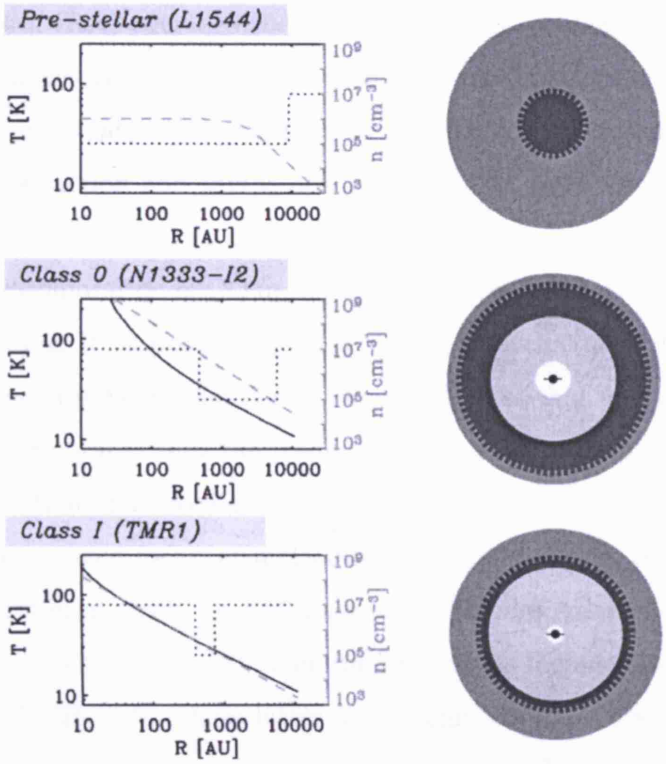

Figure 1.7: Proposed chemical structure for low-mass pre- and protostellar objects (from Jørgensen et al. (2005)). The left column gives the temperature and density as functions of radius (black solid and grey dashed lines, respectively) for three archetypical low-mass pre- and protostellar objects: L1544 (pre-stellar core), N1333-I2 (class 0, $M_{\rm env} > 0.5\ M_{\odot}$ protostar) and TMR1 (class I, $M_{\rm env} < 0.5\ M_{\odot}$ protostar). The black dotted lines indicate the derived abundance structures. The right column gives the depletion signature for each class of object with, going from the outside to the inside, the dark grey indicating the region where the density is too low for depletion ($n < n_{\rm de}$), the black indicating the region where the molecules deplete and the light grey indicating the region where they evaporate ($T > T_{\rm ev}$).

Class I, will finish when the star builds-up enough mass to ignite deuterium fusion in its core. It may last from $10^5 - 10^6$ years, depending on the mass of the collapsing object.

As the object is still accreting and ejecting a bipolar outflow, its spectral energy distribution evolves slowly from a flat to a negative mid- to far-IR SED (although models predict strong dependence between the shape of SEDs and the viewing angle, as is shown in Figure 1.8). These have been found to be well modelled with radiative transfer models of an extended envelope with a typical mass of $M_{env} < 0.5\,M_{\odot}$, a bipolar-outflow and an accretion rotating disc. Typical spatial sizes have decreased to a few *thousands* AUs. Protostars are difficult to observe at short wavelengths because they are highly embedded

on their parent cloud. IRAS provided the first observational evidence of Class I sources by observing them as unresolved sources. But with mm-wavelength interferometers, embedded protostars can be isolated from their parent clouds by applying low-frequency filters during image reconstruction and this is how the first dust disks around protostars were discovered.

Similarly to the evaporation of CO in the Class 0 phase, as the proto-star slowly begins to heat its surroundings it evaporates the molecular species that were depleted during the Class 0 stage. These are called 'hot-cores'. New molecules that formed in surface grain reactions are also evaporated into the medium. Such is the case for several deuterated species, as deuterization of molecules is favoured in dust grain mantles. In the case of high-mass hot cores, a true forest of molecular lines are observed, but are harder to be detected in low-mass protostars. Complex organic molecules composed of up to thirteen atoms have been indentified to date[3]. Identified molecules include ones such as CH_3CN, $HCOOCH_3$ and CH_3CH_2OH . These latter are thought to be produced by gas-phase reactions after the initial compounds have been evaporated. Understanding the chemical reactions that take place on the surface of dust grains represents one of the main challenges of the cross-diciplinary study of Astrochemistry, and is not restricted to young stellar objects but will extend to later stages of stellar evolution. The study of hot-core chemistry is dedicated to understand how complex, possible pre-biotic molecules may form in circumstellar environments.

Although grain-growth may already be occurring, it is not significant enough to decouple dynamically dust from gas. However dust particles are now confined in a thick disk-like structure, where their probabilities of colliding with other dust grains increase. If the relative velocities between dust grains are low enough, they may permit colliding particles to stick and grow into larger grains (Natta et al. 2007). Information on gas velocities in early CS disks is important because it contains information on when dust coagulation takes place.

[3]as updated regurlarly in Alwyn Wootten's webpage at `http://www.cv.nrao.edu/~awootten/allmols.html`

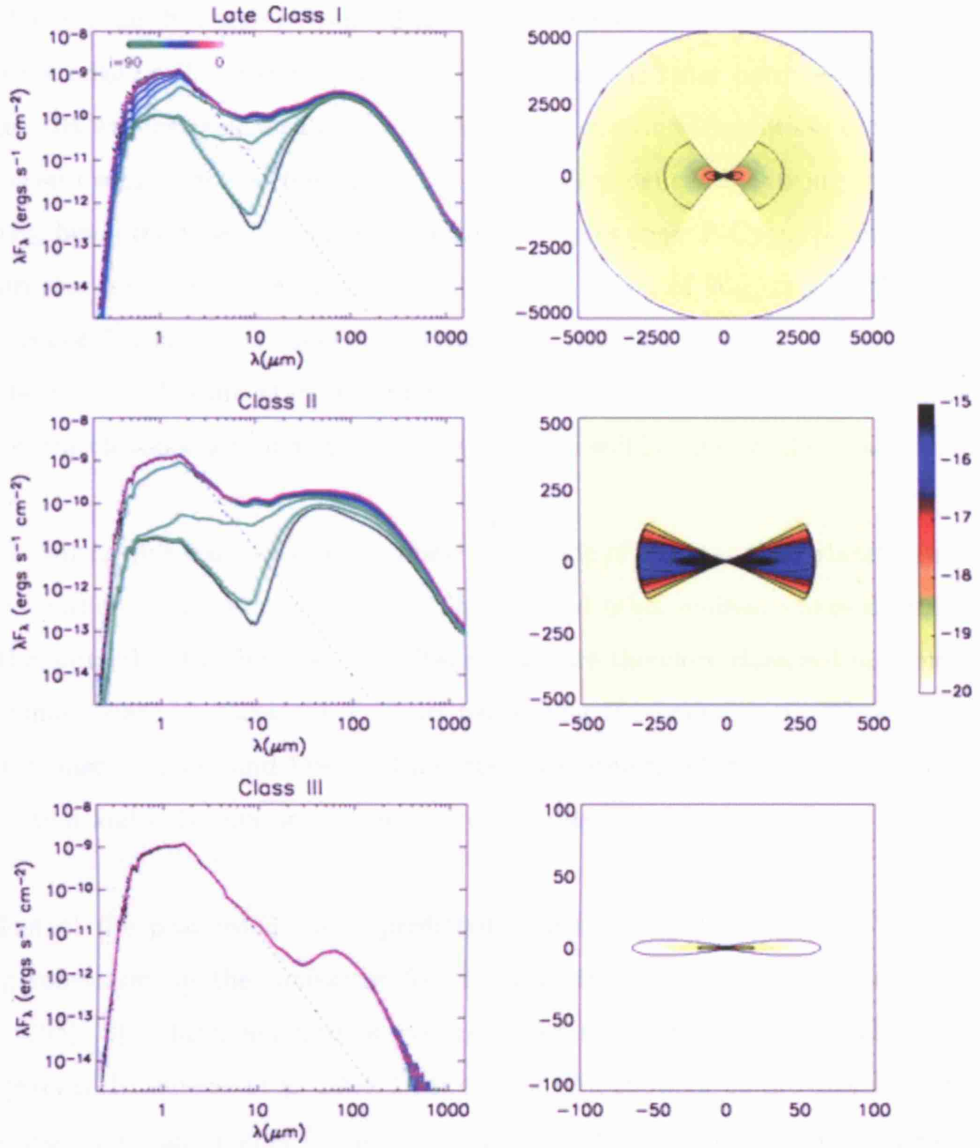

Figure 1.8: SEDS (left) and densities (right) of Class I, Class II, and Class III sources from radiative transfer simulations from Whitney et al. (2003*a*). For the SED models, the colours indicate inclination, as shown in the top left panel: dark green is edge-on, and pink is pole-on. The density images are plotted to log scale (in units of g cm^{-3}), with the contours matching the tick marks in the colour bar. The size range is noted in the axes in AU. Note that the Class II and III sources (disks) are much smaller than the envelope sources.

1.1.4 The Class II/T Tauri phase

The main ejection-accretion phase is now over. The core of the star has now become hot enough to ignite deuterium fusion. Most material has been either ejected or accreted onto the star, with few $\sim 0.01\,M_\odot - 0.04\,M_\odot$ of material remaining in an optically thick CS

disk. The typical disk scales observed are of a few *hundreds* AUs. If the orientation of the disk is not edge-on (i.e in the line of sight of the star), the star becomes visible at optical and near-IR wavelengths, although with large photometric variabilities. Close to the star, there is still some material falling onto the star, as evidenced by strong emission optical lines (H_α being the most prominent), which sometimes show P-Cygni profiles. A classical T Tauri star is defined by an equivalent line-width in H_α of $W_{H_\alpha} > 10$Å (Herbig & Bell 1988). Some T Tauri stars also emit strong X-ray emission and can be detected by X-ray space telescopes. T Tauri stars are typically 10^6 years old, and correspond to the Class II phase in the classification of Shu et al. (1987), which will last for another few million years.

It is during this relatively stable phase of the life of the star that planets are thought to form within the circumstellar disk. The Hα and other emission lines decrease as the accretion onto the star diminishes. T Tauri stars are therefore classified in terms of their evolutionary state: a Classical T Tauri has strong Hα emission, in Weak T Tauri the emission lines decrease and Post T Tauri stars are objects where there are no more signs of accretion and only very small fractions of CS dust.

Most of the primordial gas is predicted to dissipate within 3 to 10 Myr, imposing strong constraint on the timescales for the formation of gas giant planets (Zuckerman et al. 1995). Still, large amounts of gas are sometimes detected in much older MS debris disk systems (Brandeker et al. 2004; Dent et al. 2005), showing up the extent the processes of gas dissipation and planet formation remain poorly understood. Nevertheless, it is still believed that circumstellar disks of dust and gas around low-mass stars 1-10 Myr old are the sites of planet formation and are therefore called *protoplanetary disks*, despite the lack of direct observational evidence of actual planets forming within T Tauri disks. Great efforts in current astrophysics are devoted to understanding the structure, composition and evolution of CS matter around T Tauri stars.

The first direct measurements of CS disks around T Tauris came from detections of dust-continuum and molecular CO emission with mm-interferometers, which provided enough angular resolution to resolve disks located in nearby SF associations (Beckwith & Sargent 1991; Sargent & Beckwith 1994; Dutrey et al. 1996; Guilloteau et al. 1999). On-going millimetre wave surveys reveal that T Tauri disks are indeed rich in gas and that

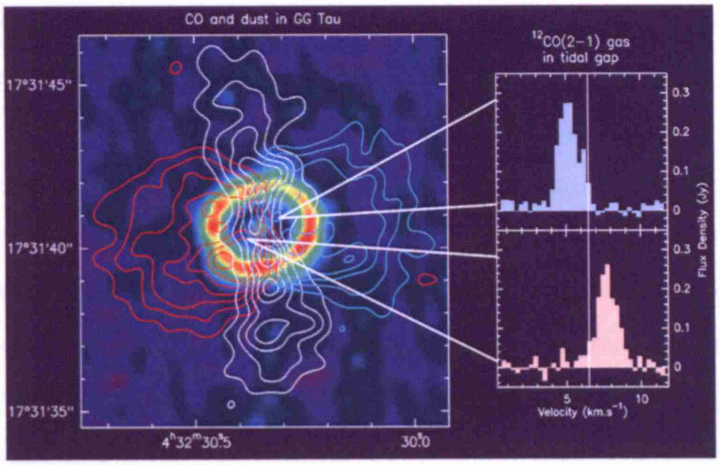

Figure 1.9: This composite image shows the presence of CO gas in Keplerian motion, with red- and blue-shifted components (red and blue contours), molecular out-flows (white contours) and a CS disk (intensity plots representing the dust continuum) around the binary T Tauri system GG Tau. Dust continuum is shown as the intensity plot, overlayed with CO emission line contours. Notice the ring structure of the dust continuum, implying a tidal gap formed by the presence of a binary star. Adapted from Guilloteau et al. (1999).

their kinematics are Keplerian (Pascucci et al. 2005; Dent et al. 2005). Figure 1.9 shows the very particular case of the T Tauri binary system GG Tau, in which a circumbinary ring of dust is seen (whose inner hole is a consequence of tidal interactions between the binary system), together with blue- and red-shifted CO gas emission consistent with a more extended rotating disk of gas. Several efforts are currently dedicated to determine the gas content of T Tauri stars and their dependence on stellar parameters such as age, multiplicity and mass (Dent & Clarke 2005).

Physically self-consistent models of T Tauri disks (Kenyon & Hartmann 1987; D'Alessio et al. 1998 1999 2001), in conjunction with SED data (Kenyon & Hartmann 1995), and comparisons with resolved scattered-light images (Cotera et al. 2001) indicate that T Tauri stars are surrounded by optically thick flared disks. This means that the thickness of the disc increases with radial distance from the star, allowing larger parts of the disk to be illuminated by stellar radiation. Scattered-light models by Whitney & Hartmann (1992) showed indeed that flared disks are more easily detected in scattered light than non-flared (flat) disks. Figure 1.8 shows the density structure of T Tauri's (Class II; Class I and Class III sources are also shown) derived from the models of D'Alessio et al. (1999)

and their observable SEDs at different inclination angles, as predicted from radiative transfer simulations by Whitney et al. (2003*a*). SED modelling also predicts that the lack of 10 μm excess emission may be indicative of the presence of dust depletion in the inner 7 AU (Calvet et al. 2002), which could be associated with dust clearing by the presence of a shepherding planet. Flaring has also been proposed to explain the SEDs of the intermediate-mass counterparts of T Tauri the Herbig Ae/Be stars (Meeus et al. 2001; Dullemond & Dominik 2004). The absence of flaring has been associated to self-shadowing of higher portions of the disk by an inner, optically thick wall.

When a flaring geometry is present, the area of the illuminated surface of the disc increases and so does the amount of energy re-radiated into the inner layers of the disk. This allows the characterisation of three different temperature zones in the disk (schematized in Figure 1.10, from Bergin et al. (2007)): (1) the disk's upper atmosphere or photo-dissociated region (PDR) where most molecules are dissociated by the strong stellar UV radiation. The physical conditions in the PDR in protoplanetary disks are studied by tracing the species produced by dissociation of molecular species (such as C I and C II in the case of CO, Ceccarelli & Dominik 2005); (2) the disk mid-plane is too cold and most molecules are depleted into grains; (3) a warm middle region exists thanks to the reprocessing of stellar radiation by the disk's atmosphere. Molecules containing heavy elements are depleted into grains, but several light-element bearing species can be observed in the sub-mm (H_2D^+ has been observed recently around TW Hya and DM Tau; Ceccarelli & Dominik 2005).

It is at these stages that significant grain-growth is supposed to take place, from sub-micron sizes to cm and even km sized-bodies (planetesimal), and eventually planets. Interpretation of the far-IR and sub-mm parts of their SEDs are indicative that significant grain-growth has taken place (Natta et al. 2007). Small grain populations are also present, as revealed by scattered light and polarisation images in the near-IR (attributed to sub-micron and micron sized particles, Lucas et al. 2004). Small particles (such as PAHs) have been detected in the more massive HAeBe stars (mostly coming from the upper layers of the disk, where PAHs can be excited by UV photons), but are still searched for around T Tauri's, whose UV radiation fields are probably too small to trigger PAH fluorescence emission. A flared disk geometry increases the surface of the disk exposed to UV-photons, and thus is found to enhance the detectability of PAHs (Habart et al. 2004). Such a population of very small grains (VSGs) should not survive dust-coagulation, therefore it

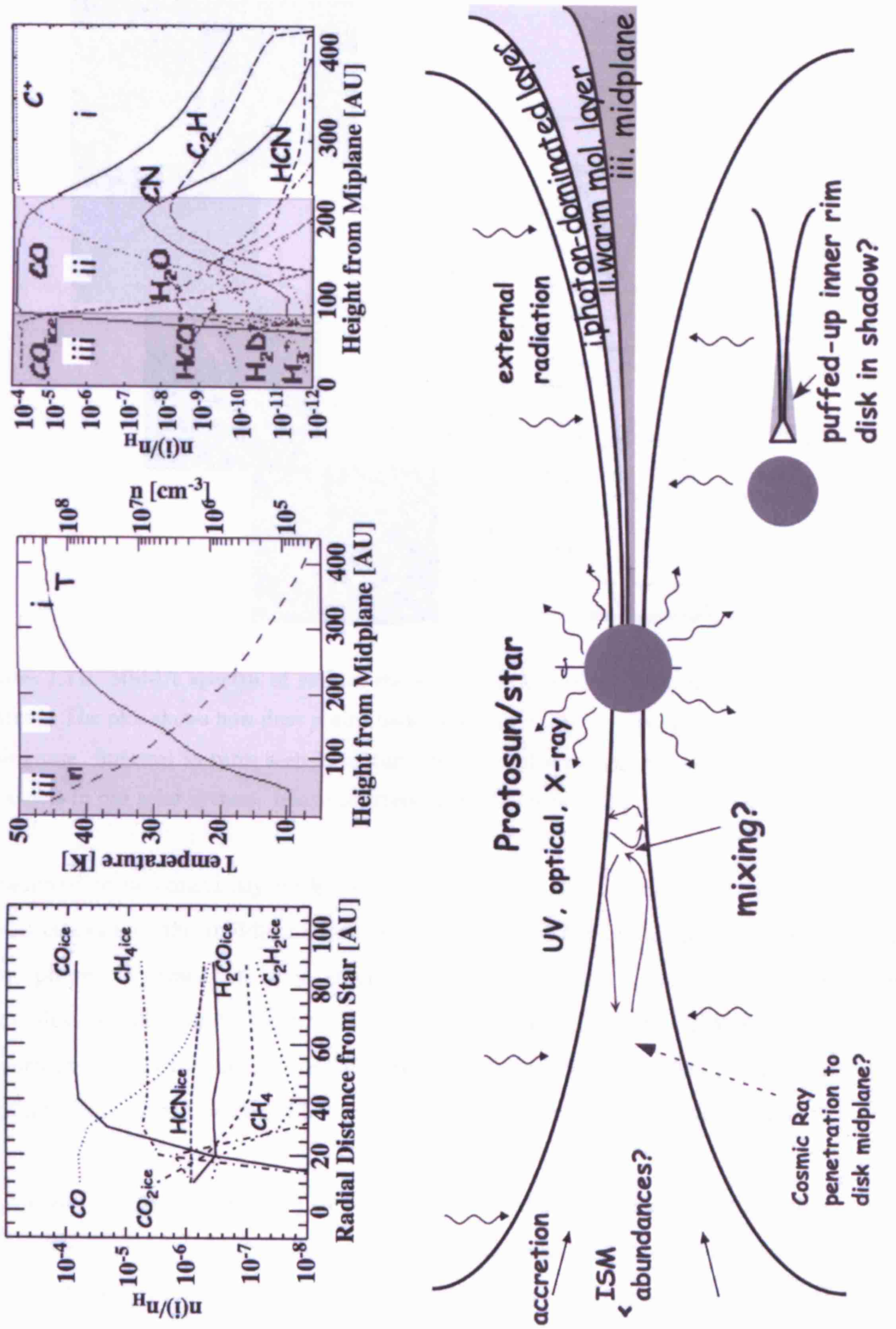

Figure 1.10: Chemical structure of protoplanetary disks, adapted from Bergin et al. (2007). Vertically the disk is schematically divided into three zones: a photon-dominated layer, a warm molecular layer, and a mid-plane freeze-out layer. The CO freeze-out layer disappears at $r \lesssim 30 - 60$ AU as the mid-plane temperature increases inward. Various non-thermal inputs, cosmic ray, UV, and X-ray drive chemical reactions. Viscous accretion and turbulence will transport the disk material both vertically and radially. The upper panels show the radial and vertical distribution of molecular abundances from a typical disk model at the mid-plane (Aikawa & Herbst 1999) and $r \sim 300$ AU (van Zadelhoff et al. 2003). A sample of the hydrogen density and *dust* temperature at the same distance is also provided (D'Alessio et al. 1999). In upper layers ($\gtrsim 150$ AU) the *gas* temperature will exceed the

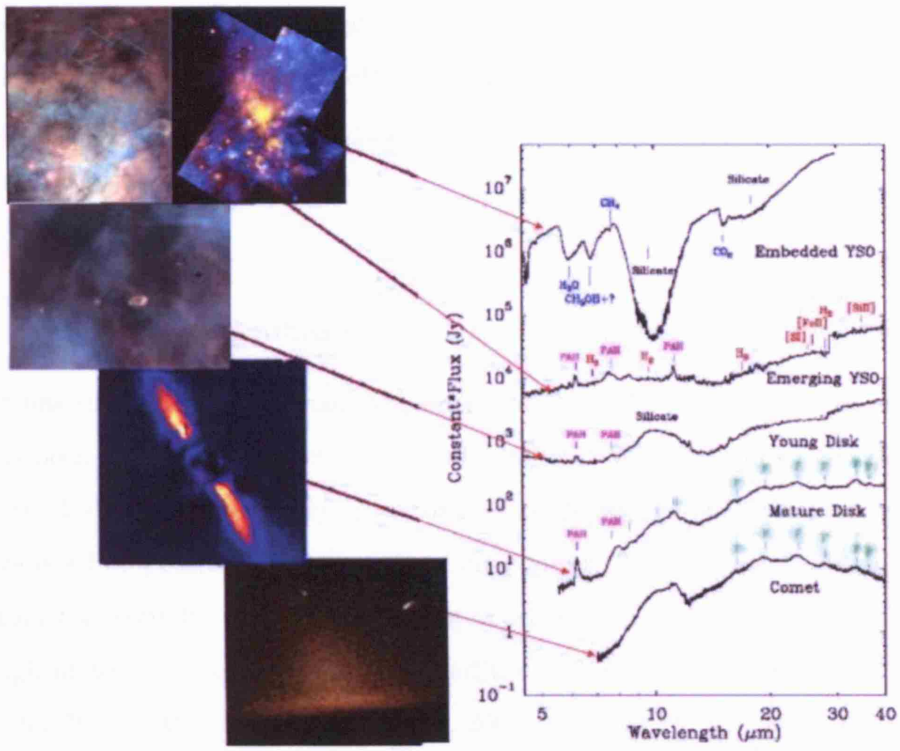

Figure 1.11: Mid-IR spectra of several stages of star formation, with major molecular species marked. The plot shows how dust grains undergo considerable processing from a young to mature disk phase. Spectral features seen in mature disks resemble notably the spectral features seen in comets in our solar system. Image courtesy of the Cores to Disks (csd) *Spitzer* Legacy team.

is believed to be constantly replenished by collisions. What is not clear is whether these VSGs co-exist in the middle regions of the disks, as PAH emission traces only the disk atmosphere. If present in large amounts, VSGs may affect strongly the gas, either via dynamical coupling or by heating it via the photoelectric effect. As VSGs play such an important role in evolutionary gas disk models (Dullemond et al. 2006), constraining their populations is an important unaccomplished task of astronomical observations.

Silicate species (a rock or a mineral whose structure is dominated by bonded silicon and oxygen atoms) are the building blocks of rocky planets, planetesimals and asteroids. Mid-IR spectra from the Infrared Space Observatory (ISO) showed that several HAeBe stars had strong mid-IR fluxes attributable to emission from very hot silicate grains (as shown in Figure 1.11). *Spitzer* has recently proved that silicate grains are also present in T Tauri stars, and that they have undergone high processing (i.e. change in the crystalline

properties of the grains, Natta et al. 2007). Radial processing of dust grains has been observed in both T Tauri and HAeBe stars using mid-IR interferometry, showing that the proportion of crystalline to amorphous silicates increases in the inner regions of disks (Millan-Gabet et al. 2007).

1.1.5 The debris disk phase

The star has just entered the main sequence. Most of the CS material of the T Tauri phase has been accreted or blown-away by the system. What remains is what is called a *debris disk*. Debris disk have very little, or no gas. Most of the original gas content has been dissipated or possibly accreted into giant planets. The dust observed in the far-IR comes from collisions between larger bodies and not from primordial material. There is not enough material to form new planets and the system enters a very stable phase that may last for $10^7 - 10^9$ years (Habing et al. 2001).

Most debris disks were found by their stars' mid- to far-IR emission being in excess with the expected photospheric emission (e.g., Aumann 1984; Backman & Paresce 1993; Mannings & Barlow 1998; Silverstone 2000; Zuckerman & Song 2004). The amount of dust present in the disk may be estimated by the percentage of stellar flux that is re-radiated by the disk at infrared wavelengths. This is usually called the infrared excess $L_{IR}/L_{\star}$. Important advances in understanding the evolution of debris disks have been achieved by studying the decay of their IR-excesses with time (Backman & Paresce 1993; Silverstone 2000; Song 2000; Song et al. 2001; Habing et al. 2001; Dominik & Decin 2003). Recent *Spitzer* surveys suggest that 24μm excesses associated with warm (T$\sim$ 150 K) dust are rare for stars older than 150 Myr (Rieke et al. 2005). Colder (T$<$ 70 K) outer disks are common around older stars (Kim et al. 2005).

Resolved imaging of debris disks reveals their spatial structures and the density profiles. In addition, gaps or warps in the observed disk structures can indicate the presence of shepherding planets. The first resolved imaging of a debris disk was the discovery of the scattered light disk around β Pictoris, showing the presence of an assymetric edge-on disk (Smith & Terrile 1984). Now all the Fab Four and a few other debris-disk systems have been imaged at many different wavelengths. Striking features such as rings, clumps and assymetries are revealed, together with clear variations in morphology at different wave-

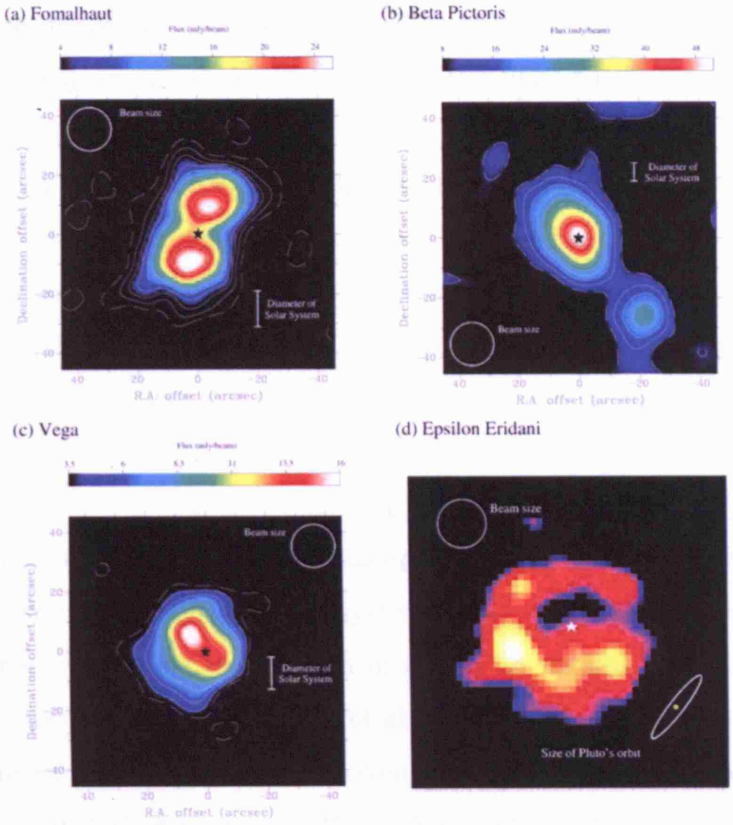

Figure 1.12: 850 μm images of the Fab Four, taken from Holland et al. (1998). The images reveal striking asymmetries in the structure of the disks, such as clumps and rings which have been explained in terms of shaping by the presence orbiting planets (Wyatt 2006). Indeed, a planet has already been discovered around ϵ Eridani via radial-velocity monitoring (Hatzes et al. 2000).

lengths. While scattered light images in the optical and near-IR probe the small grain population (typically sub-μm sizes), the mid-IR probes the presence of warm dust, PAH and silicate emission bands. Far-IR and sub-mm data trace the presence of cold dust at temperatures similar to KBOs in our solar system. At 850 microns the Fab Four present remarkable morphologies (as shown in Figure 1.12, taken from Holland et al. 1998), with cleared interiors and offset peaks that may have been sculpted by orbiting planets (Wyatt 2006).

Theoretical efforts are concentrated on interpreting the observed density distributions, these can be interpreted in terms of sculpting by planets, although the effect of binary companions or stellar flybys have also been explored (Beust et al. 2005). Still, the number of resolved debris-disks systems is very low. Only about 10% of currently known debris

disks have been imaged at any wavelength. The HST has been leading such discoveries by using its coronographic camera (Schneider & HST/GO 10177 Team 2005).

Dust has been found to dissipate as the system ages and gas is believed to become rare in older debris disks. This definition has often been used to link it to the timescales for giant planet formation. However, recent observational results suggest that gas is present in systems defined as debris-disks (Dent et al. 2005). β Pictoris itself was recently found to be surrounded by a large gas disk rotating in a stable Keplerian motion (Brandeker et al. 2004).

The presence of narrow atomic gas absorption features toward β Pictoris was known even before dust was identified in the system. Two types of absorption features were identified: a narrow absorption line seen in almost all studied lines and always centred at the radial velocity of the star (Hobbs et al. 1985). This component represents most of the gas content and was called the stable component, probably associated with a rotating circumstellar gas disk (Lagrange et al. 1998). Around the stable component, time-variable narrow absorption features are seen, most of them redshifted with respect to the star (Figure 1.13). These features were attributed to gas falling toward the star, probably caused by evaporation of orbiting planetesimals. This was called the Falling Evaporating bodies (FEB) scenario. However it was the discovery of the stable component which caused most problems to theoreticians, as most atomic and ionic species should be quickly blown away by β Pictoris' strong radiation pressure. Vast amounts of H_2 were proposed to act as a braking agent to stop the gas from being blow away (Lagrange et al. 1998), but observations were unable to confirm such high H_2 densities. The situation got worse with the discovery of resonantly scattered emission from Na I gas spread over a resolved Keplerian disk (Olofsson et al. 2001; Brandeker et al. 2004). Most species should indeed be blown away unless there is much more gas present than really observed. In a very recent paper, Roberge et al. (2006) claimed the detection of a large overabundance of carbon around β Pictoris, suggesting that these large amount of C should stabilise the gas disk from evaporating. However these results are unable to constrain our understanding on the presence of gas around β Pictoris and other MS debris disk systems. Most efforts are currently engaged in accurately determine the gas content of debris disks and in estimating the timescales and processes leading to gas dissipation.

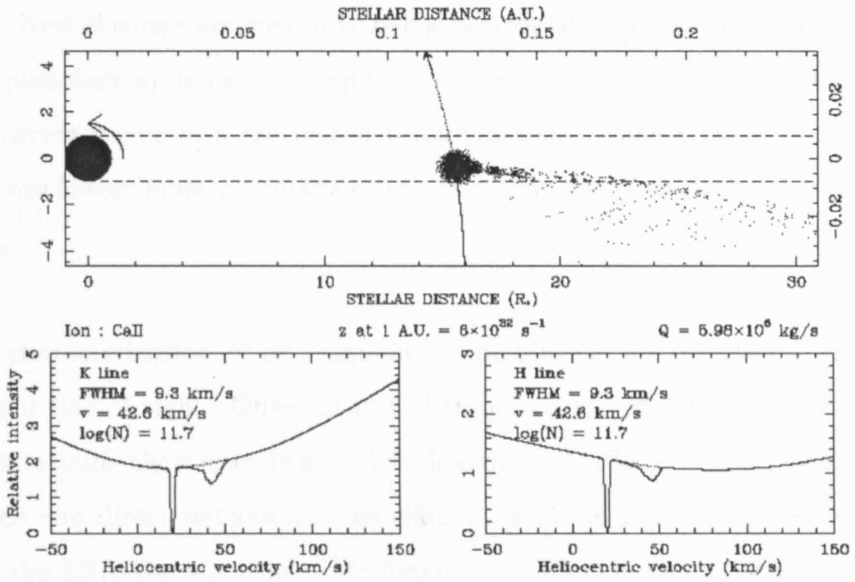

Figure 1.13: Plot of the modelled observations of a FEB in both Ca II K and H lines, from Beust et al. (1998). The upper plot shows a 2-D view of the Ca II cloud corresponding to the passing FEB, together with the star itself and a small part of the orbit. The line of sight is sketched as two parallel dashed lines. The lower plots show the synthetic Ca II K and H line profiles. In each plot, the dotted spectrum corresponds to the "quiet" profile when no FEB is present, while the other ones corresponds to the simulated feature, together with the stable central component (centred at 20 km s^{-1} and with FWHM $\sim$1.7 km s^{-1}). The fitting characteristics of the variable lines are indicated on the plots

1.1.6 The mature main-sequence phase

The star attains its *mature main-sequence phase*, an evolutionary state similar to that of our Sun. Most of the primordial material has been dissipated or locked in planets. The infrared excesses due to circumstellar dust are nearly undetectable. It is at this stage that planets in our solar system had enough time to cool down and, in the case of the earth to develop the conditions for life. It is around this type of star that most radial-velocity planet searches are carried out.

Over 178 extra-solar planets have been detected to date by different methods, proving that mature main-sequence stars with planetetary systems may be common. Most of them have been shown to be very different to our own solar system, challenging previous theoretical models that were focused in explaining the formation of our Solar System as seen today. Most exoplanets are giant planets found very close to the central stars (less

than 1 AU). New theories are currently being developed in order to understand this new plethora of planetary systems. An improvement in observational capabilities is also necessary, as current techniques are biased toward massive planets only. A 14 earth-mass planet tops the lowest-mass planetary companion that has been detected to date (Santos et al. 2004).

Further characterization of an exoplanet is possible if the orientation of its orbit is parallel to our line of sight. Observations of transits and occulations of the planet have allowed to determine their sizes (e.g., McCullough et al. 2006). Several ongoing missions are dedicated the direct detection of exoplanets, such as the NASA Terrestrial Planet Finder and the ESA Darwin space interferometers. Planets are more easily detected in the mid-IR, where the star to planet flux ratio is *only* 10^6. The detection of water, methane and other molecules that are associated with life as seen on the Earth is also one of the main scientific goals of such projects.

1.2 This work

Great advances in the understanding of the process of planet formation have been made in past two decades. However, following the fifth Protostars and Planets international meeting, held in 2005, several questions still remain unanswered (Meyer et al. 2007):

- When does the transition from gas-rich to gas-depleted disk occur?
- When exactly does the transition from optically-thick T Tauri disk to optically-thin debris disk occur?
- How do debris disks evolve around sun-like stars?
- Can we infer the presence of planets from the SED and/or resolved disk morphology?
- Is there any connection between debris disks and radial velocity-discovered planets?
- What is the incidence of infrared excess as a function of spectral type?
- What is the incidence of infrared excess as a function of stellar age?
- Can any statistical conclusions be drawn about the evolution of debris disks or does each system follow its own, probably stochastic, evolution?

This thesis aims to tackle some these questions by studying the physical conditions in young MS star systems with dust and/or gas disks.

- **Incidence of dust-excesses around early A-type stars:** The first part of this work is dedicated to a search for dusty early A-type stars in the northern galactic plane. Data from the IPHAS Hα survey is first used to select a sample of galactic A-type stars. This sample is then correlated with data from the *Spitzer Space Telescope* in order to search for 8-micron and 24-micron excesses associated with warm dust orbiting the stars. The improved photometric sensitivities of these new galactic surveys allow the list of known galactic 'Vega-like' sources to be extended to unexplored optical magnitude ranges ($13.5 < r < 18.5$ mags).

- **Resolved imaging polarimetry of dusty young stars:** Resolved images are crucial for understanding the dynamics and evolution of protoplanetary disks. Observing the detailed disk structure requires high-contrast, high-spatial resolution imaging very close to the bright central star. As a consequence, only a handful of these systems have yet been resolved. The second part of this work shows how near-infrared polarimetric imaging on the 3.8-meter United Kingdom Infrared Telescope can be used to obtain reflected-light images of dust-disks around dust excess stars. This technique allows one to automatically suppress the unpolarised light from the central star, increasing the dynamic range for detecting polarised light scattered from the dust present in circumstellar discs. Monte Carlo scattering simulations are used to fit the J-, H- and K-band polarization images of the detected disks, in order to provide new constraints on their physical parameters.

- **Search for circumstellar gas around dusty MS stars:** The third part of this thesis is dedicated to study the gas content and dynamics around dust-excess stars. The evolution of circumstellar gas is thought to be strongly linked to the formation of gaseous giant planets similar to Jupiter, Saturn and most currently known extra-solar planets. However, the timescales over which circumstellar gas discs dissipate remained poorly constrained, mainly due to the observational difficulties associated with detecting small amounts of circumstellar gas. An analysis of high-resolution

(R 50 000) optical spectroscopic data for a sample of 'Vega-like' candidates from the catalogue of Mannings & Barlow (1998) is presented. Modelling of the stellar spectra can allow one to search for narrow absorption features due to circumstellar gas and possible Falling Evaporating Bodies.

CHAPTER 2

A Galactic search for β Pictoris analogues

2.1 Photometric searches for circumstellar dust

Multi-wavelength photometry remains the fundamental tool for detecting dust excesses around pre-main sequence and main sequence (MS) stars. Almost all MS stars surrounded by dust disks have been discovered from the shape of their spectral energy distributions (SEDs), which show excesses with respect to the stellar photospheres at infrared (IR) and longer wavelengths (see Figure 1.1). Only with the advent of space observatories has the discovery of such MS systems been possible. Most surveys for dusty MS stars known to date have used the Infrared Astronomical Satellite (*IRAS*) database (Aumann 1985; Walker & Wolstencroft 1988; Cheng et al. 1992; Oudmaijer et al. 1992; Mannings & Barlow 1998; Sylvester & Mannings 2000; Silverstone 2000). Mannings & Barlow (1998, MB98 hereafter) correlated the *IRAS* Faint Source Catalogue (FSC, Moshir 1989) with the Michigan Spectral Catalogue (Houk & Smith-Moore 1988) listing 73 objects as new 'Vega-excess' stars. It must be noted that $\sim$ 20 of these stars were of spectral type B, which have been sometimes excluded from Vega-excess surveys as there exists a possibility that IR emission arises from free-free emission rather than CS dust (Zuckerman 2001). Additionally, a careful comparison with Hipparcos Tycho positions led Sylvester & Mannings (2000) to conclude that some of the stars listed in MB98 were not physically associated with the *IRAS* FSC sources.

For his PhD thesis, Silverstone (2000) carried out one of the most comprehensive searches to date of the *IRAS* catalogues for Vega-excess stars. He correlated the *IRAS*

FSC with the Michigan Spectral Catalogue for southern stars and with the Smithsonian Astrophysical Observatory (SAO; Whipple 1966) for northern stars that: (a) have 60 microns *IRAS* fluxes, (b) Hipparcos parallax and (c) spectral type in the B9 to K range. Silverstone's final catalogue included close to 200 Vega-excess stars. He found that the occurrence of dust excesses is dominated by the more luminous A-type stars (up to 50 % of his total stars). Silverstone concluded that this is a result of the flux-limited nature of the *IRAS* survey, as for a specific amount of dust, CS disks around brighter central stars are more easily detected.

The Infrared Space Observatory (*ISO*, Kessler et al. 1996) boosted the knowledge of Vega-excess stars by providing increased sensitivities and a larger spectral coverage compared to *IRAS*. It also allowed imaging and spectroscopy at arcsecond scales. Several Vega-excess systems were added to ones discovered with *IRAS*. Laureijs et al. (2002) found that 5 of 81 nearby main-sequence stars had 25-micron emission in excess to the photospheric level. Decin et al. (2000) also used *ISO* to search for 60−micron excess emission from 30 G-type dwarfs and found that 5 of them had far-IR excesses. *ISO* was also instrumental in detecting spectroscopic evidence for the presence of emission due to silicates and carbon-rich species (possibly PAHs, polycyclic aromatic hydrocarbon molecules) in Vega-like CS disks (Walker & Heinrichsen 2000). But probably one of the greatest achievements of *ISO* is that it gathered sufficient statistical information to constrain the possible time-dependence of the infrared excesses (e.g. Habing et al. 2001, see discussion below).

Because of the sensitivity limits of *IRAS* and *ISO*, these *early* surveys were restricted to relatively bright stars (V< 10 mags) mostly located within 50 pc from the sun. In addition, *IRAS* had low spatial resolution which led to confusion of sources, and therefore to spurious IR excesses (e.g. Sylvester & Mannings 2000). Furthermore, when interstellar reddening is important the spectral type must be known in order to apply extinction corrections and determine the intrinsic infrared excess. As a consequence, all searches for dust excesses have been restricted to stars for which spectral classifications are available.

Early attempts were made in order to determine the occurrence of IR excesses and its dependence on the stellar age. These studies suggested that the strength of infrared excesses declines with increasing stellar age (Backman & Paresce 1993; Dominik & Decin 2003). The reduction of excess intensity is believed to be associated with dust grain-

growth, settling to the disk midplane and the formation of larger rocky bodies (i.e the disks become optically thinner). It was also proposed that the inner parts of the disks would evolve faster than the outer regions (Hayashi et al. 1985). As a consequence, disk emission at short wavelengths associated to smaller particles would decay on shorter timescales than longer wavelengths excesses (Strom et al. 1989). Habing et al. (2001) concluded that *most* A, F, G and K stars arrive on the main sequence surrounded by a disk, and that the disk will then decay abruptly at about 400 Myr. Silverstone (2000) and Song et al. (2001) showed that in contrast to the postulate of Habing et al. (2001), there was still a small number of stars that showed infrared excesses at ages larger than 400 Myr. The work from Silverstone (2000) also indicated that the dust opacity, τ, is anti-correlated with the age of the systems, in agreement with the results of Habing et al. (2001). However, given instrumental and volume limitations of the *IRAS* and *ISO* surveys, these early works were unable to constrain the timescales for protoplanetary disk evolution.

Several authors investigated the incidence of dust excesses statistically using the *IRAS* database. Typical estimates from *IRAS* and *ISO* observations for the incidence of dust excesses around MS stars range between 10-20% (considering excesses at any wavelength beyond 12 μm, Cheng et al. 1992; Plets & Vynckier 1999; Lagrange et al. 2000). Song et al. (2001) found a similar incidence for a sample of 200 A-type stars located within 50 pc of the Sun. But *IRAS* searches were always restricted to stars located within a maximum of 50 pc from the Sun, because of the low sensitivity of *IRAS* for detecting bare MS stellar photospheres beyond such distances.

Recent results from *Spitzer*

The *Spitzer* Space Telescope is a NASA second-generation infrared space telescope, launched in 2003. With a notably improved sensitivity compared to its predecessors *IRAS* and *ISO*, *Spitzer* was expected to completely renew our infrared views of debris-disks (Zuckerman & Song 2004). *Spitzer's* instrument sensitivity is increased over a factor of 100 to 1000 times over that of *IRAS*, and with 10 times better spatial resolution due to smaller pixel size than *IRAS*. Equipped with mid- and far-infrared cameras, *Spitzer* is able to probe both the warmer/inner and cooler/outer regions of dusty CS disks. Radiative transfer in protoplanetary disks predicts that dust at different temperatures will be located at different

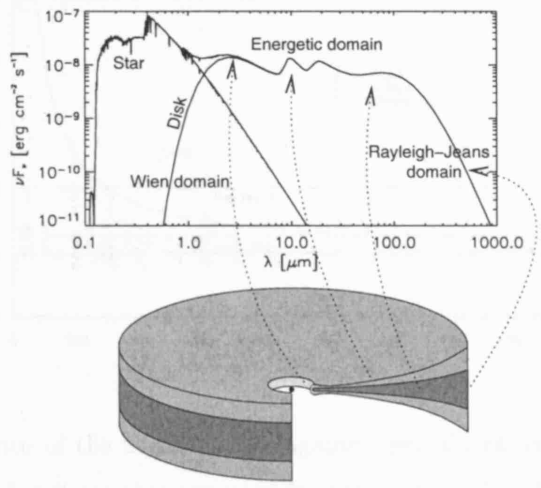

Figure 2.1: Different wavelengths trace dust at different radii. This image, adapted from Dullemond et al. (2006), shows the schematic structure of a protoplanetary disk and how different regions of the disk contribute to the different parts of the system's SED (refer to text for details).

radial distances with respect to the central stars, with the hottest components closest near to the central star (e.g., Dullemond et al. 2006). This is illustrated in Figure 2.1: near-IR excesses reveal the presence of dust located within 0.1 AU (the inner rim), while mid-IR observations (3.6 to 12 μm) trace the 1 to 10 AU region, where the most of the silicate emission is thought to arise. Excesses at 24 to 60 μm correspond to warm dust from the disk's surface layer, located within 10 to 60 AU, and colder dust located beyond 60 AU can is studied at far-IR (beyond 70 μm) and sub-mm and mm wavelengths. Therefore, the spectral range covered by *Spitzer*, which spans from 3.6 to 160 μm, is suitable to study the presence of hot (3.6 to 8 μm), warm (24 μm) and cold CS dust (70 and 160 μm). During its two years of operation *Spitzer* has carried out photometric and spectroscopic observations of well defined samples of MS stars, providing new constraints on the occurrence of dust-excesses and particularly in the timescales of this phenomena (Meyer et al. 2004; Uchida et al. 2004; Gorlova et al. 2004; Jura et al. 2004; Stapelfeldt et al. 2004; Sloan et al. 2004; Rieke et al. 2005; Beichman et al. 2005*ba*; Chen et al. 2005; Su et al. 2005; Uzpen et al. 2005; Stauffer et al. 2005; Low et al. 2005; Kim et al. 2005; Bryden et al. 2006; Hines et al. 2006; Smith et al. 2006; Silverstone et al. 2006; Sicilia-Aguilar et al. 2006).

Rieke et al. (2005) observed a sample of 76 A-type stars using the Multiband Imaging Photometer (MIPS) on board *Spitzer* in order to search for 24-μm excesses. They sup-

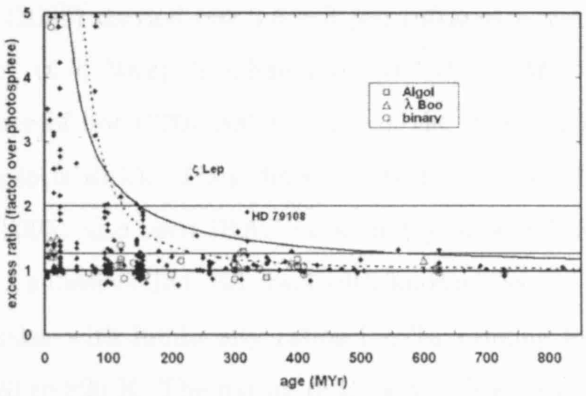

Figure 2.2: The dependence of the 24-μm excess against age. Excess emission, indicated as the ratio of the measured flux density to that expected from the bare stellar photosphere, adapted from Rieke et al. (2005). A value of 1 represents no excess. The thin solid line represents an inverse time dependence, while the thin dashed line is inverse time squared.

plemented this sample with 24-μm and 25-μm data from *ISO* and *IRAS* in order to get a total sample of 266 stars. In conjunction with accurate age estimates, they found that for stars younger that 10 Myr, 50 % of the stars did not show an excess at 24 μm, while for stars aged a few hundred Myr old only 7 % showed a 24-μm excess. This suggested a time dependence for the 24-μm excess which roughly follows a t_0/t law, with $t_0 \sim 150$ Myr (see Figure 2.2). This suggests that many stars enter the MS with little or no dust in the $10 - 60$ AU region (for the case of A-dwarfs).

Beichman et al. (2005*b*) studied 26 FGK stars with detected planets using MIPS. They found no 24-μm excess amongst their sample, but found that 25% showed 70-μm excesses at 3 sigma or better. Stauffer et al. (2005) found that of 20 G stars in the Pleiades, 10 % have an IR excess from 3.6 to 70 μm. Chen et al. (2005) found that of a sample of 40 F- and G-type nearby stars in the Scorpius-Centaurus association, 14 have 24-μm excesses and 7 show strong 70 μm excesses. Kim et al. (2005) reported observation of 5 solar-like stars, of which 3 had 70-μm excesses. Also using MIPS, Bryden et al. (2006) found that from a sample of 69 FGK MS stars, 8 had detectable 70-μm excesses but only 1 had a 24-μm excess. These results suggested that, in contrast to inner/warmer disks, cold-outer disks similar to our Solar System's Kuiper Belt Objects are a fairly common phenomena.

Silverstone et al. (2006) carried out 3.6 – 8 μm Infrared Array Camera (IRAC) observations of 74 young (t < 30yr), Sun-like stars ($0.7\,M_{\odot} < M < 1.5\,M_{\odot}$), in order to investigate the presence of hot (220-1000 K) dust in the inner regions of CS disks (similarly to the Beta Pictoris disk). They detected strong excesses from 5 optically thick disks. Uzpen et al. (2005) also used IRAC photometry to search for mid-IR excesses in the IRAC bands. Of a subset of 184 MS stars with known spectral type, 18 had excesses attributable to CS disks, with luminosity ratios $L_{IR}/L_{\star}$ ranging from 10^{-2} to 10^{-3} and temperatures from 220 to 820 K. The nature of these CS disks is attributed to a a ring of optically thin particles more similar to our asteroid belt than to Kuiper Belt Objects.

The observational results obtained with the *Spitzer* Space Telescope confirm that both the temperature of the excesses and their magnitude decay with time. In particular they show an earlier decay of hot and warm excesses (detected between 2-24 μm) compared to excesses associated with colder dust (measured at wavelengths longer than 24 μm). This is thought to be due to faster timescales for inner-disk clearing. *Warm* dust is located in the region where the formation of terrestrial-like planets take place, and therefore its evolution is thought to be linked to the timescales of earth-like planet formation. From *Spitzer* surveys it is now generally accepted that 24 μm excesses are rare in stars older than $\sim$ 10 million years (Myr). Colder disks (T< 100 K) are common in stars of any age, suggesting that the colder/outer parts of the disks have larger clearing timescales than their warmer/inner counter parts.

Churchwell et al. (2005) have completed the *Spitzer* Galactic Legacy Infrared Mid-Plane Survey Extraordinaire (GLIMPSE) of the inner galactic plane. This survey has generated a highly reliable point source catalogue containing up to 30 million sources with detected fluxes between 3.6 to 8 μm, with the majority having 2 Micron All-Sky survey (2MASS) J-, H- and K- counterparts. Complementing this work, a group led by Sean Carey are currently carrying out the MIPS Galactic survey (MIPSGAL), which spatially overlaps the GLIMPSE survey at 24 and 70 μm. Once combined, these datasets represent a considerably improved version of the *IRAS* FSC (both in spatial resolution, pointing accuracy and sensitivity) and open up great opportunities for new searches for dusty MS stars with mid-IR excess. However, most of the stars present in the Glimpse catalogue have not been spectrally classified, making the mining for dust-excess stars particularly difficult.

2.1.1 This work

Pre-*Spitzer* surveys have attempted to quantify what percentage of MS stars displayed mid-IR excesses, but these early works were volume-limited and lacked enough sensitivity to give accurate statistical estimates. Current searches using *Spitzer* data are beginning to provide the first reliable estimations, but are been still limited to relatively small samples (few hundred objects) for which spectral classifications are available. In this work we present a search for 8 μm and 24 μm excesses over a large ($\sim$ 3000) sample of early-type A-dwarf stars. This sample, observed as part of the currently ongoing INT/WFS Photometric H-alpha Survey of the Northern Galactic plane (IPHAS, Drew et al. 2005), was selected in terms of their optical (r'-i') and (r'-H_α) colours. Cross-correlation with near- and mid-IR photometry from the 2MASS and GLIMPSE surveys enables one to construct their dereddened 0.6 μm to 8 μm SEDs and to search for warm (T $\sim 150 - 800$ K) mid-IR excesses.

In addition, early-release post basic-calibration 24-μm images from the MIPSGAL *Spitzer* survey are searched for possible 24-μm associations with IPHAS A-type stars. In contrast to 8-μm excesses, 24-μm excess emission arises from colder dust. The main aim of this work is to investigate the incidence of mid-IR excesses around a large unbiased sample of early A-type stars. This sample covers previously unexplored optical magnitude ranges (r' > 13.5 mags) and adds significantly to the number of catalogued dust-excess MS stars.

2.2 IPHAS observations and Data reduction

The INT/WFS Photometric H-alpha Survey of the Northern Galactic plane (IPHAS; Drew et al. 2005) is a multi-national observing programme fully dedicated to surveying the northern galactic plane. The northern galactic latitude range of $-5 < b < +5$ represents a total sky area of 1800 square degrees. The limiting magnitude of the IPHAS survey is r' $\sim$ 20.5, allowing it to go much deeper than previous Hα surveys, which are 40 years old and incomplete even to $m_V = 12.5$. Two broad-band Sloan r' and Sloan i' filters, in conjunction with a narrow band Hα filter, provide photometric information to

Table 2.1: IPHAS filters properties

Filter	Central wavelength [Å]	FWHM [Å]	Zeropoint [Jy]
Sloan r′	6240	1500	3173
Sloan i′	7743	1500	2515
Hα	6568	95	2974

describe the stellar population in a given region of the galactic plane. To date over 100 million stars have been catalogued in terms of their positions, r′, i′ and Hα magnitudes, with 200 million expected to be catalogued by the end of the survey.

IPHAS observations are made using the Wide Field Camera (WFC) with a narrow band Hα filter and Sloan r′ and i′ filters, at the 2.5-m Isaac Newton Telescope (INT), La Palma, Spain. The WFC, an imager made of four 4k×2k EEV CCDs arranged in an L shape, provides a field of view of 34 × 34 arcmins. Its pixel size of 0.3333 arcsec is sufficient to provide high quality sampling with the usual ∼1 arcsecond seeing encountered at the El Roque de Muchachos Observatory. The transmission profiles of the filter used for IPHAS observations are plotted in Figure 2.3. The r′ filter is the most blue sensitive, with a central wavelength of 6240 Å. The Hα filter has a FWHM transmission 95 Å and is centred at 6568 Å, towards the red end of the r′ filter. The i′ filter has a central wavelength of 7743 Å. Filter characteristics (Drew et al. 2005) and corresponding zeropoints are presented in Table 2.1. The zeropoints were calculated by convolving the model Vega spectrum from Deacon (1991) with the IPHAS filter pass-bands and the WFC mean response.

In order to account for the gaps between CCDs on the WFC, observations for a given field of view are paired with a second observation offset 5 arcmin-West and 5 arcmin-South. These are usually referred as the *on* and *off* exposures of a given field. The total number of pointings required to cover the survey area is 7635, with many sources being imaged twice. The exposure time in the Hα filter is 120s, while for the broadband filters the exposure times are 30s. Flat fields and dark frames are acquired at the beginning and end of each night.

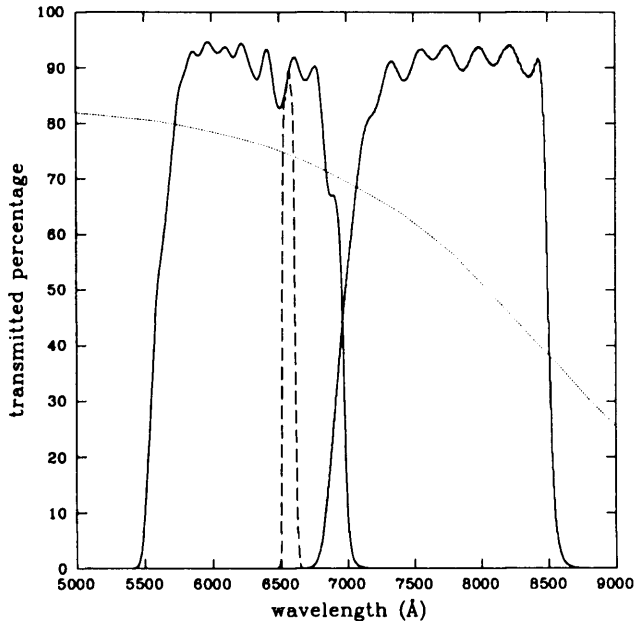

Figure 2.3: The transmission profiles of the filters used in all IPHAS observations. The r′ and i′ profiles are plotted as solid lines, whilst the Hα filter is shown dashed. The mean response of the WFC CCD at the working temperature is shown as a dotted line (Drew et al. 2005).

Raw data are transfered to the Cambridge Astronomical Survey Unit (CASU[1]), where it is pipeline-processed. The pipeline calibrates the raw data and extracts sources from the Hα, r′ and i′ processed images. Catalogue generation follows the procedure described by Irwin (1985) which includes several features such as background fitting over scales of 20-30 arcsecond, detection and de-blending of a group of images as well as parameterisation of the detected images. An initial approximate world coordinate system (WCS) is refined using several all-sky catalogues (including those of the United States Naval Observatory, the automated Plate Measurements and 2MASS) to give an internal precision better than one 0.1 arcsec. The precision with respect to the 2MASS Point Source Catalogue is 0.1 arcsec.

Sources are classified following their extraction characteristics, e.g., *0 = noise like, 1 = non-stellar, -1 = stellar, -2 = probably stellar, -9 = saturated.* Photometric standards observed during the night are used for flux calibration in each passband. The Hα zero-point is obtained by treating the Hα filter as a standard Johnson-Cousin R-band filter to obtain a Vega-like magnitude used for calibration. A final catalogue is then produced by

[1]`http://apm2.ast.cam.ac.uk/cgi-bin/wfs/dqc.cgi`

combining the catalogues from each filter. A merged object catalogue for a single pointing can contain from ten to fifty thousand objects (stellar and non-stellar). A typical IPHAS (r'-i') versus (r'- Hα) colour-colour diagram is shown in Figure 2.4.

2.3 A-dwarf stars and their location in the (r'-i'), (r'- Hα) plane

2.3.1 Why A-dwarf stars ?

Dwarf stars of early A-type are 2-3 times more massive and 8 to 50 times more luminous than our Sun, with an average temperature of T$\sim$ 10000 K. Being main sequence they are abundant. In addition, their high luminosity allows them to be traced to large distances. It is found that early surveys for debris disk stars are highly biased toward A-type stars, not only because they are MS but also because for a given amount of dust the disk will reprocess more stellar radiation around the brightest stars (see Section 2.1). Therefore, it is not purely coincidental that three of the four stars around which dust-excesses were first detected were indeed A-type stars (Vega AOV, Fomalhaut A3V and Beta Pictoris A5V; Gillett 1986). Over 50% of known dusty-disks are associated with an A-type star. Regarding searches for infrared excesses (Silverstone 2000), A-type stars are clearly favoured with respect to other spectral types.

Despite representing the Rosetta stone in debris-disk studies, because of their paucity of absorption lines A-type stars have been generally excluded from Doppler planet searches. However, modelling of the circumstellar discs Vega and Fomalhaut are suggestive of the presence of giant planets (Wyatt 2006). Because the A0V star Vega is defined to have zero intrinsic colours across all optical and infra-red (IR) bands, this implies that the observed colours of early A-type stars are close to the colour excesses, allowing one to avoid adding additional uncertainties to the colour excesses (introduced when estimating intrinsic colours).

It is clear that A-type stars are excellent candidates to search for IR excesses due to orbiting dust grains. In Section 2.3.2 we will show that A-type stars can be readily selected in terms of their location in the (r'-i'), (r'- Hα) colour-colour plane. As a consequence, an

unbiased sample of A-type stars can be extracted from IPHAS observations.

2.3.2 Location of A-dwarf stars in the IPHAS (r'-i'), (r'- Hα) plane

The intensity of Hα absorption peaks at T$\sim$ 10000 K, the temperature of early A-type MS stars. As a consequence, for a given r' magnitude and reddening, the (r'- Hα) colour of an A0V star will be a minimum compared to that of other stellar types. Synthetic (r'- Hα) and (r'-i') colours for stars of various luminosity classes and spectral types for the IPHAS filters were derived by Drew et al. (2005) using the catalogue of stellar spectral energy distributions (SEDs) by Pickles (1998). To guarantee agreement with the Vega-based zero magnitude scale, the synthetic colour (r'-i') is defined as follows:

$$(r' - i') = -2.5 \log \left(\frac{\sum T_{r'} F_{\lambda} \Delta\lambda}{\sum T_{r'} F_{\lambda,Vega} \Delta\lambda} \right) + 2.5 \log \left(\frac{\sum T_{i'} F_{\lambda} \Delta\lambda}{\sum T_{i'} F_{\lambda,Vega} \Delta\lambda} \right), \qquad (2.1)$$

where $T_{r'}$ and $T_{i'}$ are the transmission profiles of the Sloan r' and i' filters used for IPHAS observations (plotted in Figure 2.3), multiplied by the mean WFC CCD spectral response curve. $F_{\lambda,Vega}$ is an adapted version of the SED of Vega due to Hayes (1985). The (r'- Hα) colour is evaluated in a similar fashion, by substituting the Hα filter numerical transmission profile for the i' filter profile.

Figure 2.5 (from Drew et al. (2005)), shows the synthetic colour-colour diagrams in the (r'-i'), (r'- Hα) plane. The positions of MS, Giant and Supergiant stars are mapped for three different values of E(B-V). It can be seen that, as the reddening increases, the minima of the loci of MS stars trace out an approximately parabolic line. For the reasons described above, this line indicates the positions of A-type stars in the (r'-i'), (r'- Hα) plane as a function of reddening. It is therefore known as the *early-A reddening line.* Spectroscopic follow-up observations of test fields in Taurus have confirmed that stars lying in this area of the colour-colour plane are indeed early A-type stars (A0-A5; Drew et al. 2005, their figure 9).

When fitting synthetic colours with real data, one must take into account the fact that Vega's SED includes a strong Hα absorption feature. Because CASU uses standard field stars for calibrating the observed magnitudes, there is an offset in the observed (r'- Hα) colour between the catalogues and the synthetic data.

The best way to account for this is to apply a shift in (r'- Hα), given that the cali-

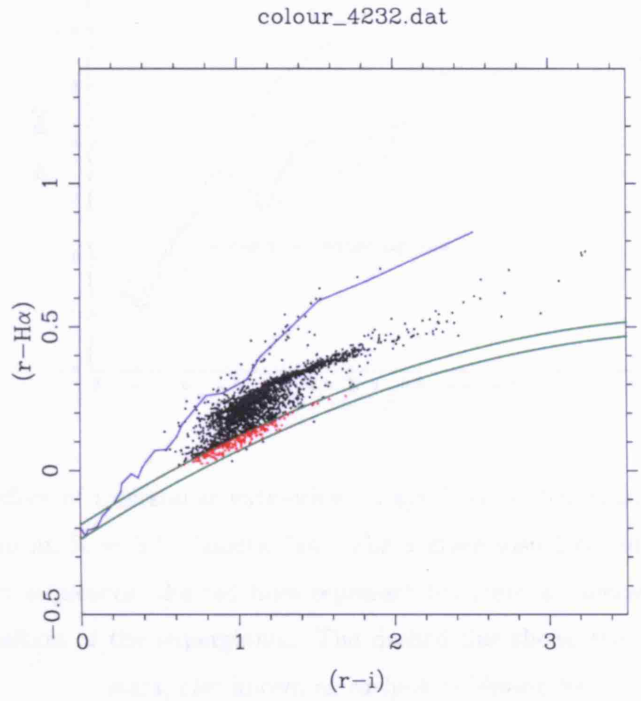

Figure 2.4: The (r′- Hα)-(r′-i′) colour plane for a test field (field number 4232). The fit of the synthetic MS and early-A stellar tracks to the data is achieved after applying a shift of −0.23 in (r′- Hα). An *early-A* strip width of (r′-H_α) = 0.05 (green lines) was used to select for A-type dwarfs (red dots). The blue line corresponds to the unreddened MS track.

bration in (r′-i′) is secure enough. The shift has been found to be always negative and ranging between −0.1 and −0.25 (Drew et al. 2005). Figure 2.4 shows the (r′- Hα)-(r′-i′) plot for a test field. A vertical shift of −0.23 was applied to the synthetic unreddened MS and reddened early A-type tracks in order to obtain a better fit to the data.

2.4 Selection of a sample of A-type dwarf stars from the IPHAS data

In order to obtain a sample of early A-type stars that can be cross-correlated with the GLIMPSE point-source catalogue, all the available IPHAS data in the regions that overlap

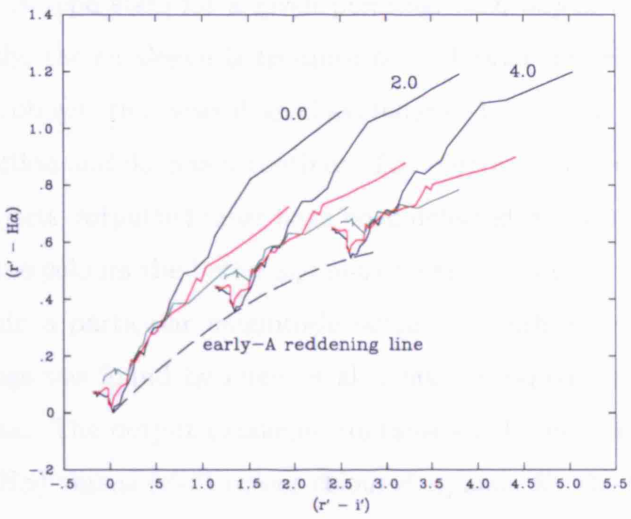

Figure 2.5: The effect of interstellar extinction on synthetic stellar tracks in the (r′-i′), (r- Hα) plane, according to an R = 3.1 Galactic law. For a given visual colour excess, the black lines represent the main sequences, the red lines represent the giant sequences and the green bottom lines show the position of the supergiants. The dashed line shows the reddening track of A0V stars, also known as *early-A reddening line*.

with the GLIMPSE survey were downloaded ($30 < l < 65$ and $|b| < 1$). To ensure the quality of the sample, only data observed with seeing better than 1.7 arcsec was downloaded. Only 50 % (145 of 298) of the IPHAS fields for this region were obtained. The remaining 50 % of the pointings were either observed under poor conditions or have not been observed yet. The complete list of the processed IPHAS catalogues is presented in Table 2.2. The central coordinates of each pointing are listed in both Equatorial J2000 and Galactic coordinate systems, arranged in order of increasing galactic longitude. Column 6 gives the average seeing measured at El Roque de los Muchachos observatory during the *on* and *off* integrations of each field. Field numbers (column 1) correspond to internal IPHAS field names.

2.4.1 Pre-processing of IPHAS catalogues

The pipeline-processed IPHAS catalogues come in the format of ASCII tabulated file. They contain IPHAS astrometry and photometry for both the *on* and *off* pointings of a given field. When available, 2MASS measurements have been included. When select-

ing/extracting the A-type stars for a given pointing, each object catalogue is processed individually. Firstly, the catalogue is trimmed of its header information. Then a FORTRAN code selects objects that were flagged as stellar (-1 or -2) by the CASU automated point-source extraction and detection routines. The Fortran routine also pairs the *on* and *off* catalogues. Objects outputted must have been detected in both the *on* and *off* observations, but only the colours the better signal-to-noise observation is outputted. Objects were selected within a particular magnitude range, of which an r' magnitude range of $14 < m_{r'} < 18$ mags was found by Drew et al. (2005) to represent the best photometry for the IPHAS data. The output catalogue contains all the photometric information to be plotted as (r'- Hα) versus (r'-i') colour-colour diagrams, for the further identification of A-type dwarf stars.

2.4.2 Identification of A-type stars

A graphic Perl Data Language (PDL[2]) routine plots an (r'- Hα)-(r'-i') diagram for the given field and allows the user to interactively fit the positions of the unreddened MS track and the early A-reddening track (by applying an empirical shift as described in Section 2.3.2). Once a good agreement is achieved, the program prompts the user for a width of the early A-reddening strip for object selection. This width is defined as starting from the location of the fitted early A-type reddening track upward. The width that will best represent the location of A-type stars will depend on the stellar population of each field, and therefore must be estimated by eye. In Figure 2.4, a strip width of (r'-H_α) = 0.05 was applied to the reference field IPHAS 4232, where the the A-type candidate stars lying within the strip are plotted in red. The value of the width was imposed to never exceed 0.07. Once the early A-reddening *strip* has been defined, the programme identifies the stars lying within the strip and then extracts the corresponding objects with all their photometric information (r',i', Hα magnitudes, associated uncertainties, and 2MASS JHK photometry if available).

[2]http://pdl.perl.org

Table 2.2: Summary of processed IPHAS object catalogues

Field ID	l [deg]	b [deg]	RA	DEC	Seeing [arcsec]	Total Stars	Total A-type dwarfs	Total with GLIMPSE Correlations
4205	29.58	-0.80	18:48:08.94	-3:21:0.0	0.9	874	137	0
4188	29.73	-0.30	18:46:40.25	-2:59:0.0	1.5	1545	178	3
4213	30.15	-0.71	18:48:53.05	-2:48:0.0	1.1	612	50	32
4196	30.31	-0.21	18:47:24.49	-2:26:0.0	1.1	942	175	129
4222	30.72	-0.62	18:49:37.12	-2:15:0.0	1.0	589	67	51
4189	31.04	0.37	18:46:40.62	-1:31:0.0	1.5	1698	136	99
4254	31.14	-1.03	18:51:49.68	-2:04:0.0	1.3	1425	175	75
4232	31.30	-0.53	18:50:21.29	-1:42:0.0	1.0	2737	214	152
4214	31.45	-0.04	18:48:53.12	-1:20:0.0	1.0	2548	359	237
4197	31.61	0.45	18:47:25.01	-0:58:0.0	1.0	2043	191	58
4265	31.71	-0.94	18:52:33.68	-1:31:0.0	1.5	4327	211	115
4242	31.87	-0.45	18:51:05.41	-1:09:0.0	1.3	4059	388	181
4223	32.03	0.05	18:49:37.33	-0:47:0.0	1.3	3246	423	0
4206	32.19	0.54	18:48:09.30	-0:25:0.0	1.0	1183	97	0
4275	32.28	-0.85	18:53:17.65	-0:58:0.0	1.3	5864	351	81
4190	32.35	1.03	18:46:41.45	-0:03:0.0	1.3	1570	125	3
4253	32.44	-0.36	18:51:49.47	-0:36:0.0	1.3	4314	537	0
4233	32.60	0.13	18:50:21.48	-0:14:0.0	1.1	2286	306	13
4215	32.76	0.63	18:48:53.54	0:08:0.0	1.1	1164	103	77
4285	32.86	-0.77	18:54:01.56	-0:25:0.0	1.5	7301	501	0
4263	33.02	-0.27	18:52:33.49	-0:03:0.0	1.4	3737	389	70
4243	33.17	0.22	18:51:05.58	0:19:0.0	1.3	1170	131	97
4297	33.43	-0.68	18:54:45.46	0:08:0.0	1.3	4000	540	242
4274	33.59	-0.18	18:53:17.57	0:30:0.0	1.3	1058	79	64
4255	33.75	0.31	18:51:49.73	0:52:0.0	1.3	885	62	49
4235	33.91	0.80	18:50:22.03	1:14:0.0	1.2	596	55	41
4309	34.00	-0.59	18:55:29.42	0:41:0.0	1.1	935	75	57
4286	34.16	-0.10	18:54:01.61	1:03:0.0	1.4	637	63	49
4266	34.32	0.40	18:52:33.84	1:25:0.0	1.5	837	82	64
4348	34.42	-1.00	18:57:41.24	0:52:0.0	1.3	343	17	13
4246	34.48	0.89	18:51:06.18	1:47:0.0	1.2	549	34	30
4322	34.58	-0.50	18:56:13.36	1:14:0.0	1.2	835	55	44
4298	34.73	-0.01	18:54:45.60	1:36:0.0	1.3	961	94	82
4276	34.89	0.48	18:53:17.88	1:58:0.0	1.0	464	31	25
4361	34.99	-0.91	18:58:25.07	1:25:0.0	1.3	903	27	17
4256	35.05	0.97	18:51:50.27	2:20:0.0	1.2	370	40	24
4334	35.15	-0.41	18:56:57.25	1:47:0.0	1.3	779	41	29
4288	35.47	0.57	18:54:01.88	2:31:0.0	1.5	451	50	44
4299	36.04	0.66	18:54:45.84	3:04:0.0	1.6	717	85	74
4336	36.45	0.26	18:56:57.35	3:15:0.0	1.3	313	28	28
4401	36.71	-0.64	19:09:36.45	3:04:0.0	1.3	706	72	56
4325	37.19	0.84	18:56:13.71	4:10:0.0	1.5	210	14	11
4415	37.28	-0.55	19:01:20.27	3:37:0.0	1.6	362	44	37
4388	37.44	-0.06	18:59:52.68	3:59:0.0	1.5	333	34	29
4402	38.01	0.03	19:00:36.50	4:32:0.0	1.5	278	16	13
4417	38.58	0.12	19:01:20.30	5:05:0.0	1.5	439	24	24
4389	38.74	0.61	18:59:52.75	5:27:0.0	1.5	325	24	22
4459	39.00	-0.28	19:03:31.64	5:16:0.0	1.6	679	76	68
4403	39.32	0.70	19:00:36.52	6:00:0.0	1.4	565	36	27
4504	39.41	-0.68	19:05:42.97	5:27:0.0	1.4	1073	102	93
4473	39.57	-0.19	19:04:15.41	5:49:0.0	1.4	647	58	52
4416	39.89	0.79	19:01:20.28	6:33:0.0	1.5	817	50	35
4488	40.14	-0.10	19:04:59.19	6:22:0.0	1.5	1008	129	88
4458	40.30	0.39	19:03:31.62	6:44:0.0	1.7	1310	154	137
4534	40.55	-0.50	19:07:10.52	6:33:0.0	1.4	1059	97	82
4503	40.71	-0.01	19:05:42.95	6:55:0.0	1.1	1176	103	89
4518	41.28	0.09	19:06:26.71	7:28:0.0	1.1	1213	82	68
4593	41.54	-0.80	19:10:05.70	7:17:0.0	1.1	903	73	64
4533	41.85	0.18	19:07:10.48	8:01:0.0	1.6	986	78	61
4502	42.01	0.67	19:05:42.78	8:23:0.0	1.2	1010	111	101
4609	42.11	-0.71	19:10:49.52	7:50:0.0	1.5	773	46	31
4517	42.59	0.76	19:06:26.46	8:56:0.0	1.2	1005	80	75
4624	42.68	-0.61	19:11:33.34	8:23:0.0	1.5	1130	69	57
4592	42.84	-0.12	19:10:05.66	8:45:0.0	1.2	880	46	35
4532	43.16	0.85	19:07:10.12	9:29:0.0	1.2	2106	248	184
4607	43.41	-0.03	19:10:49.45	9:18:0.0	1.5	799	94	73
4682	43.66	-0.91	19:14:28.73	9:07:0.0	1.5	2782	150	95
4623	43.98	0.07	19:11:33.25	9:51:0.0	1.3	1125	107	60
4590	44.14	0.55	19:10:05.41	10:13:0.0	1.1	2153	334	269
4699	44.24	-0.82	19:15:12.66	9:40:0.0	1.6	1366	99	87
4605	44.71	0.65	19:10:49.07	10:46:0.0	1.5	3485	436	312
4714	44.81	-0.72	19:15:56.63	10:13:0.0	1.5	1469	136	101
4683	44.96	-0.23	19:14:28.75	10:35:0.0	1.6	1696	150	70
4620	45.28	0.75	19:11:32.73	11:19:0.0	1.2	4395	392	269
4665	45.69	0.35	19:13:44.59	11:30:0.0	1.5	1122	167	138
4635	45.85	0.84	19:12:16.41	11:52:0.0	1.2	4230	584	281
4679	46.26	0.45	19:14:28.38	12:03:0.0	1.2	1321	265	225
4649	46.42	0.94	19:12:59.97	12:25:0.0	1.7	2946	380	159
4802	46.93	-0.82	19:20:20.63	12:03:0.0	1.7	1464	146	84
4663	46.99	1.04	19:13:43.53	12:58:0.0	1.6	1943	191	57
4817	47.50	-0.72	19:21:04.70	12:36:0.0	1.8	1043	93	80
4831	48.07	-0.62	19:21:48.80	13:09:0.0	1.8	1792	22	16
4801	48.23	-0.13	19:20:20.42	13:31:0.0	1.8	1927	212	165

cont. on next page

cont. from previous page

4816	48.80	-0.03	19:21:04.48	14:04:0.0	1.8	2088	184	137
4859	49.21	-0.42	19:23:17.20	14:15:0.0	1.6	1736	165	121
4830	49.36	0.07	19:21:48.57	14:37:0.0	1.8	1660	47	0
4902	49.63	-0.80	19:25:30.00	14:26:0.0	1.8	2419	199	160
4916	50.19	-0.70	19:26:14.31	14:59:0.0	0.9	2174	232	191
4857	50.50	0.28	19:23:16.58	15:43:0.0	1.6	1983	143	111
4930	50.76	-0.59	19:26:58.69	15:32:0.0	0.9	2331	91	69
4901	50.92	-0.10	19:25:29.72	15:54:0.0	1.6	1983	120	91
4973	51.18	-0.97	19:29:11.95	15:43:0.0	0.9	1460	142	64
4944	51.33	-0.49	19:27:43.14	16:05:0.0	1.1	1946	118	95
4915	51.48	0.00	19:26:14.02	16:27:0.0	0.9	2384	236	186
4986	51.75	-0.87	19:29:56.62	16:16:0.0	0.9	1695	59	52
4928	52.05	0.11	19:26:58.16	17:00:0.0	0.9	1984	255	119
4899	52.20	0.60	19:25:28.54	17:22:0.0	1.7	1995	156	117
5000	52.32	-0.76	19:30:41.19	16:49:0.0	1.3	2357	207	178
4972	52.47	-0.27	19:29:11.83	17:11:0.0	1.2	1283	86	73
4942	52.62	0.22	19:27:42.38	17:33:0.0	0.9	1687	118	94
4912	52.77	0.70	19:26:12.55	17:55:0.0	0.9	2044	190	147
5015	52.88	-0.65	19:31:25.81	17:22:0.0	1.2	2380	174	106
4985	53.03	-0.16	19:29:56.29	17:44:0.0	0.9	1008	35	34
4926	53.34	0.81	19:26:56.63	18:27:59.9	0.9	2075	147	109
4999	53.60	-0.05	19:30:40.82	18:17:0.0	1.3	1364	118	97
4970	53.75	0.43	19:29:10.98	18:38:59.9	1.6	1694	171	116
4939	53.90	0.92	19:27:40.50	19:00:59.9	1.1	3148	402	218
5014	54.17	0.06	19:31:25.45	18:49:59.9	1.3	3285	324	175
4983	54.32	0.54	19:29:55.14	19:11:59.9	0.9	5067	188	65
4997	54.89	0.66	19:30:39.36	19:44:59.9	1.3	5019	436	139
5098	55.00	-0.70	19:35:54.90	19:11:59.9	0.9	3108	287	92
5069	55.15	-0.21	19:34:24.73	19:33:59.9	0.8	4650	400	174
5041	55.30	0.28	19:32:54.41	19:55:59.9	0.9	4928	183	89
5112	55.57	-0.58	19:36:39.94	19:44:59.9	1.1	4229	619	292
5083	55.72	-0.09	19:35:09.55	20:06:59.9	0.9	4422	561	305
5025	56.02	0.88	19:32:08.01	20:50:59.9	1.1	2828	60	23
5126	56.14	-0.47	19:37:25.09	20:17:59.9	0.9	4457	399	195
5097	56.28	0.02	19:35:54.46	20:39:59.9	0.9	2286	139	113
5039	56.58	1.00	19:32:52.14	21:23:59.9	0.9	2723	190	85
5140	56.70	-0.35	19:38:10.34	20:50:59.9	1.6	2467	198	165
5111	56.85	0.14	19:36:39.48	21:12:59.9	1.0	1207	70	63
5080	57.00	0.62	19:35:08.16	21:34:59.9	0.8	1734	168	48
5124	57.41	0.25	19:37:24.30	21:45:59.9	1.0	689	79	74
5095	57.56	0.74	19:35:52.71	22:07:59.9	0.9	1645	102	85
5138	57.98	0.37	19:38:09.21	22:18:59.9	1.5	1558	85	39
5108	58.13	0.86	19:36:37.36	22:40:59.9	0.9	2288	178	94
5152	58.54	0.49	19:38:54.23	22:51:59.9	1.5	1867	133	94
5262	59.24	-0.73	19:45:00.13	22:51:59.9	1.1	3095	240	190
5277	59.80	-0.61	19:45:45.96	23:24:59.9	1.1	2592	207	169
5261	60.51	0.01	19:44:59.57	24:19:59.9	1.3	4143	413	262
5275	61.07	0.13	19:45:45.38	24:52:59.9	1.1	3989	387	224
5273	62.33	0.88	19:45:42.67	26:20:59.8	1.1	2978	246	162
5285	62.89	1.01	19:46:27.69	26:53:59.8	1.0	4273	288	93
5489	65.02	-0.76	19:58:11.41	27:48:59.8	1.5	2900	196	63
TOTAL						260223	23050	12786

2.4.3 Results: An IPHAS sample of A-type stars

Table 2.2, column 7, summarizes the number of objects catalogued in each field, and that are the input for A-type extraction. Column 8 shows the effective number of A-type dwarfs extracted for each IPHAS field. Of a total of 260223 input stars, 23050 objects were selected as early A-type on the basis of their IPHAS colours. It is found that on average the A-type star population corresponds to less than 10% of the total field stars. The numbers in Column 9 will be explained in Section 2.5.5.

Table 2.3: GLIMPSE sensitivities

Channel	λ [μm]	Zeropoint [Jy]	Lower flux limits [mJy/mag]	Upper flux limits [mJy/mag]	FWHM [arcsecond]
channel 1	3.6	277.5	0.6/14.2	439/7	1.66
channel 2	4.5	179.5	0.4/14.1	450/6.5	1.72
channel 3	5.8	116.5	2/11.9	2930/4	1.88
channel 4	8.0	63.13	10/9.5	1590/4	1.98

Observational sensitivities of the GLIMPSE survey. Only sources with fluxes greater than the lower limits quoted in Table 2.3 and having signal-to-noise ratios greater than 3 are included in the GHRC. The zeropoint (luminosity of a 0th magnitude star) in each channel is given for conversion from fluxes to magnitudes. From the *Spitzer* Observer Manual Version 4.0[3] and the GLIMPSE Legacy Data Products Notes version 1.5[3].

2.5 Correlation of the sample of A-type stars with the GLIMPSE catalogue

GLIMPSE - the Galactic Legacy Infrared Mid-Plane Survey Extraordinaire - is a fully sampled, confusion limited, 4-band near- to mid-infrared survey of the inner two-thirds of the Galactic disk with a spatial resolution of 2 arcseconds. The Infrared Array Camera (IRAC) imaged 220 square degrees at wavelengths centred on 3.6, 4.5, 5.8, and 8.0 μm in the Galactic longitude range 10 to 65 degrees on both sides of the Galactic Centre, over a Galactic latitude range of +/- 1 degrees. GLIMPSE was completed in 2005, and the data acquired is in the public domain, downloadable from the *Spitzer* Science Centre server (SSC[3]). GLIMPSE data products come as two point-source catalogues and flux-calibrated mosaicked images from each IRAC band.

2.5.1 IRAC observations

The *Spitzer* Infrared Array Camera (IRAC) is a four-channel imaging camera with a 5.2 x 5.2 arcmin field of view at 3.6, 4.5, 5.8, and 8μm (Fazio et al. 2004). The four detectors are 256 x 256 pixels in size, with a pixel size of 1.2x1.2 arcsecs. The diffraction-limited angular resolution (FWHM) measured in-orbit for the four different channels is shown in Table 2.3. Two adjacent fields of view are imaged in pairs (3.6 and 5.8μm; 4.5 and 8.0μm), using dichroic beam-splitters.

The GLIMPSE observations consist of two 1.2 second integrations at each pointing

[3]http://ssc.spitzer.caltech.edu/

position, for a total 77000 pointings on all 4 IRAC bands. Acquired data are transferred to the SSC where they are processed with IRAC's validated pipeline. This performs flux calibration (using observed photometric standards), sky-flat and dark-bias subtractions. Detailed description of the Pipeline processing can be found in the GLIMPSE Pipeline Description document (GPD[4]). Point source extraction is performed with a modified version of DAOPHOT, prior to band-merging of sources in a final catalogue.

2.5.2 The GLIMPSE Highly-Reliable Catalogue

The GLIMPSE Highly-Reliable Catalogue (GHRC) contains point-like sources whose selection requirements meet a 95% reliability criteria, determined by the fact that a source must be detected **twice** in one band and **at least once** in an adjacent band. This is called the *2+1* criterion. Of the stars satisfying this criterion, only sources with fluxes within the faint/bright limits shown in Table 2.3 were included in the catalogue. The fluxes in the two bands satisfying the *2+1* criterion are required to have signal-to-noise ratios (S/N) greater than 5. For the other two bands the constraints are less stringent, requiring only that their fluxes have a S/N> 3 to be included as detections. The GHRC contains $\sim$ 31 million sources.

The *Spitzer* pointing accuracy is 1 arcsecond (Werner et al. 2004). After pointing refinement with the 2MASS PSC, whose absolute accuracy is better than 0.2 arcsecond, the GLIMPSE absolute accuracy is expected to be better than 0.5 arcsecond. Only 0.25% of the GLIMPSE data have confusion flags, i.e sources within less than 1 arcsecond.

2.5.3 Correlation of the A-type sample with the GLIMPSE HRC

Each IPHAS A-type star catalogue is correlated with its overlapping GLIMPSE HRC field using a PDL routine. For each star present in the input A-type star catalogue, the program reads its sky RA and DEC coordinates and looks for GLIMPSE objects that lie within 0.5 arcseconds (i.e. the GLIMPSE absolute pointing accuracy). Table 2.4 quantifies the dependence between matching radial distance and the number of correlated sources for an IPHAS test field. The number of correlated sources increases with increasing matching radial distance, but at the expense of poorer true correlations. We prefer to adopt

[4]`http://www.astro.wisc.edu/sirtf/docs.html`

Table 2.4: Percentage of A-type stars matched as a function of radial separation.

Maximum separation (arcsec)	Number of matches	Percentage of stars matched
0.1	1	0.2
0.3	72	15.1
0.5	258	54.4
0.7	286	60.3
1.0	291	61.3

A total of 474 stars from test fields 4857, 4930 and 4901 were selected.

Table 2.5: Confusion estimates

RA-Dec shift (arcsec)	Number of matches	Percentage of stars matched
1	3	0.63
5	3	0.63
10	5	1.05
15	8	1.68
30	7	1.47

Percentage of matched stars as a function of a shift in both RA and Dec of the positions of the A-type catalogue stars. The maximum separation for matches was set to 1 arcsecond.

GLIMPSE's absolute pointing accuracy of 0.5 arcseconds as the matching radius for the IPHAS-GLIMPSE correlation.

2.5.4 Confusion estimates

In order to estimate the confusion of the A-type star catalogue/GLIMPSE correlations, we shifted the sky positions of our test A-type star catalogue stars by a chosen amount in both RA and Dec and then attempted to correlate the objects again. The results of this experiment are shown in table 2.5, where we show the number of correlated stars for a given coordinate shift, for a maximum separation of 1 arcsecond for matches. Using a matching radius of 1 arcsecond led to zero correlations for any coordinate shift value. Smaller values of the maximum separation for matches produced even lower correlations.

2.5.5 Results

Column 9 in Table 2.2 summarizes the results from the IPHAS/GLIMPSE A-type star correlation procedure. Of an input of 23050 IPHAS selected A-type stars, 12786 objects have reliable detections in at least 2 IRAC bands (i.e have entries in the GLMC). Of these 12786 objects, 11347 have positive detections in all 2MASS near-IR bands. Table 2.6 shows the observed distribution of stars along the different pass-bands and their observed mean magnitudes. In order to inspect for stars with unusual colours, the observed magnitudes

Table 2.6: Summary of the statistics for the IPHAS/GLIMPSE sample of A-type stars.

Band	Number of stars	Mean observed magnitude
r	12786	16.784
i	12786	15.671
J	12329	13.949
H	11993	13.449
K	11387	13.175
3.6	11292	12.901
4.5	11307	12.919
5.8	4713	12.135
8	4211	12.108

were de-reddened using the relations described in Appendix A. These are based on the optical and near-IR reddening relations of Cohen et al. (1981) for A0V stars, and on the relations of Indebetouw et al. (2005) for the IRAC bands.

In order to construct full de-reddened SEDs, we required that all stars have positive detections in all 2MASS and IRAC bands. This means flagging entries having a flux or flux uncertainty = −99.999 in the GPSC and similarly = 0.000 in the 2MASS PSC. This constraint led to a sub-sample of 3062 A-type stars with fully sampled 0.6 to 8 μm SEDs.

2.5.6 Stars with 8μm excesses

Figure 2.6 shows the (J-H)-(K-8) colour-colour diagram for the 3062 stars having detected fluxes in all IPHAS, 2MASS and IRAC bands. E(K-8) colour excesses are calculated by taking the differences between the dereddened K and 8 μm magnitudes. Since the stars of our sample should be mostly A0 and A5 dwarfs, their de-reddened observed colours correspond closely to their colour excesses. In accord to the local mass function in Miller & Scalo (1979), and to how A stars behave under reddening in the colour-colour plane (as described in the Pickles Library), the most likely mass-function weighted average spectral type is A2 (for A0-A5 being pulled out by our colour-colour plane selection). An A2V spectral type implies an absolute magnitude of M_V=1.6 mag (or $M_{r'}$= 1.58, Houk et al. 1997) and an intrinsic r'-i' colour of 0.05, which is the value we adopted to estimate the colour excesses. (K-8) and (K-12$_{IRAS}$) colours were used in previous searches for warm disk candidates (Uzpen et al. 2005; Aumann & Probst 1991), as MS stars should exhibit minimal colour differences at these wavelengths.

The majority of stars (96.2%) have −0.55 <(K-8)< 0.55, with a mean colour excess $E(K-8) = 0.02$ and a standard deviation of 0.2731. This distribution is consistent with

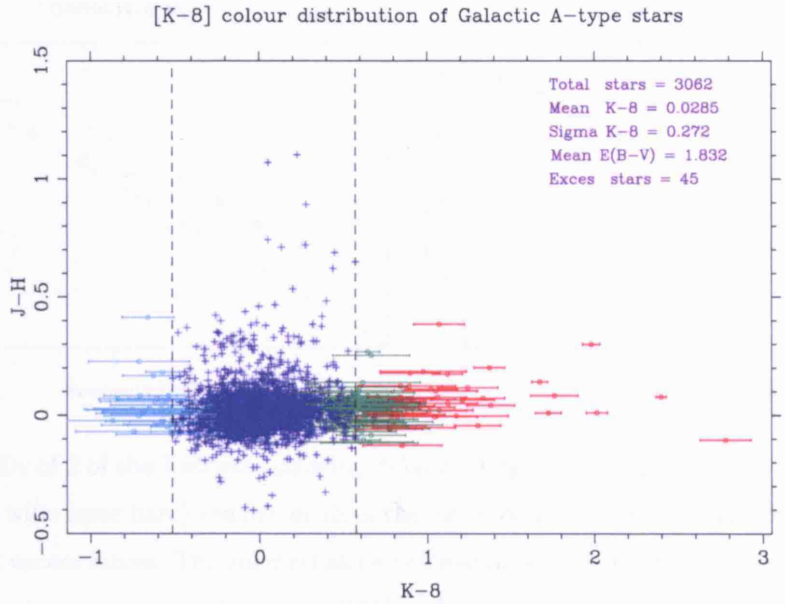

Figure 2.6: Dereddened (J-H)-(K-8) colour-colour diagram for the 3062 sample A-type stars. The vertical lines denotes 2 times the standard deviation from the mean (K-8) colour of the sample. Objects having detectable (K-8) colour excesses are plotted in red, whereas objects with normal colours are plotted in blue. Light-blue dot denotes the 33 stars that have bluer (K-8) colours than expected for A-type stars, although they all lie within 1 σ of their photometric errors from the main group. Green dots represent 59 stars whose E(K-8) colours could be indicative of an 8μm excess but do not satisfy the E(K-8)$> 0.55 + 1\sigma$ criterion (see text for details).

most stars being A-type dwarfs. 105 of the 3062 stars have excesses larger than twice the dispersion of the main group (E(K-8)> 0.55). Of these 105 stars, only 45 stars have (K-8) colours larger than 0.55 consistently within 1σ of the photometric errors. Therefore, similarly to the search done by Uzpen et al. (2005), a reliable colour excess detection will have to meet E(K-8)$> 0.55 + 1\sigma$ (and would also be required to have detections in all IRAC bands). Applying this criterion we conclude that 45 stars have definite E(K-8) colour excesses. In addition, we note that there are no symmetric points satisfying this criteria in the negative direction of the distribution (i.e. E(K-8)$< -0.55 - 1\sigma$), suggesting these 45 stars with 8μm excesses correspond to a real population of excess objects and are not spurious. However, preliminary inspection of the dereddened SEDs of the 45 stars showed that 7 of the stars had SEDs deviating significantly from that of an A-type star, resembling more those of cooler spectral types stars. This can be seen in Figure 2.7 where the SEDs of 2 of these 7 objects are shown against the SED of an A0 and of a G5 dwarf (the latter obtained from Kurucz model atmospheres listed in DIPSO). These 7 stars were

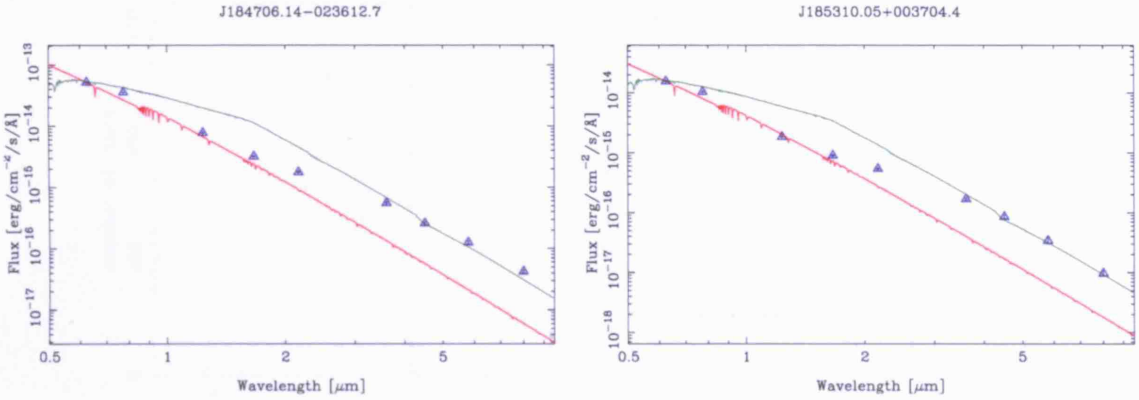

Figure 2.7: SEDs of 2 of the 7 objects showing dubious A-type identifications. The observed SEDs (blue triangles with error bars) are flatter than the SEDs of an A-type star (red line), which leads to false mid-IR excess fluxes. The spectral slope of these objects is better described with the SEDs of a cooler G5 dwarf (green line).

excluded from further analysis.

There are an additional 59 stars that have E(K-8) colours larger than 0.55 mags but not within 1σ of the photometric errors. In addition there is a population of 33 negative outliers, but their amplitudes are quite small and always fall within 1σ of the colours of the main distribution. This suggests that nearly half of the 59 stars on the positive side have real excesses.

Following Clarke et al. (2005), we plot in Figure 2.8 shows the distribution of (K-8) excesses of the sample. The distribution is clearly asymmetric about 0, with the long tail seen on the positive side corresponding to excess stars. The negative side follows a Gaussian distribution with FWHM=0.4, centred at E(K-8)=-0.05. The width of the distribution can be attributed to the combined effect of reddening estimation, the spectral type assumption, and mainly to the intrinsic scatter of the A-type sample.

Mirroring of the negative distribution allows us to identify the fraction of stars in the positive side having an 8μm excess. By E(K-8)=0.55, the percentage of stars having an excess is 80. Therefore, by assuming a detection threshold of E(K-8)>0.55 we allow for having at least an 80% probability of finding an excess object within that interval.

In Table 2.7 we list the photometric parameters of 28 IPHAS A-type stars having 8μm

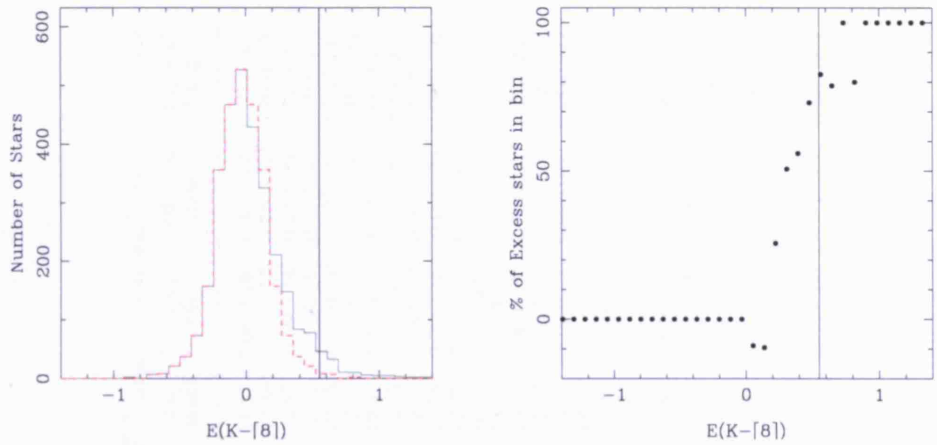

Figure 2.8: *Left-hand panel*: Distribution of (K-8) excesses of the 3062 stars (solid line). Mirroring of the negative side of the distribution (dashed line) is used to estimate the fraction of the excess stars located in the positive side. The vertical line at E(K-8)=0.55 denotes twice the standard deviation from the mean E(K-8) colour of the entire sample . *Right-hand panel*: Percentage of excess stars as a function of E(K-8). By E(K-8)=0.55, the percentage of stars having an excess reaches 80%.

excesses. We have excluded 10 stars for which we have also detected 24μm fluxes that are definitely in excess of the expected stellar photospheric values. These are discussed along with other 24μm detections in Section 2.6.1.

Table 2.7: Photometric parameters for 28 IPHAS A-type stars with 8μm excesses

Reference ID	IPHAS ID	GLIMPSE ID	r′ (mag)	r′-i′ (mag)	r′-J (mag)	J (mag)	J-H (mag)	J-K (mag)	J-[3.6] (mag)	[3.6] (mag)	[3.6]-[4.5] (mag)	[3.6]-[5.8] (mag)	[3.6]-[8.0] (mag)
1	J184639.77-022321.4	G030.2612-00.0278	16.05(0.00)	1.18(0.00)	3.03(0.02)	13.02	0.54(0.03)	0.92(0.03)	1.75(0.09)	11.27	0.08(0.16)	0.48(0.17)	0.67(0.20)
2	J184635.98-010456.3	G031.4170+00.5826	17.27(0.02)	1.10(0.03)	2.91(0.04)	14.36	0.65(0.05)	0.94(0.07)	1.47(0.11)	12.89	-0.30(0.17)	0.73(0.37)	0.79(0.27)
3	J185113.90-011705.4	G031.7648-00.5399	15.34(0.02)	0.63(0.03)	1.91(0.04)	13.43	0.38(0.04)	0.49(0.04)	0.80(0.09)	12.63	-0.36(0.14)	0.28(0.29)	1.12(0.20)
4	J185312.47-010651.4	G032.1418-00.9018	15.70(0.01)	0.57(0.01)	1.70(0.05)	14.00	0.32(0.08)	0.35(0.09)	0.78(0.11)	13.22	-0.17(0.16)	0.47(0.36)	0.80(0.26)
5	J185457.60+000839.3	G033.4617-00.7178	15.58(0.00)	0.82(0.00)	2.13(0.05)	13.45	0.39(0.07)	0.61(0.06)	0.90(0.09)	12.55	-0.08(0.12)	-0.10(0.23)	0.75(0.19)
6	J185342.82+014905.7	G034.8094+00.3229	16.33(0.01)	1.04(0.01)	2.74(0.02)	13.59	0.49(0.03)	0.89(0.03)	1.58(0.09)	12.01	0.11(0.11)	0.13(0.19)	0.48(0.18)
7	J185704.71+015647.9	G035.3074-00.3667	17.39(0.00)	1.27(0.01)	3.12(0.04)	14.27	0.61(0.06)	0.97(0.06)	1.78(0.12)	12.49	-0.19(0.16)	-0.13(0.35)	0.66(0.20)
8	J185900.57+034950.0	G037.2035+00.0648	17.42(0.00)	1.45(0.01)	3.83(0.02)	13.59	0.65(0.03)	0.94(0.04)	1.28(0.08)	12.31	0.00(0.13)	0.24(0.26)	0.98(0.20)
9	J190153.07+051106.7	G038.7359+00.0471	17.08(0.05)	1.36(0.07)	3.39(0.05)	13.69	0.59(0.04)	0.91(0.04)	1.32(0.07)	12.37	-0.08(0.12)	0.00(0.16)	0.78(0.17)
10	J190441.00+055641.3	G039.7301-00.2238	17.43(0.04)	1.36(0.06)	3.23(0.04)	14.20	0.75(0.05)	1.10(0.04)	1.45(0.08)	12.75	-0.06(0.15)	-0.06(0.35)	0.99(0.19)
11	J190310.58+064125.8	G040.2211+00.4509	15.98(0.01)	0.79(0.01)	2.22(0.04)	13.76	0.39(0.06)	0.59(0.06)	1.04(0.11)	12.72	-0.12(0.16)	0.34(0.29)	1.01(0.21)
12	J191100.65+094543.7	G043.8402+00.1432	15.18(0.01)	1.18(0.01)	3.00(0.02)	12.18	0.57(0.03)	1.04(0.03)	2.00(0.05)	10.18	0.59(0.08)	1.01(0.07)	1.81(0.05)
13	J191512.38+120907.4	G046.4351+00.3390	17.54(0.04)	1.19(0.05)	2.89(0.06)	14.65	0.58(0.07)	0.82(0.08)	0.89(0.10)	13.76	0.09(0.17)	0.92(0.34)	2.07(0.16)
14	J192531.09+141828.3	G049.5169-00.8640	16.06(0.02)	0.86(0.03)	2.16(0.04)	13.90	0.39(0.07)	0.58(0.07)	0.58(0.15)	13.32	0.06(0.19)	1.02(0.36)	1.23(0.24)
15	J193018.84+171218.8	G052.6139-00.4953	17.82(0.02)	1.71(0.02)	4.34(0.04)	13.48	0.75(0.06)	1.08(0.07)	1.41(0.08)	12.07	0.14(0.11)	0.52(0.17)	1.29(0.20)
16	J193209.51+171326.9	G052.8424-00.8723	16.02(0.04)	0.79(0.05)	1.91(0.05)	14.11	0.32(0.05)	0.47(0.06)	0.82(0.11)	13.29	-0.14(0.25)	0.49(0.36)	0.94(0.27)
17	J193104.30+194309.8	G054.9051+00.5553	15.11(0.02)	0.61(0.03)	1.71(0.02)	13.40	0.11(0.03)	0.29(0.04)	0.42(0.09)	12.98	-0.07(0.14)	0.17(0.23)	0.91(0.25)
18	J193505.07+194725.5	G055.4238-00.2369	17.72(0.00)	1.33(0.03)	3.23(0.02)	14.49	0.50(0.03)	0.81(0.04)	1.02(0.09)	13.47	0.18(0.14)	0.99(0.29)	1.13(0.26)
19	J193532.67+220857.0	G057.5371+00.8165	17.10(0.01)	1.12(0.01)	2.95(0.03)	14.15	0.46(0.04)	0.60(0.05)	0.94(0.09)	13.21	-0.08(0.15)	0.30(0.35)	0.84(0.26)
20	J194518.08+224630.9	G059.1942-00.8348	17.27(0.01)	1.12(0.01)	2.91(0.03)	14.36	0.53(0.05)	0.76(0.05)	1.05(0.11)	13.31	0.12(0.16)	0.57(0.36)	1.03(0.23)
21	J194516.03+225606.4	G059.3285-00.7480	17.04(0.03)	0.93(0.04)	2.49(0.05)	14.55	0.39(0.06)	0.51(0.06)	0.69(0.11)	13.86	-0.09(0.20)	0.93(0.34)	0.99(0.24)
22	J194527.23+230004.9	G059.4074-00.7520	16.99(0.06)	1.00(0.08)	2.61(0.07)	14.38	0.45(0.05)	0.59(0.05)	0.99(0.13)	13.39	0.01(0.19)	0.74(0.29)	0.79(0.29)
23	J194456.93+231441.3	G059.5601-00.5296	17.17(0.03)	1.03(0.04)	2.53(0.07)	14.64	0.55(0.08)	0.74(0.09)	0.99(0.13)	13.65	-0.03(0.17)	1.41(0.28)	0.97(0.30)
24	J194517.93+241547.1	G060.4816-00.0892	16.66(0.08)	0.92(0.11)	2.57(0.09)	14.09	0.51(0.04)	0.66(0.06)	0.85(0.07)	13.24	0.02(0.13)	0.26(0.33)	0.94(0.25)
25	J194412.33+242454.9	G060.4889+-00.2025	16.61(0.07)	0.85(0.10)	2.31(0.07)	14.30	0.36(0.04)	0.59(0.04)	0.63(0.12)	13.67	0.09(0.16)	1.04(0.33)	1.04(0.22)
26	J194512.55+242107.3	G060.5484-00.0270	16.22(0.06)	0.79(0.08)	2.10(0.08)	14.12	0.43(0.08)	0.62(0.08)	0.89(0.09)	13.23	-0.03(0.12)	0.16(0.34)	1.00(0.17)
27	J194518.54+242116.7	G060.5622-00.0453	16.41(0.05)	0.86(0.07)	2.29(0.06)	14.12	0.39(0.05)	0.56(0.07)	0.91(0.07)	13.21	-0.04(0.11)	0.75(0.23)	1.30(0.14)
28	J194527.76+242904.0	G060.6920-00.0106	15.46(0.06)	0.58(0.08)	1.64(0.06)	13.82	0.30(0.04)	0.47(0.04)	0.64(0.10)	13.18	0.07(0.13)	0.77(0.28)	0.85(0.22)

Observed colours at the different IPHAS, 2MASS and IRAC bands.

Table 2.8: Derived parameters for IPHAS A-type stars with 8μm excesses

Reference ID	IPHAS ID	GLIMPSE ID	$A_{r'}$ (mag)	d (kpc)	3.6μm (mJy)	4.5μm (mJy)	5.8μm (mJy)	8μm (mJy)	T$\leq$ (K)	$L_{IR}/L_{\star}$
1	J184639.77–022321.4	G030.2612–00.0278	4.59(0.01)	1.03(0.02)	4.7(6.7)	2.8(3.9)	4.3(6.0)	3.1(5.3)	762	3.7e-03(1.2e-03)
2	J184635.98–010456.3	G031.4170+00.5826	4.28(0.10)	2.08(0.04)	0.6(2.8)	-	1.2(2.3)	0.7(3.4)	253	3.6e-03(1.4e-02)
3	J185113.90–011705.4	G031.7648–00.5399	2.45(0.08)	1.98(0.02)	-	-	-	1.3(4.8)	196	1.5e-02(8.0e-02)
4	J185312.47–010651.4	G032.1418–00.9018	2.22(0.06)	2.61(0.02)	0.29(2.9)	-	-	0.5(3.3)	489	1.6e-03(2.7e-03)
5	J185457.60+000839.3	G033.4617–00.7178	3.18(0.00)	1.58(0.02)	-	-	-	0.8(3.9)	112	7.5e-01(5.0e-01)
6	J185342.82+014905.7	G034.8094+00.3229	4.04(0.04)	1.51(0.03)	1.9(5.4)	1.3(6.8)	1.0(2.9)	1.1(4.8)	767	2.5e-03(8.6e-04)
7	J185704.71+015647.9	G035.3074–00.3667	4.95(0.00)	1.61(0.04)	1.5(5.0)	-	-	1.0(5.6)	651	1.8e-03(2.4e-03)
8	J185900.57+034950.0	G037.2035+00.0648	5.67(0.01)	1.18(0.04)	-	-	-	1.4(4.5)	173	1.5e-02(5.5e-02)
9	J190153.07+051106.7	G038.7359+00.0471	5.28(0.13)	1.20(0.04)	-	-	-	1.0(4.8)	114	5.2e-01(5.2e-01)
10	J190441.00+055641.3	G039.7301–00.2238	5.31(0.13)	1.39(0.04)	-	-	-	1.0(4.9)	114	7.2e-01(5.0e-01)
11	J190310.58+064125.8	G040.2211+00.4509	3.07(0.04)	2.01(0.02)	0.6(2.9)	-	-	1.1(4.9)	405	2.3e-03(3.3e-03)
12	J191100.65+094543.7	G043.8402+00.1432	4.59(0.02)	0.69(0.02)	15.3(14.4)	22.3(16.0)	25.5(21.6)	33.6(55.4)	655	1.2e-02(1.2e-03)
13	J191512.38+120907.4	G046.4351+00.3390	4.65(0.16)	1.98(0.05)	-	-	-	1.4(9.1)	208	1.9e-02(5.6e-02)
14	J192531.09+141828.3	G049.5169–00.8640	3.34(0.08)	1.83(0.03)	-	-	0.9(2.0)	0.7(4.0)	216	6.2e-03(4.8e-02)
15	J193018.84+171218.8	G052.6139–00.4953	6.65(0.04)	0.90(0.07)	-	-	1.0(2.6)	2.9(5.3)	248	3.8e-03(7.5e-03)
16	J193209.51+171326.9	G052.8424–00.8723	3.08(0.16)	2.04(0.03)	-	-	-	0.5(3.3)	414	1.7e-03(4.1e-03)
17	J193104.30+194309.8	G054.9051+00.5553	2.36(0.08)	1.86(0.02)	-	-	-	0.6(3.0)	197	8.4e-03(7.9e-02)
18	J193505.07+194725.5	G055.4238–00.2369	5.17(0.02)	1.69(0.11)	-	-	0.8(2.7)	0.6(3.5)	289	2.2e-03(6.2e-03)
19	J193532.67+220857.0	G057.5371+00.8165	4.39(0.05)	1.83(0.06)	-	-	-	0.5(3.2)	220	3.9e-03(3.4e-02)
20	J194518.08+224630.9	G059.1942–00.8348	4.36(0.04)	2.00(0.05)	-	-	-	0.6(4.3)	347	1.7e-03(3.9e-03)
21	J194516.03+225606.4	G059.3285–00.7480	3.63(0.15)	2.52(0.05)	-	-	0.5(2.2)	0.3(3.4)	249)	2.9e-03(2.9e-02)
22	J194527.23+230004.9	G059.4074–00.7520	3.89(0.29)	2.19(0.05)	-	-	0.7(2.8)	0.4(3.0)	513)	1.3e-03(1.9e-03)
23	J194456.93+231441.3	G059.5601–00.5296	4.03(0.13)	2.23(0.06)	-	-	1.3(3.9)	0.4(3.0)	281	2.3e-03(6.1e-03)
24	J194517.93+241547.1	G060.4816–00.0892	3.60(0.37)	2.15(0.04)	-	-	-	0.5(3.0)	192	8.5e-03(4.1e-01)
25	J194412.33+242454.9	G060.4889+00.2025	3.32(0.37)	2.39(0.04)	-	-	0.7(2.3)	0.4(3.7)	214	5.2e-03(2.8e-02)
26	J194512.55+242107.3	G060.5484–00.0270	3.10(0.28)	2.22(0.04)	-	-	-	0.6(5.5)	208	8.2e-03(9.5e-02)
27	J194518.54+242116.7	G060.5622–00.0453	3.33(0.25)	2.16(0.04)	0.2(2.7)	-	0.8(3.2)	1.0(7.3)	366	2.9e-03(3.0e-03)
28	J194527.76+242904.0	G060.6920–00.0106	2.28(0.30)	2.27(0.02)	-	-	0.7(2.4)	0.5(3.5)	392	1.4e-03(2.3e-03)

Derived parameters for stars with 8μm excesses with respect to a normalised A0V star SED. The reference SEDs were normalised to match the observed K-band fluxes. Excess fluxes at each wavelength are presented in units of mJy, with the figures within brackets denoting the signal-to-noise ratios of the detections. Only excess fluxes with detected S/N ratios larger than 2 are shown. $A_{r'}$ correspond to the visual extinction in the r′ band, while *d* correspond to the spectrophotometric distance derived assuming the absolute magnitude of an A2 dwarf. For $A_{r'}$, *d* as well as for T and $L_{IR}/L_{\star}$, the values within brackets represent the 1 σ uncertainties.

2.5.7 The mid-IR excesses

In order to characterise the strength of the mid-IR excesses we normalised the photospheric SED of an A0 dwarf to the observed stellar SEDs (the model SED corresponded to a Kurucz model atmosphere with T = 9400 and log g = 3.95). The photospheric model SED was normalised to the dereddened K-band fluxes. In general this gave a good fit to the optical and near-IR data-points, suggesting that the stars are indeed A-type stars.

The mid-IR excesses (in mJy) were calculated by taking the ratio of the observed and the model SEDs (monochromatic stellar flux interpolated to the central wavelength of each IRAC pass-band). The signal-to-noise ratio of the excesses is defined as the ratio of the excess (in mJy) to the photometric uncertainty (in mJy) of the overall flux measurement. The strength of the mid-IR excesses determined for the 28 stars are shown in Table 2.8. Only excesses detected with a S/N higher than 2 are shown. All of the measured excesses have a S/N of 3 or higher. Visual extinctions in the r′ band, $A_{r'}$, derived using the relations in Appendix A, are also shown. The spectrophotometric distances are derived from the observed r′ magnitudes and the r′ band extinctions, assuming the absolute r′ magnitude of an A2V star ($M_{r'}$=1.58):

$$d = 10^{(r'-A_{r'}-1.58+5)/5)/1000}. \tag{2.2}$$

The observed SEDs are assumed to be the sum of a model stellar atmosphere SED ($SED_\star$) and a cooler black body of a given temperature ($SED_{\rm disk}$)

$$SED_{mod} = SED_\star + SED_{\rm disk}. \tag{2.3}$$

As all the stars from our sample are thought to be A-type, we assume that $SED_\star$ is constant and always equal to the photospheric SED of an A0 dwarf (as described in the previous paragraphs). For each of the 28 stars in Table 2.8, we found the model that minimised the chi-squared (χ^2) difference between the modelled SED_{mod} and the observed data-points, where

$$\chi^2 = \sum \frac{(y_i - y_{mod})^2}{\sigma_i^2}. \tag{2.4}$$

In order to find the best model-fit to the data we use the variable-metric routine Migrad of the Minuit package from CERN[5]. The iterative process finds simultaneously the best fit

[5] http://seal.web.cern.ch/seal/work-packages/mathlibs/minuit/home.html

temperature of the black body (T [K]) and its angular diameter in the sky (corresponding to the square-root of the flux normalisation constant). Errors on individual parameters are estimated by searching parameter space for the $\chi^2 = 1$ contour. Table 2.8 shows the best-fit black body temperature derived for each of the 28 stars. Figure 2.11 shows the results from our black-body fitting routine. The de-reddened optical IPHAS, 2MASS and GLIMPSE data points are plotted in blue, with photometric error-bars. The solid line in red corresponds to the reference photospheric SED normalised to the K-band flux. The pink dashed line represents our best-fit black-body and the solid green line represents the resulting best-fitting model SED_{mod}. The optical data points were excluded from the fitting routine as the IPHAS absolute calibration is not completely accurate yet (J. Drew, private communication), as can be seen in some cases where r′ and specially i′ deviate from the fitted SED. It should be noted that the derived temperatures correspond to upper limits to the possible temperatures of the disks, and only with photometric data at longer wavelengths can the disk temperatures be fully constrained.

Once the best fitting temperatures and normalisation constants have been determined, the bolometric infrared excesses, $L_{IR}/L_{\star}$, can be determined from :

$$\frac{L_{\rm IR}}{L_{\star}} = \frac{A_{disk}}{A_{\star}} \cdot \frac{T_{disk}^4}{T_{\star}^4}, \tag{2.5}$$

where A_{disk} and $A_{\star}$ represent the K-band normalisation factors and $T_{\star}$=9400 [K]. These correspond to distance-independent, best-fit values of $L_{IR}/L_{\star}$, with uncertainties dependent only on the derivation of T_{disk} and A_{disk}. The resulting $L_{IR}/L_{\star}$ values for our sample of 28 A-type stars are presented in the last column of Table 2.8.

2.5.8 Discussion

We find that none of the 28 objects show near-IR excesses, which rules out the presence of very hot dust associated with small particles in the inner parts of the disks. This supports the hypothesis that the objects in this sample are relatively evolved systems, older than T Tauris, Herbig Ae and transition objects (as expected from the lack of Hα emission given their (r′- Hα) colours). Accordingly, very few objects show excesses at wavelengths shorter than 5.8 μm, imposing strong constraints on the presence of hot dust. Only 3 objects have T_{disk} >500 within the errors. We find that the dust excesses can be well fitted by black

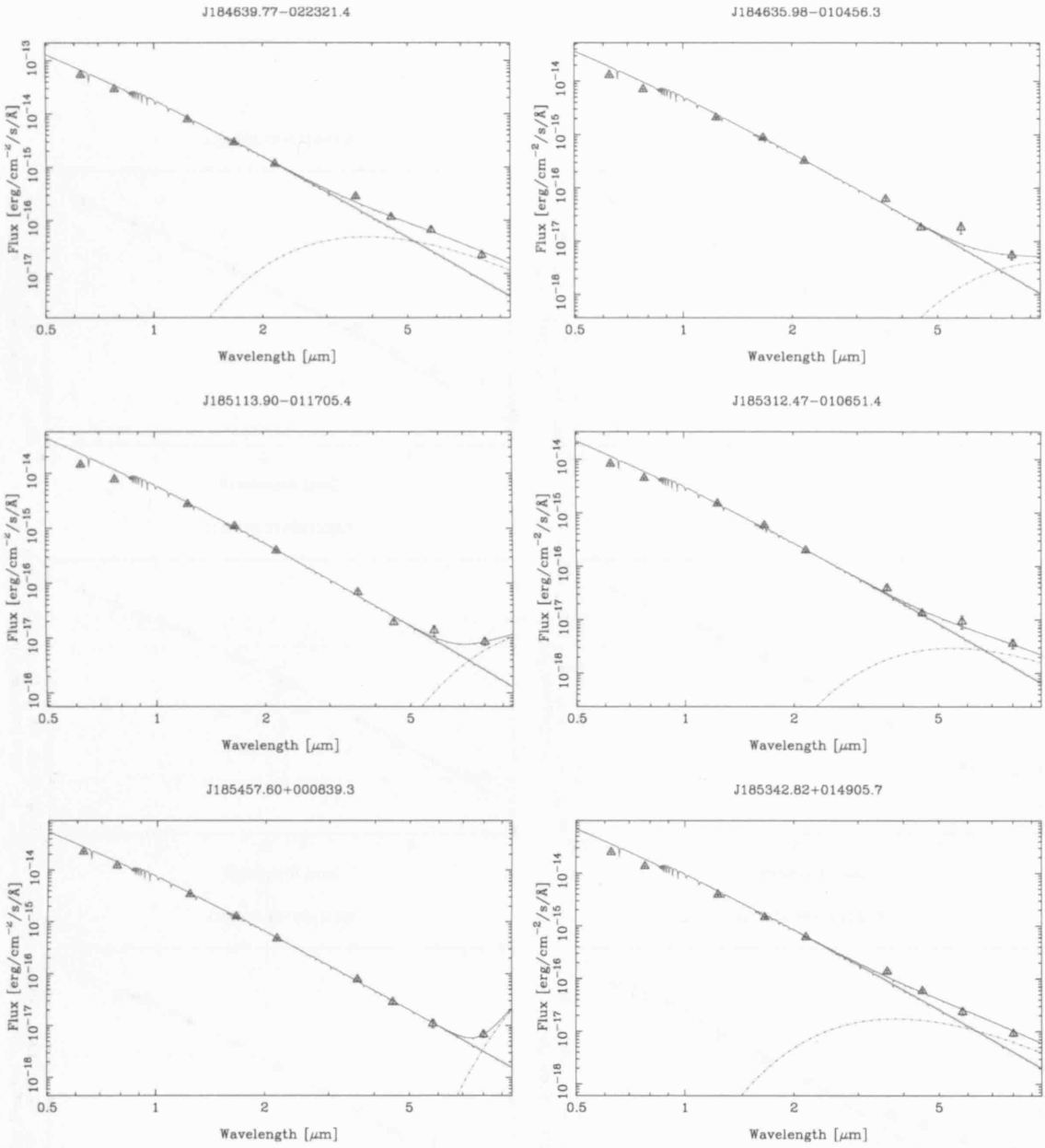

Figure 2.9: De-reddened optical IPHAS, 2MASS and GLIMPSE photometry for the IPHAS-selected A-type stars with 8μm excesses (blue triangles with error bars denoting the 1σ photometric error of each measurement). For each star, the red solid line corresponds to the reference photospheric SED normalised to the K-band flux. The pink dashed line represents the black-body that, added to the stellar SED, minimizes the χ^2 fit to the data (solid green line). Only the 2MASS and GLIMPSE data points were included in the best-fitting routine, as the IPHAS absolute calibration is not completely accurate yet.

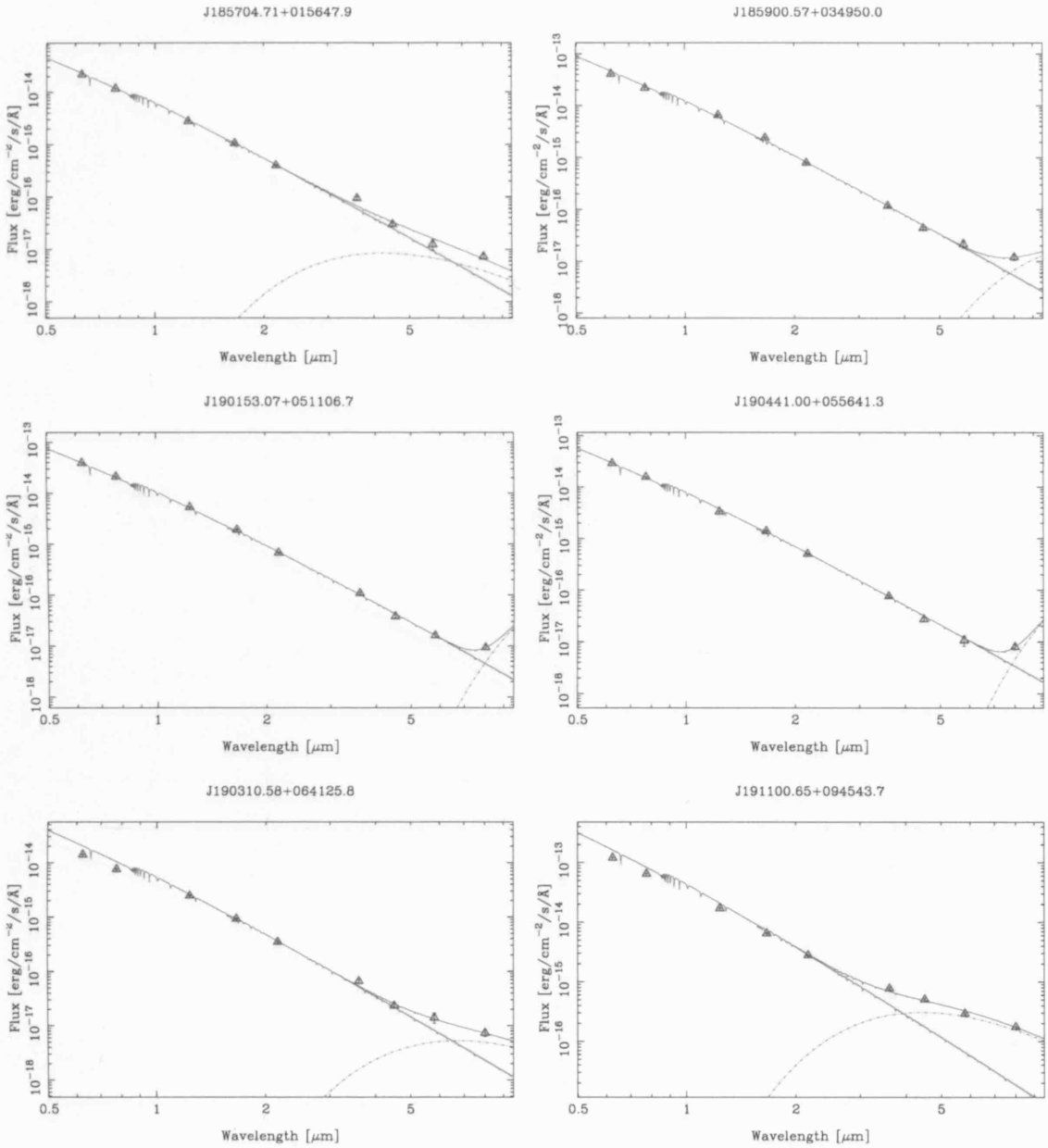

Figure 2.9: *continued*

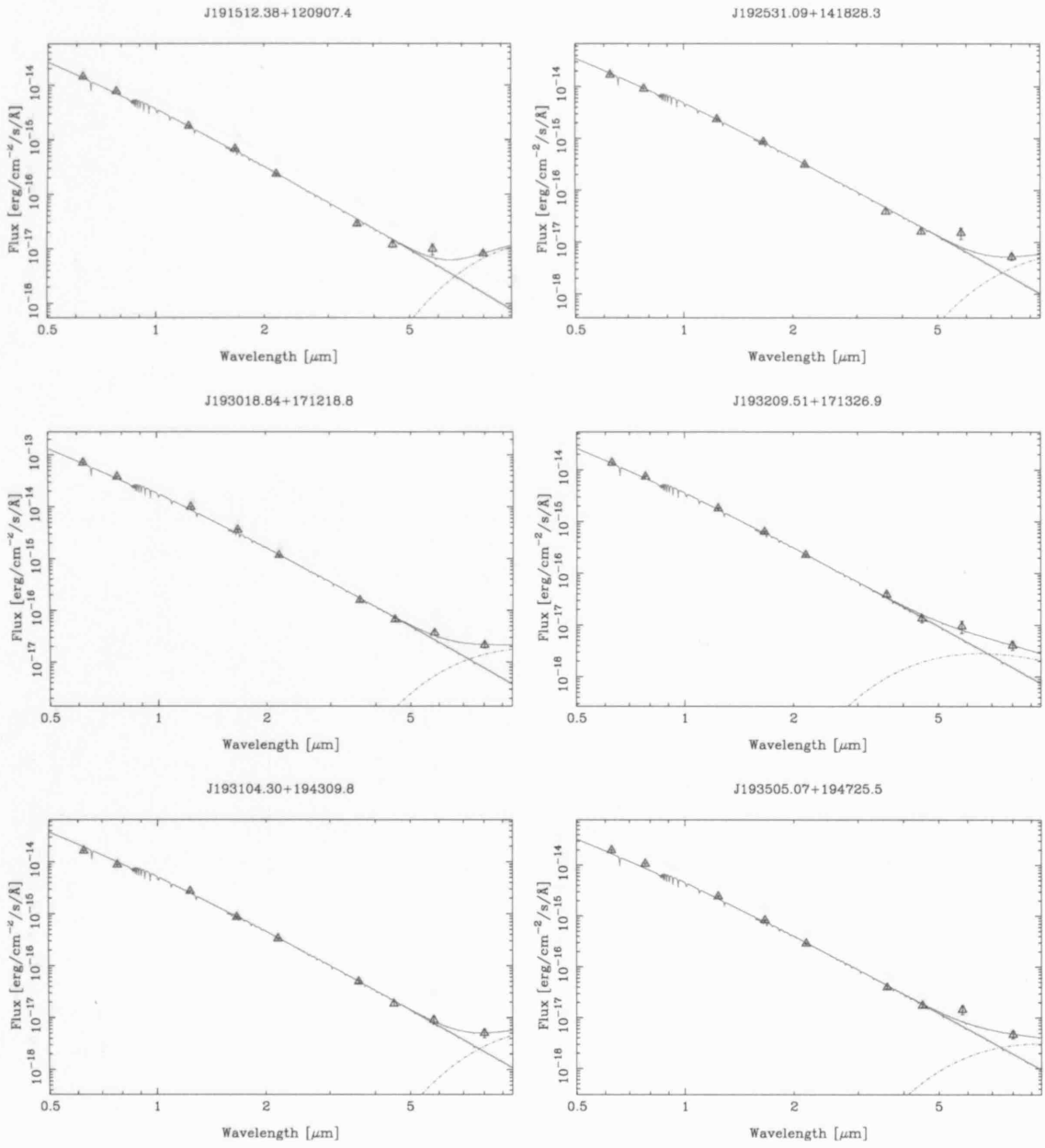

Figure 2.9: *continued*

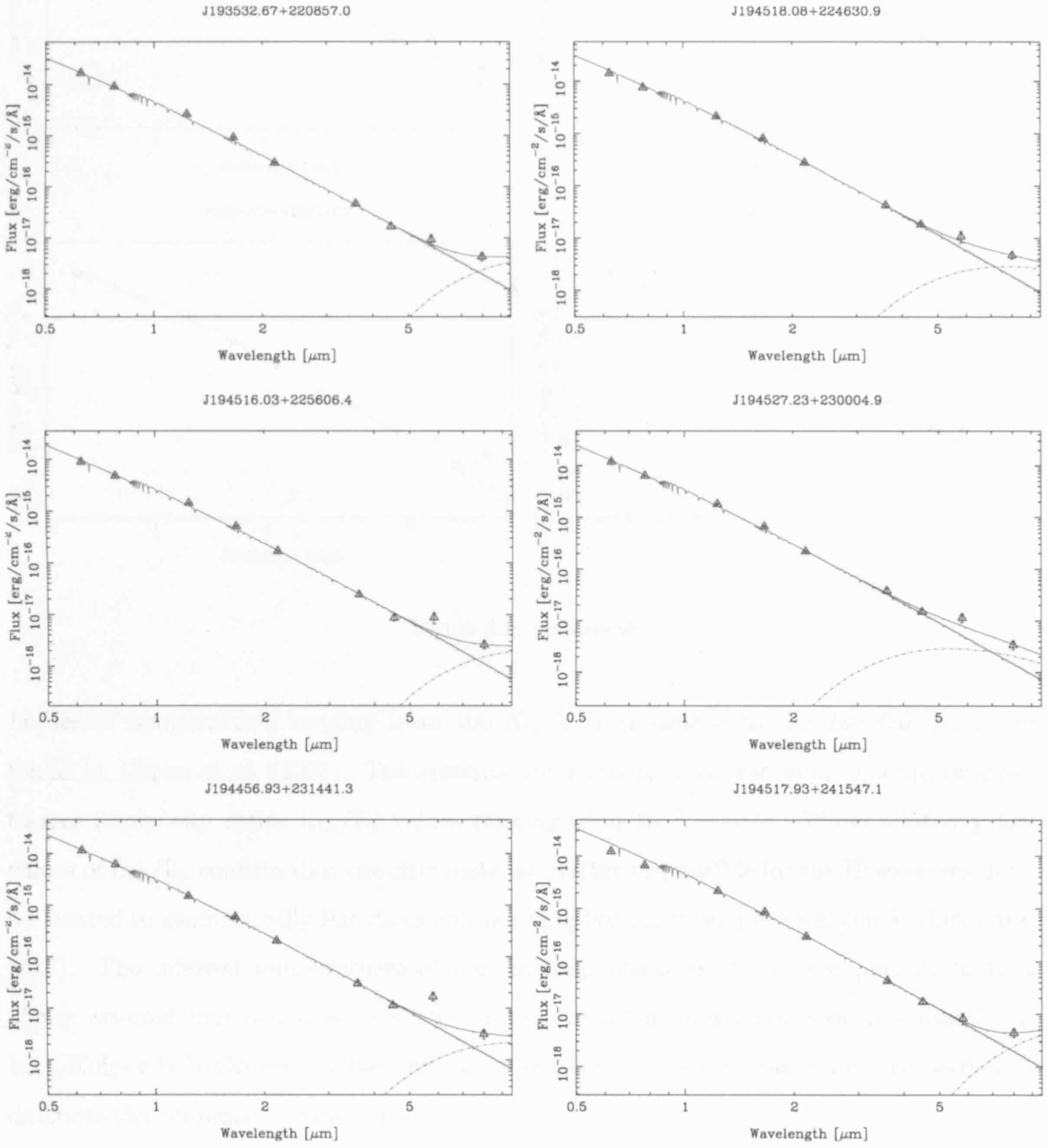

Figure 2.9: *continued*

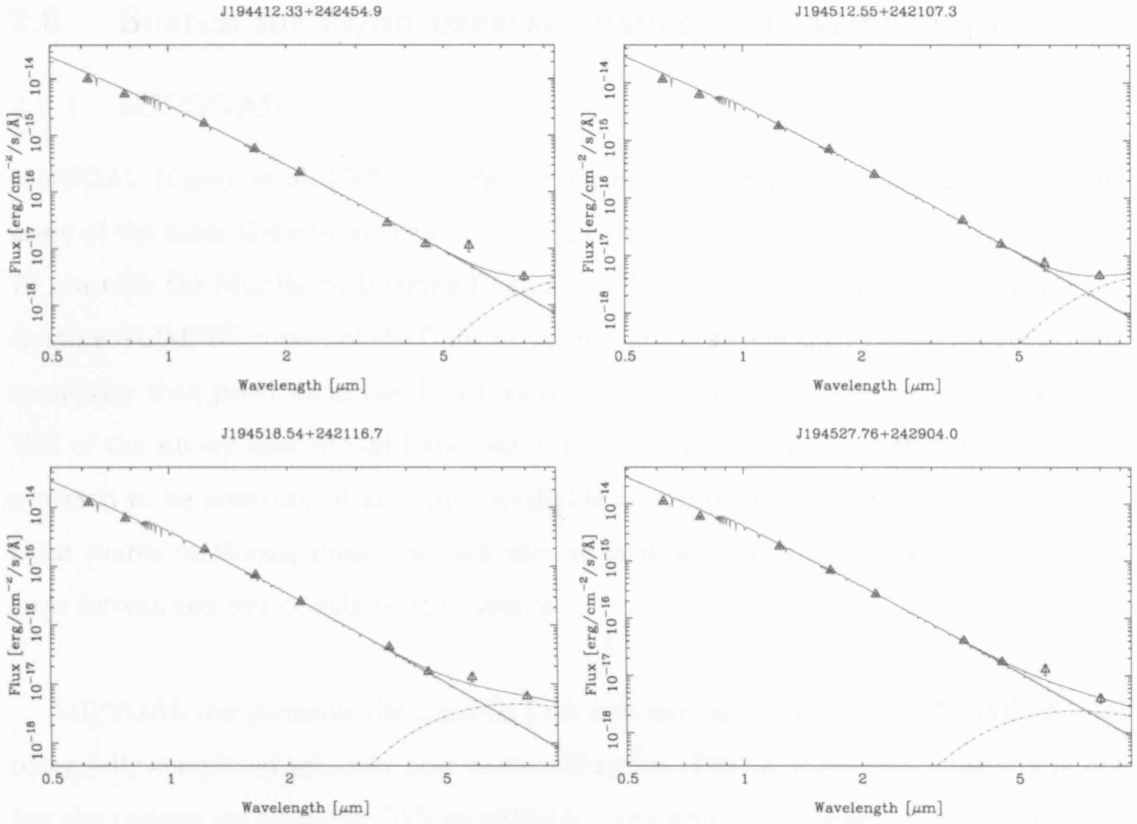

Figure 2.9: *continued*

bodies of temperatures ranging from 100-700 K (comparable to the 220-820 [K] range found by Uzpen et al. (2005). The systems are found to have fractional bolometric disk-to-star luminosity ratios $L_{IR}/L_{\star}$ values ranging from $10^{-3} - 10^{-1}$. These relatively low values of $L_{IR}/L_{\star}$ confirm that the circumstellar matter responsible for the IR excesses must be located in geometrically flat disks and not in spherical envelopes (Kenyon & Hartmann 1987). The inferred temperatures of the emitting black-bodies are comparable to that of the asteroid belt in our solar system rather than the cooler temperatures associated with Kuiper Belt Objects. Observations at wavelengths larger than 8 μm are needed to diagnose the presence of cooler dust.

2.6 Search for 24μm excesses using MIPSGAL data

2.6.1 MIPSGAL

MIPSGAL (Carey et al. 2005) is a *Spitzer* legacy survey that will cover 220 square degrees of the inner Galactic plane ($65 < l < 10$ and $-10 < l <$ -65 for $|b| < 1$) at 24 and 70 μm with the Multiband Imaging Photometer for *Spitzer* (MIPS). It complements the existing GLIMPSE survey of the Galactic plane and has significantly better resolution and sensitivity than previous infrared surveys covering the plane at these wavelengths. Over 75% of the survey area should have useful data at 70μm, while over 99% of the plane is expected to be unsaturated at 24μm. Available data products will include a high quality point source catalogue, image mosaics and, to facilitate the study of extended emission, large format and source-subtracted mosaics.

MIPSGAL complements the Galactic Disk area covered by IPHAS and GLIMPSE. Not being fully completed yet, only post basic-calibration (PBCD) mosaicked images of only a few sky regions are available. Where available, data from the on-going *Spitzer* MIPSGAL survey were downloaded in order to search for possible 24μm excesses present in the sample of 3062 A-type dwarfs selected from the IPHAS and GLIMPSE surveys. The availability of 24μm data-points provides better constraints when modelling the temperatures of the emitting dust.

2.6.2 MIPS

The Multiband Imaging Photometer for *Spitzer* (MIPS, Rieke et al. 2004) enables imaging and photometry at 24, 70 and 160μm. The telescope point spread function (PSF) size ($\approx 1.22\,\lambda/D$) is 5.7 arcsecond at 24μm. The 128×128 pixel Si:As 24μm array provides sampling above the Nyquist limit of $\approx \lambda/2D$ by having pixel sizes of 2.55 arcsecond. The telescope's pointing accuracy at 24μm is $\sim$ 1.2 arcsecond.

The accuracy of photometry is often confusion-limited. Because MIPS provides much smaller effective beams and higher sensitivity at these wavelengths than any previous mission, predicting the confusion limit set by such sources is difficult. Early mission data from MIPS produced the following 5-sigma limits for confusion due to extragalactic

sources: 56 microJy at 24 μm, 3.2 mJy at 70 μm, and 40 mJy at 160 μm (Dole et al. 2003). At 24 and 70 μm, the confusion mainly results from the high density of resolved sources. There is a range of values expected, and moreover it can be a function of where exactly one looks in the sky. Confusion due to Galactic sources is a strong function of position.

2.6.3 MIPSGAL images

MIPSGAL basic-calibrated mosaicked images can be downloaded from the SSC. Since just the 24μm PBCD images can be used for science analysis[6], only the 24μm images were downloaded. Images come in units of MJy/sr and can be used for flux estimation purposes. The best zeropoint to convert 24μm fluxes to magnitudes is 7.3 Jy, as computed from an extrapolation of the Vega spectrum (provided by the SSC).

Based on preliminary analysis of mosaic images, for low background regions sources with fluxes down to 1 mJy can be extracted. This corresponds to a magnitude at 24μm of approximately 9.6 magnitudes, for purely photospheric fluxes of an A0V star (Sean Carey, private communication).

In many cases the images for a given pointing were not yet available. In total 82 images were downloaded, each covering a sky-area of approximately 6.5×0.3 degrees^2. We found that 1860 of the 3062 stars from the A-type sample had their sky positions scanned by the available MIPSGAL dataset.

2.6.4 Image inspection for GLIPHAS correlation

Using a PDL routine, MIPS images are inspected at the position of each of the 1860 A-type stars from our sample. The PDL routine displays the region where the sample star should be located, marking the position of the star with a circle. This routine allows one to change the flux contrast scale, to zoom in and out, and to select for possible point-like correlated sources. The default contrast is set to a linear scale between the minimum and maximum within a 3×3 pixel box located at the A-type star position. Therefore, in most of the cases when the candidate star is not detected, the displayed scale represents the

[6] as stated in the MIPS data-handbook at `http://ssc.spitzer.caltech.edu/mips/dh/`

variation in the background.

A first run over all the 1860 stars was done. At this stage anything that looked different from just noise or background emission was selected. 55 objects were selected at this stage. However at a second stage of more careful analysis, only 33 stars were found to being distinguishable from extended emission or random noise. A final filter, applied when computing the object fluxes, required that the selected 24μm candidate objects must be fittable with MIPS Point Response Function (PRF). This helped ensure that the detected sources are indeed point-like sources associated with the A-type stars from our sample.

2.6.5 Flux extraction

The 24μm fluxes of the 33 stars with tentative detections were extracted individually by fitting a measured MIPS PRF to the candidate star. As a first step an average PRF was constructed for each image by selecting a few stars of similar brightness to the candidate star. The Image Reduction and Analysis Facility (IRAF[7]) package DAOPHOT, and particularly the task DAOPSF was used for this purpose. Once created, this PRF was used to fit the image of the candidate star and to extract its flux. The sky background was computed using an annular region of 10 pixels in width and located 12 pixels in radius away from star. This background estimation is subtracted when calculating the star's flux. Residual images were produced and subsequently inspected to look for possible extraction artifacts or over/under-subtraction.

For 28 of the 33 candidate stars, the PRF fitting procedure was capable of providing flux estimates. In 4 cases, the candidate stars were too faint to allow for a detection of 3σ above the mean local background. The remaining star could not be fitted because it was not PRF-like. Inspection of the GLIMPSE images confirmed that it corresponded to the blending of 3 sources.

2.6.6 Results

We found that 28 of 1860 A-type stars observed by MIPSGAL have positive detections at 24μm. In Table 2.9 the photometric parameters of the stars having 24μm detections are

[7] `http://iraf.noao.edu/`

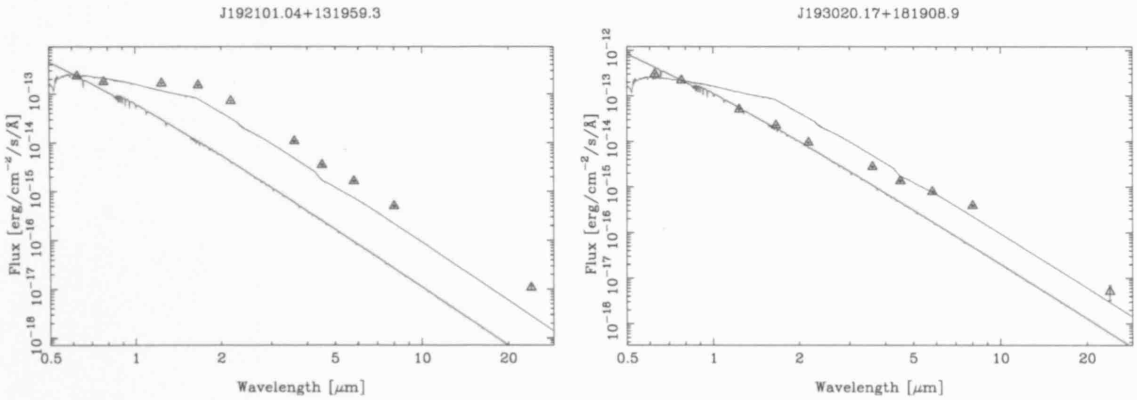

Figure 2.10: SEDs of the 2 objects showing dubious A-type identifications. The observed SEDs (blue triangles with error bars) are flatter than the SEDs of an A-type star (red line), which leads to false mid-IR excess fluxes. The spectral slope of these objects is better described with the SEDs of a K0 dwarf (green line, left-hand panel) and of a G5 dwarf (green line, right-hand panel).

presented.

In order to estimate whether these detections correspond to excesses with respect to the stellar photospheres, we follow a similar procedure to that used for estimating the strength of our 8μm excess stars (see Section 2.5.7), i.e. by normalising an A-type photospheric SED to the dereddened 2.2μm flux and subtracting it from the observed SED. The 24μm fluxes were not de-reddened, as extinction is expected to be negligible at this wavelength. Preliminary inspection of the dereddened SEDs of the 28 stars showed that 2 of the stars had SEDs deviating significantly from that of an A-type star (resembling more those of cooler spectral types stars, as can be seen in Figure 2.10). These 2 stars were excluded from further analysis.

Table 2.10 shows the derived infrared excesses, along with other quantities such as r$'$ extinction, $A_{r'}$, and spectrophotometric distances. The signal-to-noise ratio of the excesses are estimated using the photometric flux uncertainties for each band. We find that 23 of the 26 stars have 24μm excesses with a S/N>2. 10 of these stars were also selected as having 8μm excesses in the search described in Section 2.5.6. These all correspond to stars with 8μm excesses having a S/N larger than 5.5. We note that 5 of the stars also show excesses at shorter wavelengths. Three other stars have 24μm fluxes consistent within 2σ to what is expected from their stellar photospheric emission.

Table 2.9: Photometric parameters for IPHAS A-type stars with 24μm excesses

Reference ID	IPHAS ID	GLIMPSE ID	r′ (mag)	r′-i′ (mag)	r′-J (mag)	J-H (mag)	J-K (mag)	J-[3.6] (mag)	[3.6] (mag)	[3.6]-[4.5] (mag)	[3.6]-[5.8] (mag)	[3.6]-[8.0] (mag)	[24] (mag)
1	J184852.87-024005.1	G030.2659-00.6478	14.80(0.01)	1.24(0.01)	3.08(0.02)	0.52(0.03)	0.81(0.04)	1.06(0.06)	10.66	0.05(0.09)	0.25(0.13)	0.19(0.09)	8.33(0.42)
2	J184847.84-023133.7	G030.3828-00.5644	14.48(0.02)	1.09(0.03)	2.79(0.03)	0.44(0.03)	0.70(0.03)	0.97(0.08)	10.72	-0.03(0.10)	0.15(0.13)	0.76(0.11)	7.75(0.34)
3	J185640.65+011842.4	G034.6967-00.5673	14.71(0.02)	0.76(0.03)	1.86(0.03)	0.33(0.03)	0.47(0.04)	0.83(0.07)	12.02	0.07(0.11)	0.40(0.19)	0.89(0.23)	8.21(0.36)
4	J185129.16+015841.2	G034.6980+00.8911	14.94(0.01)	1.22(0.01)	2.91(0.02)	0.45(0.04)	0.66(0.04)	0.83(0.06)	11.20	0.04(0.09)	-0.03(0.13)	0.44(0.10)	9.22(0.42)
5	J185438.33+023708.8	G035.6276+00.4824	17.90(0.02)	1.72(0.03)	4.73(0.03)	0.79(0.04)	1.17(0.03)	1.63(0.06)	11.54	0.00(0.10)	0.06(0.13)	0.30(0.12)	6.54(0.12)
6	J185737.14+031708.5	G036.5604+00.1246	15.19(0.01)	2.38(0.01)	6.01(0.02)	1.13(0.05)	1.70(0.03)	2.11(0.04)	7.07	0.06(0.06)	0.10(0.04)	0.20(0.04)	6.69(0.12)
7	J185958.14+035410.7	G037.3773-00.1149	17.65(0.01)	1.99(0.01)	5.11(0.02)	0.85(0.03)	1.31(0.03)	1.86(0.08)	10.68	0.00(0.09)	0.07(0.13)	0.37(0.11)	4.79(0.11)
8	J190033.62+043113.0	G037.9937+00.0362	17.65(0.03)	1.97(0.04)	4.95(0.04)	0.77(0.04)	1.21(0.03)	1.65(0.07)	11.05	0.03(0.11)	-0.01(0.13)	0.09(0.20)	6.39(0.19)
9	J190309.80+063448.0	G040.1214+00.4032	17.25(0.01)	1.30(0.01)	3.65(0.03)	0.61(0.04)	0.92(0.04)	1.17(0.09)	12.43	0.03(0.11)	0.20(0.24)	0.19(0.24)	8.54(0.39)
10	J190253.58+063954.6	G040.1664+00.5019	17.61(0.01)	1.49(0.01)	4.03(0.04)	0.70(0.07)	1.08(0.06)	1.37(0.06)	12.21	0.17(0.10)	0.41(0.10)	1.52(0.13)	6.04(0.12)
11	J190355.55+064411.9	G040.3475+00.3067	14.24(0.04)	0.90(0.06)	2.50(0.04)	0.34(0.04)	0.57(0.04)	0.81(0.07)	10.93	0.05(0.09)	0.02(0.13)	0.54(0.10)	6.84(0.16)
12	J192103.73+122536.9	G047.3469-00.7968	17.61(0.00)	1.66(0.01)	4.15(0.03)	0.68(0.05)	1.02(0.04)	1.43(0.08)	12.03	0.04(0.09)	0.02(0.17)	0.20(0.11)	6.38(0.10)
13	J191958.33+123419.1	G047.3501-00.4939	17.16(0.03)	1.77(0.04)	4.48(0.05)	0.72(0.06)	1.06(0.05)	1.36(0.08)	11.32	0.09(0.10)	0.28(0.14)	0.36(0.11)	5.02(0.11)
14	J191955.70+123815.5	G047.4030-00.4537	17.95(0.01)	1.93(0.01)	4.86(0.03)	0.76(0.05)	1.15(0.04)	1.44(0.07)	11.65	0.10(0.08)	0.07(0.13)	0.53(0.09)	6.69(0.14)
15	J192115.63+125034.3	G047.7368-00.6441	14.92(0.09)	0.89(0.13)	2.30(0.09)	0.41(0.04)	0.60(0.04)	0.73(0.07)	11.89	0.05(0.10)	0.26(0.17)	0.18(0.12)	9.22(0.42)
16	J191957.49+134520.3	G048.3938+00.0644	17.36(0.05)	1.93(0.07)	4.81(0.05)	0.76(0.04)	1.12(0.03)	1.40(0.06)	11.15	0.13(0.08)	0.11(0.13)	0.65(0.09)	7.24(0.11)
17	J192504.23+145820.6	G050.0506-00.4535	16.97(0.04)	1.36(0.05)	3.31(0.05)	0.49(0.05)	0.85(0.05)	1.11(0.09)	12.55	0.02(0.12)	-0.08(0.34)	0.69(0.26)	8.03(0.22)
18	J192645.73+145637.4	G050.2195-00.8267	17.22(0.00)	1.43(0.01)	3.46(0.05)	0.56(0.06)	0.89(0.06)	1.05(0.09)	12.71	0.02(0.12)	0.41(0.22)	1.60(0.15)	9.15(0.44)
19	J193158.24+172335.3	G052.9689-00.7516	17.15(0.02)	1.31(0.02)	3.33(0.03)	0.62(0.04)	0.90(0.04)	1.42(0.11)	12.40	-0.32(0.14)	0.42(0.23)	0.81(0.16)	7.63(0.27)
20	J192933.03+183415.5	G053.7252+00.3191	14.15(0.01)	0.68(0.01)	1.81(0.02)	0.42(0.03)	0.77(0.03)	1.31(0.05)	11.03	0.21(0.07)	0.38(0.09)	1.34(0.06)	4.98(0.07)
21	J192914.01+184005.1	G053.7744+00.4315	14.53(0.02)	0.85(0.03)	2.12(0.03)	0.36(0.03)	0.52(0.03)	0.79(0.05)	11.62	0.22(0.09)	0.51(0.15)	2.01(0.08)	4.52(0.11)
22	J193657.34+195145.9	G055.7013-00.5859	17.27(0.03)	2.44(0.04)	6.48(0.04)	1.47(0.03)	2.12(0.03)	2.47(0.05)	8.32	-0.15(0.07)	0.06(0.06)	0.19(0.06)	7.50(0.25)
23	J193643.03+200108.6	G055.8105-00.4606	17.89(0.03)	1.51(0.04)	3.74(0.04)	0.67(0.04)	0.92(0.05)	1.35(0.10)	12.80	-0.02(0.16)	0.29(0.20)	0.17(0.34)	5.63(0.14)
24	J193756.38+205905.6	G056.7929-00.2379	14.46(0.02)	0.71(0.03)	1.76(0.03)	0.27(0.03)	0.42(0.03)	0.55(0.07)	12.15	0.10(0.11)	0.10(0.15)	0.77(0.11)	7.81(0.35)
25	J193710.80+211310.4	G056.9108+00.0314	15.47(0.02)	1.23(0.03)	3.07(0.03)	0.55(0.04)	0.79(0.06)	0.99(0.07)	11.41	0.01(0.11)	-0.10(0.13)	0.06(0.16)	7.63(0.16)
26	J194541.20+243253.9	G060.7727-00.0227	15.20(0.10)	0.54(0.14)	1.53(0.10)	0.23(0.05)	0.38(0.05)	0.78(0.09)	12.89	0.35(0.13)	1.01(0.18)	1.48(0.11)	8.47(0.20)

Observed colours at the different IPHAS, 2MASS and IRAC bands together with our measured 24μm fluxes.

Table 2.10: Derived parameters for IPHAS A-type stars with 24μm excesses

Reference ID	IPHAS ID	GLIMPSE ID	A_r (mag)	d (kpc)	3.6μm (mJy)	4.5μm (mJy)	5.8μm (mJy)	8μm (mJy)	24μm (mJy)	T< (K)	L_{IR}/L_*
1	J184852.87-024005.1	G030.2659-00.6478	4.85(0.01)	0.51(0.01)	-	-	-	-	-	210	2.2e-04(3.1e-04)
2	J184847.84-023133.7	G030.3828-00.5644	4.25(0.01)	0.58(0.03)	-	-	-	4.0(8.0)	5.3(2.5)	314	1.2e-03(5.3e-04)
3	J185640.65+011842.4	G034.6967-00.5673	2.97(0.01)	1.17(0.05)	0.7(2.5)	0.5(2.0)	1.2(2.8)	1.6(3.6)	47.4(22.2)	183	1.7e-02(3.9e-03)
4	J185129.16+015841.2	G034.6980+00.8911	4.74(0.01)	0.58(0.02)	-	-	-	0.8(3.7)	3.4(2.3)	243	5.6e-04(3.7e-04)
5	J185438.33+023708.8	G035.6276+00.4824	6.73(0.05)	0.90(0.05)	-	-	-	0.5(2.8)	-	283	3.1e-04(3.0e-04)
6	J185737.14+031708.5	G036.5604+00.1246	9.29(0.01)	0.08(0.00)	-	-	-	-	-	10	7.5e-12(1.1e-09)
7	J185958.14+035410.7	G037.3773-00.1149	7.77(0.04)	0.50(0.01)	-	-	-	1.7(5.0)	87.7(9.5)	166	5.2e-03(1.2e-03)
8	J190033.62+043113.0	G037.9937+00.0362	7.68(0.04)	0.52(0.03)	-	-	-	-	19.7(5.1)	84	3.5e-03(4.1e-03)
9	J190309.80+063448.0	G040.1214+00.4032	5.09(0.04)	1.42(0.04)	-	-	-	-	2.7(2.2)	146	8.7e-04(5.8e-03)
10	J190253.58+063954.6	G040.1664+00.5019	5.81(0.05)	1.21(0.02)	-	-	0.6(3.1)	3.4(9.2)	27.9(8.8)	226	8.9e-03(1.9e-03)
11	J190355.55+064411.9	G040.3475+00.3067	3.51(0.01)	0.73(0.07)	-	-	-	2.1(7.1)	13.0(6.9)	236	1.8e-03(5.2e-04)
12	J192103.73+122536.9	G047.3469-00.7968	6.47(0.05)	0.89(0.00)	-	-	-	-	15.2(7.1)	147	3.3e-03(2.1e-03)
13	J191958.33+123419.1	G047.3501-00.4939	6.91(0.04)	0.59(0.04)	-	-	-	-	4.4(2.6)	203	4.9e-04(4.3e-04)
14	J191955.70+123815.5	G047.4030-00.4537	7.54(0.05)	0.63(0.02)	-	-	-	0.6(3.9)	6.8(3.4)	205	9.6e-04(4.6e-04)
15	J192115.63+125034.3	G047.7368-00.6441	3.48(0.02)	1.02(0.21)	-	-	-	-	9.1(9.5)	143	2.1e-03(3.4e-03)
16	J191957.49+134520.3	G048.3938+00.0644	7.53(0.04)	0.49(0.05)	-	-	-	1.5(5.5)	71.3(9.2)	168	5.3e-03(1.2e-03)
17	J192504.23+145820.6	G050.0506-00.4535	5.30(0.04)	1.13(0.09)	-	-	-	0.6(2.3)	7.4(3.0)	204	3.1e-03(2.0e-03)
18	J192645.73+145637.4	G050.2195-00.8267	5.57(0.04)	1.12(0.00)	-	-	-	2.2(8.0)	5.5(2.1)	311	2.2e-03(7.7e-04)
19	J193158.24+172335.3	G052.9689-00.7516	5.12(0.05)	1.33(0.06)	0.7(2.1)	-	1.0(2.7)	1.1(7.3)	6.5(4.8)	243	3.7e-03(1.4e-03)
20	J192933.03+183415.5	G053.7252+00.3191	2.68(0.01)	1.03(0.01)	3.8(7.0)	3.6(10.1)	3.6(7.5)	7.8(24.2)	74.4(15.2)	450	4.1e-03(2.4e-04)
21	J192914.01+184005.1	G053.7744+00.4315	3.30(0.01)	0.92(0.04)	-	0.9(2.7)	2.0(3.6)	9.4(18.8)	113.4(9.7)	211	2.7e-02(5.1e-03)
22	J193657.34+195145.9	G055.7013-00.5859	9.52(0.04)	0.19(0.01)	-	-	-	-	31.8(5.6)	90	2.7e-04(1.7e-04)
23	J193643.03+200108.6	G055.8105-00.4606	5.90(0.07)	1.31(0.10)	-	-	-	-	5.4(2.6)	164	2.6e-03(4.1e-03)
24	J193756.38+205905.6	G056.7929-00.2379	2.79(0.01)	1.13(0.06)	-	-	-	1.0(7.1)	42.0(6.5)	171	1.4e-02(3.7e-03)
25	J193710.80+211310.4	G056.9108+00.0314	4.82(0.02)	0.71(0.03)	-	-	-	-	7.0(3.7)	78	2.6e-03(3.3e-02)
26	J194541.20+243253.9	G060.7727-00.0227	2.10(0.02)	2.19(0.50)	0.5(3.0)	0.8(5.3)	1.6(5.3)	1.6(14.6)	3.0(4.7)	450	4.6e-03(4.3e-04)

Derived parameters for stars with 24μm excesses with respect to a normalised A0V star SED. The reference SEDs were normalised to match the observed K-band fluxes. Excess fluxes at each wavelength are presented in units of mJy. Within brackets is denoted the signal-to-noise of the detection. Only detections with S/N ratios larger than 2.0 are shown. For $A_{r'}$, d as well as for T and L_{IR}/L_*, the values within brackets represent the 1 σ uncertainties.

2.6.7 Modelling the black-body temperatures of the mid-IR excesses

The modelling of the observed SEDs for the 24μm excess candidates was performed in a similar fashion to that for the 8μm excess objects (described in Section 2.5.7), but now including the 24μm flux in the fit. Best-fit temperatures and derived bolometric luminosity ratios are presented in Table 2.10, and the results from our black-body fitting routine to the infrared excesses are shown in Figure 2.11. The SEDs of the three stars having 24μm consistent within 2 σ with the expected photospheric fluxes have also been included (object 1, object 5 and object 6 in Table 2.10).

2.6.8 Summary of the 24μm detections

We find that 23 of the 1860 stars show detectable 24μm excess fluxes that can be modelled as arising from warm dust (T$<$ 300 [K], T$\sim$ 200 [K] in average). This corresponds to a fraction 1.2%. This is consistent with recent *Spitzer* results from Smith et al. (2006), who found that only 1 of 112 stars located within 65 pc from the Sun had a 24μm excess. This is also similar to the fraction of stars with 8μm excesses we derived in this work.

2.7 Discussion

The incidence fraction of dust excesses derived in this work are 1.1 % and 1.2 % in the case of 8μm and 24μm excesses respectively. These fractions are notably smaller than the $\sim$ 15% quoted in pre-*Spitzer* surveys for dust-excesses around MS stars(Plets & Vynckier 1999; Lagrange et al. 2000), and particularly different than the 13 % occurrence fraction quoted by Song et al. (2001) for A-type stars with ages ranging from 50 Myr to 1 Gyr.

However Rieke et al. (2005) have shown that the decay-times (and hence the occurrence with age) are distinctly different for different degrees of excess, with large excesses decaying faster than small excesses. For instance, Rieke et al. (2005) found that only 1 % of the A-type stars older than 190 Myr had (K-24) colours larger than twice the photospheric (K-24) colour of an A-type star. In the case of the stars with 8μm excesses, by definition we have only selected stars with (K-8) colours much larger than twice the normal (K-8) colour of an A-type star. Similarly, given the sensitivities of the MIPSGAL survey and the large distances involved, it is very likely that our search is only sensitive to very large (K-24) colours, as can be derived from the values in Table 2.9, where in all except two cases the (3.6-24) colours are always larger than 1 magnitude (rising even to 7 magnitudes).

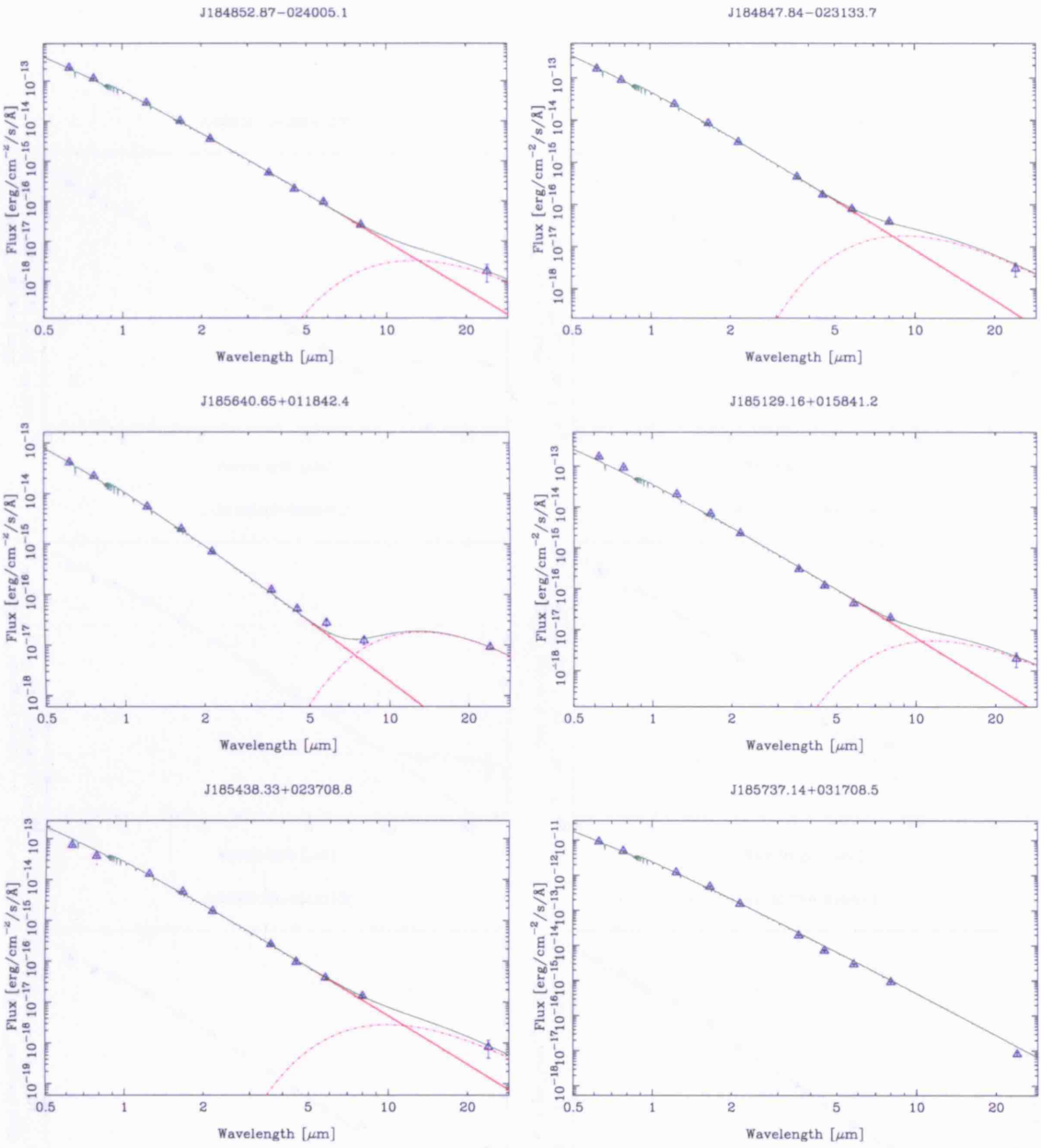

Figure 2.11: De-reddened optical IPHAS, 2MASS, GLIMPSE and MIPSGAL 24μm photometry for the IPHAS-selected A-type stars with 24μm excesses (blue triangles with error bars denoting the 1σ photometric error of each measurement). For each star, the red solid line corresponds to the reference photospheric SED normalised to the K-band flux. The pink dashed line represents the black-body that, added to the stellar SED, minimizes the χ^2 fit to the data (solid green line). Only the 2MASS and GLIMPSE and 24μm data points were included in the best-fitting routine.

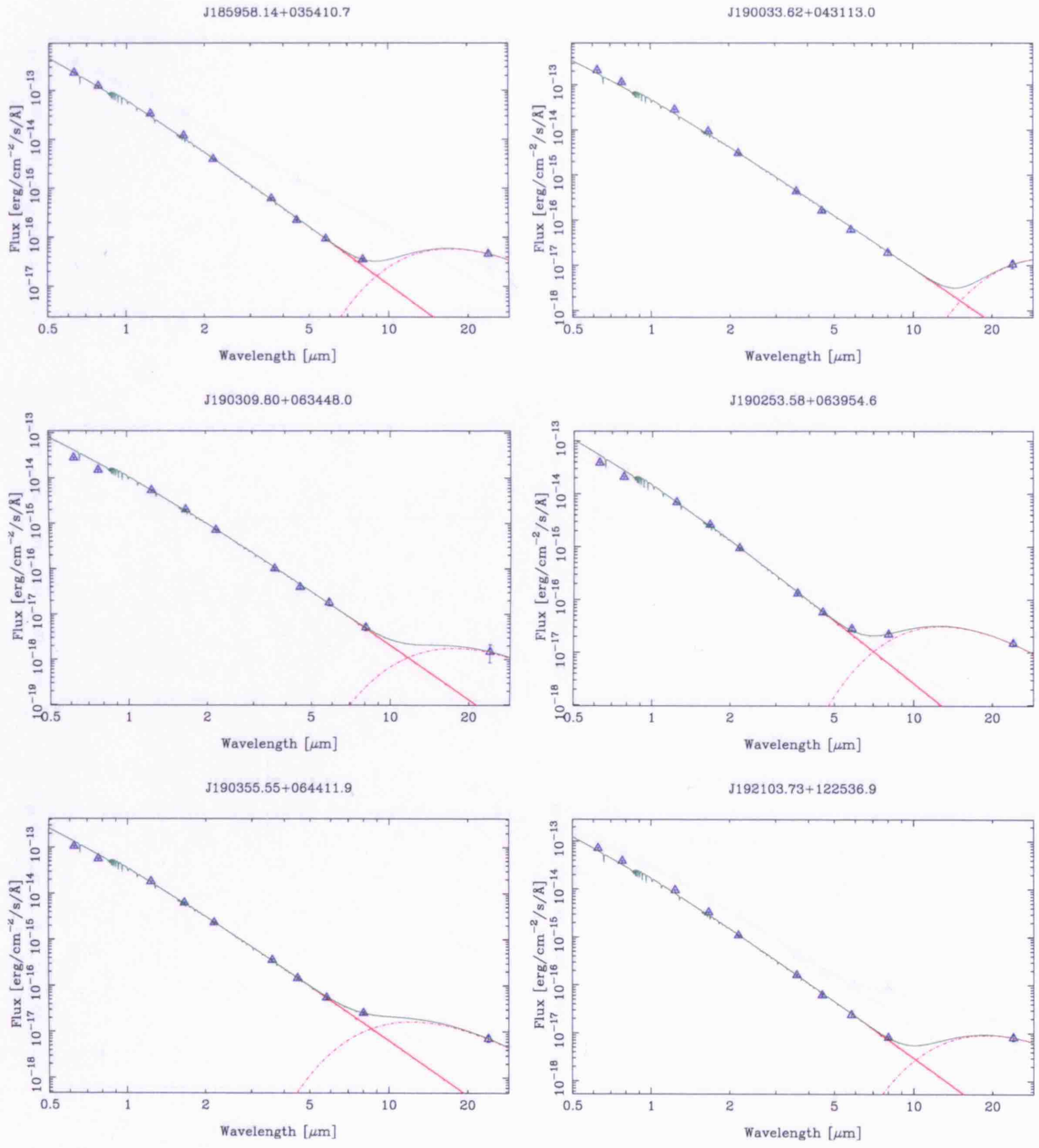

Figure 2.11: *continued*

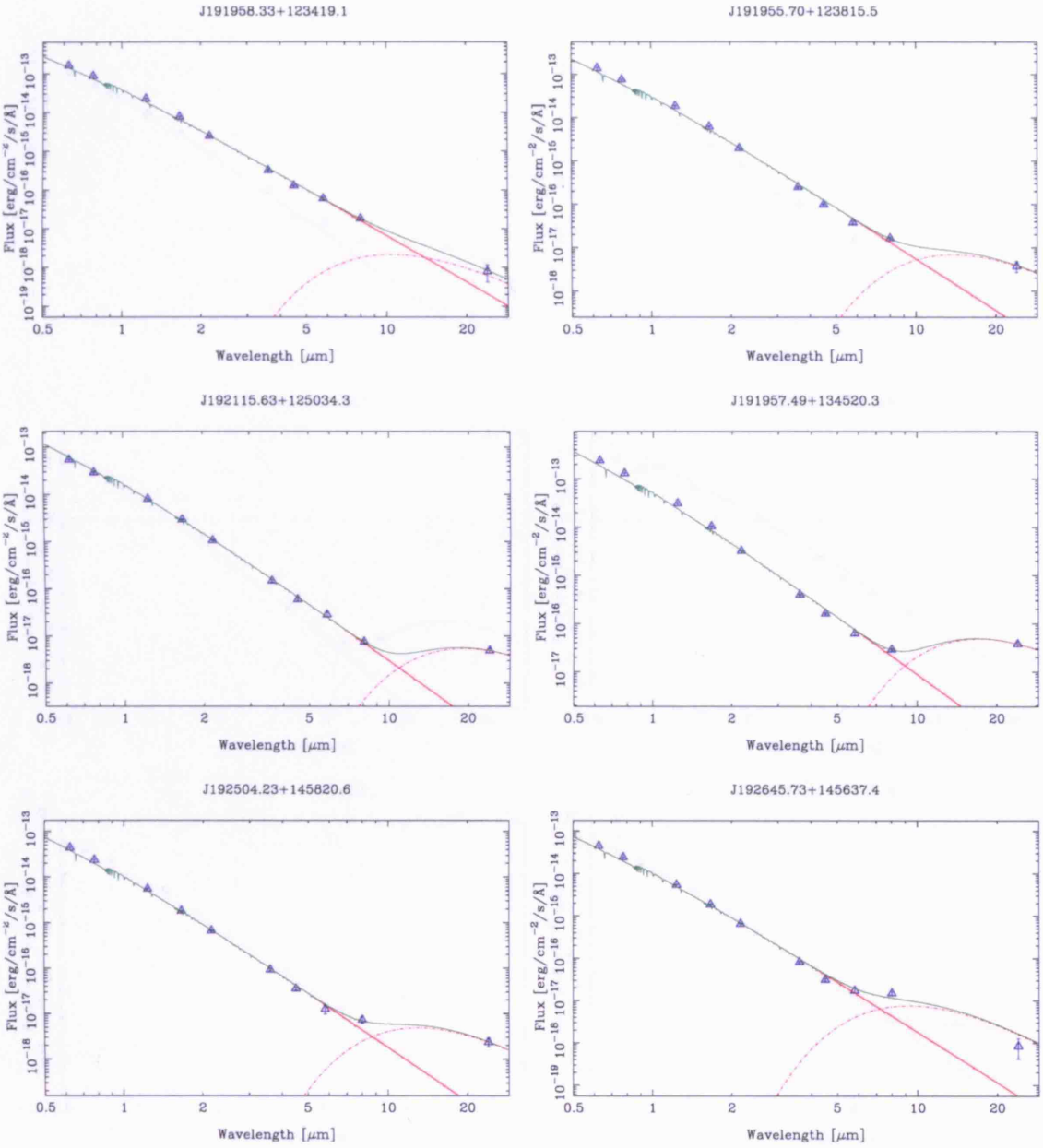

Figure 2.11: *continued*

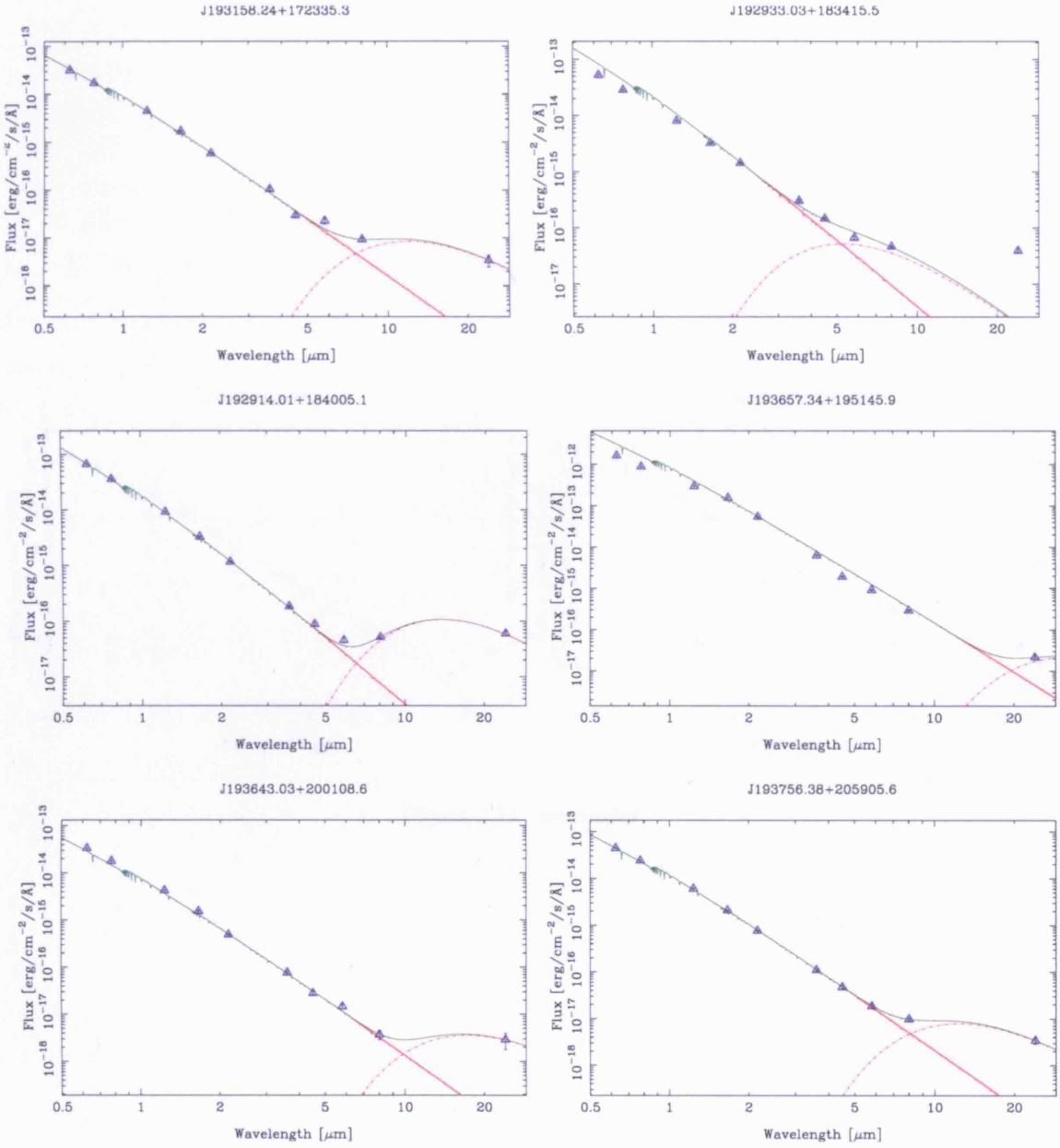

Figure 2.11: *continued*

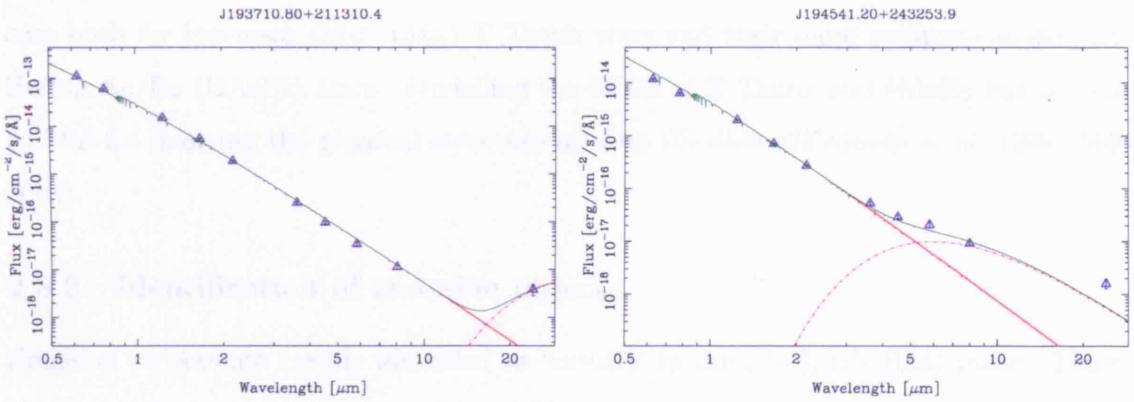

Figure 2.11: *continued*

2.8 Emission-line objects

2.8.1 Introduction

One of the main goals of the IPHAS survey is to find emission-line objects using the Hα filter. Hα emission is usually associated with young-stellar objects, such as T Tauri stars, but also with post-AGB objects, planetary nebulae, interacting binaries and other classes of evolved stars.

In this section we are interested in finding emission line objects with dust emission, such as Object 1 of Drew et al. (2005). Young optically visible emission line objects that also emit considerable amounts of flux at near-, mid- and far-IR wavelengths are often associated with objects in the transition between the pre-MS and MS phase. This is the case both for low-mass (M$<$ $1M_{\odot}$) T Tauris stars and their more massive counterpart Herbig Ae/Be (HAeBe) stars. Modelling the SEDs of T Tauris and HAeBe has proven fruitful for inferring the physical structure of their CS disks (D'Alessio et al. 1998 1999 2001).

2.8.2 Identification of emission objects

Emission objects are readily identified as 'outliers' in the (r'-i'), (r'- Hαs) plane. These objects are located above the unreddened Main Sequence. Figure 2.12 shows the presence of one emission line objects in field 4223.

The identification of these objects is evident once the correct position of the early-A and unreddened MS lines has been determined (i.e the vertical shift in (r'- Hα) described in Section 2.4.2). As the vertical shifts for all IPHAS field in Table 2.2 have already been determined, the selection of outlying objects can be automated. A PDL routine is used for this purpose, which for a given value of (r'-i') will select any objects located more than 0.3 magnitudes above the unreddened MS line.

A search over the 145 catalogues processed in Section 2.4.1 led to the identification of 21 potential emission objects. We are interested here in emission line objects with associated dust emission, for which we correlated the 21 potential Hα emitters with the GLIMPSE PSC. Only 8 objects were found to have fully-sampled optical to 8μm SEDs. The photometric properties of these objects are presented in Table 2.11. None of these

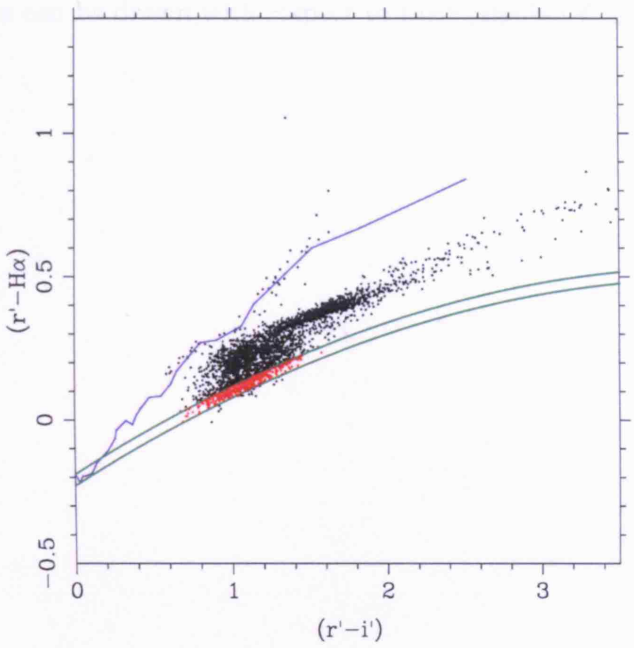

Figure 2.12: Example IPHAS colour-colour diagram showing the presence of a potential Hα emitter, located approximately 0.5 magnitudes above the unreddened Main Sequence line (solid dark line) at (r′-i′)∼ 1.3.

objects had been scanned by the currently available MIPSGAL images.

2.8.3 Nature of the emission objects

Figure 2.13 shows the observed SED of the selected emission objects. We investigate whether some of these may be T Tauri stars by fitting the SEDs with the median T Tauri observed SED published by D'Alessio et al. (1999), solid line. The median SEDs have been normalised to the 2MASS Ks flux and then reddened by eye to fit the optical data-points. The error-bars in the median SEDs denote the quartiles of the distribution.

Two objects (J192954.39+181026.4 and J192249.79+142236.4) have SEDs that may resemble those of T Tauris, but they show clear excesses in the IRAC bands. We have fitted those excesses with black bodies and found the upper limits to their temperatures to be 750±10 K and 610±11 K for J192954.39+181026.4 and J192249.79+142236.4, respectively.

The emission objects singled out in our IPHAS/GLIMPSE correlation could well be T Tauri stars, though current reddening estimates are unreliable. Follow up spectroscopy must be taken in order to accurately determine their true spectral type. Only then conclusive arguments can be drawn with respect to their possible T Tauri nature.

Table 2.11: Photometric parameters for the emission line stars

Reference ID	IPHAS ID	GLIMPSE ID	r′ (mag)	Hα (mag)	i′ (mag)	J (mag)	H (mag)	K (mag)	[3.6] (mag)	[[4.5] (mag)	[5.8] (mag)	[8.0] (mag)
1	J184839.35+002343.1	G032.9665+00.7993	15.500	14.602	14.359	12.480	11.568	11.254	10.736	10.740	10.428	9.880
2	J185607.25+003823.0	G034.0351-00.7502	17.432	16.305	15.612	13.108	11.998	11.437	10.875	10.573	10.669	10.103
3	J190958.34+072144.4	G041.5931-00.7376	17.913	16.796	15.668	12.253	11.224	10.489	9.731	9.369	8.932	8.623
4	J192249.79+142236.4	G049.2695-00.2578	16.997	15.840	15.516	12.614	11.189	9.877	8.007	7.257	6.514	5.532
5	J193002.16+163858.0	G052.0944-00.7037	15.457	14.586	14.230	12.498	11.949	11.546	10.962	10.638	10.397	10.108
6	J192711.26+173050.7	G052.5284+00.3075	15.964	15.091	14.638	12.486	11.813	11.315	10.596	10.339	10.026	9.732
7	J192954.39+181026.4	G053.4173+00.0546	17.648	16.329	16.159	13.535	12.163	11.204	9.620	8.906	8.429	7.757
8	J192909.74+190933.7	G054.1977+00.6814	14.843	14.279	14.095	12.838	12.477	12.205	11.673	11.353	11.213	10.840

Observed magnitudes at the different IPHAS, 2MASS and IRAC bands for the emission line stars.

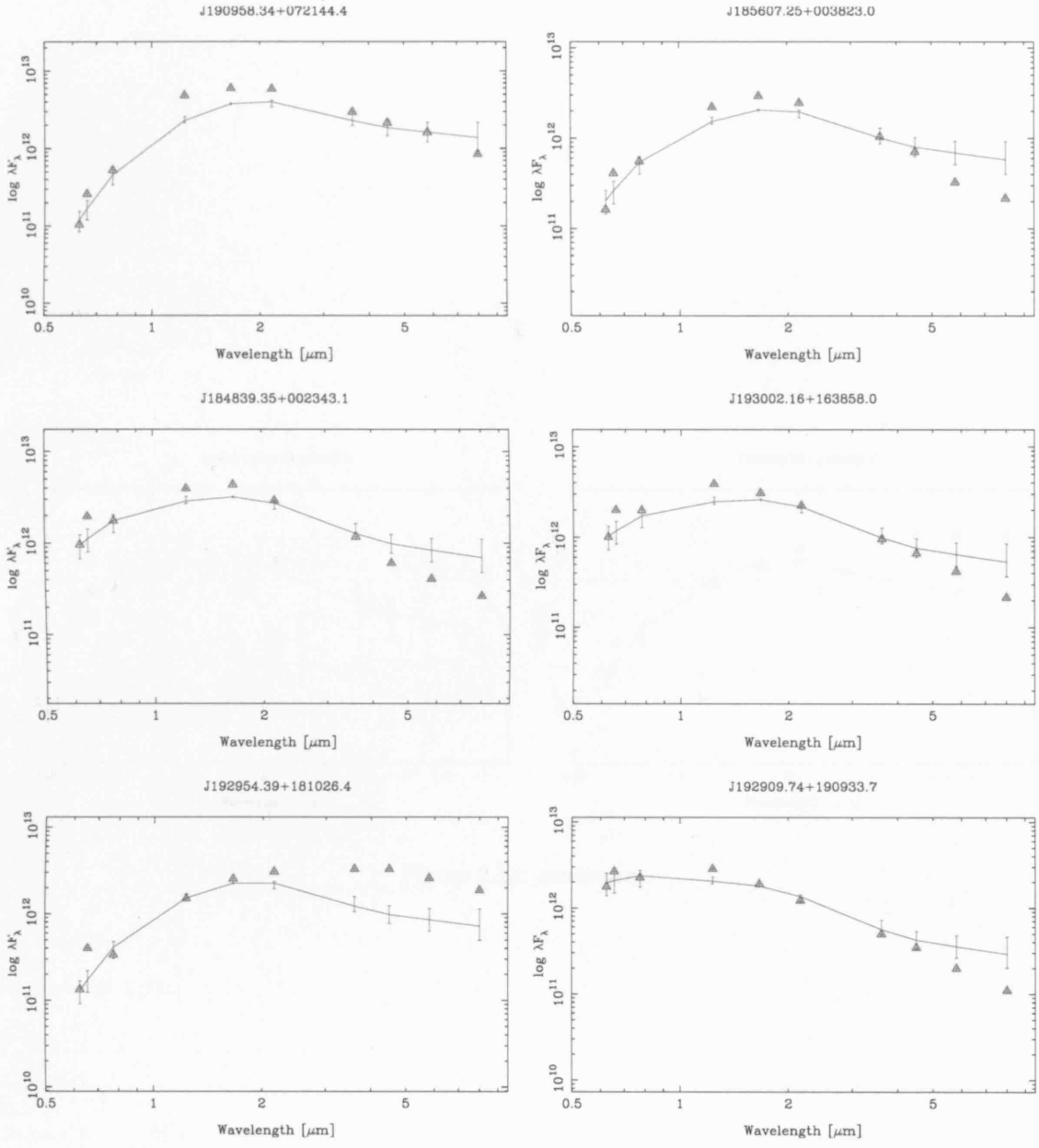

Figure 2.13: Observed SED of the selected emission objects (red triangles with error-bars). The green solid line correspond to the median T Tauri observed SED published by D'Alessio et al. (1999), normalised to the 2MASS Ks flux and then reddened by eye to fit the optical data-points. The error-bars in the median SEDs denotes the quartiles of the distribution.

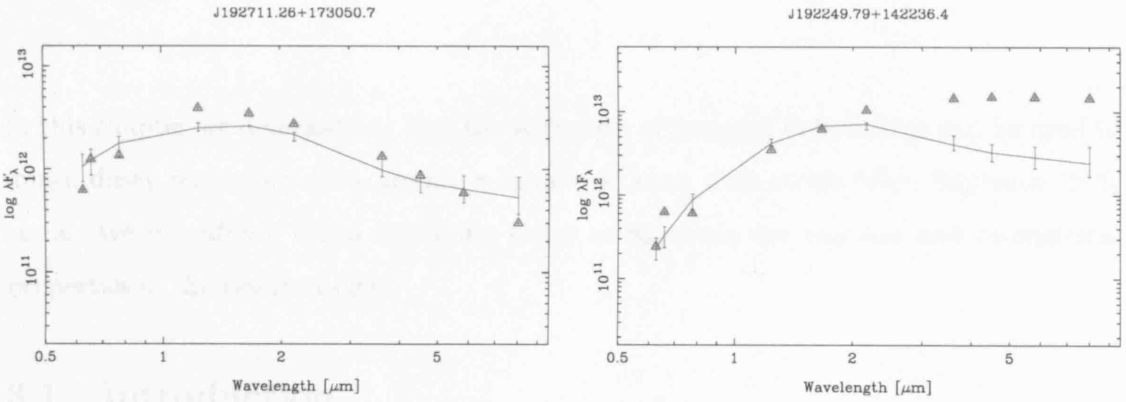

Figure 2.13: *continued*

CHAPTER 3

Near-infrared Imaging Polarimetry of dusty Main Sequence stars

In this chapter we demonstrate how the technique of Imaging Polarimetry can be used to image dusty scattering disks around a sample of know dust-excess Main Sequence (MS) stars. We use Monte Carlo scattering codes to constrain the physical and geometrical properties of the resolved disks.

3.1 Introduction

The discovery of the Vega-phenomenon in 1984 is considered one of the most important achievements of the IRAS space telescope. It discovered that several main sequence (MS) stars, including Vega, exhibited large mid- and far-infrared excesses that could not be ascribed to pure photospheric emission (Aumann 1984). Such excesses were attributed to a disk or ring of solid particles surrounding the stars, later termed 'debris-disks', and great interest was taken in these objects because of their relevance to the formation of planetary systems.

The case of young low- and intermediate-mass systems, such as T Tauri and Herbig Ae/Be (HAeBe) stars, is of particular interest (Yudin 2000; Waters & Waelkens 1998). These stars are considered to be precursors of classic Vega-like stars, such as β Pictoris, ϵ Eridani, HR 4796A, Fomalhaut and Vega itself. While planetary bodies are thought to have already formed in Vega-like systems (Aumann 1984; Beust et al. 1996; Natta et al.

2004), the circumstellar environments of T Tauri and HAeBe stars probably represent an early phase of planet formation (Bouwman et al. 2001).

From high resolution optical spectra of a sample of young dusty stars, the majority in common with our current sample and classified as HAeBe or T Tauri stars on the basis of their emission line spectra, Dunkin et al. (1997*a*) found that analysis of their absorption line spectra yielded surface gravities typical of MS stars, suggesting that they had already arrived on the MS. These type of objects have been referred to as 'transition' objects (Malfait et al. 1998) or 'dusty' Vega-excess stars (Dent et al. 2005) and they are nowadays thought to play a pivotal role in our understanding on the transition between the pre-MS (T Tauri and HAeBe stars) and the MS (Vega-like stars).

Many issues remain unclear regarding the circumstellar structures of these 'transition' objects, in particular, whether they are surrounded by flat disks or spherical envelopes is still not determined (Vink et al. 2002). Based on their spectral energy distributions, Meeus et al. (2001) introduced a classification of HAeBe stars into two groups: Group I objects have an almost flat or even rising 20-100 μm spectral energy distribution (SED), which can be well modelled by a flaring disk (Dullemond et al. 2001; Dullemond & Dominik 2004). On the other hand, Group II objects have a much bluer IR SED, and are believed to be associated with self-shadowed non-flared disks, which are predicted to be smaller in spatial extent than those of Group I sources.

High-contrast, high-spatial resolution, imaging close to bright central stars is required to test the validity of these models. Despite the efforts of many groups, limitations on instrumental capabilities have to date kept the number of directly imaged disks to a very low-number(see Zuckerman (2001) for a review). When only SEDs are available, not all parameters can be uniquely determined, e.g. the grain-size distribution and the spatial density profile are usually not separable.

Imaging polarimetry provides a powerful technique for detecting dust-disks around bright stars. Since only the light from the disks is expected to be polarized, the bright central stars are automatically suppressed in polarized light images. The utility of imaging polarimetry was demonstrated over ten years ago when Gledhill et al. (1991) detected polarized emission from the nearby Beta Pictoris disk (> 1000 AU in radius at a distance of 19.3 pc; Crifo et al. (1997)). The light was found to be 17% polarized and extended up to 30 arcseconds from the star (R- waveband). Kuhn et al. (2001) also used imaging polarimetry to detect polarized light around the A5Ve star HD 169142. More recently,

using the Very Large Telescope (VLT), Apai et al. (2004) tested the power of imaging polarimetry on an 8-m class telescope, detecting the presence of polarized emission as close as 0.1 arcsecond ($\sim$ 6 AU) from the classical T Tauri star TW Hya.

We have carried out a JHK imaging polarimetry survey for a sample of ten 'transition' objects (so called 'dusty' Vega-excess stars), selected from the surveys of Sylvester et al. (1996) and Mannings & Barlow (1998), along with TW Hya. Modelling of their SEDs had predicted angular sizes that could be resolvable at near-infrared (near-IR) wavelengths using the near-IR imaging instrument UIST on the 3.8-m United Kingdom Infrared Telescope (Sylvester & Skinner 1996; Sylvester et al. 1997). Our primary aim is to detect the signature of extended polarized emission from a scattering disk around the target stars. Note that even if the disk is too small to be resolved with UKIRT, a net polarization can be observed, indicating the presence and orientation of a disk on the sky.

3.1.1 Target sample

We have selected a sample of eleven young stars with dust disks from the surveys of Sylvester et al. (1996) and Mannings & Barlow (1998). All targets show mid- and far-IR excesses due to warm and cold dust grains. Most of them have been thoroughly studied using spectrophotometric techniques. Spectral types, effective temperatures, surface gravities, elemental abundances and overall line-emission characteristics are available for the majority of the sample (Dunkin et al. 1997*ab*). A summary of our sample is shown in Table 5.1, where we have listed respectively their names, spectral classification, infrared excess fractions $L_{IR}/L_{\star}$, distances and V-band magnitudes (as listed in the SIMBAD database).

The IR excesses of our targets are all much larger than those of true Vega-like stars (which are typically $L_{IR}/L_{\star} < 10^{-3}$ for Vega-like stars; Sylvester et al. 1996). Their surface gravities indicate they have recently reached the MS (Dunkin et al. 1997*ab*). HD 123160, HD 123356, HD 141569 and HD 145263 have relatively low IR excesses compared to the rest of our sample. The remaining stars have considerably larger IR excesses ($L_{IR}/L_{\star} > 0.1$), suggesting that they might be in a somewhat younger evolutionary state. HD 142666, HD 143006, HD 144432 and HD 169142 have near-IR excesses attributable to hot dust emission, resulting in (J-H) and (H-K) colours coincident with the locus of HAeBe and T Tauri stars (Sylvester et al. 1996). It has been proposed that the dust responsible for the near-IR excesses is a main agent for the optical polarization, and thus that Vega-

Table 3.1: Programme stars observed

Name	Sp class	L_{IR}/L_*	Distance [pc]	V
HD 98800	K5Ve	$8.4{\cdot}10^{-2}$	46^{7}_{5}	8.8
HD 123160	G5V	$4.4{\cdot}10^{-3}$	15.7	8.62
HD 123356	G1V	$5{\cdot}10^{-2}$	41	9.7
HD 141569	A0Ve	$8.4{\cdot}10^{-3}$	99^{8}_{7}	7.0
HD 142666	A8Ve	0.34	114	8.65
HD 143006	G5Ve	0.56	82	10.21
HD 144432	A9/F0Ve	0.48	252^{152}_{69}	8.17
HD 145263	F0V	$2{\cdot}10^{-2}$	116^{18}_{14}	8.95
HD 150193	A1V	0.37	150^{50}_{30}	8.88
HD 169142	A5Ve	$8.8{\cdot}10^{-2}$	145	8.15
TW Hya	K7 Ve	0.25	56^{8}_{6}	11.1

Spectral classifications and IR excesses are from Sylvester et al. (1996), Dunkin et al. (1997*a*) and Sylvester & Mannings (2000). An 'e' after the luminosity class indicates the presence of Hα emission. HD 141569, HD 123356, HD 144432, HD 150193 and HD 98800 have binary companions at separations of 6.8, 2.2, 1.2, 1.1 and 0.8 arcseconds respectively (Augereau et al. 1999; Sylvester & Mannings 2000; Pérez et al. 2004; Mora et al. 2001; Prato et al. 2001). Distances with quoted uncertainties are from parallactic measurements listed in the Hipparcos catalogue (Perryman et al. 1997), while values without errors come from spectrophotometric estimations published by Sylvester et al. (1996) and Sylvester & Mannings (2000).

like 'prototypes' showing almost no near-IR excess should present low polarization values (Yudin 2000). HD 142666, HD 143006, HD 144432 and HD 169142 have been detected in CO in the survey by Dent et al. (2005), indicating they still have substantial gas content.

3.2 Observations

The J-band data presented in this work was acquired on April 29th 2003, using the dual-beam polarimeter module IRPOL2 in conjunction with the near-IR camera UIST on UKIRT at Mauna Kea observatory. The resulting field of view was of 15×60 arcseconds, with 0.12 arcseconds per pixel. H- and K-band data for TW Hya, HD 150193 and HD 141569 were also acquired, on April 30th 2003, using the same observing procedure.

Dual-beam imaging polarimetry was obtained using a lithium niobate Wollaston prism, along with a rotating half-wave plate. By observing at four different half-wave plate positions (separated by 22.5 degrees), linear polarimetry is acquired. A detailed description of this standard dual-beam polarimetry configuration can be found in Berry & Gledhill (2003). Basically, two orthogonally polarized images are simultaneously recorded. The subtraction of these two images leads to the suppression of unpolarized light (mainly from the central star), and to the highlighting of polarized light (e.g. scattered light from the

disk).

We observed a total of 11 objects. Since most of our targets are bright (K< 8), several short exposures (< 1s) were co-added, in order to overcome saturation problems. Typical integration times ranged from 315 to 475 seconds. A non-destructive readout mode was used (ND+STARE). Point Spread Function (PSF) and flux calibrators were regularly interspersed, and polarized standards from the UKIRT calibration catalogue were also observed. In order to minimise the effects of pixel to pixel variations in the detector on derived polarization values, each measurement was repeated at 3 different array (jitter) positions.

3.3 Data reduction

All data were identically reduced using the STARLINK data-reduction pipeline ORAC-DR[1]. Dark subtraction and flat-fielding are carried out, and the dual-beam imaging polarimetry package POLPACK (Berry & Gledhill 2003) was then used to perform component image alignment and to combine the data to form resultant I, Q and U Stokes images. Stokes Q and U images are summed to create the polarised intensity and percentage polarisation images, following the standard relation:

$$PI = (Q^2 + U^2)^{-1/2} \tag{3.1}$$

$$P = \frac{PI}{I}, \tag{3.2}$$

where I is the total intensity. The angle of polarisation θ in each pixel is calculated as:

$$\theta = 0.5 \arctan(U/Q) \tag{3.3}$$

Propagation of the variance estimates from the raw data through the calculation provides errors on the final I, Q and U images, and on the derived polarized quantities P and PI (degree of polarization and polarized flux, respectively).

The values of P presented in this work correspond to the degree of polarization averaged over 0.36 arcsecond square bins (3×3 pixels), after applying a 2 σ cut. In this way, only measurements with an error in the degree of polarization of less than one-half of the polarization are considered.

[1] http://www.oracdr.org/

Table 3.2: Photometric measurements

name	Filter	Magnitude	Magnitude 2MASS	FWHM [arcseconds]	FWHM reference [arcseconds]
HD 98800	J	6.36 ± 0.02	6.39 ± 0.02	0.84	0.87
HD 123160	J	5.78 ± 0.03	5.81 ± 0.02	1.30	1.23
HD 123356	J	5.94 ± 0.02	5.89 ± 0.02	0.94	0.93
HD 141569	J	6.88 ± 0.02	6.87 ± 0.03	0.85	1.09
HD 141569	H	7.05 ± 0.02	6.86 ± 0.02	0.41	0.45
HD 141569	K	6.84 ± 0.02	6.82 ± 0.02	0.38	0.39
HD 142666	J	7.32 ± 0.02	7.35 ± 0.02	0.93	0.92
HD 143006	J	8.12 ± 0.03	8.35 ± 0.02	0.86	0.95
HD 144432	J	7.13 ± 0.03	7.09 ± 0.02	0.85	0.84
HD 145263	J	8.10 ± 0.02	8.08 ± 0.02	0.69	0.67
HD 150193	J	6.94 ± 0.02	6.94 ± 0.02	0.66	0.65
HD 150193	H	6.63 ± 0.02	6.21 ± 0.02	0.53	0.51
HD 150193	K	5.92 ± 0.02	5.47 ± 0.02	0.39	0.37
HD 169142	J	7.44 ± 0.02	7.31 ± 0.02	0.66	0.58
TW Hya	J	8.16 ± 0.02	8.21 ± 0.02	0.82	0.88
TW Hya	H	7.58 ± 0.02	7.55 ± 0.02	0.51	0.46
TW Hya	K	7.29 ± 0.02	7.29 ± 0.02	0.53	0.49

Photometry was performed using 3.5 arcsecond apertures and calibrated using observed UKIRT standards. Photometric magnitudes from the 2MASS point-source catalogue have been included. FWHMs measured both in the targeted stars and repective PSF references are presented.

3.4 Results

3.4.1 J- band imaging polarimetry and photometry

J- band photometry is presented in Table 3.2, together with 2MASS photometry. The photometric values derived from our measurements are generally in good agreement with the 2MASS values. HD 143006's J- band magnitude shows a 0.23 magnitude deviation with respect to previous J- band photometry, suggesting that the object has brightened since the 2MASS measurements. HD 169142's J- band magnitude is fainter than the 2MASS photometry, but is consistent with J- band measurements from Sylvester et al. (1996).

Table 3.3 presents measured integrated polarizations for our targeted stars. In the case of resolved centrosymmetric patterns (as in the cases of TW Hya and HD 169142), the integrated polarization will appear less than the actual resolved polarizations, since integrating the polarization vectors over all orientations can average to zero. As an example, TW Hya's maximum resolved polarization is 15 ± 0.5 % at 1.6 arcseconds from the star, while its integrated polarization is only 0.233 ± 0.025 %. The J- band instrumental polarization was estimated from observations of unpolarized standards, which showed percentage polarization levels of less than 0.5 percent. These values represent the real precision of our polarimetric measurements (mostly residuals from the alignment procedure),

Table 3.3: Polarimetric measurements

name	Filter	P [%]	θ
HD 98800	J	0.21 ± 0.02	-70 ± 11
HD 123160	J	0.12 ± 0.01	80 ± 13
HD 123356	J	0.26 ± 0.01	84 ± 9
HD 141569	J	0.55 ± 0.02	-77 ± 9
HD 141569	H	0.22 ± 0.02	-71 ± 8
HD 141569	K	0.08 ± 0.02	-59 ± 10
HD 142666	J	1.32 ± 0.02	75 ± 3
HD 143006	J	0.17 ± 0.02	6 ± 12
HD 144432	J	0.49 ± 0.02	3 ± 8
HD 145263	J	0.37 ± 0.03	23 ± 11
HD 150193	J	3.14 ± 0.02	57 ± 4
HD 150193	H	2.04 ± 0.01	52 ± 5
HD 150193	K	1.41 ± 0.03	48 ± 6
HD 169142	J	0.22 ± 0.03	-37 ± 6
TW Hya	J	0.23 ± 0.02	51 ± 6
TW Hya	H	0.18 ± 0.02	56 ± 7
TW Hya	K	0.10 ± 0.02	50 ± 8

Integrated percentage polarizations were computed using the polarimetry tool-box in GAIA†, which allows vectors within a chosen aperture to be selected for integration

†(`http://www.starlink.rl.ac.uk/`). This calculates the mean Stokes Q and U values and returns the polarization integrated over the annular region defined by 0.4 <radius< 3.5 arcseconds. This excludes the inner regions which are usually dominated by alignment and subtraction residuals. Polarization position angles are in degrees and measured from North to East.

and should again not be confused with the statistical errors on the integrated polarizations quoted in Table 3.3.

Targets for which we detect evidence of polarizing circumstellar material are discussed individually below (TW Hya, HD 169142, HD 150193 and HD 142666). The remaining stars from our sample do not show any evidence of dusty polarizing disks. This suggests that their polzarization levels are too faint to be detected by our observations, as exemplified by the non-detection of the disk around HD 141569. The intensity distribution of HD 141569's ring-like disk is known to peak at 3.3 arcseconds from the star (Augereau et al. 1999), a scale resolvable with UKIRT. However our J-band polarimetric observations were not able to detect it. Combining the HST J-band coronographic observations of HD 141569's disk (Augereau et al. 1999) and our polarimetric data, we derive upper-limits on the polarization level of HD 141569's disk. From this we conclude the disk is so faint that even if it was 100% polarized it would still fall below our detection limit. With HST observations Augereau et al. (1999) showed that the surface brightness of HD 141569's disk peaks at 0.199 ± 1.2 mJy arcsec^{-2}. This is one order of magnitude fainter than that of TW Hya's disk (5.7 ± 1.4 mJy arcsec^{-2}; Weinberger et al. (2002)), and could explain why the disk around TW Hya could be seen in polarized light, while

the one around HD 141569 was not.

J-band imaging polarimetry of four of our eleven targets is presented in Figures 3.1, 3.2, 3.4 and 3.5 using the same format for each target. Polarization vector maps are superimposed upon total intensity contours. Total intensity grey-scales are also plotted, with the purpose of highlighting the position of the central source. The polarization vectors are oriented parallel to the E vector, with their length proportional to the degree of linear polarization, as indicated by the scale vector on each diagram.

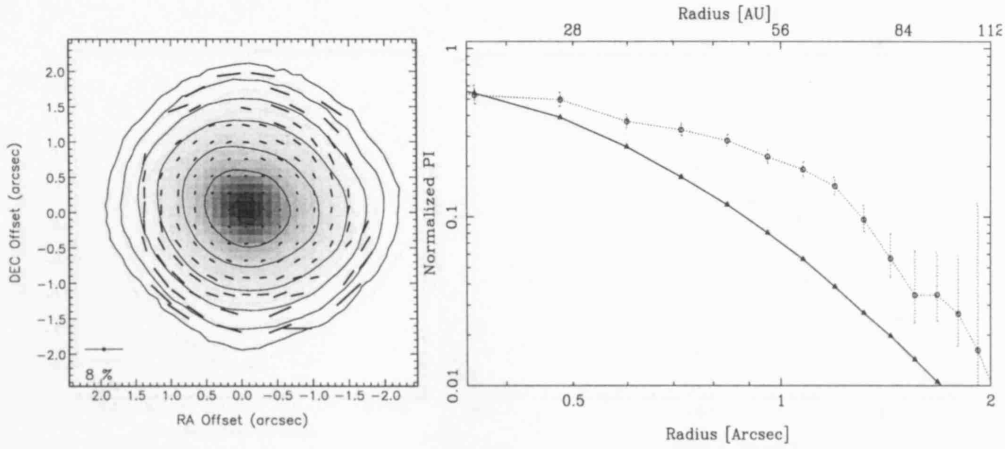

Figure 3.1: *Left panel:* J-Band imaging polarimetry of TW Hya. Polarization vector maps are superimposed upon total intensity maps, showing both contours and grey-scale images. Polarization measurements have been binned in 3×3 square bins and a 2σ cut applied to avoid spurious values. North is up and East is to the left. *Right panel:* Normalized radial polarized intensity distribution around TW Hya (dotted line) compared to the total intensity radial profile of the PSF calibrator star HIP 54690 (solid line). The data have been binned over 1-pixel width rings and the error bars correspond to the statistical errors of each bin. Both x- and y- axis are plotted on logarithmic scale.

TW Hya:

Our observations show a centro-symmetric polarization pattern (Figure 3.1, left panel), revealing the signature of a scattering disk seen near to face-on. The polarization values increase with increasing radius, up to $\sim$ 15 % at 1.6 arcseconds, although these have larger uncertainties than those close in. We note the $\sim$ 15 % percentage polarization values we measure at 1.6 arcseconds include direct unpolarized flux from the star in the estimate of the disk's total scattered light intensity, and so represent a lower limit on the disk's intrinsic polarization. Please refer to Section 3.5 and Figure **??**, left panel, for an estimate on the intrinsic polarization of TW Hya's disk. We estimate the extension of the polarizing disk by comparing the polarized intensity (PI) radial profile of TW Hya to the total intensity radial profile of the PSF reference star HIP54690 (Figure 3.1, right panel). Extended polarized structure can be traced from $\sim$ 0.4 arcseconds up to at least $\sim$ 1.5 arcseconds. This is comparable to the extension of TW Hya's polarizing disk as seen in the Ks- band with the VLT (1.4 arcseconds in radius, Apai et al. (2004)).

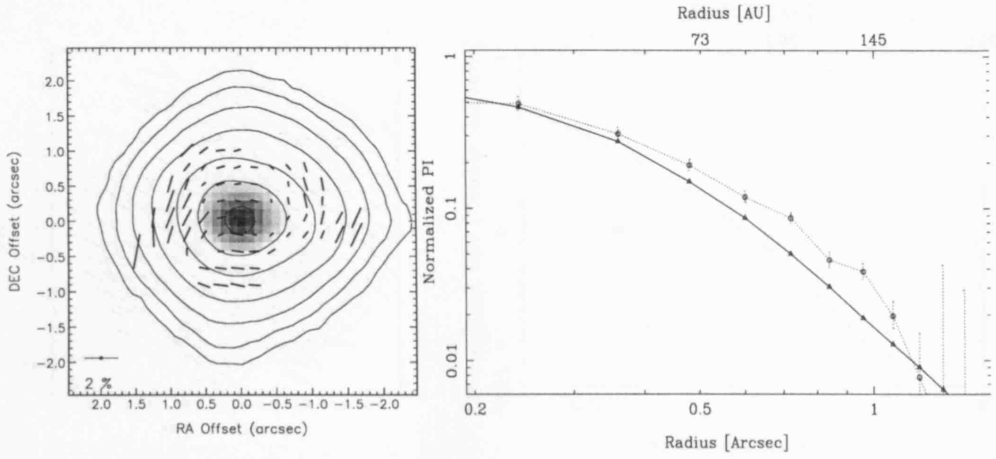

Figure 3.2: *Left panel:* J-band imaging polarimetry of HD 169142, presented in the same format as for Figure 3.1. The polarization vector map of HD 169142 suggests the marginal detection of a centro-symmetric pattern. *Right panel:* The J-band PI radial profile for HD 169142 (dotted line). The solid line corresponds to the total intensity radial profile of the PSF reference star, FS 140. Azimuthal values have been binned over 1-pixel width concentric rings. The error bars represent the statistical errors. Both x- and y- axis are plotted on logarithmic scale.

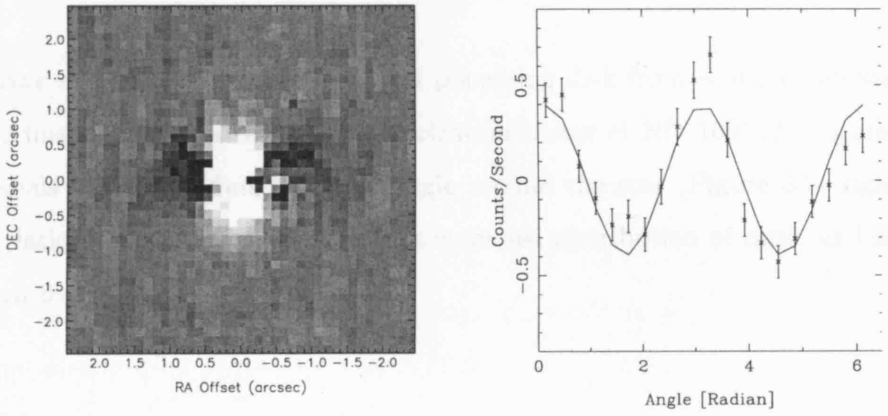

Figure 3.3: Q- Stokes image of HD 169142 (left panel). HD 169142's Q- Stokes image shows sinusoidal modulation with angle (right panel). The crosses mark the data points binned over 18 degree bins, centred on HD 169142, using an annulus extending between 0.6 and 2.2 arcseconds. The solid curve represents the best sinusoidal fit to the data.

HD 169142:

Our UKIRT observations just marginally resolve a centro-symmetric pattern around HD 169142 (Figure 3.2, left panel). The PI radial profile of HD 169142 (Figure 3.2, right

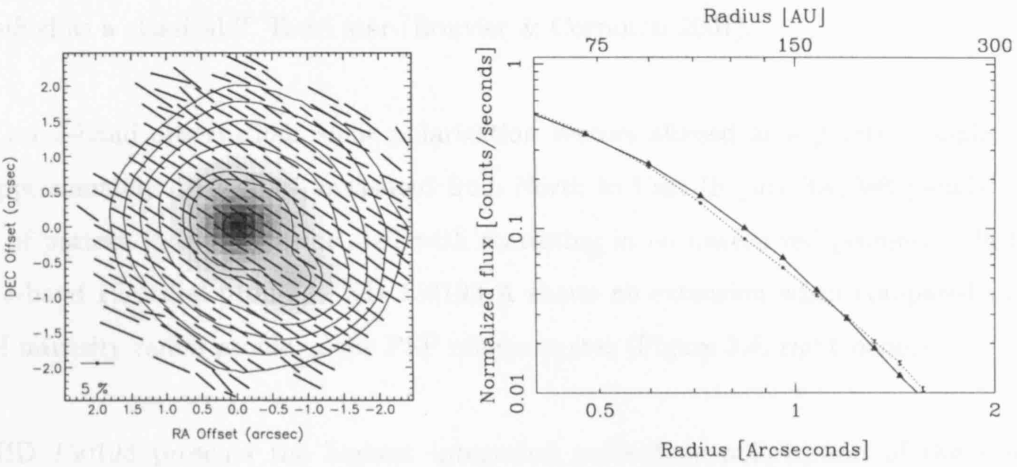

Figure 3.4: *Left panel:* J-Band imaging polarimetry of HD 150193. Polarization vectors are superimposed upon total intensity maps shown as both grey-scale and contour images. The polarization measurements have been binned in 3×3 square bins and a 2σ cut applied to avoid spurious values. North is up and East is to the left. *Right panel:* HD 150193 A's PI radial profile (dotted line) versus the total intensity radial profile of the PSF reference star HIP 80425 (solid line). The region containing HD 150193 B was excluded when computing HD 150193 A's PI radial profile. Both x- and y- axis are plotted on logarithmic scale.

panel) shows the detection of an extended polarizing disk from ~ 0.4 to about 1.2 arcseconds radius. Inspection of the Q- polarization image of HD 169142 (Figure 3.3, left panel) reveals a clear modulation with angle around the star (Figure 3.3, right panel). The modulation reveals the presence of an extended distribution of dust, as has already been shown by Kuhn et al. (2001).

HD 150193:

Recent adaptive optics H-band coronographic observations of the binary system HD 150193 A-B (1.1 arcseconds separation) at the 8.2-m Subaru telescope (Fukagawa et al. 2003) have revealed the presence of a scattering disk around the primary star, extending from the edge of the coronographic mask (0.5 arcseconds radius, or 50 AU) to about 1.3 arcseconds. An asymmetry of the disk in the direction of the binary companion was detected, suggesting that the companion has a distorting effect on the disk structure. HD 150193 A is known to be a A2 IV Herbig Ae star (Mora et al. 2001), whilst HD 150193 B has recently been

classified as a classical T Tauri star (Bouvier & Corporon 2001).

Our J-band observations show polarization vectors aligned at a position angle (PA) of approximately 57 degrees, measured from North to East (Figure 3.4, left panel). This sort of pattern is usually associated with scattering in an unresolved geometry. In fact, the J-band PI radial profile of HD 150193 A shows no extension when compared to the total intensity radial profile of the PSF reference star (Figure 3.4, right panel).

HD 150193 presents the highest integrated percentage polarization of the sample (3.15% at PA=57 degrees), of which a significant part is thought to be interstellar in nature (HD 150193 is located near the edge of the ρ Ophiuchus cloud). Yudin (2000) estimated the interstellar polarization to be 2.5 % at 21 degrees PA in the V- band, and concluded that the intrinsic optical polarization of HD 150193 is 4.2%, at 65 degrees PA. By comparing our measured PA and Yudin's intrinsic PA, we conclude that most of the polarization we detect in the J band must be intrinsic to the disk, with a large amount of polarizing material in the line of sight of the star. We note that the integrated polarization that we measure around the system of 3.15% is in agreement with Whittet et al. (1992), given systematic errors of $0.1 - 0.2\%$.

HD 142666:

This A8Ve star (Dunkin et al. 1997*b*) was catalogued as a probable Herbig Ae star by Gregorio-Hetem et al. (1992), yet no CS disk has been directly observed around it. HD 142666 shows evidence of CS activity; a double-peaked Hα profile (Dunkin et al. 1997*b*), photometric variability, and a large IR excess attributed to CS dust (Sylvester et al. 1996). Meeus et al. (1998) interpreted the variable photometric behaviour of HD 142666 as evidence of clumps of CS material crossing the line of sight of the star. If the CS structure is flattened, then the CS disk would be more likely to be orientated edge-on. Yudin et al. (1999) measured 0.5% intrinsic optical polarization, considerably larger than those of the Vega-like 'prototypes' (0.02% and 0.007% for β Pictoris and Vega respectively; Leroy 1993).

Figure 3.5, left panel, shows our J-band imaging polarimetry of HD 142666. HD 142666

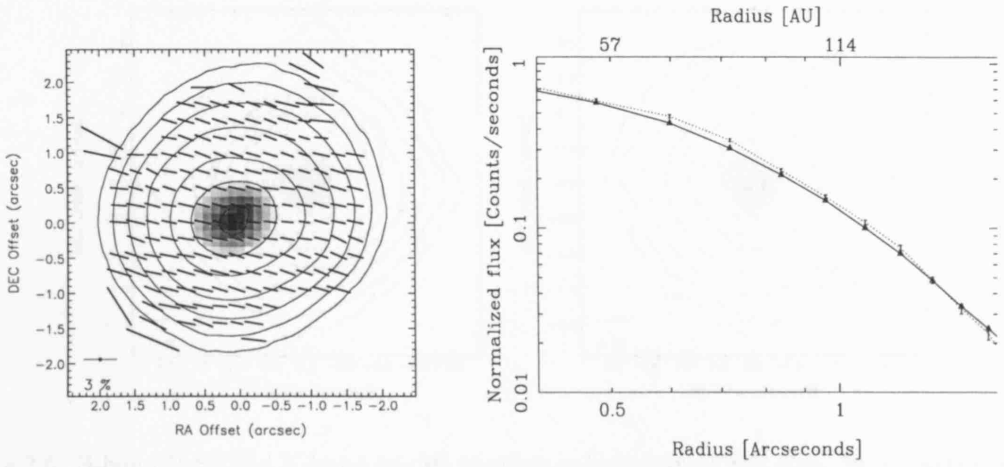

Figure 3.5: *Left panel:* J-Band imaging polarimetry of HD 142666. North is up and East is to the left. *Right panel:* HD 142666 's PI radial profile (dotted line) versus the total intensity radial profile of the PSF reference star HIP 77815 (solid line). Both x- and y- axis are plotted on logarithmic scale.

presents a polarization pattern with vectors aligned at $\sim$ 75 degrees PA and a 1.2 % mean polarization. As with HD 150193, the PI radial profile of HD 142666 shows no evidence of extension (Figure 3.5, right panel). Combining catalogued polarization values and Hipparcos distances, Yudin et al. (1999) derived a distance-polarization law that predicts a 0.3 % contribution at V due to interstellar polarization, with a position angle of about 100 degrees at optical wavelengths. They estimated a V-band intrinsic polarization of $p \approx 0.5$ % PA of 70 degrees. The polarization we measure in the J- band is too high to be completely interstellar in nature. In addition, we measure a polarization PA similar to that of the intrinsic optical polarization estimated by Yudin et al. (1999). Yudin et al. (1999) also noted that the polarization of HD 142666 probably increases toward IR wavelengths, as is confirmed by our J- band measurements. This implies no significant interstellar contribution to the 1.2% J-band polarization that we measure, so we conclude that the polarization detected is intrinsic to the system.

3.4.2 H- and K- band imaging polarimetry

H- and K-band imaging polarimetry was obtained for TW Hya, HD 150193 and HD 141569 on April 30th 2003. H and K photometric values are shown in Table 3.2, while H- and K-band polarimetric measurements are presented in Table 3.3. We note that HD 150193 appears fainter by $\sim$ 0.4 magnitudes in both the H- and K- band with respect to the

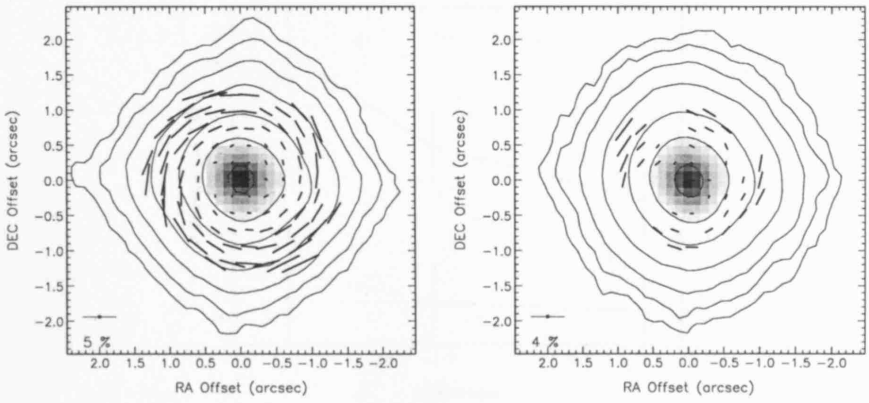

Figure 3.6: H-band (left) and K-band (right) imaging polarimetry of TW Hya. Polarization vector maps are superimposed upon total intensity maps, shown as both contour and grey-scale images. North is up and East is to the left.

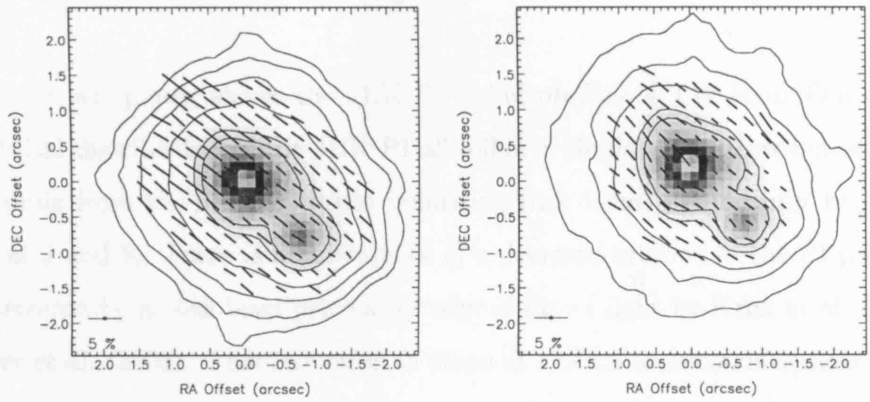

Figure 3.7: H-band (left) and K-band (right) imaging polarimetry of HD 150193. Polarization vector maps are superimposed upon total intensity contour and grey-scale images. North is up and East is to the left.

2MASS measurements.

TW Hya's H- and K- band imaging polarimetry are shown in Figure 3.6, left and right panels respectively, whilst Figure 3.7 shows the H- and K- band imaging polarimetry of HD 150193 (left and right panels, respectively). Alignment and subtraction residuals dominate the central parts of the images (radius< 0.4 arcseconds). Typical values for instrumental polarization were < 0.4 percent in both H- and K- band (as measured from unpolarized standards). As in the J- band, HD 141569 did not show any evidence of extended polarized structure and is therefore not shown. The near-IR spectral dependence

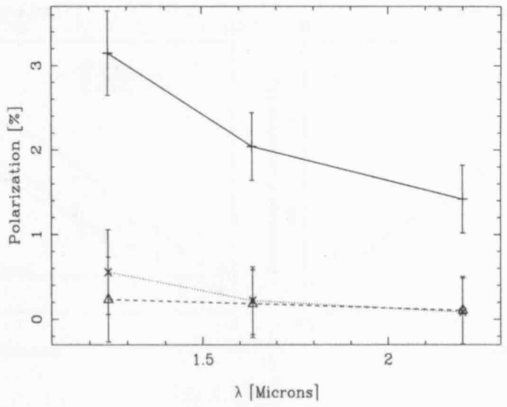

Figure 3.8: Near-IR polarization spectral dependence for HD 150193, HD 141569 and TW Hya (solid, dotted and dashed lines respectively). The error bars correspond to the instrumental errors.

of the polarization for our three stars targeted at JHK is shown in Figure 3.8.

Figure 3.9, left panel, shows the JHK PI radial profiles of TW Hya. Our data show that the radial distribution of the JHK PI all follow a similar behaviour between 0.5 and 1.3 arcseconds from the star, with the polarizing disk being significantly brighter at H than it is at J and K. There is also evidence of a decrease in slope in the PI profiles from 1.3 to 2 arcseconds, as has been previously seen in direct light by Krist et al. (2000) and Weinberger et al. (2002). This reduction in slope at $r > 1.3$ arcseconds is clear in both H and K but is less evident at J, where a bump is seen at r$\sim$ 1.5 arcseconds at very low level (see Figure 3.1). This is consistent with the total intensity radial profiles from Weinberger et al. (2002), in which the change in slope is more evident at H than it is at J.

3.5 Discussion

Our polarimetric imaging survey has successfully detected the presence of circumstellar polarized emission around four of our eleven targets. According to proposed CS evolutionary scenarios, both the IR excess and polarization should decrease with time (Malfait et al. 1998; Waelkens et al. 1994; Yudin et al. 1999); as a consequence of processes such as planet formation, the disks should be cleared out and both the near-IR excess and the polarizing effects of CS dust should disappear. Thus, the detection of considerable amounts of polarizing material around TW Hya, HD 150193, HD 142666 and HD 169142 is consistent with a youthful nature. On the other hand, the non-detection of polarized emission

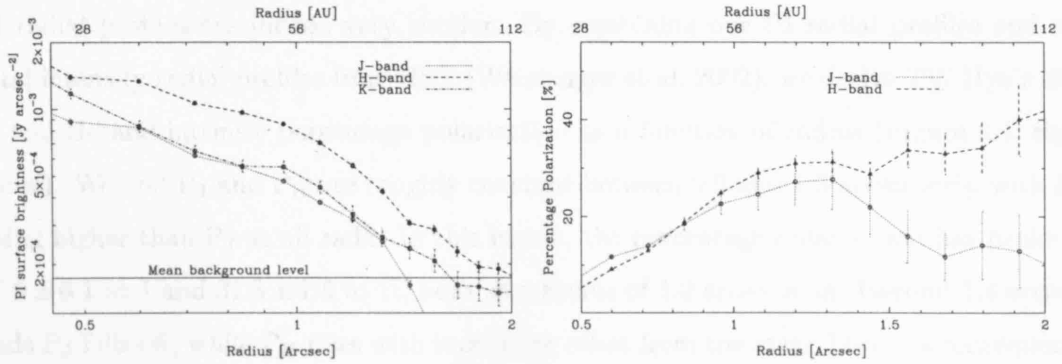

Figure 3.9: *Left panel:* J-, H- and K-band polarized intensity radial profiles of TW Hya (dotted, dashed and solid lines respectively). Both x- and y- axis are plotted on logarithmic scale. *Right panel:* J- (circles) and H-band (triangles) intrinsic percentage polarization of TW Hya's disk, derived using total intensity coronographic imaging from HST (Weinberger et al. 2002) and our UKIRT imaging polarimetry. The error bars correspond to derived statistical errors.

toward stars presenting low IR-excesses ($L_{IR}/L_{star} < 0.1$) suggests that these stars are at a more advanced evolutionary state, probably near to the beginning of their MS phase. In this context we would have expected to detect polarized emission around HD 144432 and HD 143006 (which present L_{IR}/L_{star} values and near-IR excesses even higher than those of HD 142666. The most likely reasons for not detecting their disks polarimetrically could be that either we did not integrate deep enough to detect the scattered light against the stellar flux or that the disk is symmetrically distributed but unresolved, or a combination of both effects. Dominik et al. (2003) showed that the near-IR excesses of Class II sources (such as HD 144432, HD 142666 and HD 150193) can be well modelled if there is a large presence of micron-sized grains in the inner 10 AU of their CS disks. It seems reasonable to deduce that the near-IR scattering disks around HD 144432, HD 143006 and HD 142666 are too small to be resolved by UKIRT. In fact, recent VLT mid-IR interferometric observations have successfully measured the radius of HD 144432's disk to be of 0.014 arcseconds (Leinert et al. 2004), far too small to be resolved by our UKIRT observations.

Apai et al. (2004) proposed that TW Hya's disk Ks-band polarized intensity profile and the J- and H-band total intensity radial profiles have a similar behaviour, concluding that the percentage of polarization is nearly constant between 0.9 and 1.4 arcseconds from the star. As reported in Section 3.4.2, our observations show that in this region the JHK

PI radial profiles are indeed very similar. By combining our PI radial profiles and the total intensity radial profiles from HST (Weinberger et al. 2002), we derive TW Hya's disk J- and H-band intrinsic percentage polarization as a function of radius (Figure 3.9, right panel). We find P_J and P_H are roughly constant between 0.9 and 1.3 arcseconds, with P_H being higher than P_J at all radii. In this region, the percentage polarization has peaks at 27.6 ± 6.1 at J and 31.3 ± 1.5 at H, both at a radius of 1.2 arcseconds. Beyond 1.4 arcseconds P_J falls-off, while P_H rises with increasing offset from the star. This is a consequence of the steeper J-band PI profile, as the Weinberger et al. (2002) total intensity profiles for the 1.1 and 1.6 μm NICMOS filters have the same $r^{-2.6 \pm 0.1}$ fitted slope. However, the NICMOS 1.6 μm surface brightness deviates from this single power-law beyond 1.4 arcseconds, suggesting that our P_H may be overestimated beyond this radius. Nevertheless, we can conclude that our observations, in conjunction with direct light images from the HST (Weinberger et al. 2002), indicate that the disk scattering and polarizing efficiencies peak in the H-band, suggesting there is a substantial population of sub-micron sized particles present in the disk (Bohren & Huffman 1983). This would argue against larger grains of the type suggested by Roberge et al. (2005), although this needs to be investigated more thoroughly by future modelling.

Our imaging polarimetry for HD 169142 confirms the presence of an extended CS structure. Both the Q- and U- J-band images showed modulation with angle as was already noted by Kuhn et al. (2001), suggesting that the disk is oriented near to pole-on. The disk-size of 1.2 arcseconds we measure (174 AU at HD 169142's distance) is 0.3 arcseconds smaller than the previous polarized-disk extension measured by Kuhn et al. (2001). We note that the effective exposure time used by Kuhn et al. (2001) was 2.2 times larger than the one we used, which may explain the difference in HD 169142's measured disk extension between these two UKIRT observations. Kuhn et al. (2001) also detected a scattering inhomogeneity within the CS cloud, but this was not evident in our data. It is interesting to note that HD 169142 has been proposed as a Group I source (following the Meeus et al. (2001) classification) and that its SED has been successfully modelled with a flaring-disk geometry (Dominik et al. 2003) and outer disk-radius of 100 AU.

Based on the H-band disk-radius of 1.3 arcseconds measured coronographically with Subaru by Fukagawa et al. (2003), we would have expected to resolve the disk around

HD 150193, at least in our H- and K-band observations. However we find no signs of extension when comparing our PI radial profiles of HD 150193 with the total intensity radial profiles of the PSF calibrator star. We believe our non-detection of the extended disk is due to sensitivity effects, since the Subaru observations were carried out with a nine times longer integration time and a four times larger telescope collecting area. Even though we failed to detect the disk reported by Fukagawa et al. (2003), we believe there must still be an axisymmetric structure causing the relatively large linear polarization toward this star. The alignment of the polarization vectors at 57 degrees PA is likely to be intrinsic, and not associated with interstellar polarization (as discussed in Section 3.4.1). To produce the aligned vectors such structure must be (i) optically thick at J, (ii) inclined to the plane of the sky (i.e. not face on) and (iii) too small to resolve with UKIRT. So this could be an inner, optically thick component of HD 150193's disk. We also note that HD 150193 shows the steepest spectral dependence of polarization among our three JHK targeted stars, with its polarization PA being constant within the errors at all wavelengths (as can be seen in both Figure 3.7 and in the values presented in Tables 3.3). Adopting the binary PA of 225 degrees measured by Fukagawa et al. (2003), we note that there is an apparent alignment between polarization PA (57 degrees) and the axis between the two stars, although this could be just a coincidence. Nevertheless, this behaviour has already been reported in the V-band by Maheswar et al. (2002), who suggested that it is common to several other HAeBe binary systems.

We have found for HD 142666 similar evidence of a CS scattering structure to that for HD 150193. Along with HD 150193, HD 142666 exhibits a large value of linear polarization compared to the rest of our sample and also presents aligned vectors suggesting that the CS disk was unresolved. The similarity between both stars in terms of their infrared excesses and their polarization makes it plausible to suggest a similar structure in their disks. This is consistent with the SED modelling carried out by Dominik et al. (2003), in which both disks are estimated to be comparable in size and mass.

Despite the limited size of our sample, we note that our polarimetric observations detected the presence of extended polarizing disks only around systems that have had their SEDs fitted with a flared disk geometry (Krist et al. 2000; Calvet et al. 2002; Dominik & Decin 2003). This points toward an observational selection effect predicted by Whitney

& Hartmann (1992), in which Monte Carlo scattered light models show that a flaring disk scatters up to two orders of magnitudes more light than a flat disk of similar size and mass. Detailed scattered-light modelling of our polarimetric data is, however, required to constrain the physical parameters of the detected CS disks.

CHAPTER 4

Scattered light models of the protoplanetary disk around TW Hya

4.1 Introduction

The planets in our solar system orbit around the sun following roughly circular trajectories, within a common plane of rotation (co-planarity). This suggested that the planets did not form in an spherical cloud but from a rotating 'protoplanetary disk'. Such flattened, circumstellar structures are predicted to form due to the conservation of angular momentum during the gravitational collapse of a rotating protostellar cloud. Protoplanetary disks around young, low-mass stars (such as T Tauri and HAeBe stars) were discovered by their strong infrared emission, which can overwhelm the stellar radiation by several orders of magnitude (Mendoza V. 1968; Cohen & Kuhi 1979; Rucinski 1985). Most young stars are now believed to be surrounded by protoplanetary disks (up to 50% of low-mass stars younger than 1 Myr, Rieke et al. 2004).

Early theoretical models of protoplanetary disks failed to reproduce the observed SEDs. Viscous accretion disk models were proposed a long time ago by Shakura & Sunyaev (1973) and by Lynden-Bell & Pringle (1974), in which energy released by the combined effects of viscous dissipation and accretion (accretion luminosity) within an opaque, geometrically thin disk is the main disk-emission source. These models predicted a mid- to far-IR SED slopes that fall as $\lambda F_\lambda \propto \lambda^{-4/3}$, steeper than the flattish SED observed toward most sources ($\lambda F_\lambda \propto \lambda^{-3/4}$ Rucinski 1985). In the geometrically flat passive reprocessing disk

model of Adams et al. (1987), all the energy input comes from the stellar radiation, which is absorbed by the disk and re-radiated at longer wavelengths. However, this model also fails to reproduce the observed SEDs, predicting SEDs that have similar slopes to the models of Lynden-Bell & Pringle (1974).

A solution to the failure of the models would have to invoke a disk structure different to the standard flat disk. Kenyon & Hartmann (1987) proposed that if the disk is in vertical hydrostatic equilibrium, the relative thickness of the disk $h(r)/r$ increases with increasing radius. $h(r)$ is the Gaussian scale height of the disk, which is sustained by the disk's internal pressure. This causes the disk to become proportionally thicker at larger radii, and is said to have a concave or *flared* structure. $h(r)$ scales with radius as $h(r) \propto r^{\beta}$, where β is the exponent that characterises the degree of flaring (named the *flaring exponent* accordingly). Assuming that the dust and gas are well-mixed throughout the disk, the scale height of the disk's visible photosphere (where the optical depth of the disk τ becomes $\sim$ 1 for the penetrating photons) will also become flared. Therefore, the scattering surface of the disk also becomes flared, allowing a larger area of the disk to be exposed to stellar radiation. This will cause the disk to absorb more energy than in the geometrically flat disk case, which produces larger re-radiated infrared fluxes, and flat mid- to far-IR SEDs that are more similar to the observations (Kenyon & Hartmann 1987).

The irradiated flared disk model is physically plausible if the dust and gas are well mixed up to several scale heights above the midplane at large radii, which can be achieved if the disk is in vertical hydrostatic equilibrium. Given a star+disk system in which most of the mass is concentrated in the central star with the disk orbiting in Keplerian motion, the condition of vertical hydrostatic equilibrium causes the *vertical pressure scale height*, $h(r)$, to vary with radius, as in Shakura & Sunyaev (1973):

$$\frac{h}{r} = \left(\frac{v_s^2 \, r}{G M_\star} \right)^{-1/2}, \tag{4.1}$$

where v_s^2 is the local speed of sound, G is the gravitational constant and $M_\star$ is the mass of the central star. Since the disk's internal temperature distribution T_{int} is proportional to the speed of sound, this means that h/r scales with radius and T_{int} as:

$$h/r \propto (T \, r)^{-1/2}. \tag{4.2}$$

Therefore, if the radial temperature distribution decreases less steeply than r^{-1} the disc becomes proportionally thicker with increasing radii. The vertical structure of protoplanetary disks and the disk temperature distribution are therefore tightly bound. The original model of Kenyon & Hartmann (1987) assumed that the disk was vertically isothermal, an assumption that has been relaxed by current models that solve self-consistently the vertical structure and the different energy transport mechanisms in the disks (Chiang & Goldreich 1997; D'Alessio et al. 1998 1999; Dullemond et al. 2001; Dullemond & Dominik 2004). These currently provide the best fits to the observed SED of T Tauri protoplanetary disks.

How long flaring can be sustained in a protoplanetary disks also depends on the time scales for dust to spiral down onto the disk midplane. These time scales depend on the size of the grains, and are $\sim$ 10^6 yr for μm-sized particles and $\sim$ 100 yr for cm-sized particles (Weidenschilling 1980). Therefore, studying the flaring of protoplanetary disks can be used to infer the evolutionary status of the circumstellar dust. For instance, a high degree of flaring in an old (age $> 10^6$ yr) CS disk would be indicative of dust replenishment in the upper layers , since most dust particles should have already settled near the midplane. Erosion and fragmentation of larger particles would cause a population of small dust particles well-mixed with the gas, which would be easily transported upward by turbulent and convective gas motions (Weidenschilling 1984).

Resolved images are crucial for constraining SED modelling of protoplanetary disks. They provide direct information on the spatial distribution of the dust, which is used to break degeneracies found in the disk parameters when only SED data are available. In the case when the disk is seen close to edge-on, the vertical structure of the disk can be inferred. The HST scattered light images of the classical T Tauri star HH 30 may be the most representative case of flaring occurring in a protoplanetary disk. As seen in the optical and near-IR (Figure 4.1, from Cotera et al. 2001), the image shows two, almost parallel, reflection nebulae separated by a dark dust lane, the latter corresponding to the optically thick disk midplane seen in absorption due to the edge-on orientation. The width of the dark lane increases at larger radii. Modelling of the HH 30 SED and scattered light images by different authors indicate that the the disk is significantly flared (Burrows et al. 1996; Cotera et al. 2001).

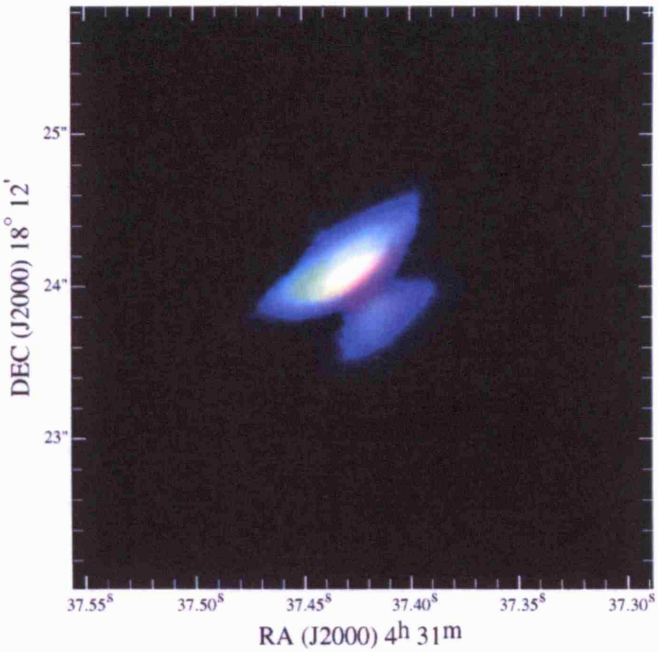

Figure 4.1: HST three-colour composite image of HH 30 from Cotera et al. (2001). WFPC2 F675W is blue, NICMOS F110W is green, and NICMOS F204M is red. The figure illustrates the asymmetric reflection nebula caused by the scattering of photons on the disk's atmosphere. The star and some of the disk's reflected light are obscured by the dense midplane of the disk. From the structure of both the reflection nebula and the disk's midplane it can be inferred that the disk is flared.

In contrast, when an optically thick disk is seen close to face-on (pole-on), scattered light (optical or near-IR) comes mostly from the disk's upper-layers. The stellar radiation will penetrate any part of the disk to an optical depth of 1, which makes it almost impossible to estimate the density of grains below this scattering surface. Nonetheless, the reflected light from the scattering surface provides important information on the disk vertical and radial structure. The best known case of a protoplanetary disk seen pole-on is the closest T Tauri system to Earth, the K8V emission-line star TW Hya (d$\sim$ 56 pc, Wichmann et al. 1998). TW Hya is surrounded by a circumstellar disk unusually massive for its age ($\sim 0.04 \pm 0.02\ M_{\odot}$, 10 Myr; Calvet et al. 2002; Webb et al. 1999), and the infrared excess of $L_{IR}/L_{\star} = 0.25$ for the system indicates that the disk is optically thick (Adams et al. 1987; Kenyon & Hartmann 1987). SED modelling suggests that the dust grains have undergone significant grain-growth (Natta et al. 2004), and that the disk's inner radius is truncated at 4 AU (Calvet et al. 2002), perhaps due to the presence of an unseen orbiting planet.

Several direct imaging studies of the disk around TW Hya have revealed that it is seen close to pole-on and that it extends to at least 1.8 arcseconds from the star ($\sim$ 140 AU at TW Hya's distance, Krist et al. 2000; Trilling et al. 2001; Weinberger et al. 2002). Krist et al. (2000) used single- and multi-scattering modelling codes to fit the R- and I-band HST images of TW Hya's disk. Since, in a pole-on orientation, the observed radial intensity profiles are devoid of line-of-sight projection effects, these can be used to determine the vertical structure of the disk self-consistently. Their modelling results proved a strong dependence on the degree of flaring, showing that scattered light models can be a powerful tool to constrain the geometry of protoplanetary disks seen close to pole-on. Krist et al. (2000) claimed an improvement by a factor of 4 on the determination of TW Hya's flaring coefficient β, when compared to the one derived for HH 30 by the same authors and using similar techniques. The values of the flaring coefficient β derived by Krist et al. (2000) for the different regions of TW Hya's disk are all greater than 1, suggesting that the disk is flared and not geometrically flat.

Near-IR total intensity and polarized intensity (PI) radial profiles of the disk within 0.9 and 1.4 arcseconds have however revealed that the total intensity of the disk decays with radius as $r^{-2.6}$ (Weinberger et al. 2002). This radial dependence is somehow steeper when compared to the r^{-2} dependence predicted for a flared disk from scattered light models (Whitney & Hartmann 1992). In addition, K-band PI observations with the VLT by Apai et al. (2004) detected an even steeper radial slope for the polarized intensity distribution, with the PI flux scaling with radius as $r^{-3.1}$, which supports the hypothesis that the disk is either flat or has very small flaring.

In Chapter 3 we demonstrated that imaging polarimetry can be very useful for resolving protoplanetary disks. We presented J-, H- and K-band polarised intensity radial distributions for TW Hya's disk (Hales et al. 2006). Similarly to the case of total intensity scattered light images, polarised light models show that the polarised intensity radial profile of an optically thick protoplanetary disk is strongly dependent on the degree of vertical flaring (Whitney & Hartmann 1992). In this chapter we use Monte Carlo scattering codes to simulate for the first time the observed JHK polarised intensity profiles of TW Hya's disk. We search for best fit models using different physical structures from the

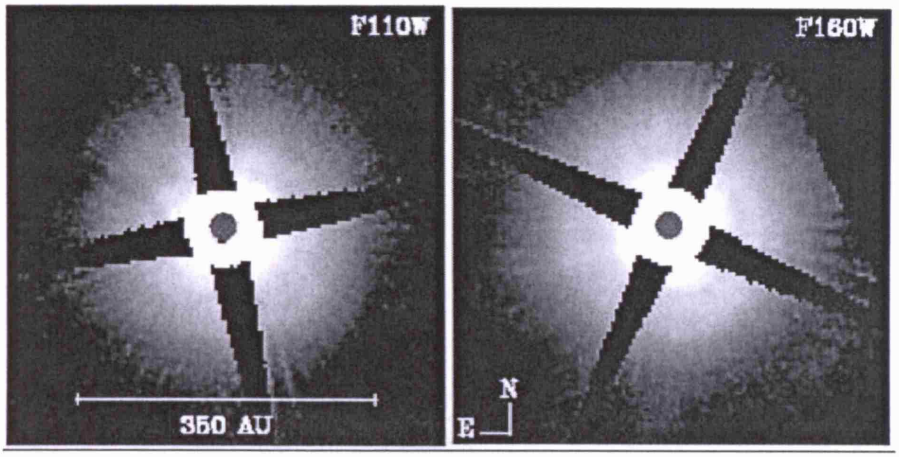

Figure 4.2: Near-IR NICMOS coronographic imaging of the disk around TW Hya, from Weinberger et al. (2002). This HST image shows that the face-on disk extends up to at least 150 AU in radius.

literature, and show that this technique, because of being highly sensitive to the location of the disk's photosphere, can be used to provide accurate constraints on the degree of flaring in TW Hya's disk. Our main aim in this chapter is to demonstrate the usefulness of imaging polarimetry data for constraining the scattering structure of protoplanetary disks.

4.2 Scattered light models

4.2.1 Disk structure

The disk is described physically by its distribution of mass in the radial and vertical directions, the volumetric mass density distribution $\rho(r, z)$. The standard geometry of a flared protoplanetary disk is described by a mass density distribution with a Gaussian scale-height, from Shakura & Sunyaev (1973):

$$\rho(r, z) \quad = \rho_0 (\tfrac{r}{R_*})^{-\alpha} \exp^{-\frac{1}{2}[\frac{z}{h(r)}]^2}, \tag{4.3}$$

where α is the density exponents and ρ_0 is the disk's midplane density at $r = R_*$. Flaring will occur if the disk is in vertically hydrostatic equilibrium (Kenyon & Hartmann 1987), so the scale height increases with radius as

$$h(r) = h_0 (r/R_*)^{\beta}, \tag{4.4}$$

with the amount of flaring being by characterised by the parameter β. Models of geometrically flat disks assume a value of $\beta = 0$ (Whitney & Hartmann 1992), while in standard flared disk models β usually has a value greater than unity.

The surface density, Σ, is defined as the vertically averaged volumetric mass density, and corresponds to the integral of Equation 4.3 between z= $-\infty$ to z= $+\infty$. Straightforward integration yields

$$\Sigma(r) = (2\pi)^{3/2}\rho_0 h_0 (r/R_*)^p, \tag{4.5}$$

where p= $\beta - \alpha$. In steady accretion disks the surface density is inversely proportional to the midplane temperature of the disk ($\Sigma(r) \propto T^{-1}$, D'Alessio et al. 1998). Physical models can determine the radial dependence of the midplane temperature, and thus constrain the possible values of the surface density radial exponent p (if $T(r) \propto r^{-a}$, then $p=\beta - \alpha$=a). The models of steady accretion disks by Shakura & Sunyaev (1973) and Lynden-Bell & Pringle (1974) predicted $T(r) \propto r^{-3/4}$, coincidentally the same temperature dependence found in passive, flat, opaque reprocessing disks (Adams et al. 1987). Nonetheless, D'Alessio et al. (1999) found that when taking into account various vertical and radial energy transport mechanisms the midplane temperature scales as $T(r) \propto r^{-1/2}$.

4.2.2 Monte Carlo Method

We use the Monte Carlo multiple scattering, absorption and polarisation code described by Whitney & Hartmann (1992), suitable for modelling images of dusty protoplanetary disks around young stellar objects in the near-IR (where most of the emitted radiation comes from the central star and then scatters in the disk). Individual unpolarised photons emitted in a random direction are followed in their scattering path throughout the disk. The Monte Carlo treatment calls a random number generator to compute the cumulative probability for scattering and absorption, which allows one to evaluate the optical depth and trajectory of the photon. Then a second call to a random number generator defines whether the photon is scattered or absorbed, depending on the dust properties. When scattered, the intensity and polarisation are computed according to the phase-function of the dust. Photons are tracked until they are finally emitted or absorbed.

The models are run at three different wavelengths corresponding to the J-, H- and Ks-bands. Total intensity and polarised light images are created by binning the emit-

ted photons by their position and direction with respect to the projected line of sight. In this case we have selected a binning factor that produces images with pixel sizes of 0.12 arcseconds, similar to the sampling of our UKIRT observations. The model images are convolved with a Gaussian profile with a FWHM that simulates the atmospheric seeing at the time of the observations (0.82 arcseconds at J, and 0.55 arcseconds at H and K).

Stokes Q and U images are summed to create the polarised intensity (I) and percentage polarisation images (P), following Equations 3.1 and 3.2. Finally, azimuthally-averaged PI radial profiles are produced in a similar way as the observations. In the case of TW Hya, where the disk is seen pole-on, azimuthal averaging over the disk's symmetry axis allows one to increase the signal to noise of the model computations given the 10^6 photons used.

4.2.3 Dust properties

The dust consists of homogeneous spheres of either amorphous carbon or revised astronomical silicate whose characteristics have been selected in order to reproduce both the SED and the wavelength-dependent opacity observed toward HH 30 (which has been interpreted as indicative of grain growth from ISM grains; Cotera et al. 2001; Wood et al. 2002). The size-distribution of the dust grains is described by a power-law with an exponential cutoff, as introduced by Kim et al. (1994):

$$n(a) = a^{-p} \exp\left(-a/a_c\right)^q, \quad for\ a_{min} < a < a_{max}. \tag{4.6}$$

The parameters a_c, p and q control the distribution. The values adopted in our models are shown in Table 4.1. The exponential term provides a smooth transition between two different regimes near $a = a_c$, which have been found to reproduce the observations better (Kim et al. 1994). Given the parameters adopted, the size-distribution contains micron and sub-micron sized particles and larger grains of up to 1 mm in size. The abundances of C in relation to Si are selected in order to match Solar abundances and assuming a gas to dust ratio of 100:1. The scattering phase functions used by the code were calculated using Mie series solutions for spherical particles and optics algorithms (Wood et al. 2002), and are read into the Monte Carlo program in order to calculate the scattering direction.

Table 4.1: Properties of the dust model

Dust model	Component	p	q	a_{min} (μm)	a_c (μm)	a_{max} (μm)
Disk midplane	Amorphous Carbon	3.0	0.6	0.005	50	1000
	Silicates	3.0	0.6	0.005	50	1000

Parameter values that describe the grain-size distribution of the dust adopted in the disk models, taken from Wood et al. (2002).

4.3 Best-fit models

In order to estimate the best-fit geometrical model for TW Hya's disk, we adopt the density structure of a flared-disk with a Gaussian scale-height as described in Section 4.2.1, Equation 4.4. We then search for the model (the combination of parameter values) that produces the best-fit to the J-, H- and Ks-band azimuthally averaged polarized intensity profiles presented in Chapter 3, Figure ??. Given the sensitivity and resolution limits of our observations, we chose to fit the PI radial profiles between 0.7 and 1.4 arcseconds from the star, where the profile slopes are consistent with other observations (Weinberger et al. 2002; Apai et al. 2004; Hines & Schneider 2006).

Each model is defined by a combination of parameters. These are the disk's total mass, inner/outer radius, flaring and density exponents (β and α), and scale height at the stellar radius h_o, which define the density distribution of the disk $\rho(r, z)$. The stellar parameters adopted for all the models are the same as listed in Calvet et al. (2002), which are $M_\star = 0.6 M_\odot$, $R_\star = 0.6 R_\odot$ and $T = 4000$ K for the stellar mass, radius and temperature respectively. A disk inner radius of least 4 AU is required to fit TW Hya's lack of excess emission below 12 μm (Calvet et al. 2002), and therefore is the value we fix in our models. There are no observational constraints on the disk's height at $R_\star$, h_0, for which we have used values listed in the literature. h_0 was fixed to the standard value of 0.025 used by Kenyon & Hartmann (1987) and Whitney & Hartmann (1992). The inclination angle of the disk has been constrained by Roberge et al. (2005) spectroscopically and by Dent et al. (2005) via CO observations to be $\sim 9^o$, and is the value we use in our models.

The disk's total mass has been constrained by SED fitting (Calvet et al. 2002; Natta et al. 2004; Wilner et al. 2005), indicating that most of the disk's dust-mass is locked into large grains (of sizes of up to a few cm). These are needed to fit the the sub-mm, mm

Table 4.2: Minuit best-fit model search

Parameter	r_0 (AU)	h_0 (R_*)	Mass ($M_\odot$)	Radius (AU)	α	β	Combined χ^2
Search 1	0.029	0.025	0.02	80-150	β+3/4	0.0-1.4	
Best-fit model	0.029	0.025	0.02	101^{+6}_{-14}	1.845	1.095±0.001	9.79
Search 2	0.029	0.025	0.02	80-150	β+1/2	0.0-1.4	
Best-fit model	0.029	0.025	0.02	91^{+4}_{-5}	1.596	1.096±0.001	5.38

Range of parameter values used during the best-fit Minuit minimisation search, for both the prescription of Lynden-Bell & Pringle (1974) and for the prescription of D'Alessio et al. (1999) (Search 1 and 2 respectively), together with their corresponding best-fit parameters. Errors on the parameters correspond to the region in which 68% of the points produce a chi-square value equal to $\chi^2_{\rm min} + 1$, and are calculated by the MINOS task in MINUIT.

and cm part of the spectrum but would not be detected in our near-IR images. Krist et al. (2000) showed indeed that scattered light models poorly constrain the total mass of TW Hya's disk, with changes of a factor of 2 in the disk's mass only affecting minimally the quality of the fit. As a consequence, in our models the disk's total mass was fixed to $M_{\rm disk} = 0.02\,M_\odot$, consistent with previous SED modelling by Calvet et al. (2002) who used $M_{\rm disk} = 0.03\,M_\odot$ for a slightly larger disk ($R_{\rm disk}$ = 140 AU), with a distribution of dust-grains with sizes up to 1 mm. Dust and gas are assumed to be in interstellar proportions, with a dust to gas ratio of 0.01. Therefore our disk models with 0.02 solar masses assume a dust mass in dust grains of $\sim 2 \times 10^{-4}\,M_\odot$, which causes the disk to be very optically thick radially at h= 0.

I searched for a best-fit model by looking for the combination of parameters that minimised the chi-square difference between the model PI profiles and the data (restricted to radii between $0.7 < r < 1.4$ arcseconds from TW Hya). The best-fit parameter search is confined to the range of parameter values listed in Table 4.2, chosen to be consistent with theoretical models and observations. I investigated the best-fit models for two different physical descriptions from the literature. In one case the value of the density exponent α is constrained by the value of β, from physical models of viscous accretion disk by Lynden-Bell & Pringle (1974) ($\alpha = \beta + 3/4$), while in the second search $\alpha = \beta + 1/2$, as described by the models of D'Alessio et al. (1999).

For each model, the chi-squared χ^2 difference between the data and the model at each wavelength is computed, defined as:

$$\chi^2_{\rm a} = \sum \frac{(y_i - y_{mod})^2}{\sigma_i^2}. \tag{4.7}$$

The above χ^2 corresponds to the *weighted least-squares*, in which y_i and y_{mod} are the data and model PI profiles, and σ_i represents the one-standard deviation errors of the observations. This method ensures that low-quality data points are down-weighted when computing the χ^2. Embedded in a PDL programme, a Perl-adapted version of MINUIT constructs a variable-metric space-parameter grid of the chi-squares for different models, and searches for the model that minimises the sum of the JHK chi-squares $\chi^2_C = \chi^2_{\rm J} + \chi^2_{\rm H} + \chi^2_{\rm K}$, called the 'combined chi-square' hereafter). Up to a thousand models were required before converging toward a model that minimises the chi-squared difference. Table 4.2 lists the best-fit model and its corresponding parameters, as found by the chi-square minimisation routine. Figure 4.3 shows the Polarized Intensity radial profiles in the J-, H- and K-band respectively.

We find that for both prescriptions studied, the best-fit models converged to practically the same value of the flaring exponent (within the errors), $\beta = 1.095 \pm 0.001$ for the prescription of Lynden-Bell & Pringle (1974) and $\beta = 1.096 \pm 0.001$ for the model of D'Alessio et al. (1999). The D'Alessio et al. (1999) model gives a lower value of the χ^2_C, about a factor of 2 better than the best-fit model obtained using the viscous accretion disk surface density. In addition, the best-fit model for the prescription of D'Alessio et al. (1999) has a smaller outer radius than the best-fit model for the prescription of Lynden-Bell & Pringle (1974), however both values agree within the uncertainties.

Since MINUIT does not produce a fully sampled parameter-space grid, it is not possible to plot the χ^2 contours in the β versus R_{outer} graph in order to show the confidence levels of the obtained fits. The robustness of each solution was tested by performing best-fit searches with different starting conditions and limits for the parameter values. For each prescription, the MINUIT search converged to the same solutions.

The goodness of the best-fit solutions can be estimated by comparing the obtained values for the minimum χ^2 to what is expected from the predicted χ^2 probability distribution given ν degrees of freedom, $P(\chi^2, \nu)$. This is usually done using the *reduced chi-square*, χ^2_ν. For a given ν degrees of freedom (ν=Number of data-points - Number of variable parameters), the reduced chi-square is defined as

$$\chi^2_\nu = \frac{\chi^2}{\nu} N_{corr}, \tag{4.8}$$

where N_{corr} is the number of correlated data-points. In our case we have 18 data point and 5 variable parameters (as α and β are tied together by the respective physical prescription). Thus we have ν=18-5=13 degrees of freedom. The number of correlated data-points can be estimated by the number of azimuthally binned points falling within one Point Spread Function (PSF), i.e:

$$N_{corr} = \frac{PSF}{\Delta bin} = 0.5/0.12 = 4.16. \tag{4.9}$$

We find that the reduced χ^2 for the best-fit models of Lynden-Bell & Pringle (1974) and D'Alessio et al. (1999) are 3.1 and 1.7 respectively. In cases where the data is well described by the model, χ^2_ν is close to 1. Models in which χ^2_ν deviates significantly from unity are either not good in describing the data-set or have underestimated uncertainties. The χ^2_ν obtained using the prescription of D'Alessio et al. (1999) is closer to 1 and therefore represents a better description of the data than the best-fit model found for the prescription of Lynden-Bell & Pringle (1974).

These working models may not be unique, nevertheless they provide a reference point for studying the behaviour of the models when varying one or more parameters. The uncertainties listed in Table 4.2 correspond to the errors estimated by the MINOS task in MINUIT. MINOS calculates the error on a parameter by evaluating χ^2_C (not χ^2_ν) out from its minimum, $\chi^2_{\rm min}$ and find where it reaches $\chi^2 = \chi^2_{\rm min} + 1$. This defines the confidence region, or 68% probability region, for that parameter (e.g. Bevington & Robinson 2003). This technique allows MINOS to produce asymmetric error estimates, as opposed to errors estimated using a parabolic approximation of the function near the minima. As follows, we now present the modelling results when systematically varying the different parameters near $\chi^2_{\rm min}$, and their effect on the observable results.

4.3.1 Models with different outer radii

Models with different outer radii are shown in Figure 4.4. The outer radius plotted in each model is 91, 101 and 111 AU (red, green and blue respectively), for the prescriptions of D'Alessio et al. (1999) and Lynden-Bell & Pringle (1974) (upper and lower panels).

Table 4.3: Models with varying radius

Parameter	Prescription	Mass $M_\odot$	Radius (AU)	β	χ^2_C
Model 1	D'Alessio[1]	0.02	81	1.095	21.85
Model 2	D'Alessio	0.02	91	1.095	5.65
Model 3	D'Alessio	0.02	101	1.095	14.52
Model 4	D'Alessio	0.02	111	1.095	25.19
Model 5	D'Alessio	0.02	121	1.095	35.3
Model 6	D'Alessio	0.02	131	1.095	38.86
Model 7	L-BP[2]	0.02	81	1.095	42.99
Model 8	L-BP	0.02	91	1.095	9.96
Model 9	L-BP	0.02	101	1.095	9.79
Model 10	L-BP	0.02	111	1.095	13.28
Model 11	L-BP	0.02	121	1.095	15.53
Model 12	L-BP	0.02	131	1.095	17.85

χ^2_C values for models with different outer radius.

[1]D'Alessio: D'Alessio et al. (1999) model prescription.

[2]L-BP: Lynden-Bell & Pringle (1974) model prescription.

The effect of increasing the outer radius does not seem to affect significantly the polarised intensity profiles within 1.2 arcseconds. Beyond that point the different size of each model becomes evident. We find a strong degeneracy between the 91 AU and the 101 AU models in both prescriptions. However, we note that while the J and Ks band profiles can be relatively well fit by any of the 3 chosen radii, the H-band profile is more sensitive to variations of the outer radius, which can be used discriminate between the different models.

4.3.2 Models with different mass

We first investigate the behaviour of the best-fit model when varying the total mass of the disk for the disk prescriptions of Lynden-Bell & Pringle (1974) and D'Alessio et al. (1999). For each prescription, the mass is chosen to be 0.01, 0.02 and 0.03 $M_\odot$ respectively. Figure 4.6 shows the effect of varying the total disk mass of the working model, for the prescription of Lynden-Bell & Pringle (1974) in the top-panel, and of D'Alessio et al. (1999) in the bottom-panel. In the case of the Lynden-Bell & Pringle (1974) prescription, the green line correspond to the best-fit model found by the minimisation routine (plotted in Figure 4.3).

We find that in both cases the PI profiles and the corresponding chi-square values do not show strong variations when the total mass of the disk is varied. This confirms the fact that the total mass of the disk is not a parameter we can constrain with our near-IR scattered light models. Even for the 0.01 $M_\odot$ model, the disk is already very optically thick

Table 4.4: Models with varying mass

Parameter	Prescription	Mass $M_\odot$	Radius (AU)	β	χ^2_C
Model 13	D'Alessio[1]	0.01	91	1.095	31.78
Model 14	D'Alessio	0.02	91	1.095	5.65
Model 15	D'Alessio	0.03	91	1.095	14.52
Model 16	L-BP[2]	0.01	101	1.095	23.23
Model 17	L-BP	0.02	101	1.095	9.79
Model 18	L-BP	0.03	101	1.095	15.78

Models with different disk masses.

[1]D'Alessio: D'Alessio et al. (1999) model prescription.

[2]L-BP: Lynden-Bell & Pringle (1974) model prescription.

($\tau > 10^5$ in the midplane), so that an increase in the disk's total mass does not affect very much the scattering surface of the disk. Figure 4.5 shows the mass density distribution of the best-fit model using the prescription for mass density of D'Alessio et al. (1999).

4.3.3 Models with different flaring exponents β

The determination of the flaring exponent β achieved by MINUIT claims a robust error of 0.003. We demonstrate the validity of this accuracy by exploring systematically the behaviour of the combined chi-squared in the neighbourhood of the minima. Table 4.5 shows modelling results for different values of β around the best-fit value of $\beta = 1.095$, varying this value with steps of 0.001. The table shows clearly how the combined chi-squared reaches its minimum at $\beta = 1.095 \pm 0.001$ for both the prescription of Lynden-Bell & Pringle (1974) the D'Alessio et al. (1999) prescription.

In addition, we have also explored models with other values of the flaring exponent, taken from the literature, which have been used to successfully model disk around T Tauri stars (Kenyon & Hartmann (1987), D'Alessio et al. (1999) and Chiang & Goldreich (1997) corresponding to 9/8, 5/4 and 58/45, respectively). All three models have higher flaring coefficients than our best-fit models, and fail to produce an accurate fit to the data. The PI profiles obtained using the different flaring exponents are shown in Figure 4.7. Using the α and β values from D'Alessio et al. (1999) does, however, produce a reasonably good fit to the data, although of poorer quality than our best-fit models.

Table 4.5: Models with different flaring exponent

Model ID	Prescription	Mass $M_\odot$	Radius (AU)	β	χ^2_C
Model 25	D'Alessio[1]	0.02	91	1.090	13.77
Model 26	D'Alessio	0.02	91	1.091	10.65
Model 27	D'Alessio	0.02	91	1.092	9.5
Model 28	D'Alessio	0.02	91	1.093	10.42
Model 29	D'Alessio	0.02	91	1.094	8.1
Model 30	D'Alessio	0.02	91	1.095	5.65
Model 31	D'Alessio	0.02	91	1.096	5.38
Model 32	D'Alessio	0.02	91	1.097	8.65
Model 33	D'Alessio	0.02	91	1.098	12.74
Model 34	D'Alessio	0.02	91	1.099	14.81
Model 35	L-BP[2]	0.02	101	1.090	28.3
Model 36	L-BP	0.02	101	1.091	19.69
Model 37	L-BP	0.02	101	1.092	17.02
Model 38	L-BP	0.02	101	1.093	15.83
Model 39	L-BP	0.02	101	1.094	10.49
Model 40	L-BP	0.02	101	1.095	9.79
Model 41	L-BP	0.02	101	1.096	11.16
Model 42	L-BP	0.02	101	1.097	14.69
Model 43	L-BP	0.02	101	1.098	28.45
Model 44	L-BP	0.02	101	1.099	33.33

Behaviour of χ^2_C when systematically the flaring exponent value in the neighbourhood of $\chi^2_{\rm min}$.

[1]D'Alessio: D'Alessio et al. (1999) model prescription.

[2]L-BP: Lynden-Bell & Pringle (1974) model prescription.

Table 4.6: Models with different flaring exponent

Model ID	Prescription	Mass $M_\odot$	Radius (AU)	β	χ^2_C
Model 19	D'Alessio[1]	0.02	91	1.125	1005.17
Model 20	D'Alessio	0.02	91	1.25	28.3
Model 21	D'lessio	0.02	91	1.288	173.48
Model 22	L-BP[2]	0.02	101	1.125	1078.18
Model 23	L-BP	0.02	101	1.25	41.23
Model 24	L-BP	0.02	101	1.288	119.28

Models with different flaring exponent listed in the literature. $\beta = 1.125$, 1.25 and 1.288 correspond to the values used by Kenyon & Hartmann (1987), D'Alessio et al. (1999) and Chiang & Goldreich (1997), respectively.

[1]D'Alessio: D'Alessio et al. (1999) model prescription.

[2]L-BP: Lynden-Bell & Pringle (1974) model prescription.

4.4 Discussion

We have carried out Monte Carlo scattering modelling of the polarized disk around TW Hya. We have constructed models using two different physical structures from the literature, and explored the best-fit geometrical models for each prescription. Our results show that this technique can be fruitful in constraining the geometry of the disk, basically its radial extension and vertical structure can be self-consistently determined. We find that the best-fit value for the flaring coefficient is independent of the prescription used (i.e. poorly dependent on the radial density distribution coefficient used). This allows us to provide constraints on the flaring coefficient that are a factor of 10 improvement with respect to previous modelling (Krist et al. 2000). We note that the prescription of D'Alessio et al. (1999) gives a better fit to the data that of Lynden-Bell & Pringle (1974), favouring the irradiated disk models of D'Alessio et al. (1999) as a better physical description of TW Hya's disk.

The value of the flaring coefficient we derive for the region between $0.7 < r < 1.4$ arcseconds indicates that the disk is flared, not geometrically flat. Krist et al. (2000) fitted the HST optical profiles within their 'zone 2' ($0.9 < r < 1.4$ arcseconds) with density and flaring coefficients of $\alpha = 1.5$ and $\beta = 1.0 \pm 0.05$, consistent within 2σ with our derived value. It is interesting to note that even though the models of Krist et al. (2000), allowed both α and β to vary freely, their derived best-fit values are also consistent with the $\beta - \alpha = -1/2$ prescription from the disk models of D'Alessio et al. (1999).

The disk's outer radius extends to at least 140 AU, therefore our modelling of the region between 40 and 80 AU is intended to provide a description of the disk's geometrical and density structure only within the fitted radius. It is interesting to note that the prescription of D'Alessio et al. (1999) requires a disk with a slightly smaller outer radius than that of Lynden-Bell & Pringle (1974), although the estimated errors for the latter are large enough to allow for consistency between the two values.

As pointed out by several authors, the disk around TW Hya seems to have different surface brightness radial profiles at different radii, deviating from a single power-law beyond 1.4 arcseconds (Krist et al. 2000; Weinberger et al. 2002; Apai et al. 2004). Our ob-

servations and modelling have describe only one region of the disk. Polarimetric modelling of the PI images of the complete disk out to larger radii would be necessary to understand the full, complex structure of TW Hya's disk. Flaring is by definition more important at large radii, as described by the disk models of Whitney & Hartmann (1992). In the case of the young 'debris disk' around β Pictoris, in which the disk is seen edge-on and thus the scale-height can be determined directly, at small radii (< 58 AU) the dust disk's scale height is similar that of the gas disk (Brandeker et al. 2004). However, beyond 100 AU the gas disk scale height is much larger than the dust-disk scale height, showing that gas and dust are not well-mixed throughout the disk. Dent et al. (2005) showed that modelling of the J=3-2 ^{12}CO line can provide information on the degree of flaring of TW Hya's gas disk. Therefore, modelling of higher-sensitivity, higher-resolution PI observations of the disk around TW Hya in conjunction with modelling of TW Hya's gas disk could allow to determine whether dust grains are well-mixed with the gas up to several scale heights, or whether they have settled toward the disk's midplane, as expected from theories of planet formation (Weidenschilling 1984).

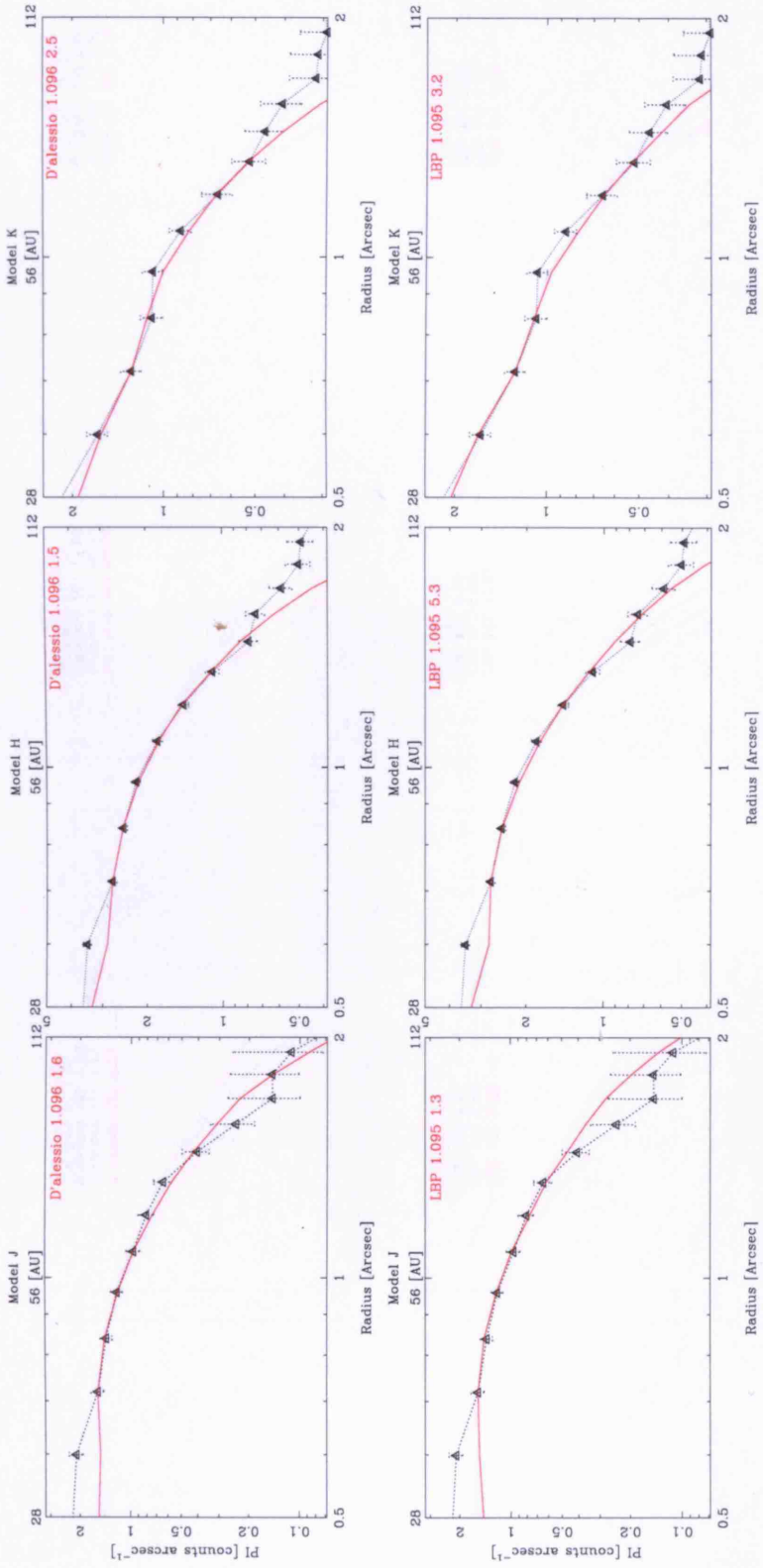

Figure 4.3: Best-fit models found with the prescription of D'Alessio et al. (1999) and with the prescription by Lynden-Bell & Pringle (1974) for the disk density distribution. The J-, H- and Ks-band PI profiles from Hales et al. (2006), are plotted from left to right (filled triangles and dotted-lines with error bars), together with the azimuthally averaged best-model PI profiles at each wavelength (red solid lines). The legend at the top right-corner of each panel indicates the prescription used, the value of β adopted and the corresponding χ^2 value for that wavelength.

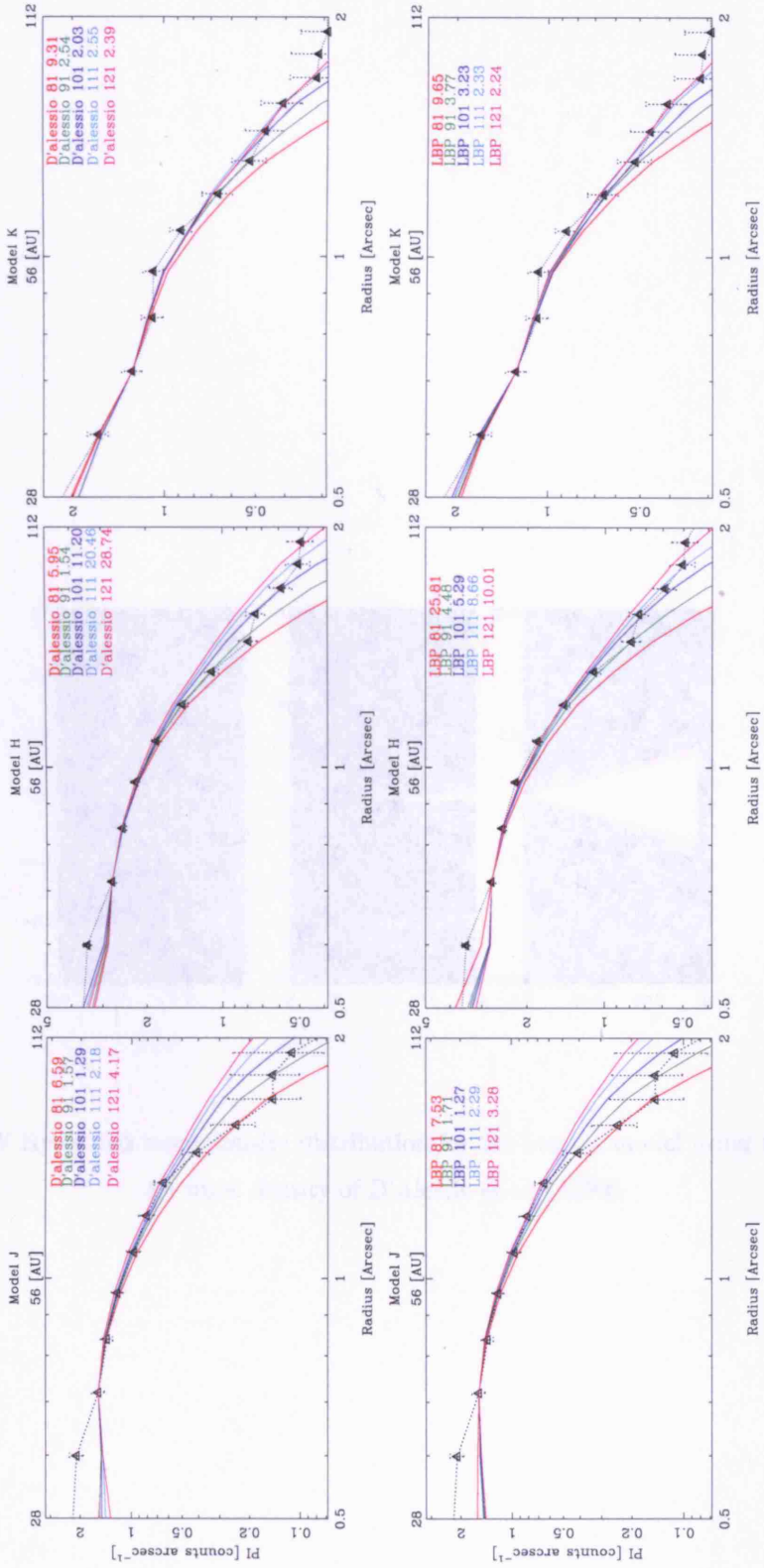

Figure 4.4: JHK PI profiles for models (solid lines) with different outer radii for both physical prescriptions for the disk density distribution studied, leaving all other variable parameters fixed to those of the best-fit model. The legend at the top right-corner of each panel indicates the prescription used in each model, the disk radius adopted and the corresponding χ^2 value at that wavelength. As in Figure 4.3, the PI observational data of Hales et al. (2006) are also plotted (dotted lines with error-bars).

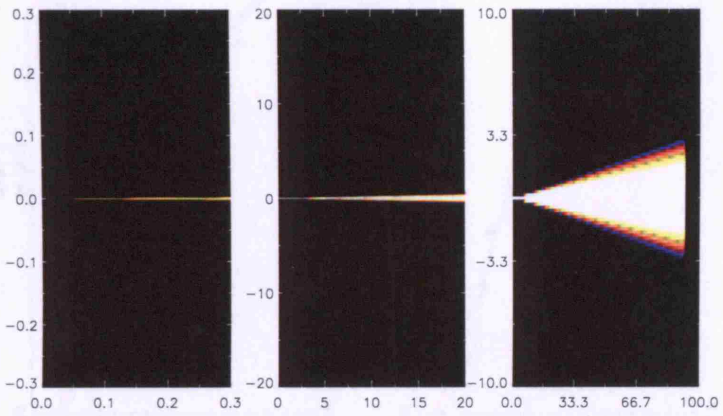

Figure 4.5: TW Hya's disk mass density distribution for the best-fit model using the prescription for mass density of D'Alessio et al. (1999)

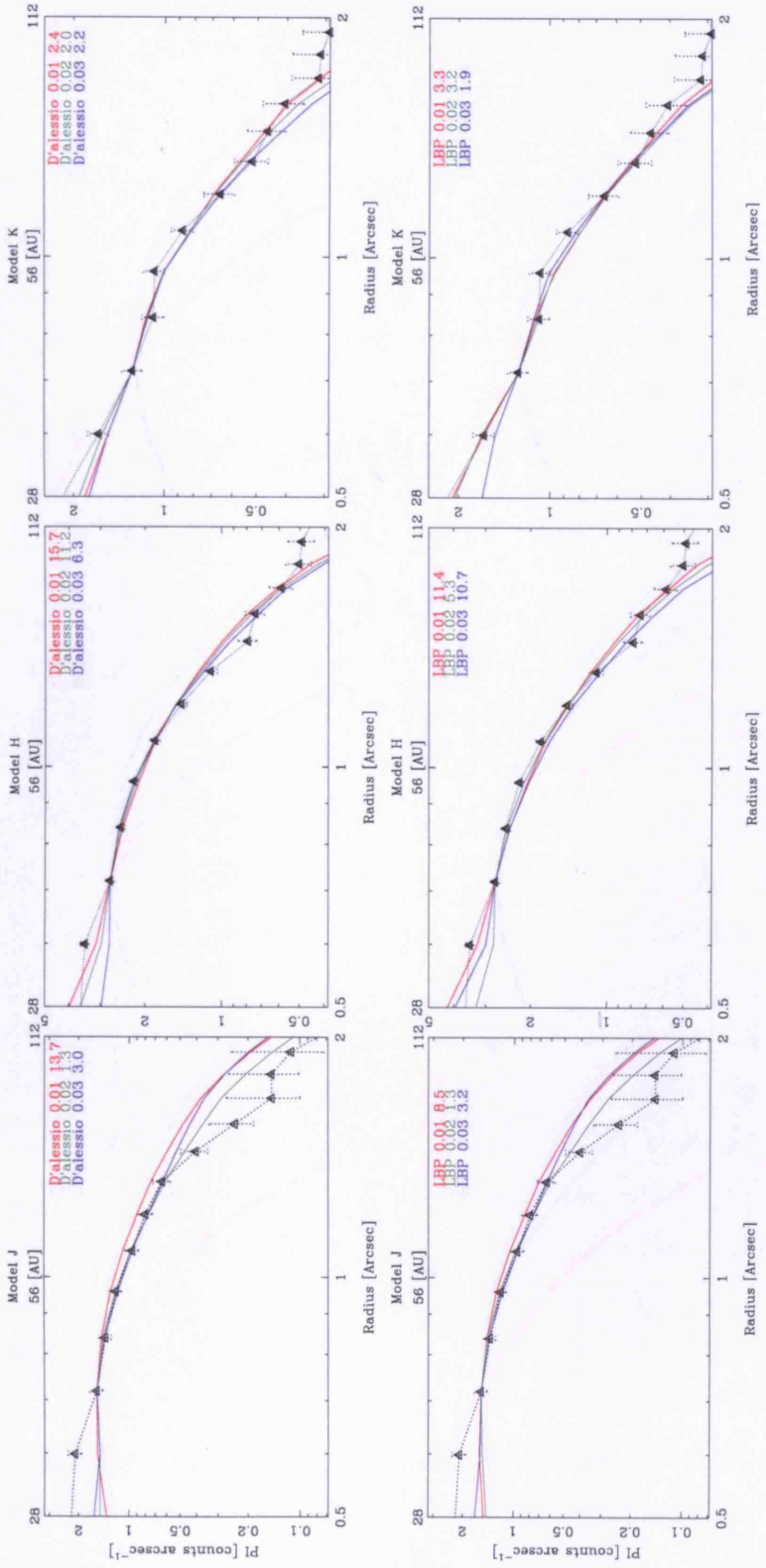

Figure 4.6: JHK PI profiles for models with different disk masses for the mass density prescriptions of D'Alessio et al. (1999) and Lynden-Bell & Pringle (1974). The legend at the top right-corner of each panel shows the prescription used, the disk mass adopted and the corresponding χ^2 value at that wavelength.

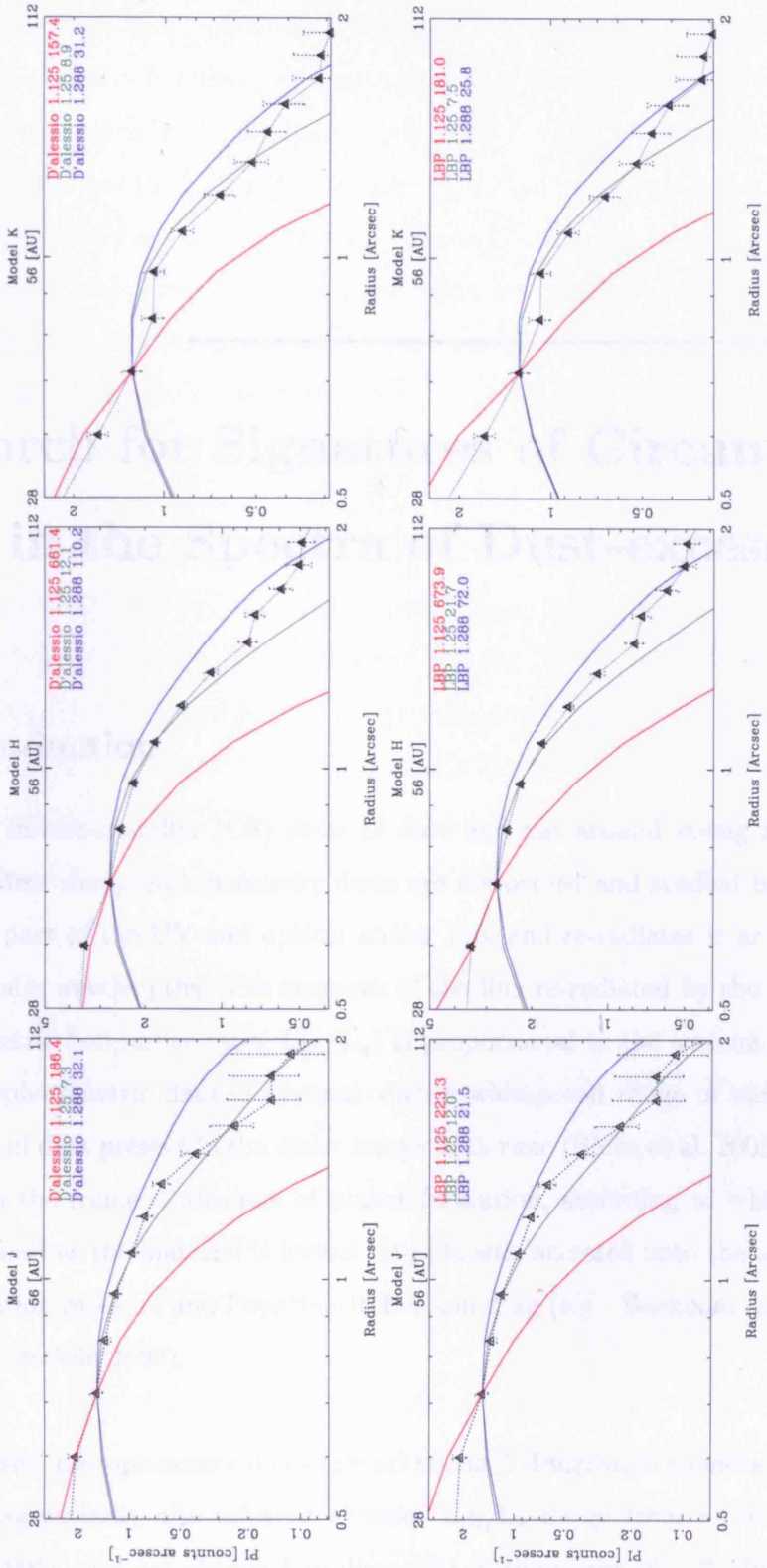

Figure 4.7: PI profiles for models with different flaring exponents. Red, green and blue correspond to the values used by Kenyon & Hartmann (1987), D'Alessio et al. (1999) and Chiang & Goldreich (1997) respectively. The legend at the top right-corner of each panel shows the prescription for mass density used, the value of the flaring exponent adopted and the corresponding χ^2 value at that wavelength.

CHAPTER 5

A Search for Signatures of Circumstellar Gas in the Spectra of Dust-excess Stars

5.1 Introduction

Planets form in circumstellar (CS) disks of dust and gas around young main sequence (MS) stars. Most dusty protoplanetary disks are discovered and studied because the CS dust absorbs part of the UV and optical stellar flux and re-radiates it at infrared (IR), sub-mm and mm wavelengths. The strength of the flux re-radiated by the dust (the disk to star bolometric luminosity ratio, $L_{IR}/L_{\star}$) is proportional to the amount of dust in the disk. Spectrophotometric data of systems with a widespread range of stellar ages show that the mass of dust present in the disks decays with time (Rieke et al. 2005). This is well understood in the frame of theories of planet formation, according to which CS matter should be cleared as the material is locked into planets, accreted onto the star, or cleared away by radiation pressure and Poynting-Robertson drag (e.g. Backman & Paresce 1993; Zuckerman & Becklin 1993).

From massive protoplanetary disks around young T Tauri stars to more evolved Vega-like debris disk systems, the infrared excesses $L_{IR}/L_{\star}$ decay from $\sim 10^{-1}$ to $\sim 10^{-6}$ (Zuckerman 2001), and are observed to disappear in timescales of 150 Myr (Rieke et al. 2005). As predicted by theoretical models of planetary formation, the timescales for the formation of massive gaseous giant planets are of the order of 3 to 10 Myr (Zuckerman et al. 1995), similar to the age of most T Tauri systems. Large amounts of molecular gas emission

are indeed detected around T Tauri stars (Dutrey et al. 1996; Dent & Clarke 2005), which in many systems can be associated with a rotating disk. However after a few million years the disks are expected to evolve into gas-depleted debris-disk systems. This corresponds to one of the defining criteria for a debris-disk, which has to: a) have lower $L_{IR}/L_{\star}$ values than T Tauri and HAeBe stars, b) the dust present in the disk must be not primordial but replenished by collisions, and c) the disk must be depleted of gas (similarly to our Solar System). However, the detection of vast amounts of CS gas in systems originally classified as debris-disk systems (in terms of their IR-excesses) has pointed out that it is still not well-known when the transition from gas-rich to gas-depleted disks occurs (Dent et al. 2005).

Currently, most efforts towards the understanding of planetary formation are aimed at constraining the timescales over which most CS gas dissipates, as this is intrinsically associated with the formation of gaseous giant planets (Meyer et al. 2007). Work using *Spitzer* to search for mid-IR spectroscopic signatures of warm gas capable of forming giant planets (located within 1 to 40 AU) shows that it dissipates on timescales shorter than 10 Myr (Pascucci et al. 2005). In a recent sub-mm survey for CO emission over a sample of MS stars with a large variety of $L_{IR}/L_{\star}$ values (classified as either HAeBe stars or more evolved Vega-like stars), Dent et al. (2005) found that CO detections are common in objects with $L_{IR}/L_{\star}$ >0.01, but rare in objects with smaller infrared excesses (< 10% of these objects). They noted that two or three stars having $L_{IR}/L_{\star}$ <0.01 do have significant amounts of CS gas located in stable Keplerian orbits around the star. These gas-rich, dusty MS systems are understood as objects transiting between their Class II and Class III phase. The detection of gas around what are supposed to be true debris-disk systems have presented the problem of explaining why the gas has not been completely blown away by the stars' strong radiative pressures or accreted into planets.

CS gas can also be studied by observing gaseous atomic species via their transitions that occur in the optical regime. Spectroscopic observations can reveal emission line profiles that may be similar to the ones observed around T-Tauris and HAeBe stars. Observations of a sample of Vega-like stars selected mainly from the sample of Walker & Wolstencroft (1988) and having a wide range of $L_{IR}/L_{\star}$ values, showed that most stars with large $L_{IR}/L_{\star}$ values (> 0.01) had single peaked, double-peaked and P-Cygni emission line profiles seen in Hα, Ca II , Na I and lines of other species (Dunkin et al. 1997*b*).

These signatures were understood as evidence of CS material still accreting onto the stars, indicative of their youth, which caused these stars to be reclassified as HAeBe stars instead of Vega-like, in accord with their large IR excesses and their emission-line properties.

Other stars in the sample studied by Dunkin et al. (1997*b*) presented very interesting absorption features that could not be attributed to photospheric absorption. Sharp absorption features centred on the core of photospheric lines were detected. These were attributed to the presence of an absorbing gas cloud moving with the radial velocity of the star. This indicated that the gas was located in the CS environment of the star, possibly in a CS disk. The remaining stars in the sample of Dunkin et al. (1997*b*) showed no indication of gas which suggests that material accretion has ceased and that if a CS disk is present, it is probably devoid of gas. These gas-depleted Vega-like systems are identified as being more evolved than their gas-active counterparts. The results from Dunkin et al. (1997*b*) showed that the majority of stars with $L_{IR}/L_{\star}$ $<8.4\times10^{-3}$ showed no indications of CS gas.

β Pictoris was the first debris-disk system to show the presence of a gas-rich CS disk. The first gaseous components of the β Pictoris disk were identified by Slettebak (1975) even before any dust was detected in the system. Slettebak noticed the presence of narrow Ca II absorption lines located at the center of the photospheric lines, which he pointed out 'are clearly of interstellar or circumstellar origins'. Later, Hobbs et al. (1985) observed similar features both in Ca II and Na I in absorption. The radial velocities of the absorptions were identical to the radial velocity of the star, which suggested that they were produced in the CS environment of the star (the presence of a coincidental IS cloud was very unlikely, specially given the proximity of β Pictoris). In addition, the high ratio of the Ca to Na equivalent widths was used to conclude that the absorptions were of CS nature, as in most interstellar clouds this ratio is of order unity or lower. Subsequent UV observations by Kondo & Bruhweiler (1985) also revealed the presence of strong Fe and Mg absorption components. All these observations showed the presence of very stable absorption components located at the centre of the rotationally broadened photospheric lines (i.e. with a similar radial velocity than of the star), which were indisputedly attributed to a CS gas disk. Furthermore, in addition to the stable component, different epoch observations detected the presence of variable red shifted absorption features around the central component, which could vary in strength and velocity within intervals of few days or even

hours (Beust et al. 1998). More rare blue wing absorption features that are comparable to the strength of the red wing features were also observed (Crawford et al. 1998*a*). A model in which solid kilometer-sized bodies evaporate while falling into the star was invoked in order to explain these temporal absorption features, termed the Falling Evaporating Body scenario (FEB; Vidal-Madjar et al. 1998, for a review).

But it was the presence of the central, stable component of the β Pictoris gas disk that kept challenging interpretations. Seen both in Na I and Ca II, and attributed to an orbiting CS gas disk, the stable component was conflicting with theoretical models in several ways. The force of the radiation pressure on atoms in the β Pictoris system exceeds the force of gravity for most species (by factor 300 in the case of Na I). Therefore most of the gas should be quickly blown away. A dense colliding ring of neutral hydrogen located further than 0.5 AU away from the star was postulated as possible mechanism to drag down the radial flow of material (Lagrange et al. 1998). The problem got worse with the detection of widespread resonantly scattered emission from Na I (Olofsson et al. 2001), and several other metallic species (Brandeker et al. 2004) orbiting in Keplerian motion around the star. The Na stable disk can be explained in terms of most of the Na atoms being in their ionised states: Na II lacks strong transition in the spectral region covered by the stellar flux, and therefore is not sensitive to the radiation pressure (Olofsson et al. 2001). But this is not applicable for most of the metallic species detected by the new VLT observations (Brandeker et al. 2004), as for instance, the radiation pressure on Fe I and Fe II should quickly blow away most of the iron atoms. The long debate on the nature of the β Pictoris disk seems to have reached a temporary consensus thanks to the recent detection of large amounts of carbon, which would act as braking agent and should keep the gas disk in Keplerian rotation (Roberge et al. 2006). This opens up several questions since it indicates that the gas is produced from material more carbon rich than our Solar System.

Several searches for CS gas have been conducted in order to identify systems similar to β Pictoris (e.g. Lagrange-Henri et al. 1990; Dunkin et al. 1997*b*; Holweger et al. 1999). Circumstellar absorption features were successfully detected around a few other Vega-like stars: 51 Oph (HD 158643), HD 256, HD 4211, HD 223884, HD 144432 and HD 35187B (Lagrange-Henri et al. 1990; Dunkin et al. 1997*b*; Dunkin & Crawford 1998). In this work we study the spectra of 16 Vega-like stars selected from the sample of Mannings & Barlow (1998). The purpose of this work is to search for the presence of narrow absorption

features in the stellar spectra, which may be indicative of the presence of a CS gas disk similar to that of β Pictoris. One of the main difficulties of this technique is to rule out the presence of interstellar (IS) absorption features, which may be very similar in profiles and strength to CS lines. This issue has been shown to require careful analysis of the line characteristics (e.g. Crawford et al. 1998*b*), and will be raised again in Section 5.5.

5.2 Target sample

The sample consists of 16 Vega-like stars taken from the catalogue of Mannings & Barlow (1998) having spectral types ranging from B8 to F7 (as listed in the Michigan Spectral Catalog for southern stars; Houk & Smith-Moore 1988). The sample was selected in terms of their infrared excesses, where stars with significantly lower $L_{IR}/L_{\star}$ values than those of Walker & Wolstencroft (1988) that were investigated by Dunkin et al. (1997*b*) were selected. The infrared excess luminosities of the systems L_{IR} were computed by fitting a black-body SED to the observed 25 μm and 60 μm *IRAS* excess fluxes and integrating over the entire spectral range. $L_{\star}$ was computed by integrating a stellar SED normalized to the 12 μm *IRAS* fluxes. A black-body SED set to the stellar effective temperatures was used to represent the stellar SED for each spectral type. Effective temperatures corresponding to each sampled spectral type were obtained from *Astrophysical Quantities* (Allen 1976). The black-body SEDs were fitted to the 25 μm and 60 μm fluxes after subtraction of the normalised stellar SED. Figure 5.1 shows the results from the SED fitting routine, where both the observed SED and the fitted *black-body+star* model are plotted. $L_{IR}/L_{\star}$ values in our sample are found to range between 1.9×10^{-3} and 3.0×10^{-6}. Based on their infrared excess values, these systems are expected to be in a more advanced evolutionary stage than the sample studied by Dunkin et al. (1997*b*). All stars have available *Hipparcos* distances and many of them have had their radial velocities ($V_{\odot}$) estimated by previous studies. Spectral standards of three spectral types were also observed in order to allow for spectral classification. Table 5.1 summarizes the properties of our sample, where we have listed the properties of our observed target sample along with those of the observed spectral standards.

Table 5.1: Properties of the stars selected for UCLES observations.

Star	Other Name	Previous Spectral Type	V	(B-V)	Distance	L_{IR} ($L_\odot$)	$L_{IR}/L_\star$	Age [Myr]	References for Age
HD 53842		F5V	7.46	0.460	$57.3^{+2.0}_{-1.9}$	1.2×10^{-3}	7.8×10^{-5}	-	
HD 61950		B8V	6.89	-0.028	$362.3^{+82.1}_{-56.5}$	1.6×10^{-1}	3.1×10^{-4}	-	
HD 75416	η Cha	B8V	5.46	-0.094	$96.9^{+4.2}_{-3.9}$	3.4×10^{-3}	3.6×10^{-5}	5	1
HD 80950		A0V	5.87	-0.016	$80.8^{+3.5}_{-3.2}$	2.9×10^{-3}	6.2×10^{-5}	80	1
HD 88955	q Vel	A1V/A2V	3.84	0.063	$31.5^{+0.6}_{-0.5}$	3.3×10^{-4}	7.6×10^{-6}	300	1
HD 91375		A1V	4.72	0.042	$79.4^{+3.1}_{-2.9}$	1.6×10^{-3}	1.2×10^{-5}	265	1
HD 99211	γ Crt	A9V	4.08	0.216	$25.7^{+0.6}_{-0.5}$	1.5×10^{-4}	4.6×10^{-6}	600	2
HD 110058		A0V	7.98	0.148	$99.9^{+11.0}_{-9.0}$	1.2×10^{-2}	3.7×10^{-4}	<100	1
HD 117360	S Cha	F5V/F6V	6.48	0.480	$35.1^{+1.5}_{-1.3}$	7.9×10^{-4}	4.8×10^{-5}	-	
HD 123247		B9.5V/B9V	6.43	0.000	$101.1^{+8.3}_{-7.1}$	1.3×10^{-2}	2.8×10^{-4}	-	
HD 166841		B8V/B9V	6.32	-0.030	$213.7^{+36.3}_{-27.1}$	4.6×10^{-2}	2.3×10^{-4}	-	
HD 176638	ζ CrA	B9V/A0V	4.75	-0.027	$56.3^{+2.9}_{-2.6}$	3.2×10^{-3}	5.2×10^{-5}	-	
HD 181327		F5V/F6V	7.04	0.480	$50.6^{+2.2}_{-2.0}$	9.7×10^{-3}	1.9×10^{-3}	12^{+8}_{-4}	3
HD 181869	α Sgr	B8V	3.95	-0.083	$52.1^{+2.8}_{-2.6}$	1.2×10^{-3}	1.7×10^{-5}	110^{3}	1
HD 191089		F5V	7.17	0.480	$53.5^{+2.7}_{-2.5}$	6.0×10^{-3}	9.6×10^{-4}	12^{+8}_{-4}	3
HD 203608	γ Pav	F7V/F6V	4.22	0.494	$9.2^{+0.1}_{-0.0}$	2.5×10^{-5}	3.0×10^{-6}	10 Gyr	4
HR 5558	β Cir	A0V	5.32	0.044	$75.8^{+5.0}_{-4.4}$	-	-	-	
HR 5670		A3V	4.06	0.100	$29.6^{+0.7}_{-0.6}$	-	-	-	
HR 6045	θ Nor	B8V	5.12	-0.104	$90.4^{+6.4}_{-5.6}$	-	-	-	

Vega-like stars observed along with spectral standards used for spectral classification. Spectral types are from Michigan Spectral Catalogue and distances are derived from parallax measures listed in the *Hipparcos* catalogue. B-V colours are taken from the Simbad database. The $L_{IR}/L_\star$ values were derived using the 25 μm and 60 μm *IRAS* excess fluxes. L_{IR} is the bolometric luminosity of the black-body that fits the infrared excesses. References: (1) Rieke et al. (2004), (2) Song et al. (2001), (3) Moór et al. (2006), (4) Bryden et al. (2006).

5.3 Observations and data reduction

Optical Echelle spectroscopy of the 16 Vega-like stars was obtained using the UCL Echelle Spectrogaph (UCLES) at the 3.9 meter Anglo-Australian Telescope (AAT). A log of the observations is given in Table 5.2. The 31.6 g/mm grating was used in conjunction with a new MIT/LL CCD, which allowed a better spectral coverage compared to the previous TEKTRONIX detector. Observations were carried out with two wavelength settings in order to cover the blue region of the spectra between 3834-5440 Å, and between 5550-9900 Å in the red. The red observations were optimized for the study of H_α, He I and the Na I D-lines, whilst the blue exposures covered the Ca II K and H lines as well as several metallic lines in the 4000-5000 Å region. The spectral resolution, estimated from measuring the FWHM of Thorium-Argon arc lines, was 0.115 Å ($\sim$ 8.8 km s^{-1}) at Ca II K (3933.663 Å), corresponding to a resolving power of R=34200. At the location of the Na I D-lines, in the red part of the spectrum (5889.951 Å), the spectral resolution and resolving power were found to be 0.168 Å and R=35200 respectively.

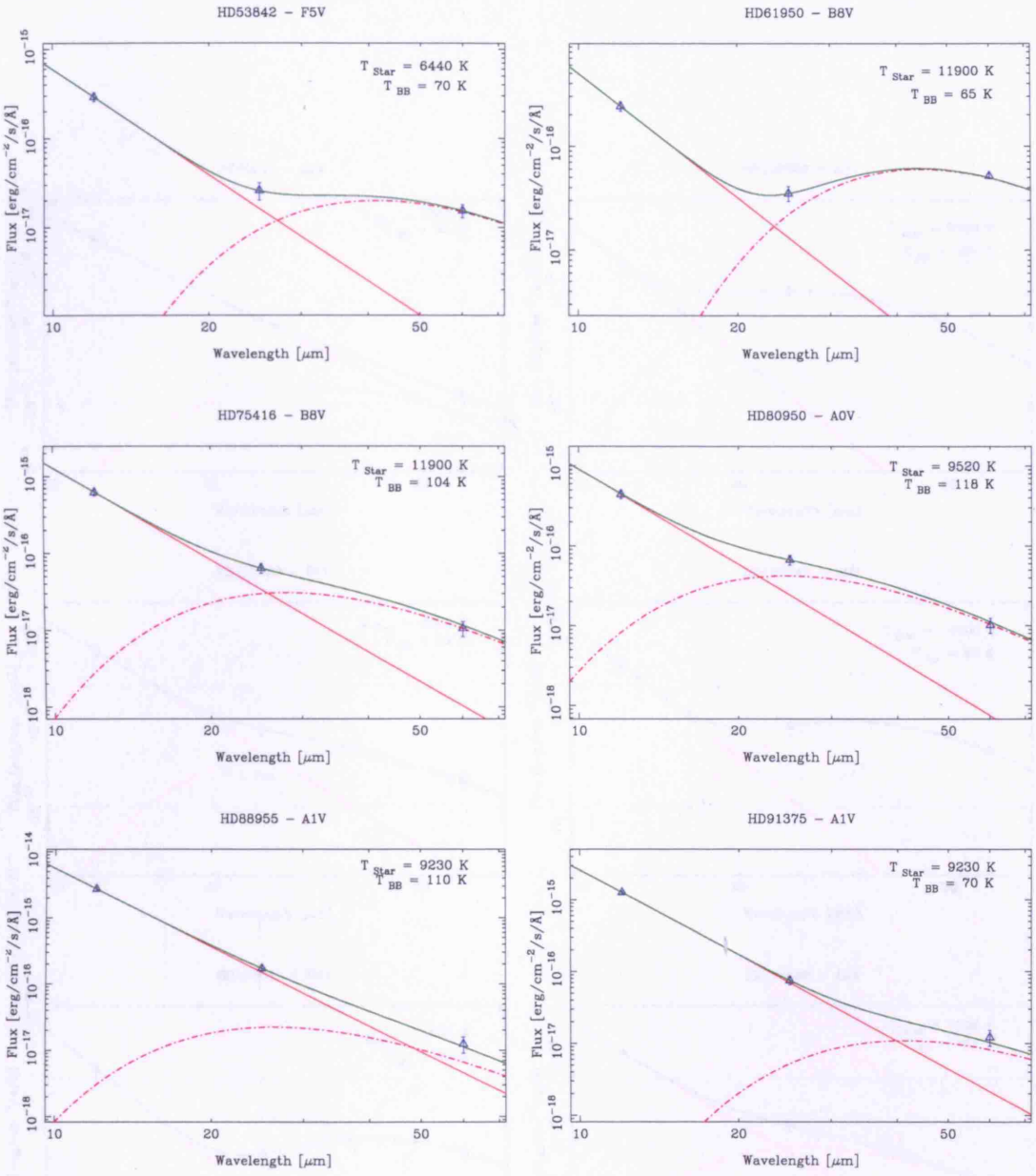

Figure 5.1: Black-body fits to the infrared excesses used in the derivation of $L_{IR}/L_{\star}$ values for stars with different spectral types in our sample. The observed *IRAS* fluxes, as listed in Mannings & Barlow (1998), are plotted in blue with error-bars denoting the 1σ photometric errors. The solid line in red corresponds to the reference photospheric SED normalised to the 12 μm flux. The pink dashed line represents the fitted black-body and the solid green line represents the resulting SED (SED_{star}+SED_{BBody}) that provides a satisfactory fit to the data. The stellar temperatures characteristic of each spectral type and the temperature of the fitted black-body are indicated in each plot.

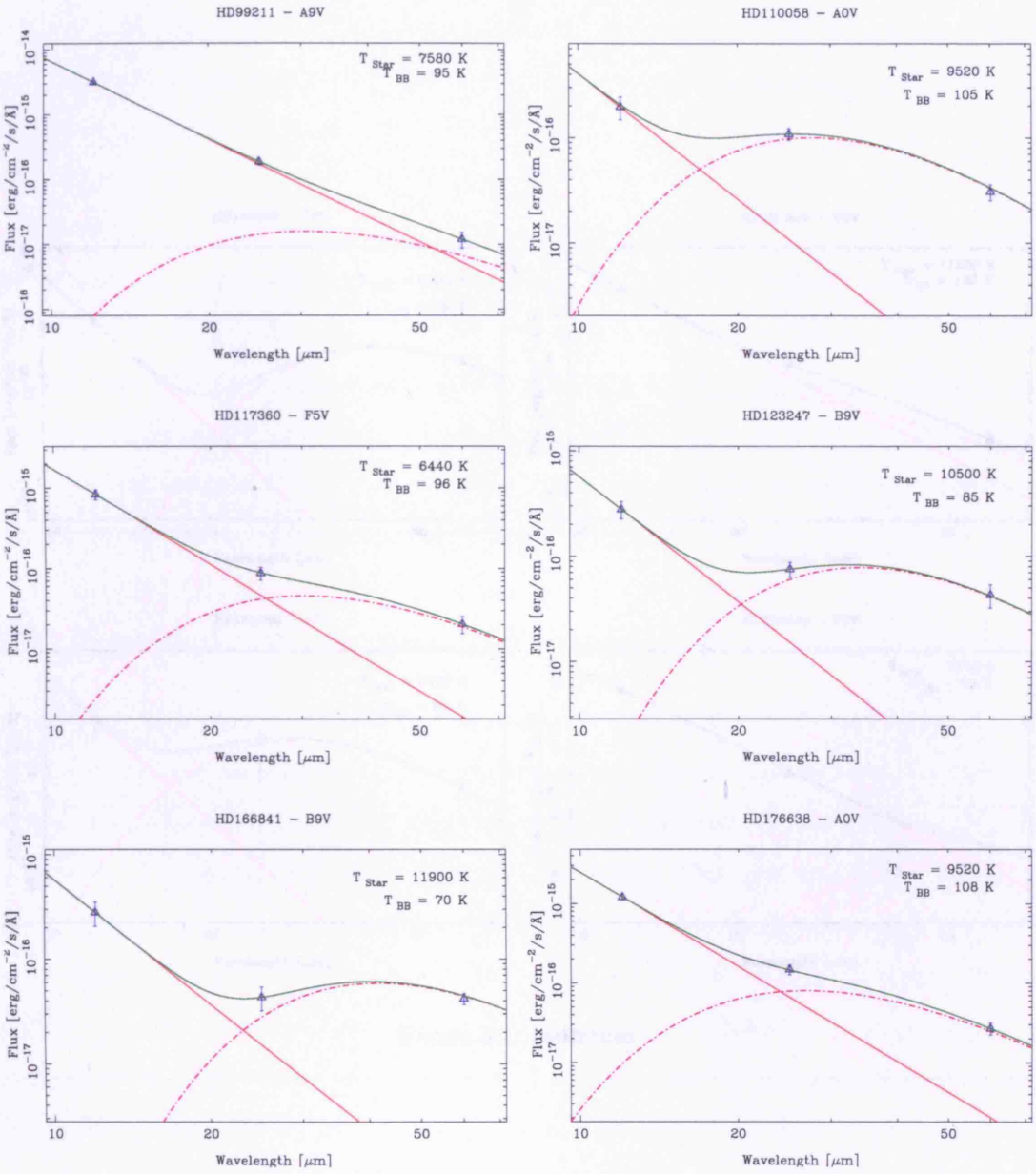

Figure 5.1: *continued*

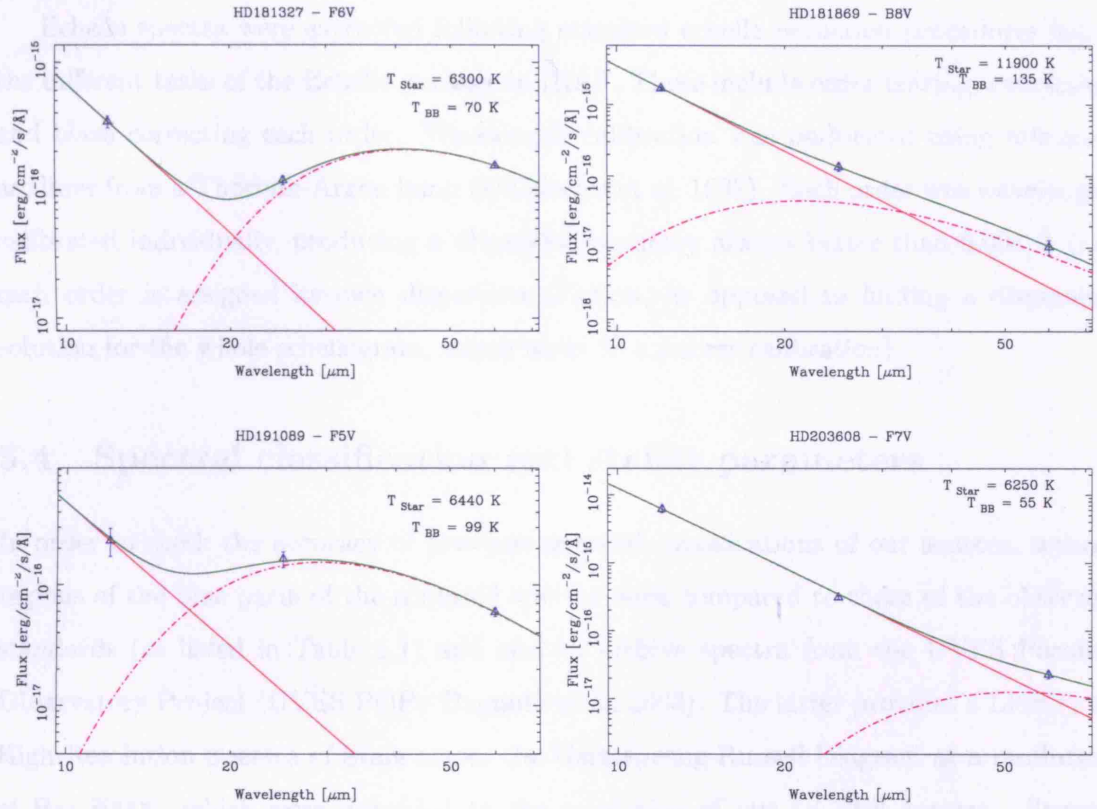

Figure 5.1: *continued*

Overscan correction, dark subtraction and flat-fielding were performed using the Image Reduction and Analysis Facility (IRAF [1]) package developed by the National Optical Astronomy Observatory (NOAO). When more than one exposure for the same star was available, the different frames were coadded and the average taken. At this stage the 'crreject' task was used in order to remove cosmic rays. When only one exposure of the object at each wavelength setting was available, no cosmic ray removal was applied as it was found to work inaccurately.

Echelle spectra were extracted following standard echelle reduction procedures using the different tasks of the Echelle package in IRAF. These include order tracing, extracting and blaze correcting each order. Wavelength calibration was performed using reference arc lines from a Thorium-Argon lamp (D'Odorico et al. 1987). Each order was wavelength calibrated individually, producing a dispersion accuracy always better than 0.004 Å (i.e. each order is assigned its own dispersion solution, as opposed to finding a dispersion solution for the whole echellogram, which leads to a poorer calibration).

5.4 Spectral classification and stellar parameters

In order to check the accuracy of previous spectral classifications of our sources, several regions of the blue parts of the acquired spectra were compared to those of the observed standards (as listed in Table 5.1) and also to archive spectra from the UVES Paranal Observatory Project (UVES POP; Bagnulo et al. 2003). The latter provides a Library of High-Resolution Spectra of Stars across the Hertzsprung-Russell Diagram at a resolution of R$\sim$ 80000, which were degraded to the resolution of our UCLES spectra. Several regions of the 4000-5000 Å part of the observed spectra of the stars were compared by eye to the spectra of the nearest spectral types. In some cases the template spectra were artificially broadened in order to match the rotational velocity of the star to be classified. No discrepancies between the target stars and their corresponding spectral templates were found, leading us to conclude that all of our stars have their previous Michigan Spectral Catalog classification confirmed. In cases when the Michigan Spectral Catalog had an uncertainty of the order of 1 or 2 spectral sub-classes, our method was able to discriminate and associate the star with one of those spectral types, as listed in Table 5.3.

[1] `http://www.iraf.noao.edu`

Table 5.2: Log of UCLES observations.

Object	RA (J2000)	Dec (J2000)	Airmass	Seeing (arcseconds)	Exposure (s)	Central Wavelength (Å)	Slitwidth (mm)	Slitlength (mm)
HD 53842	06:46:00.45	-83:59:35.2	1.780	1.5	1000	4400.03	1.05	4.96
			1.803	1.5	1000	4400.03	1.05	4.96
			1.832	1.5	1000	4400.03	1.05	4.96
			2.249	2.5	400	6699.95	1.05	4.01
HD 61950	07:36:16.97	-69:03:29.6	1.384	1.5	750	4400.03	1.05	4.96
			1.413	1.5	750	4400.03	1.05	4.96
			3.699	2.5	350	6699.95	1.05	4.01
HD 75416	08:41:14.77	-78:57:55.3	1.496	1.5	250	4400.03	1.05	4.96
			1.501	1.5	250	4400.03	1.05	4.96
			2.348	2.5	200	6699.95	1.05	4.01
HD 80950	09:17:24.97	-74:44:09.9	1.384	1.5	500	4400.03	1.05	4.96
			2.447	2.5	200	6699.95	1.05	4.01
HD 88955	10:14:44.29	-42:07:21.1	1.080	1.5	100	4400.03	1.05	4.96
			2.438	2.5	50	6699.95	1.05	4.01
HD 91375	10:30:18.21	-71:59:40.1	1.353	1.5	200	4400.03	1.05	4.96
			2.195	2.5	60	6699.95	1.05	4.01
HD 99211	11:24:53.33	-17:41:05.1	1.043	1.5	150	4400.03	1.05	4.96
			2.188	2.5	40	6699.95	1.05	4.01
HD 110058	12:39:46.24	-49:11:54.5	1.055	1.5	1000	4400.03	1.05	4.96
			1.051	1.5	1000	4400.03	1.05	4.96
			1.053	1.5	1000	4400.03	1.05	4.96
			1.345	2.5	1000	6699.95	1.05	4.01
HD 117360	13:33:10.61	-77:34:13.7	1.446	2.5	800	4400.03	1.05	4.96
			1.446	2.5	800	4400.03	1.05	4.96
			1.625	3.0	400	6699.95	1.05	4.01
HD 123247	14:07:40.85	-48:42:14.8	1.048	2.5	1000	4400.03	1.05	4.96
HD 166841	18:17:59.57	-68:13:46.0	1.318	2.3	800	4400.02	1.05	5.01
			1.256	3.0	400	6699.95	1.05	4.01
HD 176638	19:03:06.95	-42:05:39.6	1.075	2.3	250	4400.02	1.05	5.01
			1.048	3.0	80	6699.95	1.05	4.01
HD 181327	19:22:58.63	-54:32:17.2	1.127	2.0	900	4400.02	1.05	5.01
			1.150	2.0	900	4400.02	1.05	5.01
			1.119	2.3	400	6699.95	1.05	4.01
HD 181869	19:23:53.25	-40:36:56.3	1.024	2.3	100	6699.95	1.05	4.01
			1.114	2.0	100	4400.02	1.05	5.01
			1.039	2.3	40	6699.95	1.05	4.01
HD 191089	20:09:05.54	-26:13:23.1	1.013	2.3	1000	4400.02	1.05	5.01
			1.005	2.3	1000	4400.02	1.05	5.01
			1.050	2.3	400	6699.95	1.05	4.01
			1.087	2.3	400	6699.95	1.05	4.01
HD 203608	21:26:25.91	-65:21:56.9	1.207	2.0	200.0	4400.02	1.05	5.01
			1.357	2.3	100	6699.95	1.05	4.01
HR 5558	14:55:44.86	-33:51:19.9	1.006	2.5	500	4400.03	1.05	4.96
			1.164	3.0	120	6699.95	1.05	4.01
HR 5670	15:17:30.36	-58:48:04.9	1.134	2.5	200	4400.03	1.05	4.96
			1.225	3.0	40	6699.95	1.05	4.01
HR 6045	16:15:15.23	-47:22:17.4	1.085	2.5	400	4400.03	1.05	4.96
			1.048	2.5	100	6699.95	1.05	4.01

All observations were taken on the night of May 20^{th} 2000.

5.4.1 Equivalent widths

Measurement of the equivalent widths of the most prominent metallic lines present in the spectra of our targets was performed using the EW command in DIPSO (Howarth & Murray 1988). Where narrow absorption features were present within the broad stellar lines, they were excluded from the spectra during the measurement of the equivalent width using the SNIP command. EW returns the computed equivalent widths and error estimates. The EWs for the Ca II, Fe I, Fe I and Mg II photospheric lines are presented in Table 5.3.

5.4.2 Radial and rotational velocities

The heliocentric radial velocity ($V_{\odot}$) of a star can be derived by modeling the photospheric lines assuming that they have a Gaussian profile. This is not strictly valid as photospheric wings drop faster and they also tend to be slightly flatter in the cores, but to first order this is a fair approximation. Gaussian modeling of the photospheric lines was performed using the Emission Line Fitting (ELF) routine implemented in DIPSO. Although originally implemented for fitting emission lines, ELF works well for fitting absorption line profiles, to which it assigns negative line fluxes, as well as line centres and FWHM. From the best-fit line centres and Gaussian FWHM, the heliocentric velocities $V_{\odot}$ are readily derived. The component of the relative velocity between the Sun and the observed star ($V_{\odot}$) are obtained using the Doppler Formula,

$$V_{\odot} = \frac{\lambda - \lambda_o}{\lambda_o} c - (Helio), \tag{5.1}$$

where λ_o and λ refer to the observed and rest wavelength of the studied atomic transition, c is the speed of light and (Helio) is the Earth-Sun velocity correction (obtained using the Radial Velocity (RV) Starlink package). In the case of the F-type stars (and the A9 star HD 99211), whose spectra are rich in metallic species, radial velocities were derived by cross-correlating the observed spectra with template spectra from stars of similar spectral type from the UVESPOP database, for which radial velocities had already been measured (Noterdaeme et al., *in preparation*; C. Melo, private communication). The FXCORR task in IRAF was used for this purpose, which allows one to cross-correlate several echelle orders simultaneously, providing a very accurate determination of $V_{\odot}$. This is reflected in the small error estimates presented in Table 5.3, which correspond to the standard deviation of the velocities obtained in the different orders. For the case of the late B-type

Table 5.3: Measured parameters of the Vega-like stars

Star	Spectral Type	EW (Å) Ca II 3933.66 Å	EW (mÅ) Fe I 4045.81 Å	EW (mÅ) Fe I 4071.74 Å	EW (mÅ) Mg II 4481.23 Å	$v \sin i$ (km s^{-1})	$V_\odot$ (km s^{-1})
HD 53842	F5V	7.7	481	282	268	24±2	10 ±1
HD 61950	B8V	0.2	-	-	390	240 ±9	20±5
HD 75416	B8V	-	-	-	364	290 ±2	15 ±5
HD 80950	A0V	0.7	63	54	386	80 ±4	14±3
HD 88955	A1V	1.5	150	150	400	100 ±4	7±3
HD 91375	A1V	1	137	9	300	15 ±2	8±3
HD 99211	A9V	3.3	300	200	500	110 ±2	-1 ±2
HD 110058	A0V	1.1	165	127	305	180 ±4	12 ±3
HD 117360	F5V	6.9	444	261	132	11 ±2	-33 ±1
HD 123247	B9V	0.4	54	51	280	140 ±4	7 ±3
HD 166841	B9V	0.5	-	-	283	245 ±8	0 ±3
HD 176638	A0V	0.6	-	-	-	260 ±6	-27 ±3
HD 181327	F6V	8.5	500	312	286	22 ±2	-1 ±1
HD 181869	B8V	0.2	-	-	323	55±9	-4 ±5
HD 191089	F5V	7.3	597	328	331	33 ±2	-6 ±1
HD 203608	F6V	6.7	432	258	126	3 ±1	-30 ±1
HR 5558	A0V	0.9	95	66	418	180±4	1 ±3
HR 5670	A3V	2.1	190	192	530	95 ±4	9 ±2
HR 6045	B8V	0.2	-	-	219	205±5	1 ±4

Derived parameters for the observed stars. Column 2 confirms the previous spectral classification for all of our targets. Columns 3-6 list the absorption-line equivalent widths for Ca II K, Fe I and Mg II. Units are in mÅ, except in column 3 for which the units are in Å. Columns 7 and 8 list the projected rotational velocities ($v \sin i$) and the radial heliocentric velocities ($V_\odot$), respectively. The uncertainties quoted for $V_\odot$ and $v \sin i$ correspond to the dispersion obtained when deriving the quantities using the different lines. In all cases except the F-type stars, the measured equivalent width of the Mg II correspond to the blend of the two Mg II components at 4481.13 Å and 4481.33 Å. The - sign indicates that no line was detected.

and early A-type stars, these stars have intrinsically fewer metallic lines that can be used for radial velocity estimations. Therefore the most prominent photospheric lines of Ca II, Mg II and Fe I were used for performing Gaussian fitting and velocity derivation. The $V_\odot$ values listed in Table 5.3 for these stars correspond to the mean obtained using the different lines. The Mg II doublet at 4481.13 Å and 4481.33 Å is unresolved in the case of the B- and early A-type stars, and therefore was not used for radial velocity determination.

Projected rotational velocities ($v \sin i$) were derived using the STAROT package within DIPSO, which allows to artificially broaden the spectrum of a stellar template to match the spectra of the observed star. Template spectra with previously measured $v \sin i$ values for each spectral type were taken from the UVESPOP database, by selecting the stars with the lowest rotational velocities. Artificial broadening was then applied until a satisfactory fit to the observed spectra was achieved. Derived rotational velocities for our target stars are presented in column 7 of Table 5.3.

5.5 Evidence for circumstellar gas

4 of our 16 targets are found to exhibit narrow absorption features located near the centre of the photospheric Ca II H & K lines (these stars are HD 61950, HD 75416, HD 110058 and HD 166841). No narrow absorption components can be seen in either the Ca II K or Na I D line profiles of the remaining stars of our sample. In addition, a narrow feature was also detected in the Ca II H & K spectrum of the spectral standard HR 5558. These features, shown in Figure 5.2, are too narrow to be photospheric in nature and therefore they must be produced by absorption of stellar light by either an IS or CS gas cloud. Similar absorption features are seen in the Na I D lines, with the exception of HD 61950 and HD 75416, for which only Ca II data were available. Figure 5.3 shows the H & K regions of HD 61950 and HD 75416 in the heliocentric velocity frame, with the radial velocities of the stars marked by a vertical line. Figure 5.4 shows the Na I D and the Ca II H& K lines of HD 110058, HD 166841 and HR 5558 in the heliocentric velocity frame. There is a good correspondence between the radial velocities of the components from the different species, as is expected if both the calcium and sodium are located in the same cloud. For both HD 110058 and HD 166841 there is a strong absorption component that coincides, within the errors, with the radial velocity of the star. HD 61950 and HD 75416 have components that partially overlap the stellar radial velocity, while in the case of HR 5558 the velocity of the absorption feature is totally dissimilar to that of the star.

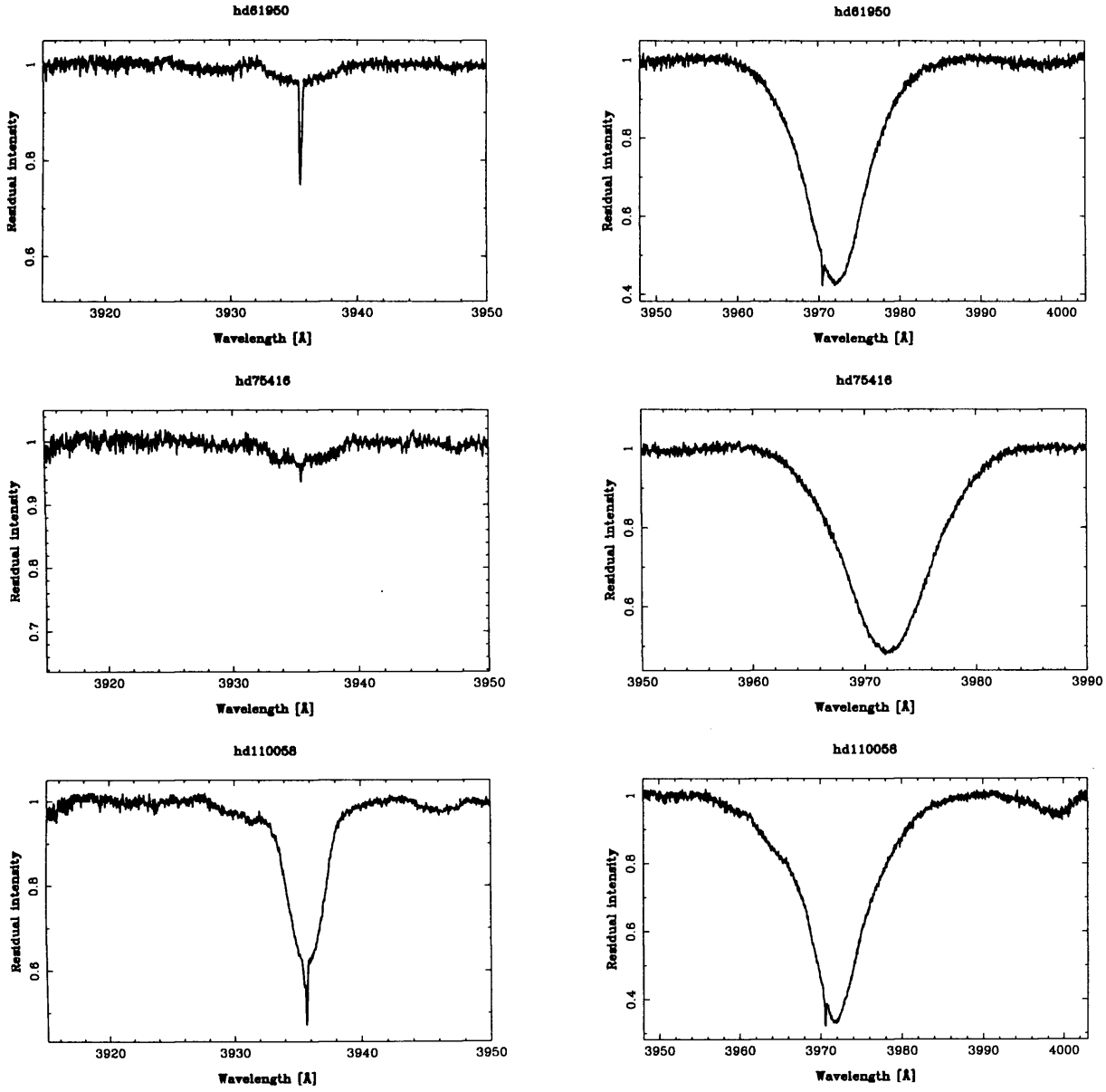

Figure 5.2: Ca II H (left) and K (right) regions of the target stars showing narrow absorption features near the centres of the photospheric lines. The spectra were normalized to unit continuum.

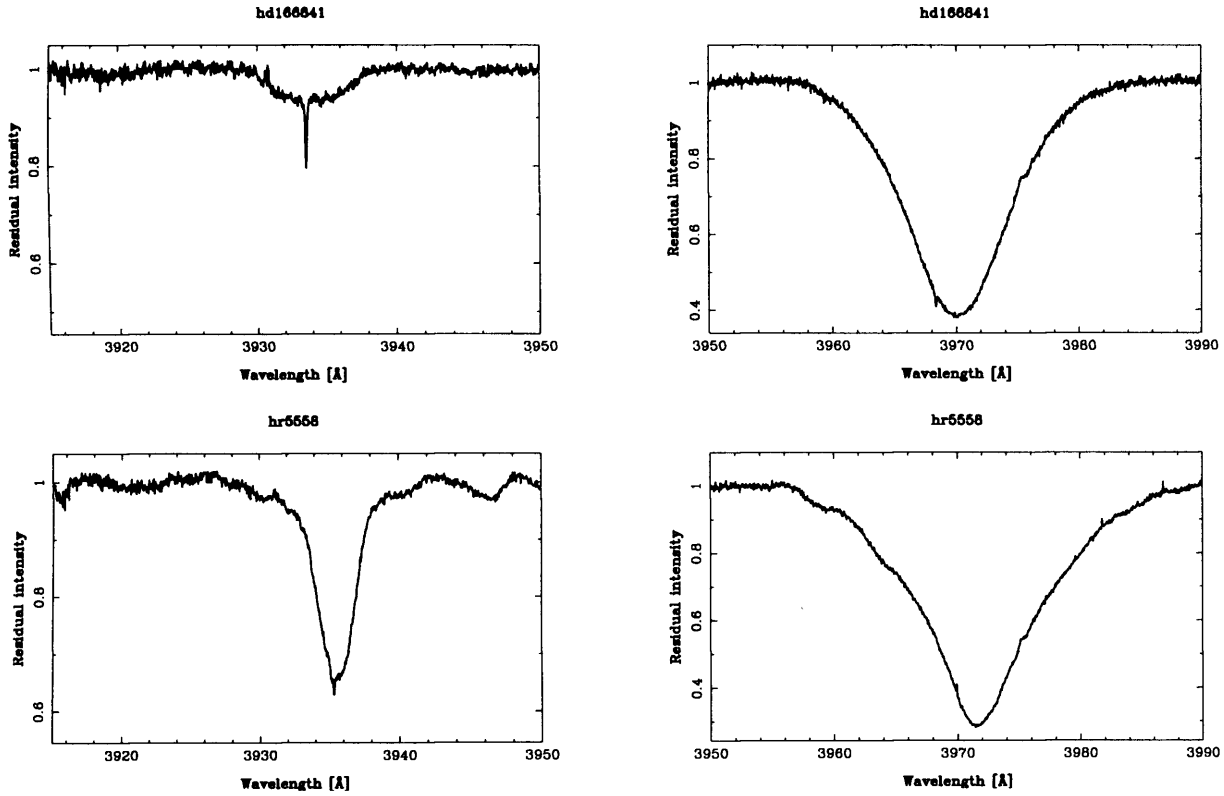

Figure 5.2: *continued*

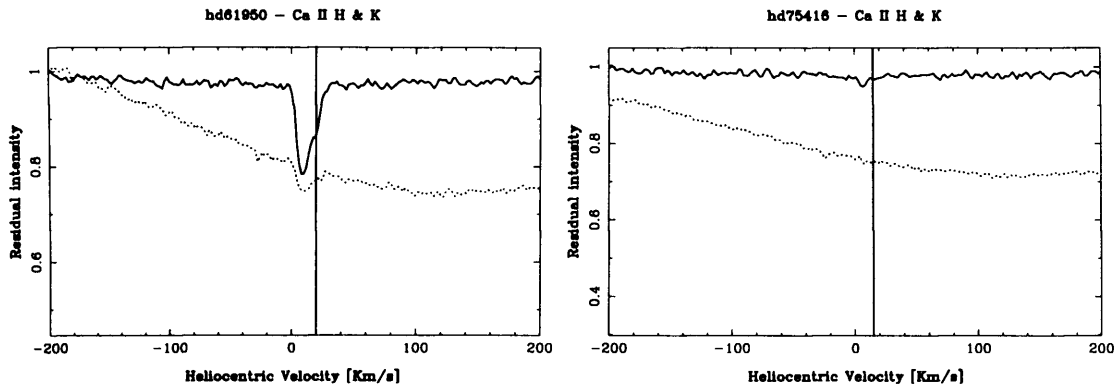

Figure 5.3: Heliocentric velocity plots of the narrow Ca II H (dotted line) and K (solid line) absorption components present in the spectra of HD 61950 and of HD 75416. The vertical lines denote the radial velocity of the star. The H line spectra have been shifted vertically for plotting purposes.

However, the fact that both the radial velocity of the star and of the absorbing cloud are similar it is not a sufficient condition to rule out IS absorption. There is not a unique criterion that may be used in order to discriminate between an IS or CS origin for absorption feature, instead it is common to refer to a set of criteria that can be used together in order to resolve the nature of the absorption features (Dunkin et al. 1997*b*). To rule out an IS origin for an absorption feature, one has to consider:

- Is the radial velocity of the narrow absorption feature the same as the stellar velocity?
- Is the radial velocity of the narrow absorption consistent or not with known interstellar velocities in the same direction?
- Is the observed N(Ca II)/N(Na I) column density ratio consistent with CS (usually>1) or IS (usually<1) values?
- Is there the presence or absence of interstellar extinction suggestive of a foreground cloud?

In order to carry out this analysis, a derivation of the equivalent widths and radial velocities of the absorption features is required. For this purpose, the spectrum of the region containing the narrow features was normalized to unity by dividing it by the photospheric profile fitted in Section 5.4.2, or normalized 'by hand' using the Continuum Draw (CDRAW) command in DIPSO. Following the normalization, one or more narrow

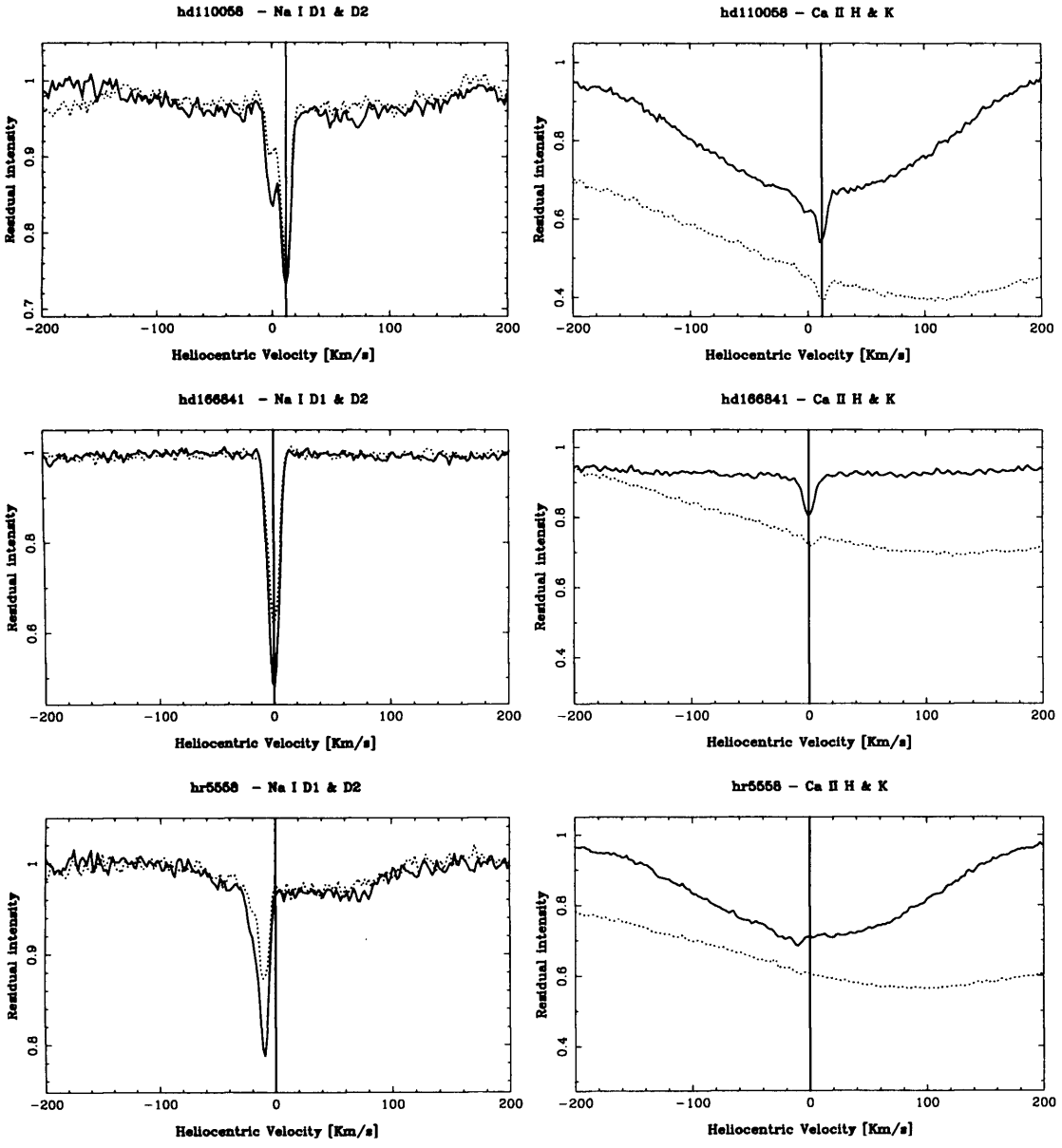

Figure 5.4: Heliocentric velocity plots of narrow absorption features seen in both the Ca II H & K lines (right-hand panel) and in the Na I D lines (left-hand panel). The solid lines correspond to the Ca II K and Na I D_2 lines. The Na I region of the spectra was divided by the spectrum of the B8 spectral standard HR 6045 in order to remove telluric absorption features.

Table 5.4: Equivalent widths and heliocentric velocities of the narrow absorption lines observed in the spectra of the target stars. The equivalent widths are in mÅ. For stars where two entries are listed, these correspond to separate velocity components.

Star	Ca II K		Ca II H		Na I D_1		Na I D_2	
	EW (mÅ)	$V_\odot$ (km s^{-1})	EW (mÅ)	$V_\odot$ (km s^{-1})	EW (mÅ)	$V_\odot$ (km s^{-1})	EW (mÅ)	$V_\odot$ (km s^{-1})
HD 61950	27.1±2.1	8.3±0.4	12.2±2.7	8.8±0.7	-	-	-	-
	14.2±1.9	17.9±0.8	6.3±2.1	17.1±0.9	-	-	-	-
HD 75416	2.5±1.1	-7.9±3.1	-	-	-	-	-	-
	2.7±0.5	6.9±0.5	-	-	-	-	-	-
	1.3±0.7	17.2±1.8	-	-	-	-	-	-
HD 110058	13.9±2.1	-1.2±0.5	5.8 ±2.5	-2.4±0.6	11.3±1.5	-1.4±0.9	28.7±2.2	-0.3±0.8
	22.3±1.3	11.8±0.1	19.6±1.9	11.9±0.3	45.5±4.9	12.9±0.7	46.9±5.2	12.0±0.5
HD 166841	20.1±1.7	0.1 ±0.2	6.1±2.1	1.5 ±0.4	93.1±9.7	-0.1±0.3	134.4±6.9	-0.1±0.2
HR 5588	-	-	-	-	4.2±1.1	-17.1±4.9	13.1±0.9	-17.4±3.8
	4.7±1.1	-10.3±0.9	-	-	20.5±3.2	-10.5±0.8	33.3±4.5	-10.2±0.6

absorption components are fitted with Gaussian profiles using ELF, which returns the equivalent width and centre of each component. Table 5.4 presents the derived equivalent widths and radial velocities of the narrow Ca II and Na I absorption features present in the spectra of our targets.

5.5.1 Cloud modeling

The IS routine in DIPSO allows for modeling of possible absorption clouds so as to obtain the physical parameters of the absorbing cloud. The input parameters of each modeled cloud are its column density (N), radial velocity (v) and the velocity dispersion (b). The line centre and line FWHM obtained by the least-square fitting routine in ELF can be used as a first estimation of v and b ($FWHM = 1.6651 \cdot b$), while an initial estimate of the column density of each component can be obtained using the relation (e.g. Hunter et al. 2006):

$$N(cm^{-2}) = 1.13 \times 10^{17} \times \frac{\mathrm{EW(m\AA)}}{f \cdot \lambda^2(\mathrm{\AA})}, \tag{5.2}$$

where EW is the measured equivalent width, f is the oscillator strength of the line (0.635 and 0.631 for the Ca II K and Na I D_2 lines respectively), and λ is the rest wavelength of the transition. The column density, and sometimes the b-values of the individual components were adjusted 'by eye' until a satisfactory fit was obtained. The model parameters that were found to reproduce successfully the data are presented in Table 5.5, while models versus data are plotted in Figures 5.5 and 5.6.

Table 5.5: Line profile parameters for narrow Ca K and Na D_2 velocity components found at the centre of the broad stellar profiles. The last column gives the N(Ca II)/N(Na I) ratio.

Star	Ca K			Na D_2			N(Ca II)/N(Na I)
	$V_\odot$ (km s^{-1})	b (km s^{-1})	log N (cm^{-2})	$V_\odot$ (km s^{-1})	b (km s^{-1})	log N (cm^{-2})	
HD 61950	8.3 ±0.4	5.6±0.2	11.49±0.03	-	-	-	-
	17.9±0.8	6.6±0.4	11.30±0.01	-	-	-	-
HD 75416	-7.9 ±3.1	10.0±0.5	10.46±0.05	-	-	-	-
	6.9 ±0.5	3.8±0.2	10.53±0.04	-	-	-	-
	17.2±1.8	4.8±0.3	10.20±0.06	-	-	-	-
HD 110058	-1.2±0.5	8.1±0.5	11.20±0.03	-0.3±0.8	5.5±0.3	11.14±0.03	1.16
	11.8±0.1	5.2±0.2	11.46±0.05	12.0±0.5	5.5±0.3	11.44±0.02	1.04
HD 166841	0.1±0.2	6.9±0.3	11.40±0.02	-0.1±0.2	6.4±0.4	11.93±0.05	0.295
HR 5588	-	-	-	-17.4±3.8	7.8±0.6	10.96±0.01	-
	-10.3±0.9	3.4±0.2	10.55±0.01	-10.2±0.6	4.7±0.3	10.98±0.01	0.371

Uncertainties in model quantities correspond to the range of values which result in satisfactory agreement between the models and the data.

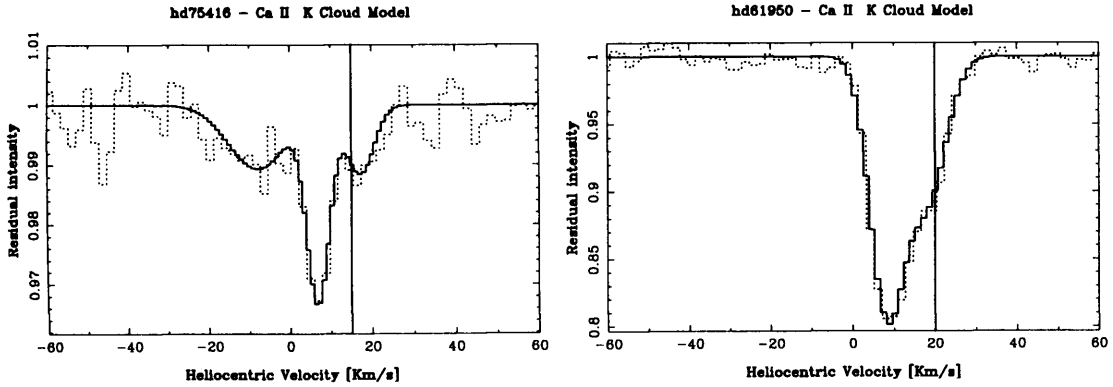

Figure 5.5: Cloud models for the Ca II K absorption features seen towards HD 61950 and HD 75416. The solid line shows the model that gives a satisfactory to the data (dotted line). The vertical line represents the heliocentric velocity of the star.

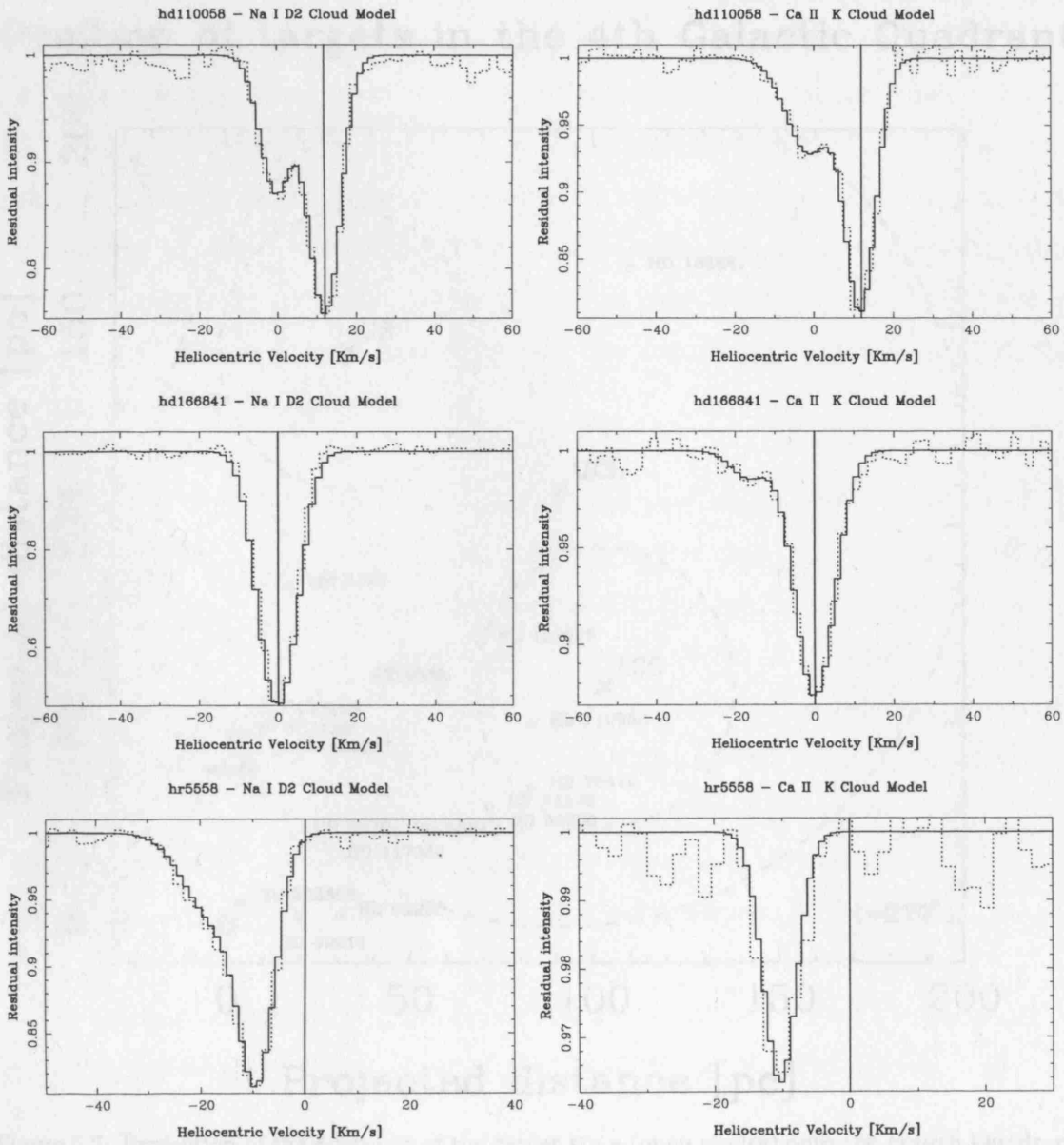

Figure 5.6: Cloud models for the Na I D_2 (left panel) and Ca II K (right panel) absorption features seen towards HD 110058, HD 166841 and HR 5558. The solid line shows the model that gives a satisfactory fit to the data (dotted line). The vertical line represents the heliocentric velocity of the star.

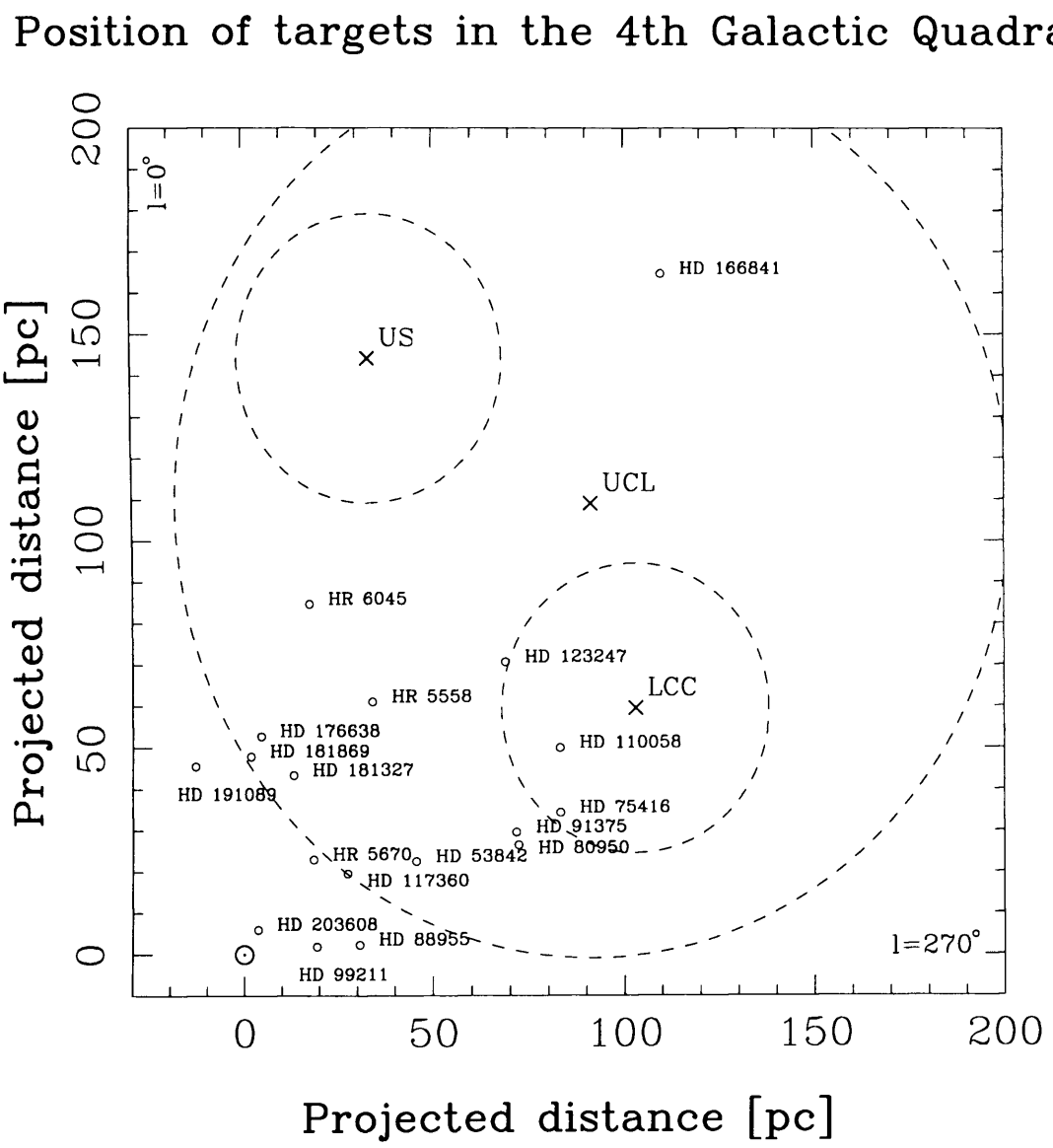

Figure 5.7: Projection of the positions of the target stars (open circles) onto the Fourth Quadrant of the Galactic plane. The dashed circles indicate the location of the UCL, LCC and US H I shells as described in de Geus et al. (1989), de Geus (1992) and de Zeeuw et al. (1999). The centre of each shell is indicated with a cross. The position of the Sun is located at the origin of the coordinates, and is marked with the $\odot$ symbol. The star HD 61950 is located too far away to appear in the plot, positioned near $(x = 330, y = 63)$.

5.5.2 Velocity Projections of known IS clouds/shells

All the stars in this study lie in the Fourth Galactic Quadrant. This region is almost entirely occupied by the Scorpius-Centaurus association, extending between $\sim 290^{\circ} - 360^{\circ}$ in longitude and being the closest OB association to the Sun (Crawford 1991). Three subgroups have been identified to reside within this association: the Upper Centaurus-Lupus (UCL), Lower Centaurus-Crux and the Upper Scorpius shells (de Geus 1992) . These subgroups have been studied extensively and their observational properties are well modeled by expanding spherical shells of gas, whose physical parameters such as shell centre, radius and expansion velocity have been derived by de Geus et al. (1989), de Geus (1992) and de Zeeuw et al. (1999). The location of our target stars with respect to the UCL, LCC and US shells are plotted in Figure 5.7.

In addition to the UCL, LCC and US shells, one must also consider the effect of the Local Interstellar Medium (LIC) within which the Sun is thought to lie. The LIC is a warm, low density IS cloud which is itself located within a hot Local Bubble (LB) in the IS medium which extends to approximately 50 pc (Crawford et al. 1997). The LIC is thought to move in the direction $l = 186^{\circ} \pm 3$, $b = -16^{\circ} \pm 3$, with a heliocentric velocity of $v = 26 \pm 1$ km s^{-1} (Lallement et al. 1995). The LB is thought to contain several small clouds located within a few tens of parsecs of the Sun, with characteristics similar to the LIC. One such possible cloud is the 'G' cloud, which appears to move at $v = 29 \pm 1$ km s^{-1} in the direction $l = 184.5^{\circ} \pm 2.3$ and $b = -20.5^{\circ} \pm 1.8$ (Lallement & Bertin 1992).

The velocity projections of these clouds and shells can be calculated using relations from Crawford (1991) and from Crutcher (1982), which are described below.

5.5.2.1 The LIC and G clouds

Given an IS cloud moving with velocity v_w in a direction (l_w, b_w), the line of sight velocity component of the cloud in a direction (l, b) is given by:

$$\frac{v}{v_w} = \sin b \cdot \sin b_w + \cos b \cdot \cos b_w \cdot \cos (l - l_w), \tag{5.3}$$

where the terms on the right-hand side correspond to the cosine of the angle between (l, b) and (l_w, b_w) .

Table 5.6: Heliocentric Velocity Projections of known IS clouds/shells in the direction of the stars presenting narrow absorption features.

Star	LIC (km s^{-1})	G (km s^{-1})	UCL (km s^{-1})	LCC (km s^{-1})
HD61950	0.65	0.91	9.44	-
HD75416	-3.91	-4.01	4.28	-
HD110058	-11.94	-14.16	-5.25	1.92
HD166841	-15.00	-15.81	-9.06	-
HR5558	-21.55	-24.70	-4.93	

5.5.2.2 The UCL, LCC and US shells

For an expanding shell model the following equation can be used to determine the velocity component for a point (l, b) on the surface of a sphere of radius r_s, centred at a distance R from the Sun at (l_o, b_o):

$$v = \pm \frac{v_o}{r_s} \sqrt{R^2(\cos\theta^2 - 1) + {r_s}^2}, \tag{5.4}$$

where $\cos\theta$ is given by the term in brackets in Equation 5.3 (substituting (l_w, b_w) for (l_o, b_o)), θ is the angle between (l, b) and (l_o, b_o) and v_o is the expansion velocity with respect to the Local Standard of Rest (LSR) or V_{LSR}. To convert from V_{LSR} to V_{Helio} one should use:

$$V_{\rm Helio} = V_{\rm LSR} + LSR(D) - (Helio), \tag{5.5}$$

where the LSR(D) is the dynamical LSR corresction and (Helio) is the Earth-Sun velocity correction, both obtained using the RV implementation. Values of the calculated projected velocity components for the different IS clouds and shells in the direction of HD 61950, HD 75416 , HD 110058 , HD 166841 and HR 5558 are presented in Table 5.6.

5.5.3 Discussion of individual stars

5.5.3.1 HD 61950

HD 61950 is a B8 dwarf that shows a distinctive two-component absorption feature seen in both the Ca H and K lines. The absorption components are centred at +8.3 and +17.9 km s^{-1}, lying near the base of the broad photospheric line. The red-most component, at +17.9±0.8 km s^{-1} coincides within the errors with the star's heliocentric velocity (20±5 km s^{-1}), although there is quite a large uncertainty on the latter due to the lack of prominent metallic lines on the spectrum of this B-type star. The Ca II equivalent width ratio suggests that for both narrow components the line is unsaturated, as the derived K:H EW

ratio is $\sim$ 2 in both cases (a Ca II K:H ratio of 2 is expected in the case of unsaturated lines, as the oscillator strength of the H-line is half that of the K-line).

Given that HD 61950 is the most distant star in our sample (d= 362 pc), it would be sensible to consider these features to be of IS origin. Assuming an intrinsic (B-V) colour of -0.08 typical for a B8V star, implies a nominal colour excess E(B-V) of 0.05, which seems reasonable for such a relatively distant star. The velocity projections of known clouds and shells predicts that the UCL shell should contribute an absorption feature at +9.4 km s^{-1} (Table 5.6), that coincides extremely well with the main absorption component seen at +8 km s^{-1}. Using the 74-inch telescope at the Mount Stromlo Observatory, Sidoli (2002) detected a strong Ca II K component of 21 mÅ equivalent width at $V_{\odot}$=+10.0 km s^{-1} versus 27 mÅ at +8.3 km s^{-1} found here, together with a second component of 3.4 mÅ equivalent width at +22.8 km s^{-1} versus 14 mÅ at +17.9 km s^{-1} found here. If the two features reported by Sidoli (2002) correspond to the two components we detected, there is suggestive evidence for variability of the strength of the component lying near the stellar velocity of +20.0 km s^{-1}. This would argue for a CS origin for the +17.9 km s^{-1} feature. This hypothesis is supported by the large rotational velocity derived for this star, which implies that any disk present would be favourably oriented. As no data for the Na I D region were available, no conclusions regarding the Ca II/Na I ratio can be reached.

However, comparison with Ca II K observations toward stars in similar directions indicate that both components in the spectrum of HD 61950 are IS in nature. The LSR velocities of the two narrow Ca II absorption components seen toward HD 61950 (l=281°, b=21°, d=362 pc) correspond to -3.7 km s^{-1} and +5.9 km s^{-1}. Hunter et al. (2006) detected two absorption components toward HD 76131 (l=273°, b=-7°, d=453 pc) at LSR velocities of -2 km s^{-1} and +8 km s^{-1}, with EWs of 110 mÅ and 21 mÅ respectively. These two velocity components are also detected in the spectra of HD 67536 (l=276°, b=-16°, d=450 pc), at LSR velocities of -4 km s^{-1} and +5.3 km s^{-1} with EW of 16 mÅ and 11 mÅ respectively. The LSR velocities of the two components detected toward HD 61950 therefore lie within the range of velocities at which the two IS velocity clouds reported by Hunter et al. (2006) are detected. It is therefore very likely that both absorption features seen toward HD 61950 are interstellar in nature.

5.5.3.2 HD 75416

HD 75416 lies at a distance of 97 pc and is also a B8V star. Gaussian modeling of the photospheric lines indicate that the star is a fast rotator ($v \sin i \sim$290 km s^{-1}) and that the stellar heliocentric velocity is +15 ±5 km s^{-1} (in agreement with the $V_{\odot} = 14 \pm 10$ km s^{-1} value derived by Evans (1967)). A colour excess of E(B-V)=−0.014 indicates a negligible amount of interstellar extinction toward HD 75416. A very weak absorption feature is detected at the centre of the photospheric Ca II K profile. Three separate cloud components at heliocentric velocities of -7.9, +6.9 and +17.2 km s^{-1}, were required in order to satisfactorily fit the observed profile (Figure 5.5). There is no evidence of corresponding features in the Ca II H region.

The cloud models imply very low calcium column densities, with the strongest components being the ones at -7.9 and +6.9 km s^{-1}. The velocity component observed at +6.9 km s^{-1} could be ascribed as arising in the UCL shell (velocity projection of +4.3 km s^{-1}), however no known clouds/shells can account for the 17.2 km s^{-1} component. This feature is interesting because, despite being very weak (only 1.3 mÅ equivalent width), it lies within the stellar velocity range. However, the lack of additional information regarding this absorption feature makes it difficult to draw any conclusions regarding the nature of this feature. Additional observations of the Na I D region could be useful in resolving the origin of these features, as they could show whether the weak absorption seen at +17.2 km s^{-1} has a Na I D_2 counterpart or not, as well as providing more information on its nature, via the by means of the Ca II/Na I ratio.

5.5.3.3 HD 110058

HD 110058 is an A0V star located at d$\sim$ 100 pc in the direction of the LCC shell. Assuming the normal intrinsic (B-V) colour for an A0V star of 0.00, HD 110058 has a colour excess of E(B-V)=0.15. HD 110058 was first identified by Mannings & Barlow (1998) as a Vega-like star, and was subsequently detected at 1350 μm by Sylvester et al. (2001), which allowed them to construct and model its relatively flat 12 μm to 1350 μm SED. These models suggested the mass of the dust around HD 110058 to be less than $5 \times 10^{-6} M_{\odot}$. Sidoli (2002) derived values of +14 km s^{-1} and 121 km s^{-1} for the heliocentric radial and rotational velocities respectively (versus our +12±3 km s^{-1} and 180±4 km s^{-1}), but no

uncertainties were quoted in his work. In a recent 're-visit' to nearby debris disk systems, Moór et al. (2006) measured the radial velocity of HD 110058 to be +21.7±1.3 km s^{-1}, although given their low instrumental resolution (1 Å) and typical measurement errors of 4-7 km s^{-1} we believe their quoted uncertainty on HD 110058's radial velocity is underestimated.

A strong, sharp, absorption component is detected in both the Calcium and Sodium regions at the very base of the photospheric line, suggesting that it results from CS material. Modeling of the absorption feature indicates that there are actually two velocity components, centred near -1 km s^{-1} and +12 km s^{-1} respectively. None of the known IS clouds/shells appear to have projections at these velocities, and so cannot account for the observed features. The second component, at +12 km s^{-1}, lies right at the stellar radial velocity of +12±3 km s^{-1} we derived, which would argue for a CS nature for this feature.

It is interesting to note that in the case of the +12 km s^{-1} component, the equivalent widths of the D_1 and D_2 lines are equal within the errors, suggesting saturation. The same effect is seen with regards to the H and K calcium lines. This could be explained by the presence of clumpy intervening material, similar to what has been modeled for β Pictoris in order to explain the same effect (Lagrange-Henri et al. 1992). For both velocity components, the Ca II/Na I ratios that we derive are close to unity, and are the largest found in our sample.

The coincidence between the radial velocities of the narrow absorption feature and the star, the lack of known IS clouds/shells that can account for absorptions at these velocities, together with the Ca II/Na I ratio of $\sim$ 1 strongly argue for a CS nature for the component seen at +12 km s^{-1}. In addition, the relatively large stellar $v \sin i$ value also suggests that, if present, a disk will be favorably oriented. The fact that the component seen at $\sim$12 km s^{-1} is saturated while the one at $\sim$-1 km s^{-1} is not, suggests that they may be different in nature. Sidoli (2002) was unable to resolve the two components detected in this work, and reported the detection of a single narrow absorption feature of 21 mÅ equivalent width at +12.0 km s^{-1}. Whether this is evidence of variability (which would strongly support a CS nature) or an instrumental limitation due to the poor sensitivity of the Mount Stromlo observations by Sidoli (2002) could be resolved by

follow-up observations with similar or higher spectral resolution and sensitivity.

5.5.3.4 HD 166841

HD 166841 is B9V star located 214 pc away from the Sun in the direction of the centre of the UCL shell. The star was first identified as a Vega-like object by Mannings & Barlow (1998), but no further studies of this object have been carried out. The value of the projected rotational velocity that we derive (245 ±8 km s^{-1}) is consistent with the star being of late B-type. Despite being a quite distant star, the E(B-V) value we estimate assuming the normal colours of a B9V star (Allen 1976) is quite low (E(B-V)=0.02).

A strong narrow absorption feature is easily seen right at the centre of the photospheric Ca II and Na I lines. Both the calcium and sodium absorption features are found to be located at $V_{\odot}$=0±1 km s^{-1}, coinciding extremely well with the radial velocity of the star. The derived equivalent width of the different component suggest that the lines are not saturated and cloud modeling indicates that Ca II/Na I column density ratio is $\sim$ 0.3.

Although the velocity projections of known clouds/shells cannot be responsible for the observed absorption feature, we investigated the presence of similar absorption components in the spectra of stars in similar directions. The LSR velocity of the component seen toward HD 166841 (l=326°, b=-22°, d=214 pc) is -1.8 km s^{-1}. Hunter et al. (2006) report a +2.4±0.1 km s^{-1} Ca II K component on the direction of HD 142758 (l=325°, b=-4°, d=4000 pc) with 65 mÅ equivalent width. Hunter et al. (2006) also detected two Ca II K absorption features in the spectrum of HD 143448 (l=324°, b=6°, d=520 pc), at -3.6±0.1 km s^{-1} (EW=18 mÅ) and +2.0±0.6 km s^{-1} (EW=59 mÅ), both referred to the LSR. These two stars are located at a higher Galactic latitude than HD 166841 and are more distant, but it is worth noting that the first component seen toward HD 143448 is similar within the errors to the one seen toward HD 166841 both in equivalent width and radial velocity.

Despite being located right at the centre of the photospheric lines, there is not enough supporting evidence to attribute this feature to a CS nature. The star is quite distant and there is some evidence of a correlated velocity structure between the feature seen toward HD 166841 and those towards stars in nearby lines of sight. One argument that

could favor a CS nature for the feature seen toward HD 166841 is the fact that when IS absorption components are detected toward field stars, generally more than one component is detected, whereas in the case of HD 166841 only one distinctive narrow absorption is observed. Observations of stars with lines of sight closer to HD 166841 than the stars quoted above could help to clarify the nature of HD 166841's narrow absorption feature.

5.5.3.5 HR 5558

HR 5558 is an A0V spectral standard located 76 pc away from the Sun. We serendipitously detected a narrow absorption feature noticeable in the Na I D lines (EW of 20 mÅ and 33 mÅ in the D_1 and D_2 lines respectively), and less evident in the Ca II K line. The feature was not detected in the Ca II H line.

There is no correspondence of the radial velocity of the absorption feature with the radial velocity of the star, suggesting that the absorption is of IS origin. This is supported by the low Ca II/Na I ratio derived. Given the diagnostics above, plus the fact that HR 5558 is not known to be a Vega-like star, we conclude that the absorption feature seen toward this star is interstellar in origin.

5.6 Conclusions

We have conducted a search for optical circumstellar absorption lines in the spectra of 16 Vega-like stars. None of the stars in our sample showed signs of emission line activity in either Hα, Ca II or Na I, suggesting that accretion of material onto the stars has ceased. This supports our original hypothesis that, based on their lower $L_{IR}/L_\star$ values, the stars from our sample are more evolved than the stars analyzed in the sample from Dunkin et al. (1997*b*). This suggests that the stars from our sample are true main sequence Vega-like stars, similar to ϵ Eridani and Vega itself, as none of them could be re-classified as HAeBe objects as happened with several of the Walker & Wolstencroft (1988) objects in the sample from Dunkin et al. (1997*b*). The lowest $L_{IR}/L_\star$ star in the sample of Dunkin et al. (1997*b*) for which Hα emission was detected was HD 141569, with $L_{IR}/L_\star = 8.4 \times 10^{-3}$. Our highest infrared excess star is HD 181327 with $L_{IR}/L_\star = 1.9 \times 10^{-3}$. This could indicate that there is 'cut-off' point between $L_{IR}/L_\star \sim 10^{-3}$ and 10^{-2} where Hα (or any) emission is no longer observed.

Four stars were found to exhibit narrow absorption features near the cores of the photospheric Ca II and Na I D lines (when Na I D data was available). In addition similar absorption features were detected in the spectrum of one our spectral standards. Careful analysis of the characteristics of these spectral features allowed us to discriminate between whether they are of circumstellar or interstellar origins. The strongest evidence for a CS nature is seen in one of the two velocity components of the absorption seen in the spectrum of HD 110058 (at +12 km s^{-1}). The good agreement between its radial velocity and that of the star, together with a Ca II/Na I column density ratio close to unity and the lack of known IS clouds or shells at the correct velocities in HD 110058's direction strongly supports a CS origin for this feature. Higher resolution follow-up observations of this star together with observations of adjacent line of sight objects could help in confirming the circumstellar origin of this feature. If confirmed, HD 110058 would represent the Vega-like star with the lowest $L_{IR}/L_{\star}$ value (3.7×10^{-4}) around which a CS gas disk has been detected.

The features detected toward HD 61059 and HR 5558 can be almost unambiguously attributed to IS absorption, while in the case of HD 75416 and HD 166841 the association is less clear. The lack of known IS absorption features within the velocity ranges of the lines seen in both HD 75416 and HD 166841 (which coincide with the stellar velocities) leaves open the question of the nature of these features. Re-observation of these two sources in order to search for variability, together with observations of stars in adjacent lines of sight, could help to disentangle the origin of these features.

CHAPTER 6

Discussion and Future Work

The work carried out in this thesis studied the properties of CS material around dusty main sequence stars. The sample consisted in stellar objects with optical properties that show they have already reached the MS, but with infrared fluxes that indicate they are still surrounded by a CS disk. By combining a set of observational techniques operating at various wavelengths, different components of the disks were allowed to be studied. Near-IR imaging polarimetry was used in order to study the presence and characteristics of scattering dust disks in a sample of dust-excess stars. Another part of this work tackled the difficult problem of studying the presence of CS gas in dusty MS systems. These studies were applied to a sample of dusty MS systems supposedly at different evolutionary stages, and was aimed to reveal physical information on how CS gas and dust evolve in these systems, possibly into planetary systems. A major part of this thesis was also dedicated to the identification of new dusty MS systems and to determine their incidence in the Galactic plane.

The assumption that the systems studied in this work are at different evolutionary stages is based mainly in the fact that they have a wide range of infrared excess values ($L_{IR}/L_{\star}$); It has become well established that $L_{IR}/L_{\star}$ decays with increasing stellar age (e.g. Rieke et al. 2005). Bona fide debris disk are associated with infrared excess values of $L_{IR}/L_{\star} < 10^{-3}$, while stars with $L_{IR}/L_{\star} > 10^{-1}$ are usually T Tauri or HAeBe stars (Zuckerman 2001).

T Tauri and HAeBe stars are by definition emission line objects, implying that gas is still being accreted onto the star and thus that they are still surrounded by large amounts of CS gas. These systems are typically a few Myr old, corresponding to the age at which gaseous planets are thought to form. Debris-disks are, on the other hand, older, gas-depleted systems. β Pictoris itself with $L_{IR}/L_{\star} = 3.3 \times 10^{-3}$ is believed to stand on the border between 'transition objects' (objects with $L_{IR}/L_{\star} \sim 10^{-3}$ but with still large amounts of CS gas) and true debris-disks. When the does transition between a gas-rich to gas depleted disk occur ? The results from this study in combination with the efforts of different surveys, may help in bringing light to this question.

The decay of $L_{IR}/L_{\star}$ has been associated with a decay of the observational signatures of CS gas, both in emission due to accretion of gas onto the star as well as in absorption by a CS gas disk (Dent et al. 2005; Dunkin et al. 1997*b*). The work of Dunkin et al. (1997*b*) showed that most stars with fractional luminosity $L_{IR}/L_{\star} > 10^{-2}$ present emission line features in either Hα, Ca II or the Na I D lines. A survey over a sample of 59 infrared-excess stars by Dent et al. (2005) showed that no CO emission is detected around stars with $L_{IR}/L_{\star} < 10^{-3}$, with the lowest $L_{IR}/L_{\star}$ star around which CO gas was detected being 49 Cet (1.0×10^{-3}). In comparison, the lowest $L_{IR}/L_{\star}$ star in the sample from Dunkin et al. (1997*b*) in which Hα emission was detected was HD 141569, with $L_{IR}/L_{\star} = 8.4 \times 10^{-3}$. The highest infrared excess star in our sample is HD 181327 with $L_{IR}/L_{\star} = 2.0 \times 10^{-3}$, with no emission line activity being detected in any of the 16 objects studied. The results obtained in this study complement surprisingly well with the works from Dunkin et al. (1997*b*) and Dent et al. (2005), which altogether indicate that there may be a 'cut-off' point near $L_{IR}/L_{\star} \sim 10^{-3}$ after which gaseous emission lines are no longer observed.

Evidence of optical circumstellar absorption lines in the spectra of HD 110058 was found. The radial velocity of the absorption and that of the star coincide, the Ca II/Na I column density ratio is close to unity and there is no knowledge of IS clouds or shells that could have components at these velocities in the direction of HD 110058. There seems to be enough evidence to support a CS origin for this feature, although follow-up observations of this star together with observations of adjacent line of sight objects are required to rule out completely an IS absorption. Given the large rotational velocity of HD 110058, together with the positive detection of CS absorption, it is very likely that the orientation

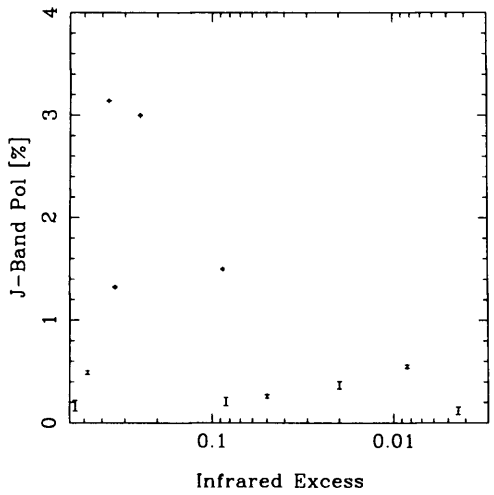

Figure 6.1: J-band integrated polarization as function of infrared excess ($L_{IR}/L_{\star}$). In the case of the resolved disks around HD 169142 and TW Hya, we have plotted the mean polarization measured in the E-vectors (1.5 and 3% respectively), as integrated polarization around their centrosymmetric patterns averages to 0.

of the presumed disk is very close to edge-on. HD 110058 is not thought to be older than 100 Myr (Rieke et al. 2004), but still, the detection of a gas-disk around HD 110058 would probably represent the less-dusty Vega-like star known to be surrounded by CS gas.

The results from the polarimetric imaging survey conducted in this work show a correlation between $L_{IR}/L_{\star}$, the presence of near-IR excess and detectability of near-IR polarization. 4 of the 6 sources having $L_{IR}/L_{\star} > 0.1$ and showing flux excesses at near-IR wavelengths had detectable near-IR polarized fluxes. The behaviour of the J-band polarisation as a function of $L_{IR}/L_{\star}$ is shown in Figure 6.1. No polarized emission was detected toward stars having $L_{IR}/L_{\star}$ lower than 0.1. This is consistent with disk evolutionary scenarios, in which both the IR excess and polarization should decrease as the systems evolve in time (Malfait et al. 1998; Waelkens et al. 1994; Yudin et al. 1999); as the disks mass is reduced, the near-IR excess and the polarizing effects of CS dust should disappear.

The Near-IR polarized emission was resolved around the classical T Tauri TW Hya and the Herbig Ae star HD 169142, indicating that scattering is occurring up to at least 100 and 140 AU respectively. On the other hand, despite having the highest near-IR polarization values in our sample, the polarized emission was not resolved around HD 150193 and HD 142666, suggesting that the CS structure responsible for such emission must be

optically thick, near to edge-on and smaller than 1 arcsecond. This inner, optically thick component is consistent with current views on near-IR excesses, which are commonly attributed to a compact inner ring, located only a few AUs from the central star (Dullemond et al. 2006). On the other hand, we note that our polarimetric observations detected the presence of extended polarizing disks only around systems that have had their SEDs fitted with a flared disc geometry (Krist et al. 2000; Calvet et al. 2002; Dominik & Decin 2003).

The multi-wavelength data acquired for TW Hya allowed the construction of a disk model that, used in conjunction with Monte Carlo scattering codes, provided important information on the geometry of the disk. This work showed that scattered light models can be used to accurately constrain the vertical height of the disk as a function of radial distance from the star (degree of flaring). Although resolved, there were not enough data points to run similar models on the scattered light images of HD 169142. Follow-up H- and K-band imaging polarimetry observations using the NAOS-CONICA system on the 8-meter Very Large Telescope have been granted and scheduled for June 2007 (program 079.C-0189). The purpose of this project is to image the extent of HD 169142's disk at sub-arcsecond resolution in order to apply the same disk modeling technique used to fit TW Hya scattering disk. HD 169142's disk has gained attention by the recent detection of a CO gas disk (Raman et al. 2006), together with the recent HST near-IR imaging of the disk (Grady et al., *in preparation*). Comparisons of the different disk models used to fit the CO data (Panic et al., *in preparation*) and the HST images with the near-IR scattering data will be used to understand the different regions of the disk. Will, for instance, the direct light HST images share a similar radial profile with polarized light images (similar to what is seen in the TW Hya disk) ? Is the CO gas well-mixed with the dust grains responsible for the detected polarization or do they occupy different regions of the disk (both vertically and radially) ?

It has been noted that disk clearing occurs in an in-out way; matter occupying the inner regions of protoplanetary disks and their observational signatures disappear before their outer-region counterparts (Backman & Paresce 1993). In this work it has been found that near-IR excess and near-IR polarization disappear first, with stars with $L_{IR}/L_{\star} < 10^{-3}$ showing no near-IR excess nor detectable polarization. This may be indicative of a) clearing out of the inner region and/or b) coagulation or c) midplane settling of the small grains

required to produce the near-IR scattering. On the other hand, mid-IR excesses and CS gas seem to disappear at similar stages. Sylvester et al. (1996) noted all systems with 12 μm excesses also had values $L_{IR}/L_{\star}$ ranging between 10^{-1} and 10^{-3}. The new 8 μm excess stars found in this work confirm this trend; their $L_{IR}/L_{\star}$ values are also found to range between 10^{-1} and 10^{-3}. This is the same $L_{IR}/L_{\star}$ range in which CS gas activity is detected in most systems. Below $L_{IR}/L_{\star} \sim 10^{-3}$ it is very likely that the systems have cleared most of the hot/warm dust together with most of the CS gas.

The search for Galactic dusty A-type stars successfully demonstrated the use of this technique for exploiting data from current and forthcoming Galactic surveys. 51 new A-type dust-excess systems were identified by cross-correlating optical ground-based IPHAS photometry with data from the *Spitzer Space Telescope*. The incidence of 8 μm and 24 μm excesses in our sample of A-type stars was found to be 1.1 % and 1.2 % respectively. This seems to be a rather low incidence fraction when compared to previous searches for dusty A-type stars (Song et al. 2001), but is consistent with recent *Spitzer* results by Rieke et al. (2005) who found that only 1 % of A-type stars older than 190 Myr had 24 μm excesses of similar strength to the ones in our sample.

The objects that have 8 μm excesses are found to have $L_{IR}/L_{\star}$ values that range between 10^{-1} and 10^{-3}, while in the systems that have a 24 μm excess $L_{IR}/L_{\star} \sim 10^{-2} - 10^{-4}$. These values of $L_{IR}/L_{\star}$ are consistent with the material responsible for the IR excesses being located in geometrically flat disks and not in spherical envelopes (Kenyon & Hartmann 1987). The 8 μm dust-excesses can be well fitted by black bodies of temperatures ranging from 100-700 K, more similar to that of the asteroid belt in our solar system rather than the cooler temperatures associated with Kuiper Belts Objects. Cooler dust may also be present (as in the 24 μm-excess systems), but observations at wavelengths larger than 8 μm are required in order to detect its presence. On the other hand, the 24 μm excesses are well fitted with black-bodies of T$<$ 300 [K]. Longer wavelength follow-up observations would be useful not only to accurately constrain the dust temperatures, but also to determine the total masses of the disk; at sub-mm and mm wavelengths the dust emission is optically thin and therefore it traces the total mass of emitting dust (e.g. Sargent & Beckwith 1994). Sub-mm and mm observations with similar spatial resolution than the one of our survey may be achieved with the current generation of interferometers such as

the Combined Array for Millimeter Astronomy (CARMA) and the Submillimeter Array (SMA).

Recent follow-up spectroscopic observations of the 10 brightest of the 28 stars with 8 μm excesses, taken with the 4.2-meter William Herschel Telescope (WHT), showed that all have strong absorption in Hα and in their blue-region Balmer lines, confirming their early A-type status. 7 of the 23 stars with 24 μm excesses were also observed, and all appeared to be A-type. Object J193002.16+163858.0 from our list of IR-excess emission line candidates was also observed with the WHT, and analysis of this preliminary data confirms the presence of Hα emission. The identification of these new Vega-like systems shows the wealth of new surveys for increasing substantially our knowledge on the occurrence and characteristics of CS disks. When both the IPHAS and MIPSGAL survey are completed, an analysis of the full data-sets will be made in order to provide a complete unbiased catalog of Galactic Vega-like stars.

APPENDIX A

Extinction corrections

The magnitude ranges explored in this work (r′ > 14 mags) correspond to galactic distances generally larger than 1 kpc for A-type stars. Interstellar extinction becomes significant at these distances, and this must be taken into account when recovering the intrinsic colours of a source. Given two photometric measurements λ_1 and λ_2 ,the colour excess between this two measurements is given by:

$$E(\lambda_1 - \lambda_2) = (\lambda_{1,\text{observed}} - \lambda_{1,\text{intrinsic}}) - (\lambda_{2,\text{observed}} - \lambda_{2,\text{intrinsic}}) \quad \text{(A.1)}$$

$$= A_{\lambda_1} - A_{\lambda_2}, \quad \text{(A.2)}$$

where A_{λ_1} and A_{λ_2} are the extinctions at wavelengths λ_1 and λ_2 respectively. In the case of early A-type stars, their intrinsic colours in all optical and near-IR wavelengths are $\sim$0. Therefore, in all optical to mid-IR wavelengths the observed colours correspond to their colour-excesses:

$$E(\lambda_1 - \lambda_2) = (\lambda_{1,\text{observed}} - \lambda_{1,\text{intrinsic}}) - (\lambda_{2,\text{observed}} - \lambda_{2,\text{intrinsic}}) \quad \text{(A.3)}$$

$$= (\lambda_1 - \lambda_2)_{\text{observed}} - (\lambda_1 - \lambda_2)_{\text{intrinsic}} \quad \text{(A.4)}$$

$$= (\lambda_1 - \lambda_2)_{\text{observed}} + 0. \quad \text{(A.5)}$$

Much work has been carried out in determining the behaviour of interstellar extinction at different wavelengths toward different regions of the Galaxy. (Cohen et al. 1981; Cardelli et al. 1989; Indebetouw et al. 2005). In order to estimate the effect of interstellar reddening

in our sample of A-type star, we use the relations from Cohen et al. (1981) to derive the following relations between the extinction at optical and near-IR wavelengths and the observed (r′−i′) colour:

$$A_r = 3.9 \cdot (r' - i') \tag{A.6}$$

$$A_i = 2.9 \cdot (r' - i') \tag{A.7}$$

$$A_J = 1.342 \cdot (r' - i') \tag{A.8}$$

$$A_H = 0.904 \cdot (r' - i') \tag{A.9}$$

$$A_K = 0.585 \cdot (r' - i'). \tag{A.10}$$

The mid-IR wavelength dependence of interstellar extinction has recently been constrained by Indebetouw et al. (2005) using IRAC on-board Spitzer, and these are the relations we use to correct for extinction in the IRAC bands.

$$A_{3.6} = 0.56 \cdot A_K \tag{A.11}$$

$$A_{4.5} = 0.43 \cdot A_K \tag{A.12}$$

$$A_{5.8} = 0.43 \cdot A_K \tag{A.13}$$

$$A_8 = 0.43 \cdot A_K. \tag{A.14}$$

BIBLIOGRAPHY

Adams, F. C., Lada, C. J. & Shu, F. H., 1987, *ApJ*, **312**, 788

Aikawa, Y. & Herbst, E., 1999, *A&A*, **351**, 233

Allen, C. W., 1976, *Astrophysical Quantities* (Astrophysical Quantities, London: Athlone (3rd edition), 1976)

Alves, J. F., Lada, C. J. & Lada, E. A., 2001, *Nature*, **409**, 159

André, P., Ward-Thompson, D. & Barsony, M., 1993, *ApJ*, **406**, 122

Apai, D., Pascucci, I., Brandner, W., Henning, T., Lenzen, R., Potter, D. E., Lagrange, A.-M. & Rousset, G., 2004, *A&A*, **415**, 671

Augereau, J. C., Lagrange, A. M., Mouillet, D. & Ménard, F., 1999, *A&A*, **350**, L51

Aumann, H. H., 1984, *ApJ*, **278**

Aumann, H. H., 1985, *PASP*, **97**, 885

Aumann, H. H. & Probst, R. G., 1991, *ApJ*, **368**, 264

Backman, D. E. & Paresce, F., 1993, in E. H. Levy & J. I. Lunine (eds.), *Protostars and Planets III*, pp. 1253–1304

Bagnulo, S., Jehin, E., Ledoux, C., Cabanac, R., Melo, C., Gilmozzi, R. & The ESO Paranal Science Operations Team, 2003, *The Messenger*, **114**, 10

Beckwith, S. V. W. & Sargent, A. I., 1991, *ApJ*, **381**, 250

Beichman, C. A., Bryden, G., Gautier, T. N., Stapelfeldt, K. R., Werner, M. W., Misselt, K., Rieke, G., Stansberry, J. & Trilling, D., 2005*a*, *ApJ*, **626**, 1061

Beichman, C. A., Bryden, G., Rieke, G. H., Stansberry, J. A., Trilling, D. E., Stapelfeldt, K. R., Werner, M. W., Engelbracht, C. W., Blaylock, M., Gordon, K. D., Chen, C. H., Su, K. Y. L. & Hines, D. C., 2005*b*, *ApJ*, **622**, 1160

Beichman, C. A., Myers, P. C., Emerson, J. P., Harris, S., Mathieu, R., Benson, P. J. & Jennings, R. E., 1986, *ApJ*, **307**, 337

Bergin, E. A., 2003, in C. L. Curry & M. Fich (eds.), *SFChem 2002: Chemistry as a Diagnostic of Star Formation, proceedings of a conference held August 21-23, 2002 at University of Waterloo, Waterloo, Ontario, Canada N2L 3G1. Edited by Charles L. Curry and Michel Fich. NRC Press, Ottawa, Canada, 2003, p. 63.*, p. 63

Bergin, E. A., Aikawa, Y., Blake, G. A. & van Dishoeck, E. F., 2007, in B. Reipurth, D. Jewitt & K. Keil (eds.), *Protostars and Planets V*, pp. 751–766

Berry, D. S. & Gledhill, T. M., 2003, in *Starlink User Notes, No 223*

Beust, H., Lagrange, A.-M., Crawford, I. A., Goudard, C., Spyromilio, J. & Vidal-Madjar, A., 1998, *A&A*, **338**, 1015

Beust, H., Lagrange, A.-M., Plazy, F. & Mouillet, D., 1996, *A&A*, **310**, 181

Beust, H., Reche, R., Augereau, J.-C. & Papaloizou, J., 2005, in I. Kamp & M. Meixner (eds.), *Nearby Resolved Debris Disks*, p. 4

Bevington, P. R. & Robinson, D. K., 2003, *Data reduction and error analysis for the physical sciences* (Data reduction and error analysis for the physical sciences, 3rd ed., by Philip R. Bevington, and Keith D. Robinson. Boston, MA: McGraw-Hill, ISBN 0-07-247227-8, 2003.)

Bohren, C. F. & Huffman, D. R., 1983, *Absorption and scattering of light by small particles* (New York: Wiley, 1983)

Bouvier, J. & Corporon, P., 2001, in H. Zinnecker & R. Mathieu (eds.), *IAU Symposium*, p. 155

Bouwman, J., Meeus, G., de Koter, A., Hony, S., Dominik, C. & Waters, L. B. F. M., 2001, *A&A*, **375**, 950

Brandeker, A., Liseau, R., Olofsson, G. & Fridlund, M., 2004, *A&A*, **413**, 681

Bryden, G., Beichman, C. A., Trilling, D. E., Rieke, G. H., Holmes, E. K., Lawler, S. M., Stapelfeldt, K. R., Werner, M. W., Gautier, T. N., Blaylock, M., Gordon, K. D., Stansberry, J. A. & Su, K. Y. L., 2006, *ApJ*, **636**, 1098

Burrows, C. J., Stapelfeldt, K. R., Watson, A. M., Krist, J. E., Ballester, G. E., Clarke, J. T., Crisp, D., Gallagher, III, J. S., Griffiths, R. E., Hester, J. J., Hoessel, J. G., Holtzman, J. A., Mould, J. R., Scowen, P. A., Trauger, J. T. & Westphal, J. A., 1996, *ApJ*, **473**, 437

Calvet, N., D'Alessio, P., Hartmann, L., Wilner, D., Walsh, A. & Sitko, M., 2002, *ApJ*, **568**, 1008

Cardelli, J. A., Clayton, G. C. & Mathis, J. S., 1989, *ApJ*, **345**, 245

Carey, S. J., Noriega-Crespo, A., Price, S. D., Padgett, D. L., Kraemer, K. E., Indebetouw, R., Mizuno, D. R., Ali, B., Berriman, G. B., Boulanger, F., Cutri, R. M., Ingalls, J. G., Kuchar, T. A., Latter, W. B., Marleau, F. R., Miville-Deschenes, M. A., Molinari, S., Rebull, L. M. & Testi, L., 2005, in *Bulletin of the American Astronomical Society*, p. 1252

Casassus, S., Cabrera, G. F., Förster, F., Pearson, T. J., Readhead, A. C. S. & Dickinson, C., 2006, *ApJ*, **639**, 951

Ceccarelli, C. & Dominik, C., 2005, in A. Wilson (ed.), *The Dusty and Molecular Universe: A Prelude to Herschel and ALMA*, pp. 349–350

Chandler, C. J., Brogan, C. L., Shirley, Y. L. & Loinard, L., 2005, *ApJ*, **632**, 371

Chen, C. H., Patten, B. M., Werner, M. W., Dowell, C. D., Stapelfeldt, K. R., Song, I., Stauffer, J. R., Blaylock, M., Gordon, K. D. & Krause, V., 2005, *ApJ*, **634**, 1372

Cheng, K.-P., Bruhweiler, F. C., Kondo, Y. & Grady, C. A., 1992, *APJl*, **396**, L83

Chiang, E. I. & Goldreich, P., 1997, *ApJ*, **490**, 368

Churchwell, E. B., Benjamin, R. A. & GLIMPSE Team, 2005, *American Astronomical Society Meeting Abstracts*, **206**

Clarke, A. J., Oudmaijer, R. D. & Lumsden, S. L., 2005, *MNRAS*, **363**, 1111

Cohen, J. G., Persson, S. E., Elias, J. H. & Frogel, J. A., 1981, *ApJ*, **249**, 481

Cohen, M. & Kuhi, L. V., 1979, *ApJS*, **41**, 743

Cotera, A. S., Whitney, B. A., Young, E., Wolff, M. J., Wood, K., Povich, M., Schneider, G., Rieke, M. & Thompson, R., 2001, *ApJ*, **556**, 958

Crawford, I. A., 1991, *A&A*, **247**, 183

Crawford, I. A., Beust, H. & Lagrange, A.-M., 1998*a*, *MNRAS*, **294**, L31

Crawford, I. A., Craig, N. & Welsh, B. Y., 1997, *A&A*, **317**, 889

Crawford, I. A., Lallement, R. & Welsh, B. Y., 1998*b*, *MNRAS*, **300**, 1181

Crifo, F., Vidal-Madjar, A., Lallement, R., Ferlet, R. & Gerbaldi, M., 1997, *A&A*, **320**, L29

Crutcher, R. M., 1982, *ApJ*, **254**, 82

D'Alessio, P., Calvet, N. & Hartmann, L., 2001, *ApJ*, **553**, 321

D'Alessio, P., Calvet, N., Hartmann, L., Lizano, S. & Cantó, J., 1999, *ApJ*, **527**, 893

D'Alessio, P., Canto, J., Calvet, N. & Lizano, S., 1998, *ApJ*, **500**, 411

Dame, T. M., Hartmann, D. & Thaddeus, P., 2001, *ApJ*, **547**, 792

de Geus, E. J., 1992, *A&A*, **262**

de Geus, E. J., de Zeeuw, P. T. & Lub, J., 1989, *A&A*, **216**, 44

de Zeeuw, P. T., Hoogerwerf, R., de Bruijne, J. H. J., Brown, A. G. A. & Blaauw, A., 1999, *AJ*, **117**, 354

Deacon, J. R., 1991, *Ph.D. Thesis, University of London*

Decin, G., Dominik, C., Malfait, K., Mayor, M. & Waelkens, C., 2000, *A&A*, **357**, 533

Dent, W. R. F. & Clarke, C., 2005, in *Protostars and Planets V*, p. 8435

Dent, W. R. F., Greaves, J. S. & Coulson, I. M., 2005, *MNRAS*, **359**, 663

D'Odorico, S., Ghigo, M. & Ponz, D., 1987, *An atlas of the thorium-argon spectrum for the ESO Echelle Spectrograph in the 3400-9000 Angstrom region* (ESO Scientific Report, Garching: European Southern Observatory (ESO), 1987)

Dole, H., Lagache, G. & Puget, J.-L., 2003, *ApJ*, **585**, 617

Dominik, C. & Decin, G., 2003, *ApJ*, **598**, 626

Dominik, C., Dullemond, C. P., Waters, L. B. F. M. & Walch, S., 2003, *A&A*, **398**, 607

Drew, J. E., Greimel, R., Irwin, M. J., Aungwerojwit, A., Barlow, M. J., Corradi, R. L. M., Drake, J. J., Gänsicke, B. T., Groot, P., Hales, A., Hopewell, E. C., Irwin, J., Knigge, C., Leisy, P., Lennon, D. J., Mampaso, A., Masheder, M. R. W., Matsuura, M., Morales-Rueda, L., Morris, R. A. H., Parker, Q. A., Phillipps, S., Rodriguez-Gil, P., Roelofs, G., Skillen, I., Sokoloski, J. L., Steeghs, D., Unruh, Y. C., Viironen, K., Vink, J. S., Walton, N. A., Witham, A., Wright, N., Zijlstra, A. A. & Zurita, A., 2005, *MNRAS*, **362**, 753

Dullemond, C. P. & Dominik, C., 2004, *A&A*, **417**, 159

Dullemond, C. P., Dominik, C. & Natta, A., 2001, *ApJ*, **560**, 957

Dullemond, C. P., Hollenbach, D., Kamp, I. & D'Alessio, P., 2006, *astro-ph/0602619*

Dunkin, S. K., Barlow, M. J. & Ryan, S. G., 1997*a*, *MNRAS*, **286**, 604

Dunkin, S. K., Barlow, M. J. & Ryan, S. G., 1997*b*, *MNRAS*, **290**, 165

Dunkin, S. K. & Crawford, I. A., 1998, *MNRAS*, **298**, 275

Dutrey, A., Guilloteau, S., Duvert, G., Prato, L., Simon, M., Schuster, K. & Menard, F., 1996, *A&A*, **309**, 493

Evans, D. S., 1967, in A. H. Batten & J. F. Heard (eds.), *IAU Symp. 30: Determination of Radial Velocities and their Applications*, p. 57

Fazio, G. G., Hora, J. L., Allen, L. E., Ashby, M. L. N., Barmby, P., Deutsch, L. K., Huang, J.-S., Kleiner, S., Marengo, M., Megeath, S. T., Melnick, G. J., Pahre, M. A., Patten, B. M., Polizotti, J., Smith, H. A., Taylor, R. S., Wang, Z., Willner, S. P., Hoffmann, W. F., Pipher, J. L., Forrest, W. J., McMurty, C. W., McCreight, C. R., McKelvey, M. E., McMurray, R. E., Koch, D. G., Moseley, S. H., Arendt, R. G., Mentzell, J. E., Marx, C. T., Losch, P., Mayman, P., Eichhorn, W., Krebs, D., Jhabvala, M., Gezari, D. Y., Fixsen, D. J., Flores, J., Shakoorzadeh, K., Jungo, R., Hakun, C., Workman, L., Karpati, G., Kichak, R., Whitley, R., Mann, S., Tollestrup, E. V., Eisenhardt, P., Stern,

D., Gorjian, V., Bhattacharya, B., Carey, S., Nelson, B. O., Glaccum, W. J., Lacy, M., Lowrance, P. J., Laine, S., Reach, W. T., Stauffer, J. A., Surace, J. A., Wilson, G., Wright, E. L., Hoffman, A., Domingo, G. & Cohen, M., 2004, *ApJs*, **154**, 10

Fukagawa, M., Tamura, M., Itoh, Y., Hayashi, S. S. & Oasa, Y., 2003, *ApJl*, **590**, L49

Gillett, F. C., 1986, in F. P. Israel (ed.), *ASSL Vol. 124: Light on Dark Matter*, pp. 61–69

Gilmour, I. & Sephton, M. A., 2004, *An Introduction to Astrobiology* (An Introduction to Astrobiology, Edited by Iain Gilmour and Mark A. Sephton. ISBN 0521546214. http://www.cambridge.org/us/catalogue/catalogue.asp?isbn=0521546214. Cambridge, UK: Cambridge University Press, 2004.)

Gledhill, T. M., Scarrott, S. M. & Wolstencroft, R. D., 1991, *MNRAS*, **252**, 50P

Gorlova, N., Padgett, D. L., Rieke, G. H., Muzerolle, J., Morrison, J. E., Gordon, K. D., Engelbracht, C. W., Hines, D. C., Hinz, J. C., Noriega-Crespo, A., Rebull, L., Stansberry, J. A., Stapelfeldt, K. R., Su, K. Y. L. & Young, E. T., 2004, *ApJs*, **154**, 448

Gregorio-Hetem, J., Lepine, J. R. D., Quast, G. R., Torres, C. A. O. & de La Reza, R., 1992, *AJ*, **103**, 549

Guilloteau, S., Dutrey, A. & Simon, M., 1999, *A&A*, **348**, 570

Habart, E., Natta, A. & Krügel, E., 2004, *A&A*, **427**, 179

Habing, H. J., Dominik, C., Jourdain de Muizon, M., Laureijs, R. J., Kessler, M. F., Leech, K., Metcalfe, L., Salama, A., Siebenmorgen, R., Trams, N. & Bouchet, P., 2001, *A&A*, **365**, 545

Hales, A. S., Gledhill, T. M., Barlow, M. J. & Lowe, K. T. E., 2006, *MNRAS*, **365**, 1348

Hatchell, J., Richer, J. S., Fuller, G. A., Qualtrough, C. J., Ladd, E. F. & Chandler, C. J., 2005, *A&A*, **440**, 151

Hatzes, A. P., Cochran, W. D., McArthur, B., Baliunas, S. L., Walker, G. A. H., Campbell, B., Irwin, A. W., Yang, S., Kürster, M., Endl, M., Els, S., Butler, R. P. & Marcy, G. W., 2000, *ApJl*, **544**, L145

Hayashi, C., Nakazawa, K. & Nakagawa, Y., 1985, in D. C. Black & M. S. Matthews (eds.), *Protostars and Planets II*, pp. 1100–1153

Hayes, D. S., 1985, in D. S. Hayes, L. E. Pasinetti & A. G. D. Philip (eds.), *IAU Symp. 111: Calibration of Fundamental Stellar Quantities*, pp. 225–249

Herbig, G. H. & Bell, K. R., 1988, *Catalog of emission line stars of the orion population : 3 : 1988* (Lick Observatory Bulletin, Santa Cruz: Lick Observatory, —c1988)

Herbst, E., 2005, in A. Wilson (ed.), *The Dusty and Molecular Universe: A Prelude to Herschel and ALMA*, pp. 205–210

Hines, D. C., Backman, D. E., Bouwman, J., Hillenbrand, L. A., Carpenter, J. M., Meyer, M. R., Kim, J. S., Silverstone, M. D., Rodmann, J., Wolf, S., Mamajek, E. E., Brooke, T. Y., Padgett, D. L., Henning, T., Moro-Martiń, A., Stobie, E., Gordon, K. D., Morrison, J. E., Muzerolle, J. & Su, K. Y. L., 2006, *ApJ*, **638**, 1070

Hines, D. C. & Schneider, G., 2006, *astro-ph/060153*

Hobbs, L. M., Vidal-Madjar, A., Ferlet, R., Albert, C. E. & Gry, C., 1985, *ApJL*, **293**, L29

Holland, W. S., Greaves, J. S., Zuckerman, B., Webb, R. A., McCarthy, C., Coulson, I. M., Walther, D. M., Dent, W. R. F., Gear, W. K. & Robson, I., 1998, *Nature*, **392**, 788

Holweger, H., Hempel, M. & Kamp, I., 1999, *A&A*, **350**, 603

Houk, N. & Smith-Moore, M., 1988, in *Michigan Spectral Survey, Ann Arbor, Dept. of Astronomy, Univ. Michigan (Vol. 4) (1988)*, p. 0

Houk, N., Swift, C. M., Murray, C. A., Penston, M. J. & Binney, J. J., 1997, in *ESA SP-402: Hipparcos - Venice '97*, pp. 279–282

Howarth, I. D. & Murray, J., 1988, in *Starlink User Note, No. 50*

Hunter, I., Smoker, J. V., Keenan, F. P., Ledoux, C., Jehin, E., Cabanac, R., Melo, C. & Bagnulo, S., 2006, *MNRAS*, **367**, 1478

Indebetouw, R., Mathis, J. S., Babler, B. L., Meade, M. R., Watson, C., Whitney, B. A., Wolff, M. J., Wolfire, M. G., Cohen, M., Bania, T. M., Benjamin, R. A., Clemens, D. P., Dickey, J. M., Jackson, J. M., Kobulnicky, H. A., Marston, A. P., Mercer, E. P., Stauffer, J. R., Stolovy, S. R. & Churchwell, E., 2005, *ApJ*, **619**, 931

Irwin, M. J., 1985, *MNRAS*, **214**, 575

Jonkheid, B., Faas, F. G. A., van Zadelhoff, G.-J. & van Dishoeck, E. F., 2004, *A&A*, **428**, 511

Jørgensen, J. K., Schöier, F. L. & van Dishoeck, E. F., 2005, *A&A*, **435**, 177

Jura, M., Chen, C. H., Furlan, E., Green, J., Sargent, B., Forrest, W. J., Watson, D. M., Barry, D. J., Hall, P., Herter, T. L., Houck, J. R., Sloan, G. C., Uchida, K., D'Alessio, P., Brandl, B. R., Keller, L. D., Kemper, F., Morris, P., Najita, J., Calvet, N., Hartmann, L. & Myers, P. C., 2004, *ApJs*, **154**, 453

Kalas, P. & Jewitt, D., 1995, *AJ*, **110**, 794

Kant, I., Hastie, W. & Ley, W., 1968, *Kant's cosmogony, as in his essay on the retardation of the rotation of the earth and his Natural history and theory of the heavens.* (New York, Greenwood Pub. Corp. [1968])

Kenyon, S. J. & Hartmann, L., 1987, *ApJ*, **323**, 714

Kenyon, S. J. & Hartmann, L., 1995, *ApJs*, **101**, 117

Kessler, M. F., Steinz, J. A., Anderegg, M. E., Clavel, J., Drechsel, G., Estaria, P., Faelker, J., Riedinger, J. R., Robson, A., Taylor, B. G. & Ximenez de Ferran, S., 1996, *A&A*, **315**, L27

Kim, J. S., Hines, D. C., Backman, D. E., Hillenbrand, L. A., Meyer, M. R., Rodmann, J., Moro-Martín, A., Carpenter, J. M., Silverstone, M. D., Bouwman, J., Mamajek, E. E., Wolf, S., Malhotra, R., Pascucci, I., Najita, J., Padgett, D. L., Henning, T., Brooke, T. Y., Cohen, M., Strom, S. E., Stobie, E. B., Engelbracht, C. W., Gordon, K. D., Misselt, K., Morrison, J. E., Muzerolle, J. & Su, K. Y. L., 2005, *ApJ*, **632**, 659

Kim, S.-H., Martin, P. G. & Hendry, P. D., 1994, *ApJ*, **422**, 164

Kondo, Y. & Bruhweiler, F. C., 1985, *ApJL*, **291**, L1

Krist, J. E., Stapelfeldt, K. R., Ménard, F., Padgett, D. L. & Burrows, C. J., 2000, *ApJ*, **538**, 793

Kuhn, J. R., Potter, D. & Parise, B., 2001, *ApJl*, **553**, L189

Lada, C. J. & Wilking, B. A., 1984, *ApJ*, **287**, 610

Lagrange, A.-M., Backman, D. E. & Artymowicz, P., 2000, *Protostars and Planets IV*, 639

Lagrange, A.-M., Beust, H., Mouillet, D., Deleuil, M., Feldman, P. D., Ferlet, R., Hobbs, L., Lecavelier Des Etangs, A., Lissauer, J. J., McGrath, M. A., McPhate, J. B., Spyromilio, J., Tobin, W. & Vidal-Madjar, A., 1998, *A&A*, **330**, 1091

Lagrange-Henri, A. M., Ferlet, R., Vidal-Madjar, A., Beust, H., Gry, C. & Lallement, R., 1990, *A&AS*, **85**, 1089

Lagrange-Henri, A. M., Gosset, E., Beust, H., Ferlet, R. & Vidal-Madjar, A., 1992, *A&A*, **264**, 637

Lallement, R. & Bertin, P., 1992, *A&A*, **266**, 479

Lallement, R., Ferlet, R., Lagrange, A. M., Lemoine, M. & Vidal-Madjar, A., 1995, *A&A*, **304**, 461

Laureijs, R. J., Jourdain de Muizon, M., Leech, K., Siebenmorgen, R., Dominik, C., Habing, H. J., Trams, N. & Kessler, M. F., 2002, *A&A*, **387**, 285

Lee, J.-E., Evans, II, N. J., Shirley, Y. L. & Tatematsu, K., 2003, *ApJ*, **583**, 789

Leinert, C., van Boekel, R., Waters, L. B. F. M., Chesneau, O., Malbet, F., Köhler, R., Jaffe, W., Ratzka, T., Dutrey, A., Preibisch, T., Graser, U., Bakker, E., Chagnon, G., Cotton, W. D., Dominik, C., Dullemond, C. P., Glazenborg-Kluttig, A. W., Glindemann, A., Henning, T., Hofmann, K.-H., de Jong, J., Lenzen, R., Ligori, S., Lopez, B., Meisner, J., Morel, S., Paresce, F., Pel, J.-W., Percheron, I., Perrin, G., Przygodda, F., Richichi, A., Schöller, M., Schuller, P., Stecklum, B., van den Ancker, M. E., von der Lühe, O. & Weigelt, G., 2004, *A&A*, **423**, 537

Leroy, J. L., 1993, *A&AS*, **101**, 551

Low, F. J., Smith, P. S., Werner, M., Chen, C., Krause, V., Jura, M. & Hines, D. C., 2005, *ApJ*, **631**, 1170

Lucas, P. W., Fukagawa, M., Tamura, M., Beckford, A. F., Itoh, Y., Murakawa, K., Suto, H., Hayashi, S. S., Oasa, Y., Naoi, T., Doi, Y., Ebizuka, N. & Kaifu, N., 2004, *MNRAS*, **352**, 1347

Lynden-Bell, D. & Pringle, J. E., 1974, *MNRAS*, **168**, 603

Maheswar, G., Manoj, P. & Bhatt, H. C., 2002, *A&A*, **387**, 1003

Malfait, K., Bogaert, E. & Waelkens, C., 1998, *A&A*, **331**, 211

Mannings, V. & Barlow, M. J., 1998, *ApJ*, **497**, 330

Mayor, M. & Queloz, D., 1995, *Nature*, **378**, 355

McCullough, P. R., Stys, J. E., Valenti, J. A., Johns-Krull, C. M., Janes, K. A., Heasley, J. N., Bye, B. A., Dodd, C., Fleming, S. W., Pinnick, A., Bissinger, R., Gary, B. L., Howell, P. J. & Vanmunster, T., 2006, *ApJ*, **648**, 1228

Meeus, G., Waelkens, C. & Malfait, K., 1998, *A&A*, **329**, 131

Meeus, G., Waters, L. B. F. M., Bouwman, J., van den Ancker, M. E., Waelkens, C. & Malfait, K., 2001, *A&A*, **365**, 476

Mendoza V., E. E., 1968, *ApJ*, **151**, 977

Meyer, M. R., Backman, D. E., Weinberger, A. J. & Wyatt, M. C., 2007, in B. Reipurth, D. Jewitt & K. Keil (eds.), *Protostars and Planets V*, pp. 573–588

Meyer, M. R., Hillenbrand, L. A., Backman, D. E., Beckwith, S. V. W., Bouwman, J., Brooke, T. Y., Carpenter, J. M., Cohen, M., Gorti, U., Henning, T., Hines, D. C., Hollenbach, D., Kim, J. S., Lunine, J., Malhotra, R., Mamajek, E. E., Metchev, S., Moro-Martin, A., Morris, P., Najita, J., Padgett, D. L., Rodmann, J., Silverstone, M. D., Soderblom, D. R., Stauffer, J. R., Stobie, E. B., Strom, S. E., Watson, D. M., Weidenschilling, S. J., Wolf, S., Young, E., Engelbracht, C. W., Gordon, K. D., Misselt, K., Morrison, J., Muzerolle, J. & Su, K., 2004, *ApJs*, **154**, 422

Millan-Gabet, R., Malbet, F., Akeson, R., Leinert, C., Monnier, J. & Waters, R., 2007, in B. Reipurth, D. Jewitt & K. Keil (eds.), *Protostars and Planets V*, pp. 539–554

Miller, G. E. & Scalo, J. M., 1979, *ApJS*, **41**, 513

Moór, A., Ábrahám, P., Derekas, A., Kiss, C., Kiss, L. L.,·Apai, D., Grady, C. & Henning, T., 2006, *ApJ*, **644**, 525

Mora, A., Merín, B., Solano, E., Montesinos, B., de Winter, D., Eiroa, C., Ferlet, R., Grady, C. A., Davies, J. K., Miranda, L. F., Oudmaijer, R. D., Palacios, J., Quirrenbach, A., Harris, A. W., Rauer, H., Cameron, A., Deeg, H. J., Garzón, F., Penny, A., Schneider, J., Tsapras, Y. & Wesselius, P. R., 2001, *A&A*, **378**, 116

Moshir, M., 1989, *IRAS Faint Source Survey, Explanatory supplement version 1 and tape* (Pasadena: Infrared Processing and Analysis Center, California Institute of Technology, 1989, edited by Moshir, M.)

Natta, A., Testi, L., Calvet, N., Henning, T., Waters, R. & Wilner, D., 2007, in B. Reipurth, D. Jewitt & K. Keil (eds.), *Protostars and Planets V*, pp. 767–781

Natta, A., Testi, L., Neri, R., Shepherd, D. S. & Wilner, D. J., 2004, *A&A*, **416**, 179

Olofsson, G., Liseau, R. & Brandeker, A., 2001, *ApJl*, **563**, L77

Oudmaijer, R. D., van der Veen, W. E. C. J., Waters, L. B. F. M., Trams, N. R., Waelkens, C. & Engelsman, E., 1992, *A&AS*, **96**, 625

Pascucci, I., Meyer, M., Gorti, U., Hollenbach, D., Hillenbrand, L., Carpenter, J., Najita, J., Kim, S., Silverstone, M., Hines, D., Padgett, D., Bouwman, J., Rodmann, J., Wolf, S. & Lunine, J., 2005, in *Protostars and Planets V*, p. 8468

Pérez, M. R., van den Ancker, M. E., de Winter, D. & Bopp, B. W., 2004, *A&A*, **416**, 647

Perryman, M. A. C., Lindegren, L., Kovalevsky, J., Hoeg, E., Bastian, U., Bernacca, P. L., Crézé, M., Donati, F., Grenon, M., van Leeuwen, F., van der Marel, H., Mignard, F., Murray, C. A., Le Poole, R. S., Schrijver, H., Turon, C., Arenou, F., Froeschlé, M. & Petersen, C. S., 1997, *A&A*, **323**, L49

Pickles, A. J., 1998, *PASP*, **110**, 863

Plets, H. & Vynckier, C., 1999, *A&A*, **343**, 496

Prato, L., Ghez, A. M., Piña, R. K., Telesco, C. M., Fisher, R. S., Wizinowich, P., Lai, O., Acton, D. S. & Stomski, P., 2001, *ApJ*, **549**, 590

Raman, A., Lisanti, M., Wilner, D. J., Qi, C. & Hogerheijde, M., 2006, *AJ*, **131**, 2290

Rieke, G. H., Su, K. Y. L., Stansberry, J. A., Trilling, D., Bryden, G., Muzerolle, J., White, B., Gorlova, N., Young, E. T., Beichman, C. A., Stapelfeldt, K. R. & Hines, D. C., 2005, *ApJ*, **620**, 1010

Rieke, G. H., Young, E. T., Engelbracht, C. W., Kelly, D. M., Low, F. J., Haller, E. E., Beeman, J. W., Gordon, K. D., Stansberry, J. A., Misselt, K. A., Cadien, J., Morrison, J. E., Rivlis, G., Latter, W. B., Noriega-Crespo, A., Padgett, D. L., Stapelfeldt, K. R., Hines, D. C., Egami, E., Muzerolle, J., Alonso-Herrero, A., Blaylock, M., Dole, H., Hinz, J. L., Le Floc'h, E., Papovich, C., Pérez-González, P. G., Smith, P. S., Su, K. Y. L., Bennett, L., Frayer, D. T., Henderson, D., Lu, N., Masci, F., Pesenson, M., Rebull, L., Rho, J., Keene, J., Stolovy, S., Wachter, S., Wheaton, W., Werner, M. W. & Richards, P. L., 2004, *ApJS*, **154**, 25

Roberge, A., Feldman, P. D., Weinberger, A. J., Deleuil, M. & Bouret, J.-C., 2006, *Nature*, **441**, 724

Roberge, A., Weinberger, A. J. & Malumuth, E. M., 2005, *ApJ*, **622**, 1171

Rucinski, S. M., 1985, *AJ*, **90**, 2321

Santos, N. C., Bouchy, F., Mayor, M., Pepe, F., Queloz, D., Udry, S., Lovis, C., Bazot, M., Benz, W., Bertaux, J.-L., Lo Curto, G., Delfosse, X., Mordasini, C., Naef, D., Sivan, J.-P. & Vauclair, S., 2004, *A&A*, **426**, L19

Sargent, A. & Beckwith, S., 1994, in M. Ishiguro & J. Welch (eds.), *ASP Conf. Ser. 59: IAU Colloq. 140: Astronomy with Millimeter and Submillimeter Wave Interferometry*, p. 203

Schneider, G. & HST/GO 10177 Team, 2005, *Bulletin of the American Astronomical Society*, **37**, 1168

Shakura, N. I. & Sunyaev, R. A., 1973, *A&A*, **24**, 337

Shu, F. H., Adams, F. C. & Lizano, S., 1987, *ArA&A*, **25**, 23

Sicilia-Aguilar, A., Hartmann, L., Calvet, N., Megeath, S. T., Muzerolle, J., Allen, L., D'Alessio, P., Merín, B., Stauffer, J., Young, E. & Lada, C., 2006, *ApJ*, **638**, 897

Sidoli, F., 2002, *M.Sci. Thesis, University College London*

Silverstone, M. D., 2000, *Ph.D. Thesis, University of California*

Silverstone, M. D., Meyer, M. R., Mamajek, E. E., Hines, D. C., Hillenbrand, L. A., Najita, J., Pascucci, I., Bouwman, J., Kim, J. S., Carpenter, J. M., Stauffer, J. R., Backman, D. E., Moro-Martin, A., Henning, T., Wolf, S., Brooke, T. Y. & Padgett, D. L., 2006, *ApJ*, **639**, 1138

Slettebak, A., 1975, *ApJ*, **197**, 137

Sloan, G. C., Charmandaris, V., Fajardo-Acosta, S. B., Shupe, D. L., Morris, P. W., Su, K. Y. L., Hines, D. C., Rho, J. & Engelbracht, C. W., 2004, *ApJl*, **614**, L77

Smith, B. A. & Terrile, R. J., 1984, *Science*, **226**, 1421

Smith, P. S., Hines, D. C., Low, F. J., Gehrz, R. D., Polomski, E. F. & Woodward, C. E., 2006, *ApJl*, **644**, L125

Song, I., 2000, *Ph.D. Thesis, University of Georgia*

Song, I., Caillault, J.-P., Barrado y Navascués, D. & Stauffer, J. R., 2001, *ApJ*, **546**, 352

Stapelfeldt, K. R., Holmes, E. K., Chen, C., Rieke, G. H., Su, K. Y. L., Hines, D. C., Werner, M. W., Beichman, C. A., Jura, M., Padgett, D. L., Stansberry, J. A., Bendo, G., Cadien, J., Marengo, M., Thompson, T., Velusamy, T., Backus, C., Blaylock, M., Egami, E., Engelbracht, C. W., Frayer, D. T., Gordon, K. D., Keene, J., Latter, W. B., Megeath, T., Misselt, K., Morrison, J. E., Muzerolle, J., Noriega-Crespo, A., Van Cleve, J. & Young, E. T., 2004, *ApJs*, **154**, 458

Stauffer, J. R., Rebull, L. M., Carpenter, J., Hillenbrand, L., Backman, D., Meyer, M., Kim, J. S., Silverstone, M., Young, E., Hines, D. C., Soderblom, D. R., Mamajek, E., Morris, P., Bouwman, J. & Strom, S. E., 2005, *AJ*, **130**, 1834

Strom, K. M., Wilkin, F. P., Strom, S. E. & Seaman, R. L., 1989, *AJ*, **98**, 1444

Strom, S. E., Edwards, S. & Skrutskie, M. F., 1993, in E. H. Levy & J. I. Lunine (eds.), *Protostars and Planets III*, pp. 837–866

Su, K. Y. L., Rieke, G. H., Misselt, K. A., Stansberry, J. A., Moro-Martin, A., Stapelfeldt, K. R., Werner, M. W., Trilling, D. E., Bendo, G. J., Gordon, K. D., Hines, D. C., Wyatt, M. C., Holland, W. S., Marengo, M., Megeath, S. T. & Fazio, G. G., 2005, *ApJ*, **628**, 487

Sylvester, R. J., Dunkin, S. K. & Barlow, M. J., 2001, *MNRAS*, **327**, 133

Sylvester, R. J. & Mannings, V., 2000, *MNRAS*, **313**, 73

Sylvester, R. J. & Skinner, C. J., 1996, *MNRAS*, **283**, 457

Sylvester, R. J., Skinner, C. J. & Barlow, M. J., 1997, *MNRAS*, **289**, 831

Sylvester, R. J., Skinner, C. J., Barlow, M. J. & Mannings, V., 1996, *MNRAS*, **279**, 915

Tafalla, M., Myers, P. C., Caselli, P. & Walmsley, C. M., 2004, *A&A*, **292**, 347

Trilling, D. E., Koerner, D. W., Barnes, J. W., Ftaclas, C. & Brown, R. H., 2001, *ApJL*, **552**, L151

Uchida, K. I., Calvet, N., Hartmann, L., Kemper, F., Forrest, W. J., Watson, D. M., D'Alessio, P., Chen, C. H., Furlan, E., Sargent, B., Brandl, B. R., Herter, T. L., Morris, P., Myers, P. C., Najita, J., Sloan, G. C., Barry, D. J., Green, J., Keller, L. D. & Hall, P., 2004, *ApJs*, **154**, 439

Uzpen, B., Kobulnicky, H. A., Olsen, K. A. G., Clemens, D. P., Laurance, T. L., Meade, M. R., Babler, B. L., Indebetouw, R., Whitney, B. A., Watson, C., Wolfire, M. G., Wolff, M. J., Benjamin, R. A., Bania, T. M., Cohen, M., Devine, K. E., Dickey, J. M., Heitsch, F., Jackson, J. M., Marston, A. P., Mathis, J. S., Mercer, E. P., Stauffer, J. R., Stolovy, S. R., Backman, D. E. & Churchwell, E., 2005, *ApJ*, **629**, 512

van Dishoeck, E. F., Jørgensen, J. K., Maret, S., Ceccarelli, C., Caux, E., Schöier, F. L., Castets, A. & Tielens, A. G. G. M., 2005, in A. Wilson (ed.), *The Dusty and Molecular Universe: A Prelude to Herschel and ALMA*, pp. 191–196

van Zadelhoff, G.-J., Aikawa, Y., Hogerheijde, M. R. & van Dishoeck, E. F., 2003, *A&A*, **397**, 789

Vidal-Madjar, A., Lecavelier des Etangs, A. & Ferlet, R., 1998, *PLANSS*, **46**, 629

Vink, J. S., Drew, J. E., Harries, T. J. & Oudmaijer, R. D., 2002, *MNRAS*, **337**, 356

Waelkens, C., Bogaert, E. & Waters, L. B. F. M., 1994, in P. S. The, M. R. Perez & E. P. J. van den Heuvel (eds.), *ASP Conf. Ser. 62: The Nature and Evolutionary Status of Herbig Ae/Be Stars*, p. 405

Walker, H. J. & Heinrichsen, I., 2000, *Icarus*, **143**, 147

Walker, H. J. & Wolstencroft, R. D., 1988, *PASP*, **100**, 1509

Walsh, A. J., Bourke, T. L. & Myers, P. C., 2006, *ApJ*, **637**, 860

Waters, L. B. F. M. & Waelkens, C., 1998, *ArA&A*, **36**, 233

Webb, R. A., Zuckerman, B., Platais, I., Patience, J., White, R. J., Schwartz, M. J. & McCarthy, C., 1999, *ApJL*, **512**, L63

Weidenschilling, S. J., 1980, *Icarus*, **44**, 172

Weidenschilling, S. J., 1984, *Icarus*, **60**, 553

Weinberger, A. J., Becklin, E. E., Schneider, G., Chiang, E. I., Lowrance, P. J., Silverstone, M., Zuckerman, B., Hines, D. C. & Smith, B. A., 2002, *ApJ*, **566**, 409

Werner, M. W., Roellig, T. L., Low, F. J., Rieke, G. H., Rieke, M., Hoffmann, W. F., Young, E., Houck, J. R., Brandl, B., Fazio, G. G., Hora, J. L., Gehrz, R. D., Helou, G., Soifer, B. T., Stauffer, J., Keene, J., Eisenhardt, P., Gallagher, D., Gautier, T. N., Irace, W., Lawrence, C. R., Simmons, L., Van Cleve, J. E., Jura, M., Wright, E. L. & Cruikshank, D. P., 2004, *ApJs*, **154**, 1

Whipple, F. L., 1966, *Smithsonian Astrophysical Observatory Star Catalog* (Smithsonian Astrophysical Observatory Star Catalog, Washington: Smithsonian Institution Press, 1966)

Whitney, B. A. & Hartmann, L., 1992, *ApJ*, **395**, 529

Whitney, B. A., Wood, K., Bjorkman, J. E. & Cohen, M., 2003*a*, *ApJ*, **598**, 1079

Whitney, B. A., Wood, K., Bjorkman, J. E. & Wolff, M. J., 2003*b*, *ApJ*, **591**, 1049

Whittet, D. C. B., Martin, P. G., Hough, J. H., Rouse, M. F., Bailey, J. A. & Axon, D. J., 1992, *ApJ*, **386**, 562

Wichmann, R., Bastian, U., Krautter, J., Jankovics, I. & Rucinski, S. M., 1998, *MNRAS*, **301**, L39

Wilner, D. J., D'Alessio, P., Calvet, N., Claussen, M. J. & Hartmann, L., 2005, *ApJL*, **626**, L109

Wood, K., Wolff, M. J., Bjorkman, J. E. & Whitney, B., 2002, *ApJ*, **564**, 887

Wyatt, M. C., 2006, *ApJ*, **639**, 1153

Yudin, R. V., 2000, *A&AS*, **144**, 285

Yudin, R. V., Clarke, D. & Smith, R. A., 1999, *A&A*, **345**, 547

Zuckerman, B., 2001, *ArA&A*, **39**, 549

Zuckerman, B. & Becklin, E. E., 1993, *ApJ*, **414**, 793

Zuckerman, B., Forveille, T. & Kastner, J. H., 1995, *Nature*, **373**, 494

Zuckerman, B. & Song, I., 2004, *ApJ*, **603**, 738